UNIVERSITY OF SOUTHAMPTON

Faculty of Engineering and Applied Science

Department of Electronics and Computer Science

Photorefractive gratings in optical fibres

by Jean-Luc Archambault

A thesis submitted for the degree of

Doctor of Philosophy

November 1994

UNIVERSITY OF SOUTHAMPTON

ABSTRACT

FACULTY OF ENGINEERING AND APPLIED SCIENCE
ELECTRONICS AND COMPUTER SCIENCE

Doctor of Philosophy

PHOTOREFRACTIVE GRATINGS IN OPTICAL FIBRES
by Jean-Luc Archambault

This thesis is an investigation of the fabrication and applications of Bragg gratings produced by the transverse illumination of optical fibres with periodic patterns of ultraviolet light. A general analysis of their optical properties is first presented which considers both the three-dimensional nature of fibre gratings as well as the nonlinear response of the glass to ultraviolet irradiation. The problem of cladding-mode coupling is treated in detail.

A review of the phenomena associated with the photosensitivity of germanosilicate fibres is presented, which includes original measurements of photoinduced birefringence. To explain their dynamics, a new model is proposed, based on the photo-thermal ionisation of germania-related oxygen-deficient centres. The effect of core dopants and known sensitisation techniques on the photoinduced index change are evaluated in over twenty different fibres.

The fabrication of fibre Bragg gratings using a line-narrowed KrF excimer laser and a three-mirror interferometer is described in detail. Narrow, broadband and high reflectivity gratings are obtained in a variety of fibres, including several germania-free fibres. The dynamics of grating formation are measured and are accurately described by theoretical calculations. The writing process is found to be more effective at higher UV intensities, as predicted by the photo-thermal ionisation model. In an investigation of the writing of gratings using single excimer laser pulses, a new regime of grating formation is identified, which occurs above a sharply defined pulse fiuence. This mechanism is used to demonstrate ~100% reflectivity single-pulse gratings. Both low and high reflectivity single pulse gratings are produced for the first time in a fibre drawing tower.

The interaction of KrF excimer laser pulses with germanosilicate fibres is investigated on a nanosecond timescale. This experiment reveals the existence of broadband transient gain and absorption in the $1 \mu m$ region of the spectrum, which provides supportive evidence for a proposed energy-level diagram of oxygen-deficient centres.

A new type of channel-dropping filter, the grating-frustrated coupler, is analysed and demonstrated. The performance of a first prototype - 0.7 nm bandwidth, 13 dB isolation, 70% transmission - shows great promise for wavelength multiplexing and line filtering applications. Several other applications are also described, including fibre lasers, dispersion compensators and sensors.

Contents

Acknowledgments

Chapter 1
Introduction

1.1. Motivation

Over the last twenty years, a vast research effort has been devoted to finding optical waveguide equivalents of bulk optics and electronics components. The availability of a wide variety of optical components is essential to the exploitation of the full potential of optical fibre systems and the future development of all-optical networks. Components based on optical fibres are particularly attractive since they are intrinsically low-loss and fully compatible with fibre systems. In practice, however, very few fibre components have had a significant impact on the design of optical networks, being often too complex, too expensive or simply unnecessary. To find a place on the market, optical components must be seen as reliable and indispensable.

In recent years, a new fibre component has been introduced which has proved to have all the necessary qualities for a rapid integration into commercial applications: the fibre Bragg grating. Fibre gratings are optical fibre equivalents of bulk dielectric mirrors or diffraction gratings. They can be used to reflect, filter or disperse light within an optical fibre. Their simplicity of manufacture and use coupled to their unique properties and numerous advantages make them ideal for a wide range of important applications in telecommunications, lasers and sensors. Consequently, fibre gratings have attracted an increasing amount of attention since the first practical demonstration by Meltz and coworkers in 1989 [1]. In fact, fibre gratings research has followed a similar trend to the explosion of activity which has followed the realisation of the erbium-doped fibre amplifier in the mid-eighties. As for the EDFA, the commercialization of fibre gratings followed the first laboratory demonstration by only a few years.

Fibre gratings research is strongly motivated by pure scientific interest. Fibre photosensitivity, the mechanism responsible for the formation of fibre gratings, was discovered as early as 1978 [2], but has not yet been fully explained. Also, the optical properties of various types of gratings and novel grating-based devices are still to be investigated.

1.2. Historical background

1.2.1. General

Fibre photosensitivity was discovered in 1978 by Hill and co-workers at the Communications Research Centre in Ottawa [2]. In this experiment, light from a single-frequency Argon laser at 514.5 nm was launched into the core of a germania-doped silica fibre. Within minutes, a substantial fraction of the input power was reflected by the fibre; it was found that this reflection was caused by an index grating which had been permanently inscribed in the fibre core. This type of grating is known as a self-organised grating, because it develops without user intervention and reflects light at the wavelength of inscription. Self-organised gratings have never produced any useful devices, since they can only operate at the writing wavelength, which must be in the blue-green region of the optical spectrum. The first fibre gratings designed for infrared wavelengths are known as relief gratings [3,4]. The fabrication of relief fibre gratings involves polishing the side of an optical fibre and physically etching a grating in the polished surface. This process can take several days and comprises a series of critical steps with no guarantee of success.

In the investigations that followed Hill's initial report, one important finding by Lam and Garside was that the growth of self-organised gratings had a quadratic dependence on the writing intensity [5]. This implied that self-organised gratings were driven by two-photon absorption and therefore that the writing of fibre gratings could be made much more efficient by using ultraviolet instead of visible light. This observation led Meltz and coworkers at the United Technologies Research Center to demonstrate for the first time in 1989 that permanent gratings could be written by exposing an optical fibre from the side to two interfering beams of ultraviolet light [1]. Using this technique, gratings can be made to operate as Bragg reflectors at any wavelength longer than the writing wavelength. In contrast with relief gratings, the side-written gratings can be produced in minutes, with very low excess loss and without apparent modification of the fibre.

Because of the numerous and important potential applications of this new technology, Meltz's discovery generated a tremendous amount of interest, resulting in a worldwide research effort on the fabrication and applications of side-written fibre gratings. Progress has been extremely rapid on several fronts, as summarised in Table I. New writing techniques have emerged, such as phase-mask techniques [6,7], point-by-point writing [8]

and single-pulse writing [9-12]. Chirped [13-19], Moiré [20] and blazed [21] gratings have all been realised within the last few years.

Year	Author	Place	Milestone	Ref.
1958	A.J. Cohen		Measurement of UV absorption changes in germania bulk glass; correlation with oxygen deficiencies	[60]
1978	K.O. Hill	CRC	First observation of photosensitivity in fibres; writing of self-organised grating with Argon laser	[2]
1985	P.St.J. Russell	T.U. Hamburg	Relief gratings on side-polished fibres	[3]
1989	G. Meltz	UTRC	Side-writing method: first photorefractive gratings for IR wavelengths	[1]
1990	D.P. Hand	ORC	Colour centre model of photosensitivity	[38]
	D.P. Hand P. Bernardin	ORC Brown U.	Compaction model of photosensitivity	[38, 61]
1991	F. Ouellette	U. Laval	Hydrogen treatment of fibres to enhance photosensitivity	[62]
	K.O. Hill	CRC	Photosensitivity in Eu^{2+}-doped fibres	[31]
	M.M. Broer L. Dong	AT&T ORC	Gratings in Ce^{3+}-doped fibres	[28, 29]
1992	C.G. Atkins	NRL	Low reflectivity single-pulse gratings	[9]
	D. Wong	OFTC	Stress-relief model of photosensitivity	[39]
	H.G. Limberger	EP Lausanne	UV-induced index change$>10^{-3}$ in untreated telecommunications fibre	[63]
	D.L. Williams	BT	Observation of bleaching of 242 nm absorption band in fibre preforms	[64]
1993	P.J. Lemaire	AT&T	UV-induced index change$>10^{-2}$ in H_2-loaded fibre	[27]
	B. Malo	CRC	Point-by-point writing technique	[8]
	D.L. Williams	BT	Boron co-doping to enhance fibre photosensitivity	[22]
	J.L. Archambault	ORC	Type II gratings, 100% reflectivity single-pulse gratings	[10]
	K.O. Hill D.Z. Anderson	CRC AT&T	Phase-mask writing technique	[6,7]
	L. Dong	ORC	Production of gratings during fibre draw	[11]
1994	P. Niay	Lille	Gratings in fluorozirconate fibres	[34]
	J.L. Archambault	ORC	Gratings in Al, P and Ta-doped silica fibres	[33]
	J. Albert	CRC	Gratings written at 193 nm	[65]

Table I - Some of the important milestones of fibre gratings research

More importantly, new methods of enhancing the photosensitivity of germania-doped silica fibres have been developed: co-doping fibres with boron [22] or aluminum [23], fabricating fibre preforms in reducing conditions [24,25], 'flame-brushing' fibres with a hydrogen flame [26] and diffusing molecular hydrogen in fibres [27]. The latter method is by far the most effective and can make most fibres extremely photosensitive. Many new photosensitive glasses have also been identified: germania-free silica fibres doped with

cerium [28-30], europium [31,32], tantalum [33], aluminum and/or phosphorus [33], cerium-doped fluorozirconate fibres [34], germania-doped [35] and phosphorus-doped [36] flame-hydrolysis silica waveguides and RF-sputtered tantala waveguides [37].

Sixteen years after Hill's discovery, there is still a lot of debate about the mechanism responsible for photoinduced index-changes in germania-doped silica fibres, not to mention other types of glasses. Two main interpretations have been put forward. One model suggests that the index change results from a reorganisation of colour centres in the glass [38] while others invoke local structural changes resulting from UV irradiation, such as stress-relief [39] or glass compaction [40].

Fibre gratings have already found a large number of applications. One of the first applications has been to use fibre gratings as feedback elements in fibre lasers [41-43]. Single-frequency [43-46], mode-locked [47] and DFB fibre lasers [48] have all been made in this way. Fibre gratings have also been used very successfully as external feedback elements for laser diodes [49]. Several transmission and wavelength-division-multiplexing filters have been demonstrated [20,50-53] as well as gain-flattening filters for fibre amplifiers [21,54]. Recently, there has been a lot of interest in using chirped fibre gratings for pulse compression and dispersion compensation [14,15,18,55]. Another important area of application is sensing. Fibre gratings can be used as local temperature, strain and pressure sensors [56-59]. Quasi-distributed sensors can be realised with arrays of fibre gratings [12].

1.2.2. Fibre gratings in the Optoelectronics Research Centre

Fibre photosensitivity research in Southampton began in the late eighties with experiments on photoinduced index changes [38] and self-organised gratings, including Bragg gratings [66], $\chi^{(2)}$ gratings [67] and rocking filters [68]. Experiments were also carried out to measure changes in absorption [69] and birefringence [70] induced by blue/green light. In 1990, Hand and Russell proposed a model based on colour centre formation to explain the observed phenomena [38].

Experiments on side-written Bragg gratings started in 1990. The experimental setup consisted of a frequency-doubled Argon laser providing 100 mW of UV light at at 257 nm and a two-mirror interferometer to generate the holographic patterns. Later, a three-mirror interferometer was used to avoid problems due to beam imperfections, as discussed in chapter 4. The gratings were typically 2-3 mm long and the highest

reflectivity obtained was 93%, for a writing time of one hour. Some of the gratings have been used in fibre laser and sensing [57] experiments.

In 1991, a line-narrowed KrF excimer laser was introduced, able to produce up to 20 W of average power at 248.5 nm. Some preliminary results were obtained using the previous interferometer. Progress was halted in early 1992, when the equipment had to be moved to a new location, which coincided with the start of this project.

1.3. <u>Basic concepts on photorefractive fibre Bragg gratings</u>

1.3.1. Definitions

A fibre Bragg grating is a short section of optical fibre, typically a few millimeters long, in which the refractive index has a periodic modulation. Fibre gratings are now commonly produced by exposing the core of a single-mode fibre to a periodic pattern of ultraviolet light, which can be generated by two beam interferometry, as illustrated in Fig. 1-1. The period Λ of the pattern is determined by the angle between the two beams. The core of most optical fibres is photosensitive at UV wavelengths, which means that exposure to UV light results in a local permanent increase of the refractive index of the fibre core. Through this mechanism, the UV interference pattern becomes permanently imprinted in the fibre core. In this thesis, unless specified otherwise, the term 'fibre grating' designates a Bragg grating written from the side by UV exposure in an optical fibre.
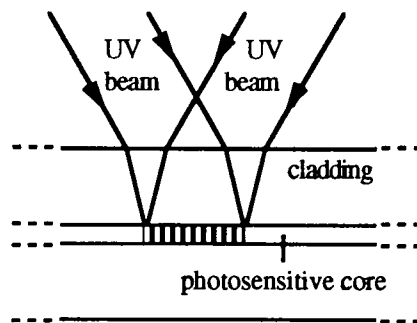
Figure 1-1 - Holographic method for writing fibre Bragg gratings

The main property of a fibre Bragg grating is to reflect light over a narrow spectral range centred at a resonant wavelength known as the Bragg wavelength, λ_B. The resonance condition which determines this Bragg wavelength is simply that reflections occurring at two successive grating lines must be in phase, which is equivalent to $\lambda_B = 2\Lambda n_{eff}$, where

n_{eff} is the effective index of the fibre mode. The reflection spectrum (calculated and measured) of a short grating is shown in Fig. 1-2. In this case, the spectral response of the grating is similar to a sinc^2 function, which is characteristic of a low reflectivity, uniform grating. The reflection spectrum is characterised by two important parameters: the grating bandwidth, $\Delta\lambda$, and peak reflectivity, R_0. These parameters are function of the grating length, L, the amplitude of its index modulation, δn and the Bragg wavelength. Another feature of fibre Bragg gratings is their strong chromatic dispersion, which can be very useful in certain applications.
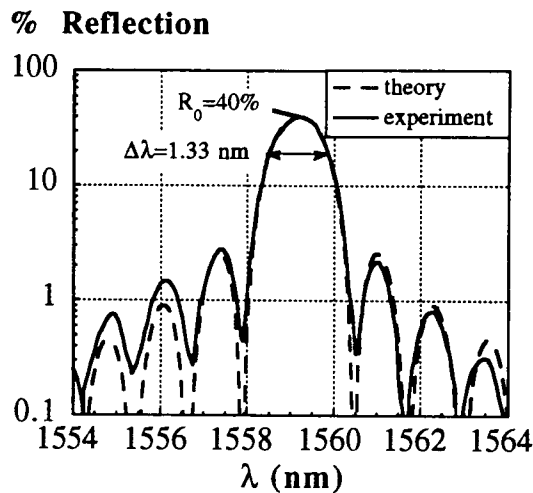
% Reflection

Figure 1-2 - Reflection spectrum (measured and calculated) of 0.68 mm-long fibre grating.

The reflection, transmission and dispersion characteristics of fibre Bragg gratings can be tailored in various ways, as summarised in Table II. Sidelobes in the reflection spectrum can be suppressed by tapering the grating profile (b). Chirping the grating (i.e. spatially varying the period) increases the bandwidth and modifies the chromatic dispersion (c). Moiré gratings can be obtained by superimposing two grating as of slightly different periods which can result in a characteristic central dip in the reflection spectrum (d). In 'blazed' fibre gratings, the grating lines are at an angle with respect to the normal to the fibre axis; instead of reflecting light inside the core, these gratings selectively tap light out of the fibre.
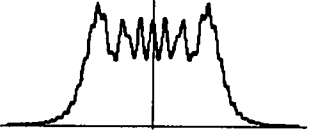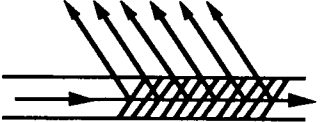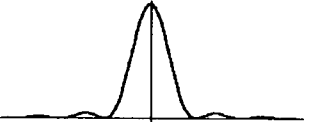
Type	Index mod.	Refl. spectrum
a) uniform		
b) tapered		
c) chirped		
d) Moiré		
e) blazed		

Table II - Main types of fibre Bragg gratings

1.3.2. Properties and advantages

The main advantage of fibre gratings is to provide a very accurate control of the absolute wavelength in a fibre system. The Bragg wavelength can be predetermined with an accuracy of about 0.1 nm at the fabrication stage and subsequently tuned over a range of up to 10 nm by straining the fibre (tuning of ~ 0.1 GHz/µstrain) or varying its temperature (tuning ~ -1 GHz/°C). With the recent progress in grating manufacturing techniques and fibre photosensitivity, a wide range of grating properties has now become accessible. Grating bandwidths as small as 6 GHz (0.05 nm) [71] and as large as 25 THz (20 nm) [72] have been reported. Reflection efficiencies well in excess of 99% are routinely obtained.

Excess losses in gratings can vary widely depending on the fabrication technique, wavelength of operation and fibre type, but can be typically 1% or less [23,73]. The birefringence of a fibre grating can be typically of order 10^{-5} [23], but this can again vary substantially depending on the type of grating. Fibre gratings can be stable for hundreds of years at room temperature and can be pre-annealed to have similar stability at a few

hundred degrees centigrade [74]. Certain types of gratings are thermally stable up to 800°C [10].

In short, fibre gratings have no major disadvantages which could proscribe their use in fibre systems. This, added to their simplicity, compactness and versatility make them highly desirable components for many commercial applications.

1.4. Objectives

The general objective of this research project has been to establish an expertise in the fabrication and applications of photorefractive fibre Bragg gratings, taking advantage of the unique resources available in the ORC. This includes:
- understanding the optical properties of fibre gratings;
- studying the mechanisms of fibre photosensitivity and optimising the fibre design;
- exploring different methods of producing gratings;
- fabricating and characterising gratings of different types with the widest possible range of parameters;
- writing gratings in different types of fibre;
- developing new components based on fibre gratings;
- supplying gratings to research groups within the ORC to develop new applications.

1.5. Summary of contents

This thesis addresses many aspects of fibre gratings technology, from theoretical modeling and the fundamental mechanisms of fibre photosensitivity to the fabrication techniques and several important applications. The next two chapters describe some of the physics of fibre gratings. Chapter 2 presents a theoretical analysis of their optical properties. Known grating properties are briefly summarised followed by detailed modeling of the short wavelength transmission loss caused by cladding-mode coupling. Chapter 3 examines the photosensitivity of germanosilicate optical fibres. Starting with a review of the literature on fibre photosensitivity and of several recent experimental results, a model is proposed to describe the interaction of UV light with germania-related oxygen deficient centres, based on the photo-thermal ionisation of the defects. The dependence of the photoinduced refractive index change with core composition and the effect of known sensitisation techniques are evaluated using data collected from over

twenty different fibres. The results of an experiment on photoinduced birefringence, performed in collaboration with A. Kamal, are also included.

The fabrication of fibre gratings is described in chapters 4 and 5. Chapter 4 gives a detailed description of the UV-interferometer used for producing the gratings, which is the result of a collaborative effort with L. Reekie. This chapter concentrates on the multiple-pulse writing technique. The dynamics of grating formation in different fibres are described and modeled. The intensity-dependence of the writing process in also investigated. Chapter 5 describes the single-pulse writing technique and in particular the Type I and Type II mechanisms. The production of both types of gratings during fibre pulling is then demonstrated. This last experiment was performed jointly with L. Dong and L. Reekie.

The interaction of single excimer laser pulses with germanosilicate fibres is further investigated in chapter 6 by monitoring the transmission of fibres at infrared wavelengths in the presence of a 20 ns pulse. The measurements were carried out with the help of L. Reekie. Chapter 7 examines the formation of gratings in germania-free fibres doped with aluminum, phosphorus, erbium:ytterbium or tantalum. The effect of hydrogen-loading on the photosensitivity of these fibre and on the absorption spectra of preform samples is also evaluated.

Several applications of fibre gratings are presented in chapters 8 and 9. Chapter 8 describes a new type of channel-dropping filter which combines a fibre grating and a polished fibre coupler and is now known as a grating-frustrated coupler. This device was developed jointly with P.St.J. Russell. This chapter includes both the theory of operation and a practical demonstration of the grating-frustrated coupler. Finally, chapter 9 contains other applications of fibre gratings which were realised in the ORC, presented from a fibre grating manufacturer's point of view. These include fibre lasers, dispersion compensators and sensors.

1.7. <u>References</u>

1. G. Meltz, W.W. Morey and W.H. Glenn, "Formation of Bragg gratings in optical fibres by a transverse holographic method", *Opt. Lett.*, **14** (15), pp. 823-825, 1989.

2. K.O. Hill, Y. Fujii, D.C. Johnson and B.S. Kawasaki, "Photosensitivity in optical fibre waveguides: application to reflection filter fabrication", *Appl. Phys. Lett.*, **32** (10), pp. 647-649, 1978.

3. P.St.J. Russell and R. Ulrich, "Grating-fibre coupler as a high-resolution spectrometer", *Opt. Lett.*, **10** (6), pp. 291-293, 1985.

4. I. Bennion, D.C.J. Reid, C.J. Rowe and W.J. Stewart, "High reflectivity monomode fibre grating filters", *Electron. Lett.*, **22** (6), pp. 341-343, 1986.

5. D.K.W. Lam and B.K. Garside, "Characterization of single-mode optical fiber filters", *Appl. Opt.*, **20** (3), pp. 440-445, 1981.

6. K.O. Hill, B. Malo, F. Bilodeau, D.C. Johnson and J. Albert, "Bragg gratings fabricated in monomode photosensitive optical fiber by UV exposure through a phase mask", *Appl. Phys. Lett.*, **62** (10), pp. 1035-1037, 1993.

7. D.Z. Anderson, V. Mizrahi, T. Erdogan and A.E. White, "Production of in-fiber gratings using a diffractive optical element", *Electron. Lett.*, **29** (6), pp. 566-568, 1993.

8. B. Malo, K.O. Hill, F. Bilodeau, D.C. Johnson and J. Albert, "Point-by-point fabrication of micro-Bragg gratings in photosensitive fiber using single excimer pulse refractive-index modification techniques", *Electron. Lett.*, **29** (18), pp. 1668-1669, 1993.

9. C.G. Askins, T.-E. Tsai, G.M. Williams, M.A. Puttnam, M. Bash-Kansky and E.J. Friebele, "Fibre Bragg reflectors prepared by a single excimer pulse", *Opt. Lett.*, **17** (11), pp. 833-835, 1992.

10. J.-L. Archambault, L. Reekie and P.St.J. Russell, "100% reflectivity Bragg reflectors produced in optical fibres by single excimer laser pulses", *Electron. Lett.*, **29** (5), pp. 453-455, 1993.

11. L. Dong, J.L. Archambault, L. Reekie, P.St.J. Russell and D.N. Payne, "Single-pulse Bragg gratings written during fiber drawing", *Electron. Lett.*, **29** (17), pp. 1577-1578, 1993.

12. C.G. Askins, M.A. Putnam, G.M. Williams and E.J. Friebele, "Stepped-wavelength optical-fiber Bragg grating arrays fabricated in line on a draw tower", *Opt. Lett.*, **19** (2), pp. 147-149, 1994.

13. K.C. Byron, K. Sugden, T. Bricheno and I. Bennion, "Fabrication of chirped Bragg gratings in photosensitive fiber", *Electron. Lett.*, **29** (18), pp. 1659-1660, 1993.

14. K.O. Hill, F. Bilodeau, B. Malo, T. Kitagawa, S. Theriault, D.C. Johnson and J. Albert, "Aperiodic in-fiber Bragg gratings for optical fiber dispersion compensation", *OFC'94 Postdeadline Papers*, paper PD2-3, San Jose, 1994.

15. B.J. Eggleton, P.A. Krug, L. Poladian, K.A. Ahmed and H.F. Liu, "Dispersion compensation by using Bragg-grating filters with self-induced chirp", *OFC'94 Technical Digest*, paper ThK3, San Jose, 1994.

16. M.C. Farries, K. Sugden, D.C.J. Reid, I. Bennion, A. Molony and M.J. Goodwin, "Very broadband reflection bandwidth (44 nm) chirped fiber gratings and narrow bandpass filters produced by the use of an amplitude mask", *Electron. Lett.*, **30** (11), pp. 891-892, 1994.

17. R. Kashyap, P.F. McKee, R.J. Campbell and D.L. Williams, "Novel method for producing all fibre photo-induced chirped gratings", *Electron. Lett.*, **30** (12), pp. 996-998, 1994.

18. J.A.R. Williams, I. Bennion, K. Sugden and N.J. Doran, "Fibre dispersion compensation using a chirped in-fibre Bragg grating", *Electron. Lett.*, **12** (30), pp. 985-987, 1994.

19. P.C. Hill and B.J. Eggleton, "Strain gradient chirp of fibre Bragg gratings", *Electron. Lett.*, **30** (14), pp. 1172-1174, 1994.

20. S. Legoubin, E. Fertein, M. Douay, P. Bernage, P. Niay, F. Bayon and T. Georges, "Formation of Moiré grating in core of germanosilicate fibre by transverse holographic double exposure method", *Electron. Lett.*, **27** (21), pp. 1945-1946, 1991.

21. R. Kashyap, R. Wyatt and P.F. McKee, "Wavelength flattened saturated erbium amplifier using multiple side-tap Bragg gratings", *Electron. Lett.*, **29** (11), pp. 1025-1026, 1993.

22. D.L. Williams, B.J. Ainslie, J.R. Armitage, R. Kashyap and R. Campbell, "Enhanced UV photosensitivity in boron codoped germanosilicate fibres", *Electron. Lett.*, **29** (1), pp. 45-47, 1993.

23. G. Meltz and W.W. Morey, "Bragg grating formation and germanosilicate fiber photosensitivity", *International Workshop on Photoinduced Self-Organisation Effects in Optical Fiber , SPIE Vol. 1546*, pp. 185-199, Quebec, 1991.

24. D.L. Williams, B.J. Ainslie, J.R. Armitage and R. Kashyap, "Enhanced photosensitivity in germanium doped silica fibres for future optical networks", *ECOC Proceedings, Vol. 1*, paper B9.5, pp. 425-428, Berlin, 1992.

25. L. Dong, J. Pinkstone, P.St.J. Russell and D.N. Payne, "Study of UV absorption in germanosilicate preforms", *CLEO'94, paper CWK4 Technical Digest*, paper CWK4, pp. 243, Anaheim, Ca., 1994.

26. F. Bilodeau, B. Malo, J. Albert, D.C. Johnson and K.O. Hill, "Photosensitization of optical fiber and silica-on-silicon/silica waveguides", *Opt. Lett.*, **18** (12), pp. 953-955, 1993.

27. P.J. Lemaire, R.M. Atkins, V. Mizrahi and W.A. Reed, "High-pressure H2 loading as a technique for achieving ultrahigh UV photosensitivity and thermal sensitivity in GeO_2 doped optical fibers", *Electron. Lett.*, **29** (13), pp. 1191-1193, 1993.

28. M.M. Broer, R.L. Cone and J.R. Simpson, "Ultraviolet-induced distributed-feedback gratings in Ce^{3+}-doped silica optical fibers", *Opt. Lett.*, **16** (18), pp. 1391-1393, 1991.

29. L. Dong, P.J. Wells, D.P. Hand and D.N. Payne, "Photosensitivity in Ce^{3+}-doped optical fibers", *JOSA-B*, **10** (1), pp. 89-93, 1993.

30. L. Dong, J.-L. Archambault, L. Reekie, P.St.J. Russell and D.N. Payne, "Bragg gratings written in Ce^{3+}-doped fibres by single excimer laser pulses", *Opt. Lett.*, **18** (11), pp. 861-863, 1993.

31. K.O. Hill, B. Malo, F. Bilodeau, D.C. Johnson, T.F. Morse, A. Kilian, L. Reinhart and O. Kyunghwan, "Photosensitivity in Eu^{2+}:Al_2O_3-doped-core fiber: preliminary results and application to mode converters", *OFC'91 Postdeadline Papers*, paper PD3, pp. 14-17, San Diego, 1991.

32. M.M. Broer, A.J. Bruce and W.H. Grodkiewicz, "Photoinduced refractive-index changes in several Eu^{3+}-doped, Pr^{3+}-doped and Er^{3+}-doped oxide glasses", *Phys. Rev. B*, **45** (13), pp. 7077-7083, 1992.

33. J.L. Archambault, L. Reekie, L. Dong and P.St.J. Russell, "High reflectivity photorefractive Bragg gratings in germania-free optical fibers", *CLEO'94 Technical Digest*, paper CWK3, p. 242, Anaheim, Ca., 1994.

34. P. Niay, P. Bernage, T. Taunay and W.X. Xie, "Fabrication of Bragg gratings in fluorozirconate fibers and applications to fiber lasers", *CLEO'94 Postdeadline Papers*, paper CPD9, pp. 21-22, Anaheim, 1994.

35. G.D. Maxwell, B.J. Ainslie, D.L. Williams and R. Kashyap, "UV written 13 dB reflection filters in hydrogenated low loss planar silica waveguides", *Electron. Lett.*, **29** (5), pp. 425-426, 1993.

36. B. Malo, J. Albert, F. Bilodeau, T. Kitagawa, D.C. Johnson, K.O. Hill, K. Hattori, Y. Hibino and S. Gujrathi, "Photosensitivity in phosphorus-doped silica glass and optical waveguides", *Appl. Phys. Lett.*, **65** (4), pp. 394-396, 1994.

37. M.P. Roe, M. Hempstead, J.-L. Archambault, P.St.J. Russell and L. Dong, "Strong photo-induced refractive index changes in RF-sputtered tantalum oxide planar waveguides", *CLEO-Europe Technical Digest*, paper CTuC6, p. 67, Amsterdam, 1994.

38. D.P. Hand and P.St.J. Russell, "Photoinduced refractive-index changes in germanosilicate fibers", *Opt. Lett.*, **15** (2), pp. 102-104, 1990.

39. D. Wong, S.B. Poole and M.G. Sceats, "Stress-birefringence reduction in elliptic-core fibers under ultraviolet-irradiation", *Opt. Lett.*, **17** (24), pp. 1773-1775, 1992.

40. P.Y. Fonjallaz, H.G. Limberger, R.P. Salathé, F. Cochet and B. Leuenberger, "Correlation of index changes with stress changes in fibers containing UV-written Bragg gratings", *ECOC'94 Proceedings*, Florence, 1994.

41. I.M. Jauncey, L. Reekie, J.E. Townsend, D.N. Payne and C.J. Rowe, "Single longitudinal mode operation of a Nd^{3+}-doped fibre laser", *Electron. Lett.*, **24** (1), pp. 24-26, 1988.

42. R. Kashyap, J.R. Armitage, R. Wyatt, S.T. Davey and D.L. Williams, "All-fibre narrowband reflection gratings at 1500 nm", *Electron. Lett.*, **26** (11), pp. 730-732, 1990.

43. G.A. Ball, W.W. Morey and W.H. Glenn, "Standing-wave monomode erbium fiber laser", *IEEE Photon. Tech. Lett.*, **3** (7), pp. 613-615, 1991.

44. G.A. Ball and W.W. Morey, "Continuously tunable single-mode erbium fiber laser", *Opt. Lett.*, **17** (6), pp. 420-422, 1992.

45. G.A. Ball and W.H. Glenn, "Design of a single-mode linear-cavity erbium fiber laser utilising Bragg reflectors", *J. Lightwave Tech.*, **10** (10), pp. 1338-1343, 1992.

46. J.T. Kringlebotn, P.R. Morkel, L. Reekie, J.-L. Archambault and D.N. Payne, "Efficient diode-pumped single-frequency erbium:ytterbium fiber laser", *IEEE Photon. Tech. Lett.*, **5** (10), pp. 1162-1164, 1993.

47. R.P. Davey, R.P.E. Fleming, K. Smith, R. Kashyap and J.R. Armitage, "Mode-locked erbium fiber laser with wavelength selection by means of fiber Bragg grating reflector", *Electron. Lett.*, **27** (22), pp. 2087-2088, 1991.

48. J.T. Kringlebotn, J.L. Archambault, L. Reekie and D.N. Payne, "1.5-µm $Er^{3+}:Yb^{3+}$-doped fiber DFB laser", *CLEO'94 Technical Digest*, paper CWP2, pp. 261, Anaheim, 1994.

49. P.A. Morton, V. Mizrahi, S.G. Kosinski, L.F. Mollenauer and T. Tanbunek, "Hybrid soliton pulse source with fiber external cavity and Bragg reflector", *Electron. Lett.*, **28** (6), pp. 561-562, 1992.

50. R. Kashyap, G.D. Maxwell and B.J. Ainslie, "Laser-trimmed four-port bandpass filter fabricated in single-mode photosensitive Ge-doped planar waveguide", *IEEE Photonics Tech. Lett.*, **5** (2), pp. 191-194, 1993.

51. J.-L. Archambault, P.St.J. Russell, S. Barcelos, P. Hua and L. Reekie, "Grating-frustrated coupler: novel channel-dropping filter in single-mode optical fibre", *Opt. Lett.*, **19** (3), pp. 180-182, 1994.

52. F. Bilodeau, K.O. Hill, B. Malo, D.C. Johnson and J. Albert, "High-return-loss narrow-band all-fiber bandpass Bragg transmission filter", *IEEE Photon. Tech. Lett.*, **6** (1), pp. 80-82, 1994.

53. V. Mizrahi, T. Erdogan, D.J. DiGiovanni, P.J. Lemaire, W.M. Macdonald, S.G. Kosinski, S. Cabot and J.E. Sipe, "4 channel fiber grating demultiplexer", *Electron. Lett.*, **30** (10), pp. 780-781, 1994.

54. R. Kashyap, R. Wyatt and R.J. Campbell, "Wide-band gain-flattened erbium amplifier using a photosensitive fiber blazed grating", *Electron. Lett.*, **29** (2), pp. 154-156, 1993.

55. R. Kashyap, S.V. Chernikov, P.F. McKee and J.R. Taylor, "30 ps chromatic dispersion compensation of 400 fs pulses at 100 Gbits/s in optical fibres using an all fibre photoinduced chirped reflection grating", *Electron. Lett.*, **30** (13), pp. 1078-1080, 1994.

56. W.W. Morey, G. Meltz and W.H. Glenn, "Bragg-grating temperature and strain sensors", in "Springer Proceedings in Physics - Optical Fiber Sensors", Springer-Verlag, Berlin, 1989, pp. 526-531.

57. M.G. Xu, L. Reekie, Y.T. Chow and J.P. Dakin, "Optical in-fibre grating high pressure sensor", *Electron. Lett.*, **29** (4), pp. 398-399, 1993.

58. M.G. Xu, J.L. Archambault, L. Reekie and J.P. Dakin, "Discrimination between strain and temperature effects using dual-wavelength fibre grating sensors", *Electron. Lett.*, **30** (13), pp. 1085-1087, 1994.

59. M.G. Xu, H. Geiger, J.L. Archambault, L. Reekie and J.P. Dakin, "Novel interrogating system for fiber grating sensors using an acoustooptic tunable filter", *Electron. Lett.*, **29** (17), pp. 1510-1511, 1993.

60. A.J. Cohen and H.L. Smith, "Ultraviolet absorption studies of germanium silicate glasses", *J. Phys. Chem. Solids*, **7**, pp. 301-306, 1958.

61. J.P. Bernardin and N.M. Lawandy, "Dynamics of the formation of Bragg gratings in germanosilicate optical fibers", *Opt. Comm.*, **79** (3,4), pp. 194-199, 1990.

62. F. Ouellette, D. Gagnon and M. Poirier, "Permanent photoinduced birefringence in a Ge-doped fiber", *Appl. Phys. Lett.*, **58** (17), pp. 1813-1815, 1991.

63. H.G. Limberger, P.Y. Fonjallaz and R.P. Salathé, "Spectral characterisation of photoinduced high efficient Bragg gratings in standard telecommunication fibres", *Electron. Lett.*, **29** (1), pp. 47-49, 1993.

64. D.L. Williams, S.T. Davey, R. Kashyap, J.R. Armitage and B.J. Ainslie, "Direct observation of UV induced bleaching of 240 nm absorption band in photosensitive germanosilicate glass fibres", *Electron. Lett.*, **28** (4), pp. 369-371, 1992.

65. J. Albert, B. Malo, F. Bilodeau, D.C. Johnson and K.O. Hill, "Photosensitivity in Ge-doped silica optical waveguides and fibers with 193 nm light from an ArF excimer laser", *Opt. Lett.*, **19** (6), pp. 387-389, 1994.

66. D.P. Hand and P.St.J. Russell, "Single-mode fibre grating written into Sagnac loop using photosensitive fibre: transmission filters", *IOOC'89 Technical Digest*, paper 21C3-4, Kobe, Japan, 1989.

67. M.C. Farries, P.St.J. Russell, M.E. Fermann and D.N. Payne, "Second harmonic generation in an optical fibre by self-written $\chi^{(2)}$ grating", *Electron. Lett.*, **23** (7), pp. 322-323, 1987.

68. P.St.J. Russell and D.P. Hand, "Rocking filter formation in photosensitive high birfringence optical fibers", *Electron. Lett.*, **26** (22), pp. 1846-1848, 1990.

69. L.J. Poyntz-Wright, M.E. Fermann and P.St.J. Russell, "Nonlinear transmission and colour centre dynamics in germanosilicate fibres at 420-540 nm", *Opt. Lett.*, **13** (11), pp. 1023-1025, 1988.

70. S. Bardal, A. Kamal and P.St.J. Russell, "Photoinduced birefringence in optical fibers: a comparative study of low-birefringence and high-birefringence fibers", *Opt. Lett.*, **16** (6), pp. 411-413, 1992.

71. J.-L. Archambault, L. Reekie and P.St.J. Russell, "High reflectivity and narrow bandwidth fibre gratings written by single excimer pulse", *Electron. Lett.*, **29** (1), pp. 28-29, 1992.

72. V. Mizrahi, P.J. Lemaire, T. Erdogan, W.A. Reed, D.J. DiGiovanni and R.M. Atkins, "Ultraviolet-laser fabrication of ultrastrong optical-fiber gratings and of germania-doped channel waveguides", *Appl. Phys. Lett.*, **63** (13), pp. 1727-1729, 1993.

73. G.A. Ball, C.G. Hull-Allen and J. Livas, "Frequency noise of a Bragg grating fibre laser", *Electron. Lett.*, **30** (15), pp. 1229-1230, 1994.

74. T. Erdogan, V. Mizrahi, P.J. Lemaire and D. Monroe, "Decay of ultraviolet-induced fiber Bragg gratings", *J. Appl. Phys.*, **76** (1), pp. 73-80, 1994.

Chapter 2
Optical properties of fibre gratings

2.1. Introduction

The theory of light propagation in waveguide gratings has been studied for many years [1,2]. Several approaches have been employed to analyse this problem, notably coupled-wave theory [1] and Bloch wave analysis [3]. Recently, a few authors have looked more specifically at the optical properties of photorefractive fibre gratings [4,5]. These models give accurate descriptions of the main properties of fibre grating. However, all of them include simplifying assumptions which mask out some of the finer features of the spectral properties of fibre gratings.

In this chapter, a very general formalism is presented, based on coupled-mode theory. It is first used to derive the 'standard' properties of fibre gratings, such as reflectivity and bandwidth, as function of the various parameters, which is an essential basis for the subsequent chapters. The general model is then applied to a detailed analysis of cladding-mode coupling, which cannot be found in the literature. Finally, aperiodic gratings are briefly examined, with particular emphasis on gratings written with a non-uniform UV beam.

2.2. Optical fibre properties

The geometry of an optical fibre is illustrated in Fig. 2-1. A standard telecommunications fibre is composed of a central core, usually 8-9 μm in diameter, surrounded by a 125 μm diameter cladding. Both the core and the cladding are made of synthetic silica; a small amount of germania is usually added to the core to raise its refractive index, thus creating a light-guiding structure. This glass fibre is coated with protective jacket commonly made of UV-curable acrylate. Throughout this chapter, we assume for simplicity that the fibre has a step-index profile, described by

$$n(r) = n_{co} = n_{cl}(1+\Delta), \quad r \leq r_{co}$$

$$= n_{cl}, \quad r_{co} < r \leq r_{cl}$$

$$= n_{ext}, \quad r > r_{cl} \quad (2\text{-}1)$$

where n_{co}, n_{cl} and n_{ext} are constants, r_{co} and r_{cl} are the core and cladding radii respectively and Δ is the relative core-cladding index difference, usually of order 1%.
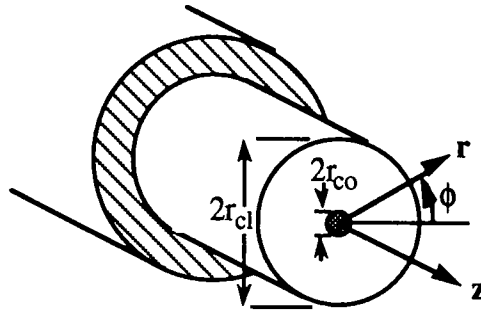
Figure 2-1 - Geometry of optical fibre

Light propagating in an optical fibre can be decomposed over the various modes supported by the fibre. These can be divided into guided core and cladding modes and radiation modes. Each mode can be designated by its azimuthal and radial numbers, l and m and is characterised by its propagation constant, β_{lm} or its effective index, $n_{lm}=\beta_{lm}/k$, where $k=2\pi/\lambda$ is the vacuum wavenumber and λ is the wavelength. The value of the effective index specifies the type of mode: $n_{cl}<n_{lm}<n_{co}$ for core modes, $n_{ext}<n_{lm}<n_{cl}$ for cladding modes and $0<n_{lm}<n_{ext}$ for radiation modes. Bound modes are discrete whereas radiation modes form a continuum. The normalised frequency of the fibre, $V=kr_{co}\sqrt{n_{co}^2-n_{cl}^2}$, determines how many core modes are supported by the fibre. In a perfectly circular fibre, only one core mode exists - the fundamental mode ($l=0$, $m=1$) - if V is less than about 2.4. In a real fibre, where the core always has some degree of asymmetry or birefringence, the 'fundamental mode' consists in fact of two slightly non-degenerate modes with orthogonal states of polarisation. The protective jacket of a fibre usually has a refractive index which is larger than that of the cladding. In that case, there are no guided cladding modes. In a side-written fibre grating, however, the jacket must be stripped over the grating region prior to writing the grating, because acrylates are opaque to UV light. The cladding is then exposed to air and can support guided modes, since $n_{ext}<n_{cl}$.

2.3. Fibre grating geometry

Fibre gratings are usually written by exposing the core of a fibre to a UV interference pattern through one side of the cladding, as shown in Fig. 1-1. In general, the cladding region is almost completely transparent to the UV writing wavelengths. The core, however can absorb very strongly at these wavelengths, because of the presence of

germania or other dopants. Only the core, therefore, is photosensitive and so we can assume that the grating lines are located within the core. The refractive index at each point in the core is changed be an amount Δn which is a function of the local UV exposure or fluence F (energy/area):

$$\Delta n(r,\phi,z) = \Delta n_s\, g(F(r,\phi,z))\,, \text{ for } r \le r_{co} \text{ and } |z| \le L/2$$

$$= 0\,, \text{ for } r \ge r_{co} \text{ or } |z| \ge L/2$$

with

$$F(r,\phi,z) = F_0(r,\phi,z)\,(1 + M\cos(Kz + \phi(z))) \tag{2-2}$$

where Δn_s is saturation value of the photoinduced index change, L is the length of the grating, $0 < M \le 1$ is the modulation depth and $\Lambda = 2\pi/K$ is the period of the interference pattern. The phase of the modulation ϕ may vary (slowly) with z if the grating is chirped. The spatial dependence of F_0 can account for variations in the UV beam profile and for the decay across the core of the UV radiation due to absorption. The function $g(F)$ is the response of the core glass with $g(0)=0$ and $g(\infty)=1$. This function depends on a number of parameters, such as the glass composition, its history, the particular UV wavelength used, etc. This is discussed in more detail in the next chapter.

We can rewrite the photoinduced index change as the Fourier series:

$$\Delta n(r,\phi,z) = \Delta n_{av}(r,\phi,z) + \sum_{j=1}^{\infty} \Delta n_j(r,\phi,z)\cos(jKz + j\phi(z))$$

$$\Delta n_{av} = \frac{\Delta n_s}{\Lambda} \int_z^{z+\Lambda} g(F(r,\phi,z'))\, dz'$$

$$\Delta n_j(r,\phi,z) = \frac{2\Delta n_s}{\Lambda} \int_z^{z+\Lambda} g(F(r,\phi,z'))\cos(jKz' + j\phi(z'))\, dz' \tag{2-3}$$

where Δn_{av} is the average index change and Δn_j is the amplitude of the jth harmonic of the index modulation, all of which can be slowly varying in z. In most cases, we are only interested the first two terms of the Fourier expansion and we then assume that

$$\Delta n(r,\phi,z) = \Delta n_{av}(r,\phi,z) + \Delta n_1(r,\phi,z)\cos(Kz + \phi(z)) \tag{2-4}$$

2.4. <u>Coupled-wave equations</u>

In the coupled-wave formalism, we treat the index modulation of the grating as a perturbation which couples together the modes of the unperturbed fibre. This approach is very accurate as long as the index modulation is small, which is true in practice for all fibre gratings. In the following analysis, it is also assumed that 1) the optical fields can be expressed as scalar quantities and 2) the envelopes of the mode amplitudes are slowly-varying in z. Both approximations are quite standard and introduce only very small errors for most cases of practical interest.

We now consider the case of forward propagating (direction $+z$) mode of an optical fibre incident on a fibre grating. Within the grating, this forward mode is coupled to backward modes. Neglecting the coupling between backward modes and other forward modes, we may write the optical field in the fibre as

$$E(r,\phi,z) = f_1(z)\, e^{i(\beta_1+\delta\beta_1)z}\, \Psi_1(r,\phi)) + \sum_j b_j(z) e^{-i(\beta_j+\delta\beta_j)z}\, \Psi_j(r,\phi) \qquad (2\text{-}5)$$

where f_1 and b_j are the amplitudes of the forward and backward propagating modes and the Ψ_j are the normalised modal field distributions for the unperturbed fibre. The mode number j represents the different combinations of the radial and azimuthal numbers l and m. The parameter $\delta\beta_j$ is the effective change in the propagation constant of mode j caused by the average index change Δn_{av} and is given by

$$\delta\beta_j(z) = k \int_0^{2\pi} \int_0^{r_\infty} |\Psi_j(r,\phi)|^2\, \Delta n_{av}(r,\phi,z)\, rdrd\phi \qquad (2\text{-}6)$$

At the grating boundaries, we have

$$f_1(-L/2) = 1$$

$$b_j(L/2) = 0 \qquad (2\text{-}7)$$

The optical field obeys the scalar wave equation

$$\nabla^2 E(r,\phi,z) + k^2(n(r)+\Delta n(r,\phi,z))^2\, E(r,\phi,z) = 0 \qquad (2\text{-}8)$$

By substituting Eqs. (2-4) and (2-5) in (2-8), we derive the following coupled differential equations for the mode amplitudes:

$$f_1' = i \sum_j \kappa_j\, e^{-iz(\theta_j+\delta\theta_j)}\, b_j$$

$$b_n' = -i\, \kappa_n^*\, e^{iz(\theta_j+\delta\theta_j)}\, f_1 \qquad (2\text{-}9)$$

where all quantities, except θ_j, depend on z.

The coupling constants are given by

$$\kappa_j(z) = \frac{\pi \delta n_j}{\lambda} \qquad (2\text{-}10)$$

where δn_j is the effective index modulation equal to

$$\delta n_j = \int_0^{2\pi} \int_0^{r_\infty} \Psi_1(r,\phi) \, \Psi_j{}^*(r,\phi) \, \Delta n_1(r,\phi,z) \, r dr d\phi \qquad (2\text{-}11)$$

For the fundamental mode and if Δn_1 does not depend on r and ϕ, then $\delta n_1(z) = \eta \Delta n_1(z)$, where η is the fraction of power in the core. The dephasing parameters are given by

$$\theta_j = \beta_1 + \beta_j - K$$

$$\delta\theta_j(z) = \delta\beta_1(z) + \delta\beta_j(z) - \varphi'(z) \qquad (2\text{-}12)$$

The resonance or Bragg condition for mode j is achieved when the forward and backward modes are phase-matched with the grating, which is when

$$\theta_j + \delta\theta_j(z) = 0 \qquad (2\text{-}13)$$

This condition may depend on z if the grating is chirped.

If we use the local reflection coefficient defined by Kogelnik [1]

$$\rho_n = \frac{b_n}{f_1} e^{-iz(\theta_n + \delta\theta_n)} \qquad (2\text{-}14)$$

then Eq. (2-9) reduces to

$$\boxed{i\rho_n{}' = \kappa_n{}^* + \rho_n\left(\theta_n + \delta\theta_n(z) + \sum_j \kappa_j \rho_j\right)} \qquad (2\text{-}15)$$

with the boundary condition given by (2-7)

$$\rho_n(L/2) = 0 \qquad (2\text{-}16)$$

By solving Eq. (2-15) for a particular set of parameters, we can calculate the reflection coefficient of the grating, $\rho(-L/2)$ or the reflectivity,

$$R = |\rho(-L/2)|^2 \qquad (2\text{-}17)$$

For a weakly reflecting grating ($|\rho_j|^2 \ll 1$), Kogelnik has derived the very useful result:

$$\rho_n(-L/2) \approx ie^{i(\theta_n + \delta\theta_n(-L/2))L/2} \int_{-L/2}^{L/2} (\kappa_n{}^* e^{iz\delta\theta_n(z)}) e^{i\theta_n z} \, dz \qquad (2\text{-}18)$$

which shows that, apart from the phase factor, the spectral response of the grating is approximately given by the Fourier transform of the grating profile, $\kappa_n{}^*(z) \, e^{iz\delta\theta_n(z)}$.

2.5. <u>Uniform gratings</u>

2.5.1. Solutions

If the grating parameters (κ_n and $\delta\theta_n$) are constant over the length of grating, then the solutions to the coupled-wave equations can be found analytically. If it is also assumed that there is only one reflected mode with amplitude $b_n(z)$ then the solutions can be expressed as

$$f_1(z) = f_+ \, e^{i\alpha_+ z} + f_- \, e^{i\alpha_- z}$$

$$b_n(z) = b_+ \, e^{-i\alpha_+ z} + b_- \, e^{-i\alpha_- z} \tag{2-19}$$

where for convenience we have redefined the dephasing parameter as

$$\theta_n = \beta_1 + \delta\beta_1 + \beta_n + \delta\beta_n - K$$

with
$$\alpha_\pm = \pm\sqrt{\theta_n^2/4 - \kappa_n^2} - \theta_n/2$$

$$f_\pm = \frac{\alpha_\mp}{\alpha_\mp e^{i\alpha_\pm L} - \alpha_\pm e^{-i\theta_n L}}$$

$$b_\pm = \frac{\kappa_n \, e^{i\theta_n L}}{\alpha_\pm e^{-i\alpha_\pm L} - \alpha_\mp} = \frac{\alpha_\mp}{\kappa_n} f_\mp \tag{2-20}$$

2.5.2. Bloch waves and field microstructure

Combining Eqs. (2-5), (2-19) and (2-20), we can derive an analytical expression of the optical field at any point within the fibre grating. If we examine Eq. (2-19) more closely, we see that the forward and backward modes are each composed of two partial waves with wavevectors that differ by $\alpha_+ - \alpha_- = 2\sqrt{\theta_n^2/4 - \kappa_n^2}$. The partial waves with amplitudes f_+ and b_- are linked together by Eq. (2-20) and the combination of the two constitutes a forward propagating Bloch wave [3]; the combination of partial waves f_- and b_+ forms the backward Bloch wave. The difference in the wavevectors of the two waves that form each Bloch wave is equal to K, the grating wavevector. Each pair of partial waves thus creates an interference pattern that mimics the index modulation of the grating [3]. The contrast of this fringe pattern is maximum when $\theta_n=0$ ($b_\pm = f_\mp$) and goes to zero when $|\theta_n|$ tends to infinity. The phase of the fringe pattern relative to the grating lines is given by the phase of α_+. For $\theta_n=0$, this phase is equal to $\pm\pi/2$; it is equal to $\pm\pi$ when $\theta_n \geq 2\kappa_n$ and 0 when $\theta_n \leq -2\kappa_n$.

2.5.3. Dispersion relation and stop band

The propagation constants of the forward partial waves of Eq. (2-19) are given by

$$\beta_{f\pm} = \beta_1 + \delta\beta_1 + \alpha_\pm \tag{2-21}$$

Defining the dimensionless parameter $\delta_n = \theta_n/2\kappa_n$, we may rewrite (2-21) as

$$\frac{\beta_{f\pm} - K/2}{\kappa_n} = \pm \sqrt{\delta_n^2 - 1} \tag{2-22}$$

This dispersion relation is plotted in Fig. 2-2.
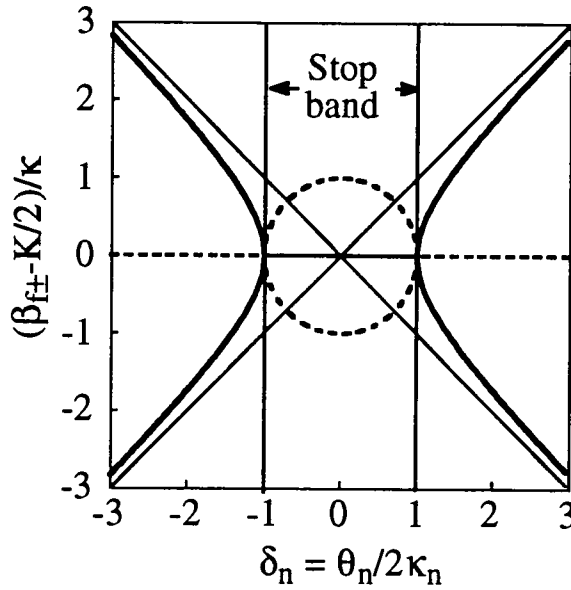
Figure 2-2 - Dispersion diagram of a Bragg grating near the Bragg condition showing real part in solid lines and imaginary part in dashed lines. Thin diagonal lines represent the dispersion relation of a uniform medium.

The region $-1 < \delta_n < 1$ is known as the stop band. It is the spectral range over which the optical field is evanescent inside the grating. At the centre of the stop-band ($\delta_n = 0$) lies the Bragg wavelength, where the forward and backward fibre modes are resonantly coupled by the grating. This is where the imaginary component of the propagation constant, the evanescent decay rate, is maximum. The Bragg wavelength is given by

$$\lambda_B = 2n_{av}\Lambda \tag{2-23}$$

where $n_{av} = (\beta_1 + \delta\beta_1 + \beta_n + \delta\beta_n)/2k$ is the average effective index of the two modes. At wavelengths such that $|\lambda - \lambda_B| \ll \lambda_B$, the dephasing parameter can be approximated by

$$\theta_n \approx \frac{-4\pi n_{av}}{\lambda_B^2} (\lambda - \lambda_B) \ ; \ \delta_n \approx \frac{-2n_{av}}{\delta n \lambda_B} (\lambda - \lambda_B) \tag{2-24}$$

Far from the Bragg wavelength, the propagation constants of the forward and backward waves tend asymptotically to $\beta_1 + \delta\beta_1$, represented by the diagonal lines in Fig. 2-2, which means that the grating is then equivalent ti a uniform medium.

2.5.4. Reflection spectrum and group delay

The complex value of $b_n(z)$ in $z=-L/2$ determines the amplitude and phase of the light reflected by the grating. The power reflectivity is given by

$$R = 1/(1+(\kappa_n L \; \text{sinc}(\kappa_n L \sqrt{\delta^2-1}))^{-2}) \qquad (2\text{-}25)$$

and the phase upon reflection by

$$\vartheta = \tan^{-1}(\sqrt{\delta^2-1} \; \cot(\kappa_n L \sqrt{\delta^2-1})/\delta) \qquad (2\text{-}26)$$

From the derivative of Eq. (2-26), we can calculate that the group delay of the reflected light relative to the incident light is

$$\frac{\tau_n}{\tau_G} = \frac{\delta^2 - \text{sinc}(2\kappa_n L \sqrt{\delta^2-1})}{2\delta^2 - 1 - \cos(2\kappa_n L \sqrt{\delta^2-1})} \qquad (2\text{-}27)$$

where $\tau_G = 2n_{av}L/c$ is the delay associated with a round-trip through a non-dispersive medium of length L. At the Bragg wavelength ($\delta=0$), the reflectivity is maximum and equal to

$$R_0 = \tanh^2(\kappa_n L) \qquad (2\text{-}28)$$

The group delay is then minimum and given by

$$\frac{\tau_0}{\tau_G} = \frac{\tanh(\kappa_n L)}{2\kappa_n L} \qquad (2\text{-}29)$$

In Fig. 2-3 a) to c), we use Eqs. (2-25) and (2-27) to calculate the optical spectra of three different uniform fibre gratings All three gratings are 5 mm long and have a Bragg wavelength $\lambda_B=1550$ nm. Each grating has a different effective index modulation: $\delta n=10^{-5}$ (a), 10^{-4} (b) and 10^{-3} (c).

The three reflection spectra of Fig. 2-3 consist of a main peak centered at the Bragg wavelength and a series of sidelobes symmetrically located at longer and shorter wavelengths outside the grating stop-band. For a weak grating ($\kappa_n L \ll 1$), such as the one in Fig. 2-3 (a), Eq. (2-25) can be approximated by

$$R \approx (\kappa_n L \; \text{sinc}(\theta_n L/2)))^2 \qquad (2\text{-}30)$$

which is the Fourier transform of the 'top-hat' grating profile, as predicted by Eq. (2-18).
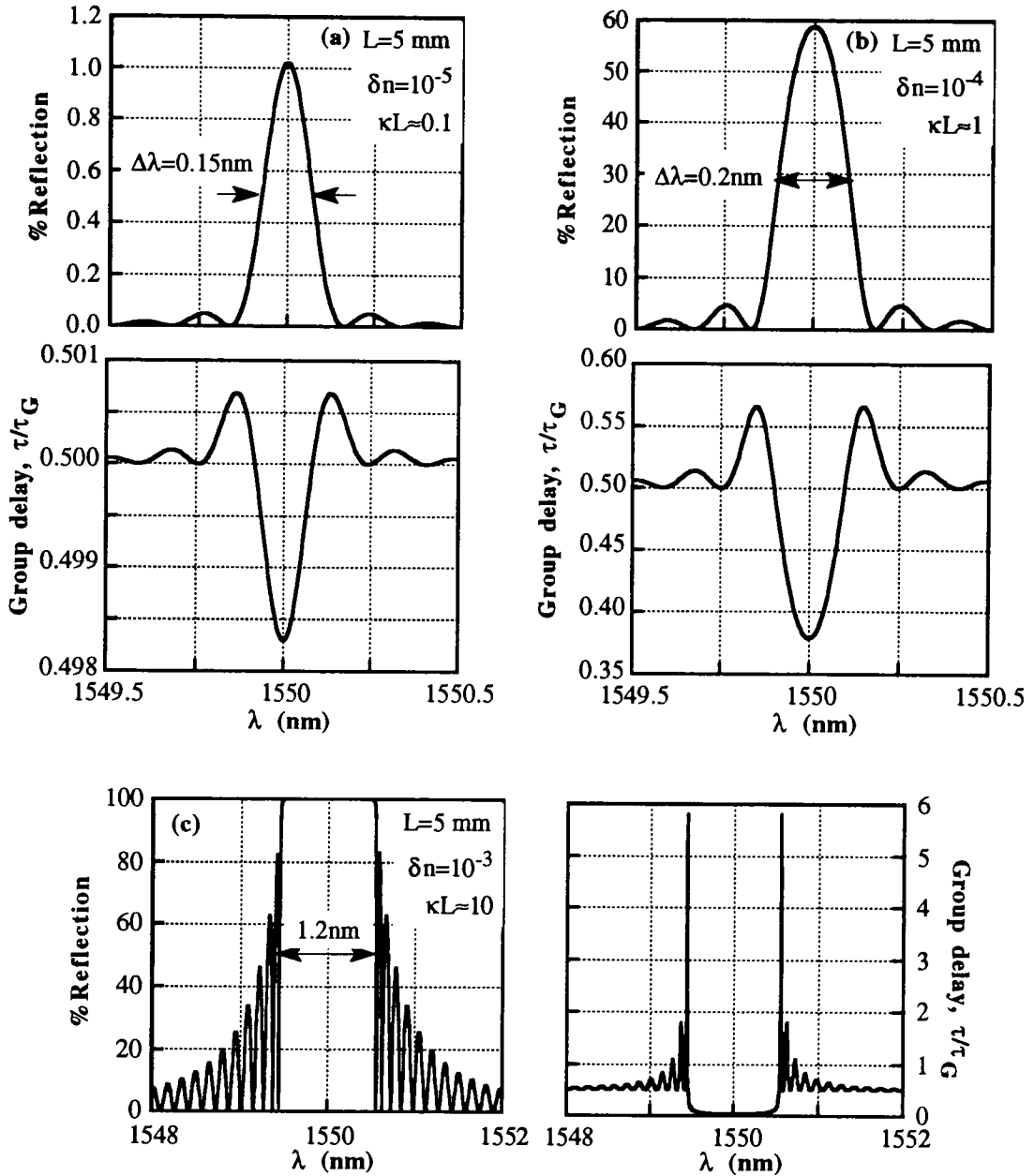
Figure 2-3 - Reflection spectra of three different gratings with a Bragg
wavelength at 1550 nm ($\Delta\lambda$=FWHM bandwidth).

The height of the central peak of each grating is given by Eq. (2-28). The width of this
peak is inversely proportional to the number of grating lines which are illuminated. At
the Bragg wavelength, we know from Eq. (2-20) that the intensity of the forward mode
decays exponentially through the grating as $e^{-2\kappa_n z}$; the 1/e evanescent decay depth is then

$$L_{1/e} = \frac{1}{2\kappa_n} = \frac{\lambda_B}{2\pi\delta n_n} \qquad (2\text{-}31)$$

If $\kappa_n L \ll 1$ (Fig. 2-3 (a)), the decay depth is much larger than the grating length. The
bandwidth of the grating is then minimum, since every grating line is illuminated. If

$\kappa_n L \gg 1$ (Fig. 2-3 (c)), then the decay depth is much less than the grating length and only a fraction of the grating lines are effectively illuminated; therefore the width of the reflection peak is much larger.

Similar arguments can be used to explain the variations in group delay at the Bragg wavelength for the different gratings. In a weak grating, every grating line contributes equally to the reflected signal. On average, the reflected light can be seen as originating from the centre of the grating and therefore $\tau/\tau_G \approx 1/2$. In a strong grating, the reflected light effectively originates from $z=-L/2+L_{1/e}$ so that $\tau/\tau_G \approx L_{1/e}/L = 1/2\kappa_n L$.

The sidelobes seen in the reflection spectra result from Fabry-Perot resonances between the two abrupt edges of the grating. The stronger the index modulation is, the larger the discontinuities in $z=\pm L/2$ and hence the higher are the sidelobes. The sidelobes can be greatly reduced by tapering or apodising the grating profile [1]. This Fabry-Perot effect also accounts for the peaks seen on the group delay plots. The group delay is maximum at the edges of the grating stop-band where it can largely exceed τ_G as the light effectively travels back and forth several times between the boundaries of the grating.

Grating strength	R_0	$\Delta\lambda$	$\Delta\lambda_{eff}$	τ_0/τ_G
$\kappa L < 0.38$ ($R_0 < 13\%$)	$(\kappa L)^2$	$\dfrac{0.44\lambda_B{}^2}{n_{av}L}$	$\dfrac{\pi^2\delta n^2 L}{2n_{av}}$	$\dfrac{1}{2}-\dfrac{\kappa^2 L^2}{6}$
$0.38 < \kappa L < 2.3$ ($13\% < R_0 < 96\%$)	-	$\dfrac{0.44\lambda_B{}^2}{n_{av}L}\sqrt{1+0.7(\kappa L)^2}$	$1.1\,R_0\Delta\lambda$	-
$2.3 < \kappa L < 8.0$ ($R_0 > 96\%$)	$1-4e^{-2\kappa L}$	$\dfrac{\delta n\lambda_B}{n_{av}}\sqrt{1+\dfrac{\pi^2}{(\kappa L)^2}(1-\dfrac{2.4}{\kappa L}+\dfrac{3.4}{(\kappa L)^2})}$	$1.3\,R_0\Delta\lambda$	$\dfrac{1}{2\kappa L}$
$\kappa L > 8.0$ ($R_0 \approx 100\%$)	1	$\dfrac{\delta n\lambda_B}{n_{av}}$	$1.5\dfrac{\delta n\lambda_B}{n_{av}}$	$\dfrac{1}{2\kappa L}$

Table III - Approximate expressions for main optical properties of uniform gratings - peak reflectivity, R_0, FWHM bandwidth, $\Delta\lambda$, effective bandwidth, $\Delta\lambda_{eff}$ and minimum group delay, τ_0.

In general, the full-width half-maximum bandwidth of a grating, $\Delta\lambda$, can be calculated by solving the equation $R(\Delta\lambda/2)=R_0/2$. Unfortunately, this equation has no exact analytical solutions. Approximate solutions can be found by using Taylor expansions as shown in Table III. This table contains the limiting values for weak and strong gratings of the peak reflectivity, bandwidth, effective bandwidth and minimum group delay.

The effective bandwidth is defined as

$$\Delta\lambda_{eff} = \int_{0}^{\infty} R(\lambda)d\lambda \qquad (2\text{-}32)$$

The effective bandwidth is in practice a useful parameter because it is very easy to measure: if a grating is illuminated with a white light source, then the effective bandwidth is equal to the optical power reflected by the grating divided by the spectral density of the source. It is also a parameter that is relatively insensitive to the imperfections of a real grating. It can therefore provide a simple and accurate measurement of the index modulation of a grating.
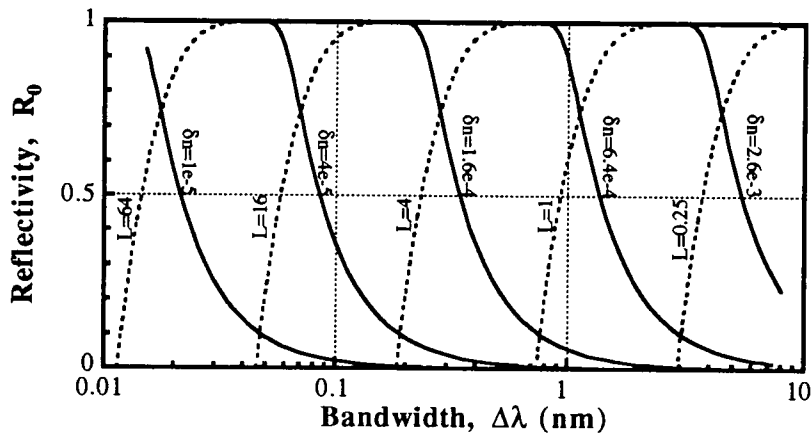
Figure 2-4 - Peak reflectivity vs FWHM bandwidth plots at constant length (dashed lines) or constant index modulation (solid lines) for λ_B=1550 nm (lengths in mm).

2.6. Coupling to cladding modes

The effective index modulation of a fibre grating for any two given modes is given by the overlap integral of Eq. (2-11). If the photoinduced index modulation Δn_1 is constant over the whole fibre cross-section, then this integral is only non-zero for degenerate modes, since non-degenerate modes are orthogonal. If such a grating could be made, then it would couple the forward propagating fundamental mode only to the backward fundamental mode. In practice, however, Δn_1 does depend on r and ϕ because the grating lines do not usually extend beyond the core and are slightly asymmetric due to the core absorption and the asymmetry of the writing process; also the grating lines may not be perfectly perpendicular to the fibre axis. All of these factors can contribute to making some or all of the overlap integrals involving non-degenerate modes non-zero. As a consequence, coupling between the fundamental mode and cladding modes is often

observed experimentally in fibre gratings, as shown in Fig. 2-5. This coupling can result in significant loss on the short wavelength side of the Bragg wavelength, which can be extremely detrimental, especially in multiplexed systems.
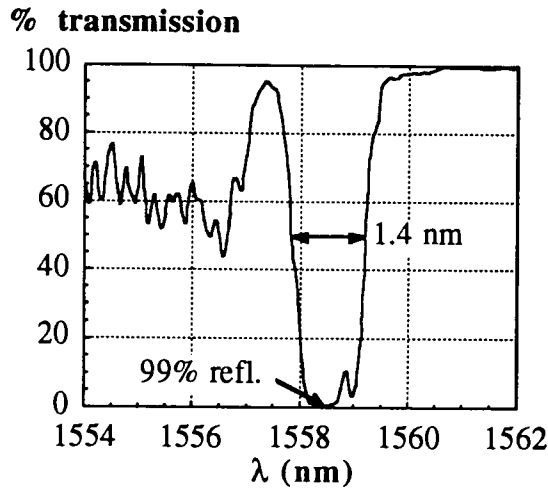
% transmission

Figure 2-5 - Experimental transmission spectrum of fibre grating: main peak at 1558.5 nm corresponds to resonant coupling to backward fundamental mode; multiple peaks on the short wavelength side are due to resonant coupling with individual cladding modes.

In this section, we evaluate the influence of the different types of transverse grating non-uniformities on the coupling to cladding modes. The first step of this calculation is to calculate the propagation constants and field distributions of the fundamental mode and the cladding modes for the step-index profile of Eq. (2-1). This involves expressing the field distribution in each of the three regions of uniform index as a combination of functions, applying the boundary conditions to derive the eigenvalue equation and solving this equation numerically. The second step is then to evaluate the overlap integrals leading to the coupling constant for each cladding mode.

2.6.1. Gratings with circular symmetry

Here, we assume that the index modulation is independent of the azimuthal coordinate, ϕ, and is uniform across the core. This is the case when the core absorption is negligible, the UV writing beams are perfectly uniform across the core and the fringe pattern is exactly orthogonal to the fibre axis. Under these conditions, the coupling constants are only non-zero for modes with the same azimuthal symmetry and therefore the fundamental mode can only be coupled to cladding modes with the same azimuthal number, $l=0$. The coupling constant for cladding mode m is given by

$$\kappa_m = k\Delta n_1 \int_0^{r_{co}} \Psi_1(r)\Psi_m{}^*(r) \, rdr \qquad (2\text{--}33)$$

Fig. 2-6 shows the relative coupling constants of the lowest order $l=0$ cladding modes against the normalised resonant wavelength of each mode, for fibres with V-values ranging from 1.6 to 2.4 and cladding diameters 10 to 30 times larger than the core diameter. The positions of the resonant wavelengths were calculated by solving the equation $\beta_1 + \beta_m = K$ and neglecting material dispersion. The Bragg wavelength λ_B is defined as the resonant wavelength of the fundamental ($m=1$) mode. The mode with the resonant wavelength closest to λ_B is the $m=2$ mode. The radial number m then increases by 1 for each successive data point away from the Bragg wavelength.
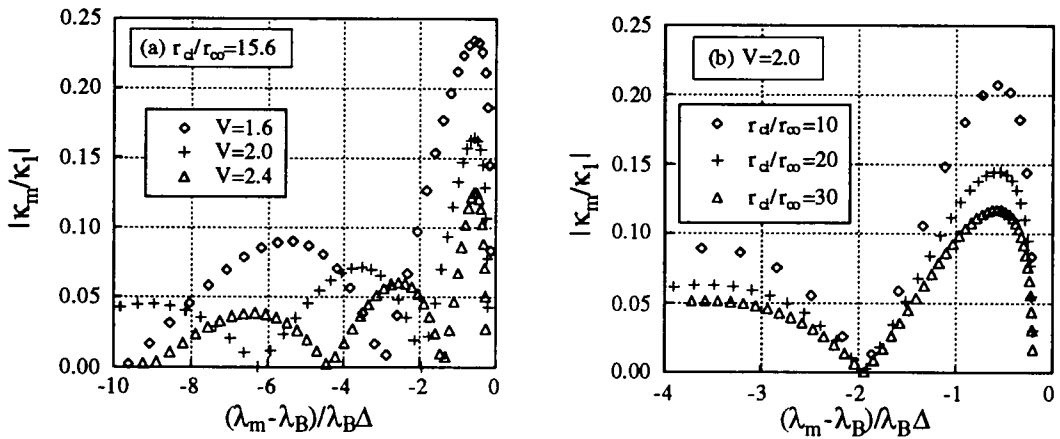
Figure 2-6 - Coupling constants to l=0 cladding modes for circularly symmetric grating, with grating lines confined to core: (a) for $r_{cl}/r_{co}=125/8$, different V-values; (b) for V=2.0, different cladding radii.

For the circularly symmetric gratings, the coupling to cladding modes is caused by the evanescent tail of the fundamental core mode which extends inside the cladding. If the fundamental mode were completely confined to the core, the integral in Eq. (2-11) would tend to zero for $m \neq 1$. This is why the coupling constants in Fig. 2-6 (a) are larger for the smaller V-values. At $V=2.4$, 17% of the power of the fundamental mode is located in the cladding; this proportion increases to 26% at $V=2.0$ and 41% at $V=1.6$. The coupling constant for a particular cladding mode increases roughly as the square root of this fraction of power. Increasing the cladding diameter reduces the fraction of power of each cladding mode in the vicinity of the core and therefore reduces its coupling constant, as seen in Fig. 2-6 (b). But at the same time, the number of cladding modes is increased: for $r_{cl}=10r_{co}$, the first lobe of Fig. 2-6 (b) contains 12 modes; this number increases to 24 modes for $r_{cl}=20r_{co}$ and 36 modes for $r_{cl}=30r_{co}$. In terms of controlling the amount

of power lost to cladding modes, there is probably not much to be gained by adjusting the cladding diameter.

Fig. 2-6 also shows how the coupling constant varies with the mode number. The number m indicates the number of zeros and hence the number of sign changes in the radial mode field distribution. The nodes that appear in Fig. 2-6 indicate that for particular cladding modes the position of the radial zeros within the core are such that the positive parts of the overlap integral of Eq. (2-11) almost exactly cancel out the negative parts. When m becomes very large, the optical field changes sign frequently within the fibre core so that the overlap integral tends to average out to zero.

The calculations shown in Fig. 2-6 demonstrate that even for a grating that is perfectly uniform across the core, the coupling constants to cladding modes can be as much as 20% of the coupling constant to the fundamental mode. In a weak grating the peak reflectivity is proportional to κ_m^2 and therefore the coupling to cladding modes can be considered negligible. In a strong grating such as the one in Fig. 2-5, however, a further reduction in the cladding mode coupling constants would be required to avoid significant losses.

2.6.2. Effect of core absorption

The UV absorption in the core causes the photoinduced index change to be asymmetric, the side of the core directly exposed to the writing beams receiving a higher UV dose than the far side. If a uniform UV beam profile and a linear absorption are assumed, then the UV fluence distribution across the core is described by

$$F_0(r,\phi) = f_0 \exp[-\alpha(\sqrt{r_{co}^2 - r^2\sin^2(\phi)} - r\cos(\phi))] \qquad (2\text{-}34)$$

where f_0 is the incident fluence and α is the UV absorption coefficient in the core. If the material response is linear, i.e. $g(F) = CF$ where C is a constant, then the index modulation amplitude can be written as

$$\Delta n_1(r,\phi) = \Delta n_{max} \exp[-\alpha(\sqrt{r_{co}^2 - r^2\sin^2(\phi)} - r\cos(\phi))] \qquad (2\text{-}35)$$

with $\Delta n_{max} = Cf_0\Delta n_s$. Eq. (2-35) constitutes a worst-case scenario, when the asymmetry of the index change is maximum. If reality, the material response $g(F)$ should be a saturating function, which would tend to reduce the degree of asymmetry. Substituting (2-35) into Eq. (2-11), we can examine the effect of the core absorption on cladding mode coupling. Because the index modulation is no longer circularly symmetric, the fundamental mode can be coupled to cladding modes with $l \neq 0$. The azimuthal dependence of the $l \neq 0$ cladding mode field distributions can either be $\cos(l\phi)$ or $\sin(l\phi)$

[6]; because the index perturbation of Eq. (2-35) has an axis of symmetry along $\phi=0$, only the modes in $\cos(l\phi)$ can have a non-zero coupling constant.

Fig. 2-7 examines the coupling to the $l=0$ cladding modes for absorptions across the core ranging from 2 to 8 dB. An 8 dB absorption would be typical of a single-mode silica fibre doped with a very high concentration of germania, for a writing wavelength of ~240 nm. A 2 dB absorption would be more characteristic of a standard telecommunications fibre. In Fig. 2-7, the coupling constants are only weakly affected by the presence of even a strong absorption in the core. The most noticeable effect is that an increase in absorption favors the coupling to the higher-order $l=0$ modes.
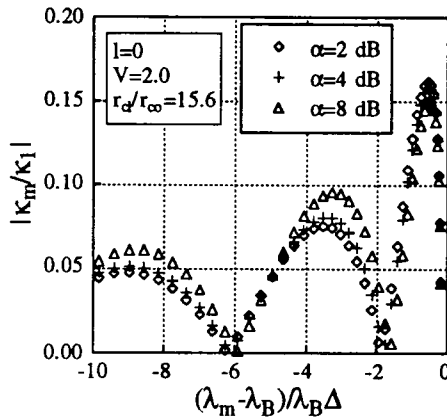
Figure 2-7 - Coupling to l=0 cladding modes for different values of core absorption.
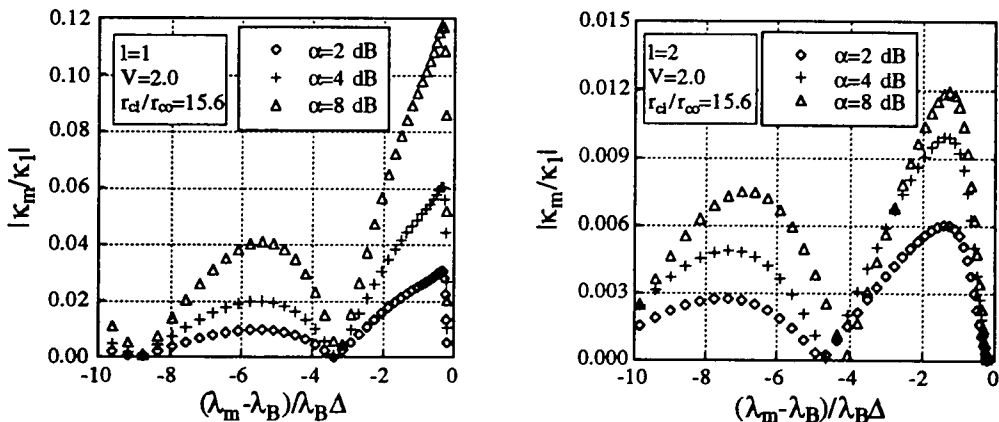
Figure 2-8 - Coupling to l=1 and l=2 cladding modes for different values of core absorption.

In Fig. 2-8, the coupling constants to the $l=1$ and $l=2$ modes are shown. We see that in a strongly absorbing fibre, the coupling to the $l=1$ modes can be comparable to that of the

l=0 modes. But the coupling constants decrease rapidly with *l*: when *l* is larger, the field of a cladding mode changes sign more frequently in the azimuthal direction and the overlap integral of Eq. (2-11) tends to average out to zero.

2.6.3. Effect of blaze angle

It is well-known that if the periodic planes of a fibre grating are not orthogonal to the fibre axis, then the coupling of the fundamental mode to higher-order modes is enhanced [7]. The angle between the normal to the grating planes and the fibre axis is known as the blaze angle. For most fibre grating applications, this angle should ideally be zero, but in practice there is always a slight error. It is therefore important to know the effect of a non-zero blaze angle on the various coupling constants to establish a tolerance factor.
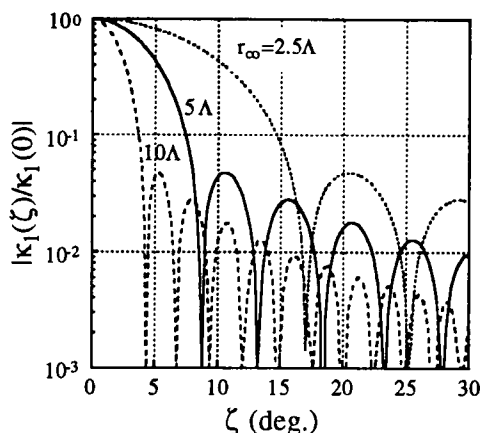
Figure 2-9 - Effect of blaze angle on fundamental mode coupling constant for V=2 and different core diameters.

The index modulation amplitude of a grating with blaze angle ζ can be expressed in terms of the index modulation of an unblazed grating as

$$\Delta n_b(r,\phi,z) = \Delta n_1(r,\phi,z) \, \exp[-iKr \cos(\phi) \tan(\zeta)] \qquad (2\text{-}36)$$

where Δn_1 has been multiplied by a phase factor which depends linearly on $r \cos(\phi)$. Fig. 2-9 shows the effect of a blaze angle on κ_1, the coupling constant of the fundamental mode, in a uniform grating. The effect is obviously stronger in a fibre with a larger core diameter, simply because the phase variation of the index modulation across the core is proportional to r_{co}. When this phase variation is larger than π ($\tan(\zeta)>\Lambda/4r_{co}$), then the forward and backward modes interfere constructively in certain regions of the core and destructively in others and therefore the coupling constant drops significantly.
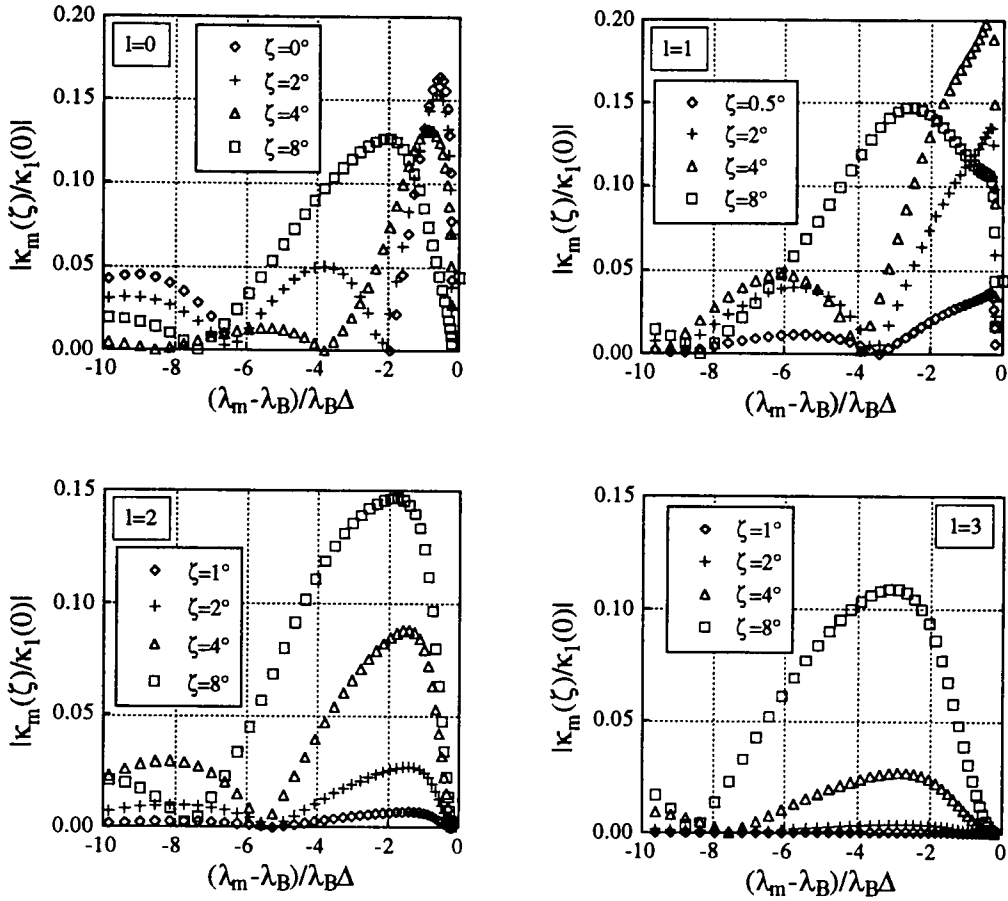
Figure 2-10 - Cladding mode coupling in grating with blaze angle ζ, for $V=2$, $r_{cl}/r_{co}=15.6$, $r_{co}/\Lambda=5$.

Fig. 2-10 shows how the coupling constants for the cladding modes with $l=0$-3 depend on the blaze angle. For $\zeta=0°$, only the $l=0$ modes are excited. As ζ increases however, coupling to the $l>1$ modes increase rapidly. For $\zeta=2°$, the coupling constants of the $l=1$ modes are comparable to those of the $l=0$ modes. For $\zeta=8°$, there is significant coupling even to the $l=3$ modes; also the dependence of the coupling constants on the mode number has become quite broad and the positions of the peaks have shifted to higher-order modes. On the whole, increasing the blaze angle tends to distribute the diffracted light over the whole mode spectrum.

2.6.4. Comparison with experimental data

In Fig. 2-11, the measured transmission spectrum of a strong ~4 mm Bragg grating is compared to a spectrum calculated from this model. The double peak structure apparent in the short wavelength side of the measured spectrum is caused by coupling to both $l=0$ and $l=1$ modes, indicating that the grating has some degree of asymmetry. This was accounted for in the model by entering a blaze angle of 1.5°. Using parameters which are

very close to the measured fibre parameters (r_{cl}/r_{co}~40, Δ~0.023, V=1.95), an excellent fit is obtained, confirming the validity of the model.
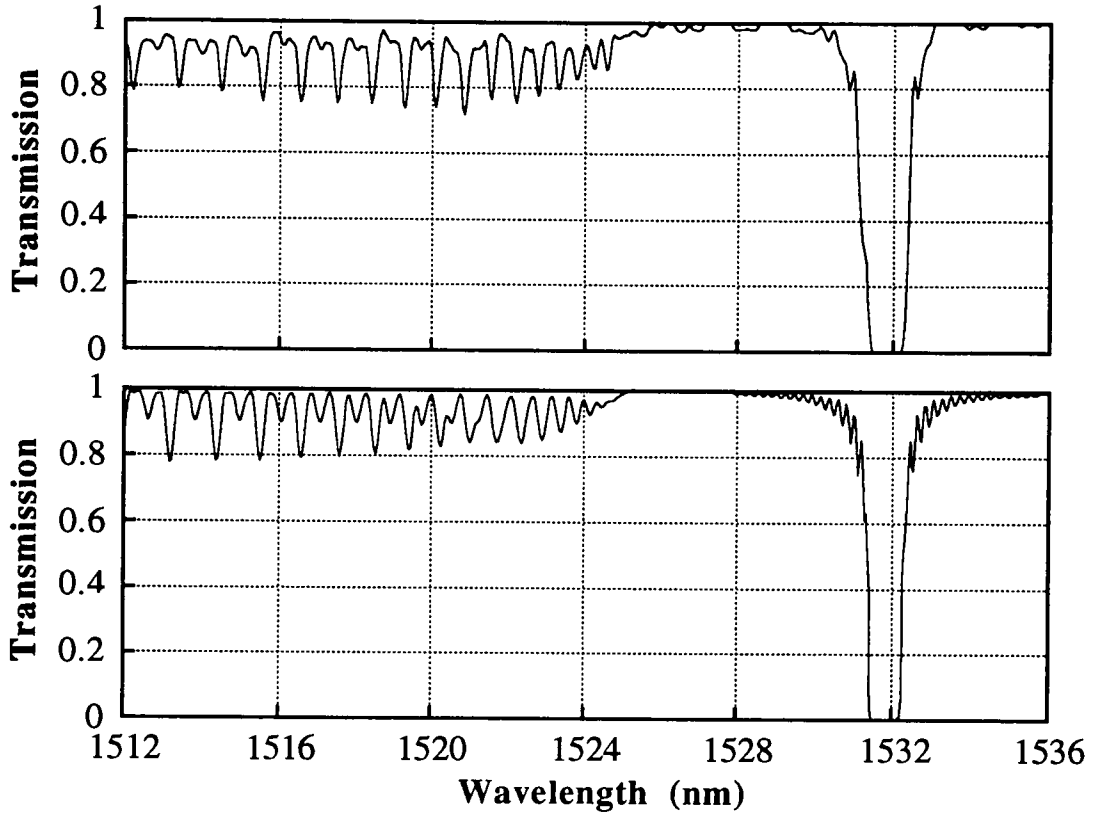
Figure 2-11 - Measured (above) and calculated (below) transmission spectrum of fibre grating. Coupling to both l=0 modes (larger peaks), and l=1 (minor peaks) is apparent. Fitting parameters are V=1.95, r_{cl}/r_{co}=37.3, Δ=0.0218, L=3.5 mm, λ_B=1531.9 nm, Δn_1=8×10^{-4} and ζ=1.5°.

2.6.5. Minimising cladding-mode coupling

In this section, the main contributing factors to cladding-mode coupling have been identified and their individual contributions have been quantified. From these results, it is clear that several precautions must be taken in order to minimise cladding-mode coupling in a fibre grating:

- the V-value of the fibre should be as large as possible to maximise the confinement of the fundamental mode;

- if the core absorption is large, the fibre should be given a prolonged UV exposure as the saturation of the index change and the bleaching of the absorption (see section 3.2.1) will tend to reduce the grating asymmetry;

- the blaze angle should be kept below ~1°.

Even if these precautions are followed, it may not be possible to reduce the cladding mode coupling to an acceptable level. The most effective way of reducing the coupling to cladding modes would be to have the grating lines extend beyond the core. This could be done in practice by designing a fibre with a photosensitive internal cladding, which ideally should be as photosensitive as the core. The benefits of this proposed method are shown in Fig. 2-12 for $V=2.0$ and $r_{cl}/r_{co}=125/8$. The data shown in this graph were obtained again using Eq. (2-11), but setting the upper limit of the integral in r to r_G instead of r_{co}, where r_G is the radius of the grating lines. As the grating lines are extended beyond the core, the cladding mode coupling constants drop extremely rapidly, peaking at 5.5% of κ_1 for $r_G=2r_{co}$ and less than 0.5% of κ_1 for $r_G=4r_{co}$, as the fraction of power of the fundamental mode interacting with the grating tends to 100%.
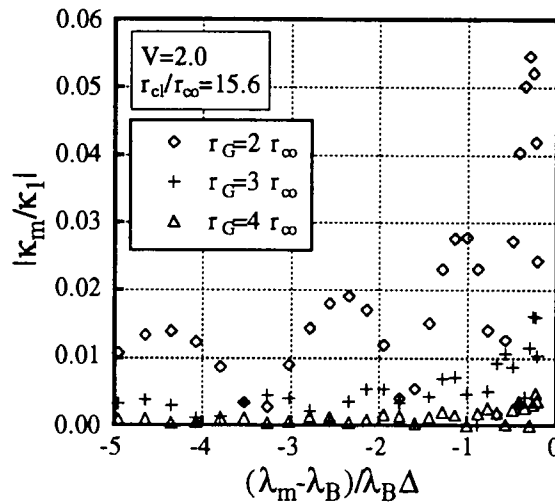
Figure 2-12 - Cladding-mode coupling with grating lines extending beyond the core and for $V=2.0$.

2.7. Non-uniform gratings

Variations in the longitudinal profile of a fibre grating strongly affect its optical properties. There are two types of grating non-uniformities: variations in the coupling constants (tapered grating) and variations in the dephasing parameter $\delta\theta_n(z)$ (chirped grating). These variations are sometimes unwanted and can degrade the performance of the grating; but they can also be added intentionally to tailor the spectral response of the grating. Chirped gratings used for dispersion compensation [8-16] or laser diode stabilisation [17] and Moiré gratings [18] are examples of the latter. In this section, we examine the effect of random non-uniformities on the optical properties of fibre gratings.

These non-uniformities can result from exposure to an uneven UV writing beam, such as the one shown in Fig. 2-13. The results derived in this section are highly relevant to the later chapters, as the laser used for producing gratings in this project does have a non-uniform beam profile.

The variations in the writing beam profile affect both the coupling constant and the average index change of the grating and therefore results in a randomly tapered and chirped grating. In general, the coupled-wave equations of a non-uniform grating do not have analytical solutions and must solved numerically. The following results were derived by integrating Eq. (2-15) numerically using the Burlisch-Stoer method [19].
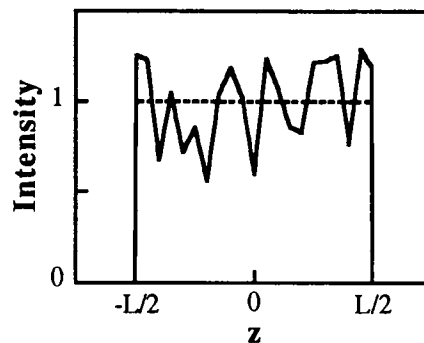
Figure 2-13 - Intensity profile of writing beam used for simulations of Fig. 2-14; dotted line: uniform beam profile.

Fig. 2-14 shows the calculated reflection spectra of two gratings obtained using the writing beam of Fig. 2-13 and compares them to the reflection spectra of a uniform gratings with the same average index modulation. A linear photosensitive response was assumed, so that the grating profiles have the same shape as the beam profile. As can be seen in Fig. 2-14, the beam non-uniformities have a much more noticeable effect on the reflection spectrum of the stronger grating. This is first because in the stronger grating, the average index fluctuations and hence the chirp of the grating are much larger. Secondly, since the coupling to the backward wave in the weaker grating is distributed throughout whole the length of the grating, the effect of the non-uniformities tends to average out whereas in the high reflectivity grating, local variations can have a much stronger effect, with Fabry-Perot resonances occurring between successive regions of high index modulation.
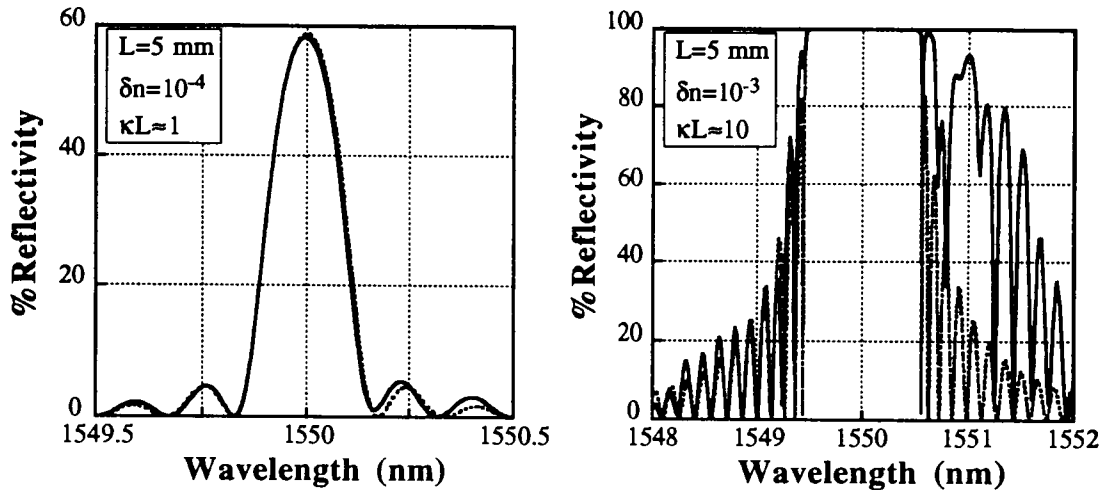
Figure 2-14 - Reflection spectra of gratings written by non-uniform beam compared to spectra of uniform gratings (dotted lines).

In general random variations of the grating profile tend to broaden the grating spectrum and reduce the reflection efficiency. Also, the reflection spectrum becomes asymmetric and with additional features appearing in the stronger gratings.

2.8. Conclusion

The theoretical results presented in this chapter provide a detailed understanding of the optical properties of fibre gratings. This constitutes an essential basis for the interpretation of experimental results in the following chapters. A general coupled-mode formalism was developed which can be used to analyse almost any type of fibre Bragg grating. This formalism was successfully applied to the detailed analysis of cladding-mode coupling, which, for the first time, provided an accurate description of the experimental data. Following this analysis, it was possible to suggest practical ways of reducing cladding-mode coupling and the corresponding short-wavelength loss in strong fibre gratings. The numerical analysis of non-uniform gratings was also implemented and used to assess the effects of random non-uniformities on grating performance. The software tools developed for this purpose could in fact be applied to any type of grating profile.

2.9. <u>References</u>

1. H. Kogelnik, "Filter response of nonuniform almost-periodic structures", *Bell Syst. Tech. J.*, **55** (1), pp. 109-125, 1976.

2. C. Elachi, "Waves in active and passive periodic structures: a review", *Proc. IEEE*, **64**, pp. 1666-1698, 1976.

3. P.St.J. Russell, "Bloch wave analysis of dispersion and pulse propagation in pure distributed feedback structures", *J. of Mod. Opt.*, **38** (8), pp. 1599-1619, 1991.

4. V. Mizrahi and J.E. Sipe, "Optical properties of photosensitive fiber phase gratings", *J. Lightwave Tech.*, **11** (10), pp. 1513-1517, 1993.

5. L. Poladian, "Graphical and WKB analysis of nonuniform Bragg gratings", *Phys. Rev. E*, **48** (6), pp. 4758-4767, 1994.

6. A.W. Snyder and J.D. Love, "Optical waveguide theory", Chapman and Hall, London, 1983.

7. R. Kashyap, R. Wyatt and R.J. Campbell, "Wide-band gain-flattened erbium amplifier using a photosensitive fiber blazed grating", *Electron. Lett.*, **29** (2), pp. 154-156, 1993.

8. F. Ouellette, "All-fiber filter for efficient dispersion compensation", *Opt. Lett.*, **16** (5), pp. 303-305, 1991.

9. K.C. Byron, K. Sugden, T. Bricheno and I. Bennion, "Fabrication of chirped Bragg gratings in photosensitive fiber", *Electron. Lett.*, **29** (18), pp. 1659-1660, 1993.

10. K.O. Hill, F. Bilodeau, B. Malo, T. Kitagawa, S. Theriault, D.C. Johnson and J. Albert, "Aperiodic in-fiber Bragg gratings for optical fiber dispersion compensation", *OFC'94 Postdeadline Papers*, paper PD2-3, San Jose, 1994.

11. B.J. Eggleton, P.A. Krug, L. Poladian, K.A. Ahmed and H.F. Liu, "Dispersion compensation by using Bragg-grating filters with self-induced chirp", *OFC'94 Technical Digest*, paper ThK3, San Jose, 1994.

12. M.C. Farries, K. Sugden, D.C.J. Reid, 1. Bennion, A. Molony and M.J. Goodwin, "Very broadband reflection bandwidth (44 nm) chirped fiber gratings and narrow bandpass filters produced by the use of an amplitude mask", *Electron. Lett.*, **30** (11), pp. 891-892, 1994.

13. R. Kashyap, P.F. McKee, R.J. Campbell and D.L. Williams, "Novel method for producing all fibre photo-induced chirped gratings", *Electron. Lett.*, **30** (12), pp. 996-998, 1994.

14. J.A.R. Williams, I. Bennion, K. Sugden and N.J. Doran, "Fibre dispersion compensation using a chirped in-fibre Bragg grating", *Electron. Lett.*, **12** (30), pp. 985-987, 1994.

15. R. Kashyap, S.V. Chernikov, P.F. McKee and J.R. Taylor, "30 ps chromatic dispersion compensation of 400 fs pulses at 100 Gbits/s in optical fibres using an all fibre photoinduced chirped reflection grating", *Electron. Lett.*, **30** (13), pp. 1078-1080, 1994.

16. P.C. Hill and B.J. Eggleton, "Strain gradient chirp of fibre Bragg gratings", *Electron. Lett.*, **30** (14), pp. 1172-1174, 1994.

17. P.A. Morton, V. Mizrahi, T. Tanbun-Ek, R.A. Logan, P.J. Lemaire and H.M. Presby, "Stable single mode hybrid laser with high power and narrow linewidth", *Appl. Phys. Lett.*, **64** (20), pp. 2634-2636, 1994.

18. S. Legoubin, E. Fertein, M. Douay, P. Bernage, P. Niay, F. Bayon and T. Georges, "Formation of Moiré grating in core of germanosilicate fibre by transverse holographic double exposure method", *Electron. Lett.*, **27** (21), pp. 1945-1946, 1991.

19. W.H. Press, B.P. Flannery, S.A. Teukolsky and W.T. Vetterling, "Numerical Recipes", Cambridge University Press, Cambridge, 1986.

Chapter 3
Photosensitivity of germanosilicate optical fibres

3.1. Introduction

Photosensitivity is defined as permanent physical or chemical changes resulting from exposure to light. It is now well-known that when germania-doped silica fibres which are exposed to blue, green, UV or even gamma irradiation, many of the glass properties can be permanently modified, such as the refractive index [1], absorption [2,3], stress [4], birefringence [5], density [6], thermal expansion coefficient [7] and nonlinear susceptibility [8]. Glass photosensitivity is a vast and complex problem because of the large number of parameters involved and the diversity of effects that are observed. The fibre composition, fabrication process, and history, the wavelength and intensity of the light source all have an influence on the photosensitivity. Also, the recent discovery of post-fabrication techniques for enhancing fibre photosensitivity, such as flame-brushing and hydrogen-loading, has added new dimensions to the problem.

In this chapter, a review of the literature on photoinduced index changes in germania-silica fibres is presented, describing the various models which have been put forward to explain the phenomenon. The dynamics of several photosensitivity-related phenomena are examined and compared; a model is put forward to explain these observations, based on dispersive charge transport and a detailed energy level diagram of oxygen-deficient defect centres. Throughout this project, a large number of fibres have been characterised for their photosensitivity. These results are tabulated, allowing different types of fibres and known methods of enhancing fibre photosensitivity to be compared. Finally, in the last section, the results of experiments on photoinduced birefringence are presented.

3.2. Defect centres and UV absorption spectrum

The normal molecular structure of silica is tetrahedral, with each silicon atom being singly bonded to four oxygen atoms. In quartz, these tetrahedra form a regular lattice, but in glass, they form a disordered structure. Since germanium atoms have the same valence they can replace the silicon atoms in the glass structure. Even though germania

incorporates well into silica, it still constitutes an impurity which can perturb the glass network, leading to the formation of 'wrong bonds' or defect centres. These defects, which are generated at the various stages of fibre and preform fabrication, are at the source of all photosensitivity-related phenomena. Their presence can be detected by several means: absorption measurements [9], electron spin resonance (ESR) experiments [10] and luminescence studies [11].

Fig. 3-1 shows the UV absorption spectrum of a germania-silica fibre preform. The main features are the absorption band at 242 nm (5.12 eV) and a strong UV edge rising at shorter wavelengths. Another band, one thousand times weaker than the 242 nm band, is present at 325 nm (3.8 eV) [12]. It has been shown that the strength of these bands correlates with the germania concentration [13] and also with the application of reducing condition during preform manufacture [13,14]. It is therefore widely accepted that the bands are associated with germanium oxygen deficient centres as suggested by Cohen and Smith in 1958 [9]. These defects are diamagnetic and therefore not detectable by ESR measurements.
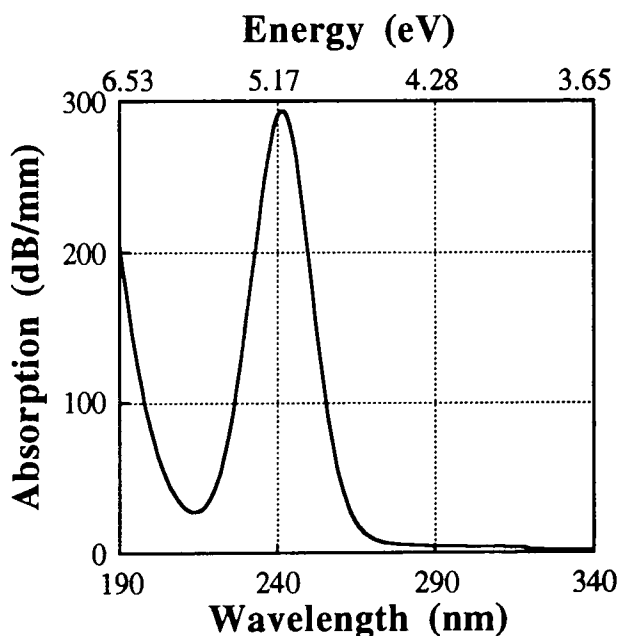
Figure 3-1 - UV absorption spectrum of MCVD fibre preform with 10 mol% GeO_2 (courtesy of L. Dong).

Two types of germanium oxygen-deficient defect structures have been proposed [11,15] as shown in Fig. 3-2. Structure (a) consists of a germanium atom having a silicon or germanium nearest-neighbour and is known as a 'neutral oxygen vacancy' (NOV) [15].

In structure (b), the germania molecule is in the reduced state GeO with the germanium atom being bonded to only two oxygens and is left with a lone pair of electrons [11].
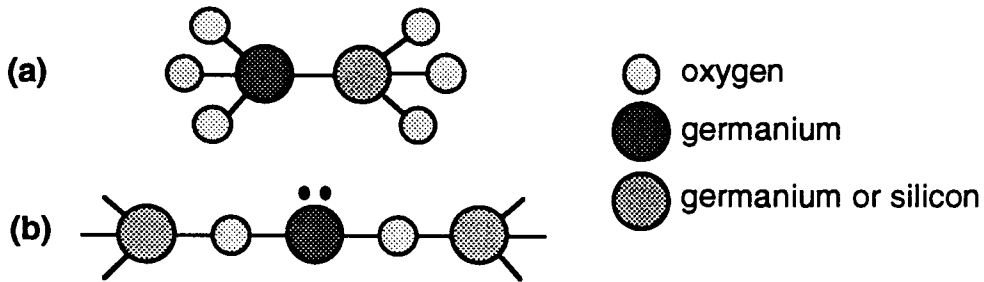
Figure 3-2 - Proposed oxygen-deficient defect structures

Several effects are known to result from the absorption of photons in the 242 nm band:

1) permanent increase in refractive index [1];

2) permanent partial bleaching of the 242 nm band [3,9];

3) permanent increase of the 195 nm band [16];

4) permanent absorption increase in the visible [17,18];

5) formation of paramagnetic GeE' centres [10];

6) decaying photoluminescence at ~410 nm and ~290 nm [11,14,19];

7) transient photodarkening in the visible [18] and infrared [20];

8) transient gain around 1000 nm [20] (see chapter 6).

Defect (a) is believed to be responsible for the formation of E' centres and the bleaching of the absorption band through the photochemical reaction illustrated in Fig. 3-3 [15]. Defect (b) is thought to be unbleachable and thus not to contribute to the photosensitivity mechanisms [15]. Another route to the formation of E' centres could be a photochemical reaction between either defect (a) or (b) in an excited state and a neighbouring defect [21].
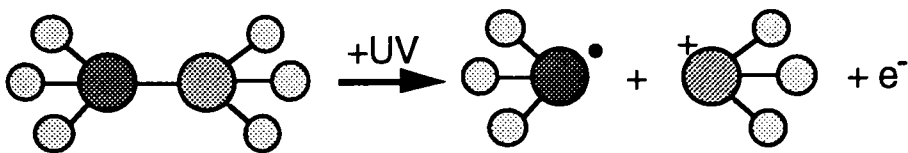
Figure 3-3 - Possible photochemical reaction for E' centre formation: a Ge-Si (or Ge-Ge) bond is ionised by UV radiation; the bond is broken, resulting in a GeE' centre, a positively charged Si or Ge centre and a free electron.

Most of the effects listed above are known to be related: the bleaching of the 242 nm absorption band was seen to follow the same dynamics as the increase of the 195 nm

band [22], the creation of GeE' centres [23] and the decay of the photoluminescence [21]; also, the luminescence decay was found to follow the growth of the photoinduced refractive index change [19].

Fig. 3-4 presents a possible energy level diagram of a germanium oxygen-deficient centre strongly inspired from the models suggested by Yuen [12], Skuja, Trukhin and Plaudis [11] and Gallagher and Osterberg [24]. It is a three-level system with a singlet ground-state S_0 located roughly in the middle of the band gap of silica, an upper singlet state S_1 and a triplet state T_1. In this model, absorption in the 242 nm band excites an electron to level S_1 where it can either decay back to S_0 by emitting a photon or to T_1 by non-radiative decay. A triplet to singlet transition has a very low probability, which is consistent with the low absorption observed at 3.8 eV and the long lifetime of the 3.0 eV fluorescence (80-130 μs [11,19,24]). The $S_1 \rightarrow S_0$ transition has a much shorter lifetime, estimated at less than 50 ns [24]. At room temperature, the 3.0 eV fluorescence is much stronger than the 4.3 eV emission; below 100K however, the 4.3 eV fluorescence dominates since the T_1 state is populated by phonons [14].
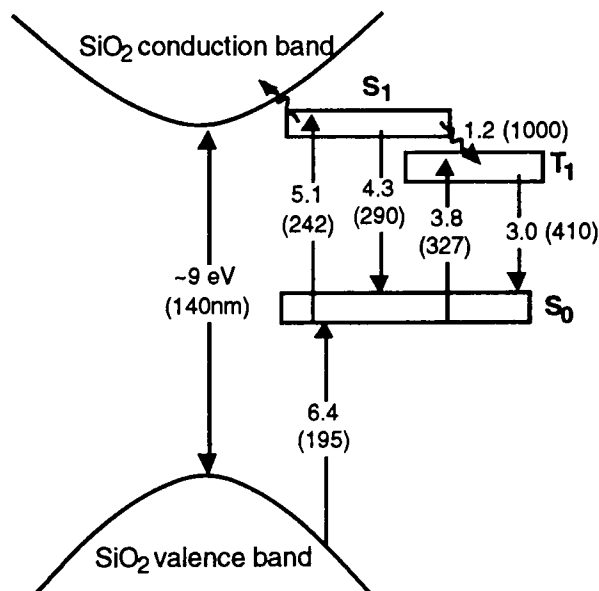
Figure 3-4 - Proposed energy-level diagram of oxygen-deficient centre. Wavy line indicates non-radiative transition.

In the proposed model, the defect is ionised by thermal excitation from S_1 to the conduction band. This model is described in detail in section 3.2.2. Once an electron has reached the conduction band, it can either return to its original site or migrate to another trapping site at a different location in the glass. The latter permanently modifies

the UV absorption spectrum, bleaching the absorption at 242 nm and enhancing it at other wavelengths.

The location of the S_0 level at mid-gap is motivated by two observations: 1) comparative experiments using pulsed and CW UV lasers have shown that the ionisation of oxygen-deficient centres is mostly a single-photon process [25] and 2) the bleaching of the 242 nm band and the growth of the 195 nm (6.4 eV) band have the same dynamics [22], suggesting that the increase at 195 nm could be due in part to transitions from the valence band to vacancies in the ionised defects.

The energy-level diagram of Fig. 3-4 is further supported by recent observations of transient gain in the 1 μm region induced by 248 nm light [20] (see chapter 6), which has been interpreted as stimulated emission from S_1 to T_1.

3.2. Dynamics of photoinduced changes

As was mentioned earlier, strong correlations have been established between the bleaching of the 242 nm absorption band, the growth of the 195 nm band, the decay of the blue luminescence and the increase of the refractive index during the exposure of a germania-silica fibre or preform to UV light within the 242 nm band. Through these various observations, the dynamics of photosensivity-related phenomena are becoming increasingly clear. In this section, a summary of the relevant experimental results found in the literature is presented along with a theoretical model based on dispersive charge transport in glass.

3.2.1. Experimental results

Decay of blue luminescence

Poirier *et al.* recently published a series of measurements on the decay of blue luminescence decay in a fibre exposed to pulsed light at 266 nm [21]. They showed that the dependence of luminescence power P with the exposure time t was very well fitted by a stretched exponential function of the form

$$P(t) = P(0) \exp[-(t/t_s)^\beta] \qquad (3\text{-}1)$$

where t_s and β are constants. For several successive measurements at different UV power levels, they found similar values of the parameter β with an average of $\beta=0.302\pm0.039$. Gilbert and Patrick reproduced the experiment with both a CW and a

pulsed UV laser at 244 nm and also found that Eq. (3-1) fitted their data very well, with β=0.305±0.025 [25].

Index change

In 1990, Hand and Russell measured by interferometry the index change induced in a germania-silica fibre by 488 nm light via two-photon absorption [2]. In this publication, the dependence of the photoinduced index change with exposure time was fitted by a sum of two saturating exponentials; however, it can be shown that their data can be very well fitted by either of the two functions:

$$\Delta n(t) = \Delta n_s \ (1-\exp[-(t/t_s)^\beta])$$
$$\Delta n(t) = \Delta n_s \ (1-\frac{1}{1+(t/t_s)^\beta}) \qquad (3-2)$$

with β=0.39±0.03. More recently, Patrick and Gilbert studied the evolution of the index modulation of fibre gratings exposed to CW light at 244 nm [26]. They found that the index change followed a power-law function, ct^β (c constant), with the exponent β ranging from 0.29 to 0.32, depending on the UV intensity level. It is also our experience that the growth of a UV-written fibre grating always follows a power-law function in the initial stages, with β parameters ranging between 0.3 and 0.5. This is discussed in more detail in the next chapter.

Absorption change

Fig. 3-5 shows the result of an experiment performed by Dong *et al.* [22], where a sample of germania-doped silica is exposed to 20 ns pulses from a KrF excimer laser at 248.5 nm with a pulse fluence of 0.25 J/cm². The sample consists of a high purity silica substrate with a 30 μm overlay of germania-doped silica, grown by modified chemical vapour deposition. The absorption α at the excimer wavelength of the Ge-doped layer is obtained by measuring the fraction of the pulse energy transmitted by the sample and plotted against the total exposure or fluence F. The data was fitted by the function

$$\alpha(F) = \alpha(\infty) + \frac{\alpha(0)-\alpha(\infty)}{1+(F/F_s)^\beta} \qquad (3-3)$$

where F_s is the saturation fluence. The initial absorption was determined by measuring the UV absorption spectrum of the sample before the exposure, which gave $\alpha(0)$=335 dB/mm. The value of $\alpha(\infty)$ depends on the tails of UV-induced absorption bands at 195 and 256 nm (see Fig. 3-9). From the data of Ref. [22], it can be shown that, at 248.5 nm, the increase in absorption due to growth of the 195 and 256 nm bands is approximately 32% of the decrease in absorption due to the bleaching of the 242 nm

band. If we assume that most of the initial absorption, $\alpha(0)$, is caused by the 242 nm band and that all of the 242 nm band is bleached for $F \rightarrow \infty$, then $\alpha(\infty) \approx 32\% \times \alpha(0) \approx 107$ dB/mm. This is the lowest possible value of $\alpha(\infty)$: if we had assumed that a fraction x of the initial absorption was unbleachable, then we would have obtained a higher value of $\alpha(\infty)$. The maximum possible value of $\alpha(\infty)$ can be taken as the final value of $\alpha(F)$ in Fig. 3-5, which is ~120 dB/mm and would correspond to $x \approx 6\%$. Equally good curve fits can be obtained from Eq. (3-3) for any value of $\alpha(\infty)$ between 107 and 120 dB/mm ($0 < x < 6\%$). The fitting parameters are then $0.08 < F_s < 0.12$ kJ/cm^2 and $0.47 < \beta < 0.79$. Similarly good fits can be obtained with the stretched-exponential function:

$$\alpha(F) = \alpha(\infty) + (\alpha(0) - \alpha(\infty)) \exp[-(F/F_s)^\beta] \tag{3-4}$$

For $107 < \alpha(\infty) < 120$ dB/mm, the fitting parameters $0.16 < F_s < 0.22$ kJ/cm^2 and $0.20 < \beta < 0.34$.
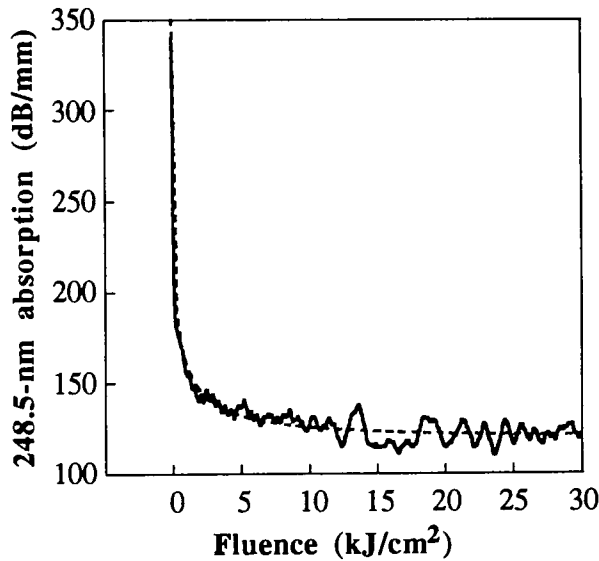
Figure 3-5 - Bleaching of 242 nm absorption band during exposure at 248.5 nm preform sample with 12.5 mol% GeO$_2$. Dashed line shows fit from Eq. (3-3).

The measurement of Fig. 3-5 therefore shows that at least 94%, if not all of the 242 nm absorption band can be bleached by 248.5 nm exposure, in contrast with the assumption that this band is caused by bleachable and unbleachable defects [15].

Birefringence change

In section 3.5, it is shown that the evolution of photoinduced birefringence under constant UV exposure also has a power-law dependence which can be fitted by one of the

functional forms of Eq. (3-2). In an elliptical fibre exposed to pulsed light at 248.5 nm, a β parameter of about 0.4 was measured.

3.2.2. Model and discussion

Power-law functions are commonly observed in a wide variety of dynamic processes in disordered materials, including mechanical relaxation and charge transport [27]. The common aspect of these processes is that they do not possess a single characteristic time scale but are driven by what is known as 'dispersive transport'. Dispersive charge transport is certainly expected in photosensitivity-related phenomena, since the rate of photoionisation of a defect under constant UV irradiation depends on the random position and orientation of that defect within the glass network and the relative positions of neighbouring trapping sites.

In the following, a model is developed which starts with the assumption that the photoionisation of defects is driven by the thermal excitation of electrons from the upper energy level of the defect centre to the conduction band. This hypothesis is supported by experimental evidence which is presented in section 4.3 and by the measurements of Hosono *et al.* who showed that the bleaching of the 242 nm band by UV exposure was much more efficient at 300K than at 77K [15]. For a population of defects having an energy gap E between the upper excited state and the bottom of the conduction band, then the fluence required to ionise (1-1/e) of the initial defect population is given by

$$F_i(E) = F_0 \exp(E/k_BT) \tag{3-5}$$

where F_0 is a constant which depends on the UV wavelength and the glass properties, k_B is the Boltzmann constant and T the temperature. Eq. (3-5) assumes a Boltzmann distribution, which is valid if $E \gg k_BT$. The population density of these defects decreases exponentially during the exposure as

$$\rho(E,F) = \rho_0(E) \, e^{-F/F_i(E)} \tag{3-6}$$

where ρ_0 is the initial distribution and F the UV exposure. The total number of occupied defect sites at a time t is then given by

$$N(F) = \int_0^\infty \rho(E,F)dE \tag{3-7}$$

The photoinduced changes, such as the bleaching of the 242 nm band, the decay of the blue luminescence and the increase in refractive index, should all be proportional to $N(0)$-$N(t)$. If $N(F)$ is known, then it is possible to calculate the initial defect distribution $\rho_0(E)$. This calculation is greatly simplified by introducing the concept of demarcation

energy, as described by Erdogan *et al.* in the context of the thermal decay of fibre gratings [28]. This energy is defined by

$$\rho(E_d, F) = e^{-1}\rho_0(E_d)$$

or $$E_d = k_B T \ln(F/F_0) \tag{3-8}$$

After exposing for a time t at a temperature T, most defects with an ionisation energy smaller than E_d have been ionised, while most defects with an ionisation energy greater than E_d are still populated. During an exposure, the demarcation increases gradually as the defects with the lowest ionisation energy become depleted. For $E \ll E_d$, $\rho(E,t) \approx 0$ and for $E \gg E_d$, $\rho(E,t) \approx \rho_0(E)$; this leads to the approximation [28]

$$N(F) \approx \int_{E_d}^{\infty} \rho_0(E)dE \tag{3-9}$$

which is equivalent to

$$\frac{\partial N}{\partial E_d} \approx -\rho_0(E_d) \tag{3-10}$$

The initial defect distribution is therefore approximately equal to the derivative of the function $N(F)$ with respect to the demarcation energy. Two possible forms of $N(F)$ have been identified from the experimental data: the stretched exponential

$$N(F) = N(0) \exp(-(F/F_s)^\beta)$$

and the power-law function

$$N(F) = \frac{N(0)}{1+(F/F_s)^\beta} \tag{3-11}$$

By substituting Eqs. (3-8) and (3-11) in (3-10), the following results can be derived: for the stretched exponential,

$$\rho_0(E) = \frac{N(0)}{\Delta E} \exp(\frac{E-E_0}{\Delta E} - \exp(\frac{E-E_0}{\Delta E})) \tag{3-12}$$

and, for the power-law function,

$$\rho_0(E) = \frac{N(0)}{4\Delta E} \text{sech}^2(\frac{E-E_0}{2\Delta E}) \tag{3-13}$$

where

$$\Delta E = \frac{k_B T}{\beta} \quad ; \quad E_0 = k_B T \ln(F_s/F_0) \tag{3-14}$$

ΔE is the characteristic width and E_0 the position of the peak of the initial ionisation energy distribution. The dispersion parameter β is therefore given by the ratio of the phonon energy to the width of the energy distribution. When β tends to 1, the distribution $\rho_0(E)$ is narrow compared to $k_B T$; in that case, all defects have similar ionisation energies which means that the system becomes non-dispersive and $N(F)$ has a simple exponential dependence. A smaller value of β implies that the defects have a

broader distribution of ionisation energies. In the limit $\beta \rightarrow 0$, the width of the energy distribution tends to infinity and $N(F)$ becomes a step-function.

The parameter ΔE is determined by the molecular structure of the glass and should therefore be independent of temperature. This imposes the relation [27-29]

$$\beta = \frac{T}{T_0} \qquad (3\text{-}15)$$

where T_0 is a constant, so that $\Delta E = k_B T_0$. In this model, the dispersion parameter β should therefore depend linearly on temperature. This is verified experimentally in the next chapter.

The distributions of Eqs. (3-12) and (3-13) are compared in Fig. 3-6. The distribution obtained from the power-law function is simply a sech^2 distribution. It is symmetrical and has a full-width at half-maximum equal to $\sim 3.53 \Delta E$. The distribution obtained from the stretched exponential is asymmetric with a FWHM of $\sim 2.45 \Delta E$. Both distributions tend to the same exponential function when E is small. It is likely that any distribution which has an exponential tail on the low energy side and then goes through a maximum could be used to describe the experimental data.
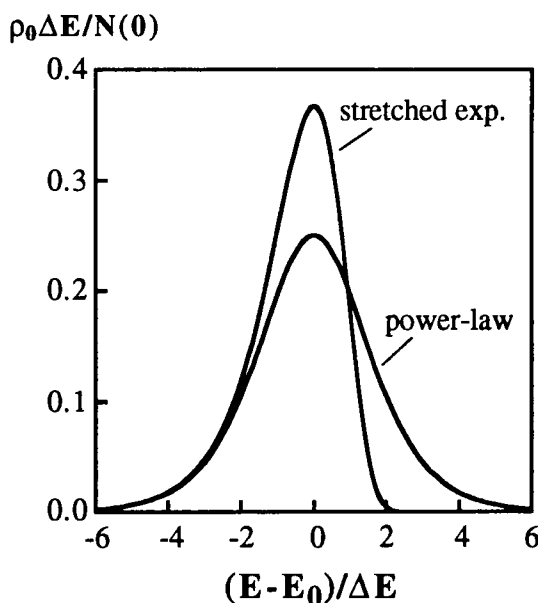
Figure 3-6 - Initial defect ionisation energy distributions calculated from Eqs. (3-12) and (3-13).

Fig. 3-7 shows the evolution of $\rho(E,F)$ for different exposures. The demarcation energy, which can now be expressed as

$$\frac{E_d - E_0}{\Delta E} = \beta \ln(F/F_s) \qquad (3\text{-}16)$$

is indicated by the vertical lines. The total population, N, is given by the area under the curve at the different stages of the exposure. In the initial stage of the exposure, the defects with the lowest ionisation energies are bleached, which displaces E_d to higher energies and rapidly slows down the ionisation rate. The fluence required to increase the demarcation energy by a fixed amount grows exponentially. Whereas the evolution of the two distributions are similar for $F < F_s$, the depletion of defects is much more rapid for $F > F_s$ in the case of the stretched-exponential, due to the asymmetry of the initial distribution. To distinguish experimentally between the two distributions, one would therefore have to go to very long exposures.
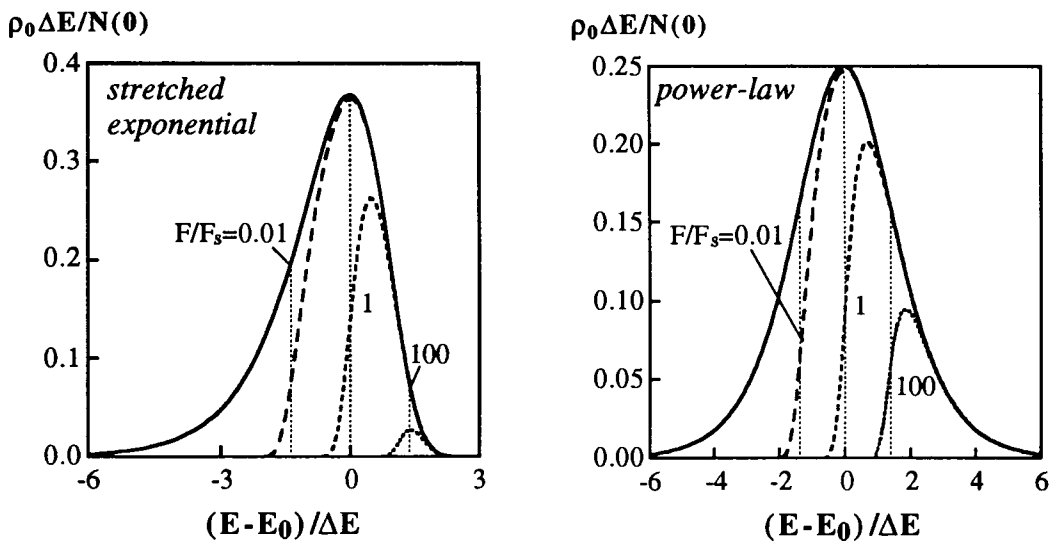
Figure 3-7 - Evolution of the ionisation energy distributions for $\beta = 0.3$.

Vertical lines show demarcation energy for the different exposures.

Fig. 3-7 is a good illustration of the approximation of Eq. (3-9), where the exact energy distribution was replaced by a step function equal to 0 for $E < E_d$ and to the initial distribution for $E > E_d$. The error introduced by this approximation in evaluating N is given by the difference between the areas under the two curves. For examples, in the case of the power-law function, the error on N in Fig. 3-7 is 3% for $F/F_s = 0.01$, 8% for $F/F_s = 1$ and 11% for $F/F_s = 100$.

According to this model, the evolution of the defect population is determined by three fundamental parameters: E_0, ΔE and F_0. These can be measured experimentally, by examining the evolution of the defect population at different temperatures. Plotting β against temperature should give a linear function with a slope equal to $k_B/\Delta E$. The

parameter F_0 can be obtained by comparing two measurements of the defect population change, ΔN_1 and ΔN_2, obtained for the same fluence F but at different temperatures. F_0 is then given by

$$F_0 = F \, (\Delta N_2/\Delta N_1)^{1/(\beta_1-\beta_2)} \qquad (3\text{-}17)$$

The third parameter, E_0, can be determined by measuring the saturation fluence, F_s, and using Eq. (3-14). These ideas are implemented in the next chapter, when analysing the dynamics of fibre grating formation.

The model presented here can only be valid as long as the initial hypothesis - that the upper level electrons access the conduction band by thermal excitation - is verified. An alternative would be to assume that the electrons are excited optically to the conduction band, by absorbing a second photon. This seems highly unlikely, simply because the photon energy is much larger than $k_B T$: this would imply having an ionisation energy distribution with a characteristic width $\Delta E = h\nu/\beta$ which would have to be larger than the band gap of silica! Therefore, it seems impossible that two-photon absorption should result in dispersive charge transport. Since the photoionisation of defects is clearly dispersive, two-photon absorption can be ruled out as the driving mechanism.

3.3. Photoinduced index change

The photoinduced refractive index change can be directly measured in fibres by several means: interferometric methods [2,30], measuring changes in mode field diameter [19] or in the refractive index profile [31]. But the method now most commonly used is to calculate the change in refractive index from the reflection or transmission spectrum of a fibre grating. However, as we saw in section 2.3, the relationship between the index modulation of a grating and the actual index change is complex and requires knowledge of the photosensitive response of the glass, of the visibility of the fringe pattern and of the UV beam profile. This method must therefore be used with care.

In this section, we use recently measured and previously published experimental data to examine how the photoinduced index change in GeSi fibres depends on the various parameters: germania concentration, reading and writing wavelength and UV intensity.

3.3.1. Dependence on germania concentration

Fig. 3-8 shows the maximum index modulation obtained by writing gratings in untreated germania-silica fibres, using the experimental setup described in the next chapter. All

these fibres were fabricated in Southampton by the standard modified chemical vapor deposition process (MCVD). There are large uncertainties on these calculated index modulations because most of these gratings were written with a non-uniform UV beam; as a consequence, the gratings were randomly chirped and tapered, as described in section 2.7. The upper bound of each error bar is the index modulation calculated from the effective bandwidth of each grating, using the expressions of Table III; the lower bound is calculated from the peak reflectivity of the grating, assuming a perfectly uniform grating. In both cases, the effective index modulation δn is divided by the fraction of power in the core η to estimate the true index modulation, Δn_1 (see Eq. (2-11)). The Ge concentrations were estimated from the refractive index profile of each fibre.
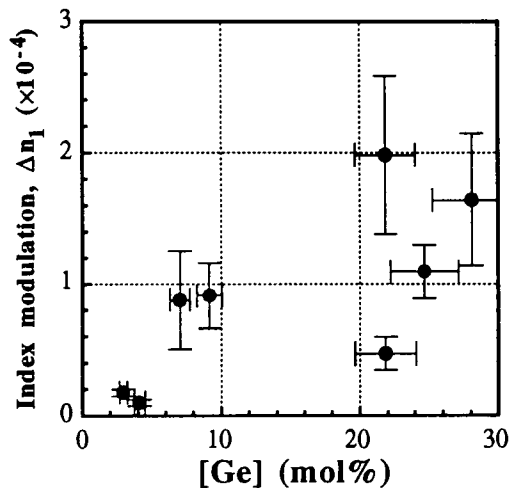
Figure 3-8 - Maximum photoinduced index modulation in Ge/Si fibres with different Ge concentrations.

Although the data of Fig. 3-8 is crude, it does show that the photoinduced index change generally increases with the concentration of germania in the fibre core. This is consistent with other measurements which showed that the 242 nm absorption [13] and the photoinduced absorption changes [22] increase linearly with Ge concentration . In fibres containing ~3 mol% of Ge, which corresponds to standard telecommunications fibres we obtain maximum index modulations of order 10^{-5}. However it must be noted that the highest photoinduced index change reported to date in an untreated germania-silica fibre was obtained in a standard telecommunications fibre [32]. In that case, the index modulation was of order 10^{-3}. The reason for this large discrepancy is not understood at the moment, but this result demonstrates that for the same glass composition, there can be large variations in photosensitivity due to other factors, such as the fabrication parameters for example.

3.3.2. Dispersion

The dispersion of the photoinduced index change is known to be very weak through the three telecommunications windows (0.8, 1.3 and 1.5 μm). Russell *et al.* measured the photoinduced index change in a fibre with 16% GeO_2 at several discrete wavelengths: 488, 633, 784 and 1550 nm [17]. They observed a slight dispersion, with an index change of ~2×10^{-4} at 488 nm decreasing monotonically to ~1.7×10^{-4} at 1550 nm (see Fig. 3-10). Malo *et al.* later measured the index change continuously between 700 and 1400 nm in a ~3 mol% GeO_2 fibre and reported that the index change was almost constant over that range at ~2.3×10^{-5} [30].

3.3.3. Dependence on writing wavelength

For the vast majority of the published work on fibre gratings, UV sources emitting within the 242 nm absorption band of optical fibres have been employed, partly because this choice of wavelength was believed to be optimal but also because few lasers operating below 240 nm are commercially available. So far, no systematic study of the effect of the writing wavelength on fibre photosensitivity has been reported. It is clear, however, that the writing process is much less efficient at 262 [33] and 266 nm [34] than at 240 to 248 nm. Very recently, there have been a few reports of fibre gratings produced at 193 nm, using ArF excimer lasers [35,36]. Albert *et al.* found that the writing of gratings at 193 nm (6.4 eV) was more efficient than at 248.5 nm, producing a faster increase of the refractive index with a higher saturation value. A potential explanation of these results can be found in the energy level diagram of Fig. 3-4: first, the 6.4 eV photons should be able to excite electrons from level S_0 directly into the conduction band, which would make the process of ionising defects more efficient; second, the same photons could repopulate the S_0 level from the valence band, thereby increasing the number of electrons participating in the process, which would explain the higher saturated index change.

3.3.4. Intensity dependence

Several authors have observed that the dynamics of UV-induced changes in GeSi fibres have an intensity dependence [21,26,37]. Using higher UV intensities or using a pulsed instead of a CW laser improves the efficiency of the writing process so that larger changes are obtained with the same total fluence. The model proposed in this thesis to explain this intensity dependence is that a higher UV intensity increases the temperature of the fibre core, which accelerates the photo-thermal ionisation of defects. This model is discussed in more detail in section 4.3.3.

3.4. Origins of photoinduced index change

Although it is now widely accepted that all UV-induced changes in GeSi fibres are initiated by the ionisation of oxygen-deficient defects, there is still a lot of speculation as to which mechanism (or mechanisms) is ultimately responsible for the photoinduced index change. Several models have been proposed over the years [2,6,38-40] which can be divided in two categories: colour centre models and structural models.

3.4.1. Colour centre model

This model was first proposed by Hand and Russell in 1990 [2]. As described earlier in this chapter, exposure of Ge/Si fibres to UV light ionises oxygen-deficient defect centres releasing photoelectrons which presumably become trapped in neighbouring sites, thus creating new colour centres. This change in colour centre populations permanently modifies the UV absorption spectrum of the glass, which, through the Kramers-Kronig causality relation, creates an index change given by

$$\Delta n(\lambda) = \frac{1}{2\pi^2} \int_0^\infty \frac{\Delta\alpha(\lambda')}{1-\lambda'^2/\lambda^2} \, d\lambda' \qquad (3\text{-}18)$$

where $\Delta\alpha$ is the absorption change. In the colour centre model, the predominant index changing mechanism is therefore the relocalisation of electrons at different sites in the glass. If the induced absorption spectrum can be expressed as a sum of gaussian absorption bands located far away from the wavelength of interest, λ, then Eq. (3-18) can be approximated by

$$\Delta n(\lambda) \approx \frac{1}{4\pi\sqrt{\pi\ln2}} \sum_i \frac{\Delta\alpha_i \Delta\lambda_i}{1-\lambda_i^2/\lambda^2} \qquad (3\text{-}19)$$

where $\Delta\alpha_i$ is the amplitude, λ_i the central wavelength and $\Delta\lambda_i$ the full-width half-maximum linewidth of the ith absorption band.

To estimate the contribution of colour centre formation to the refractive index change in a fibre, one should ideally measure the photoinduced absorption change over the whole of the UV spectrum, down to the band gap of silica. The most complete measurement was published by Atkins *et al.* [16] who measured the UV-induced absorption change in a slice of preform with 3% Ge down to 165 nm (7.5 eV). Fig. 3-9 shows a similar measurement by Dong *et al.* [22] performed in a 10 mol% Ge preform sample after a 0.12 kJ/cm^2 exposure at 248 nm.
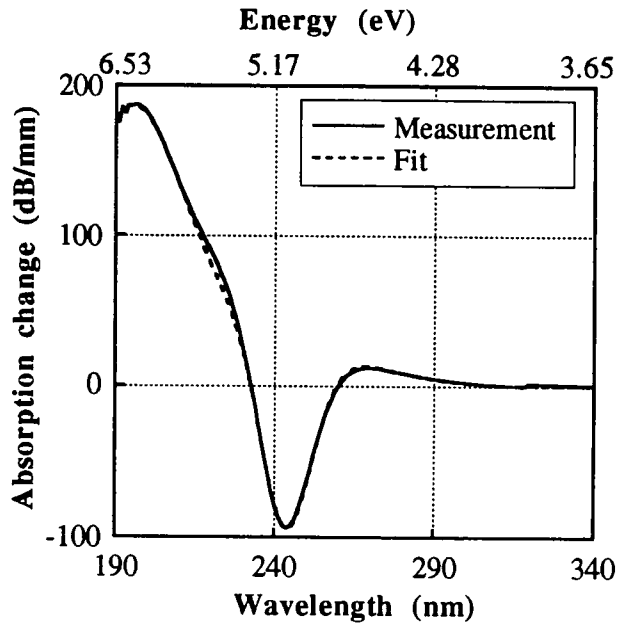
Figure 3-9 - UV-induced absorption change in preform sample with 10 mol% Ge exposed to 0.12 kJ/cm^2 at 248.5 nm fitted with three gaussian bands at 195, 242 and 256 nm (courtesy of L. Dong).

The data is well fitted by a sum of three gaussian functions centred at 195, 242 and 256 nm (6.4, 5.1 and 4.8 eV). The bleaching of the 242 nm band gives rise to a negative index change, but this is outweighed by the large increase in the 195 nm band, producing a net positive index change. A Kramers-Kronig calculation of the index change gives 6×10^{-5} at $\lambda=1550$ nm. If a saturation fluence $F_s=0.2$ kJ/cm^2 is assumed, then Eq. (3-4) predicts a saturated index change $\Delta n_s=1.0 \times 10^{-4}$. Compared to the data of Fig. 3-8 for a fibre with 10 mol% Ge, this prediction somewhat underestimates the photoinduced index change, considering that the index modulation in Fig. 3-8 represents at most half of the saturated index change.

From Eq. (3-19), the wavelength dependence of the photoinduced index change can be calculated. In Fig. 3-10, the index change calculated from the spectrum of Fig. 3-9 was multiplied by a scaling factor to best fit the data from Ref. [17]. The remarkable agreement between this fit and all four data points is strong supporting evidence for the colour centre model in the context of this particular experiment.
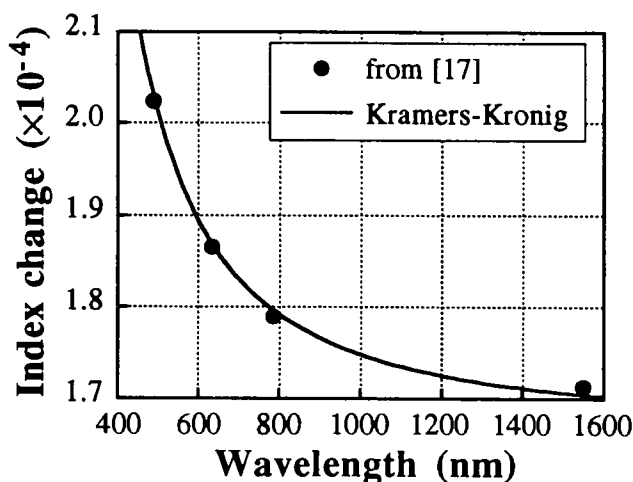
Figure 3-10 - Wavelength dependence of photoinduced index change calculated from the absorption spectrum of Fig. 3-9 compared to measured data from [17].

In general, the colour centre model gives a right order of magnitude of photoinduced index changes in standard germania-silica fibres [16,22]. It is not clear, however, whether or not the absorption changes measured in preforms between 165 and 400 nm can account for the totality of the index change, especially in fibres which show a high degree of photosensitivity [32,41].

3.4.2. Structural model

There is now strong evidence that the photoionisation of defects in germania-silica optical fibres results not only in a redistribution of electrons, but also in changes in stress [4] and glass density [6]. Glass compaction was identified early on as one of the possible mechanisms of the photoinduced index change in optical fibres [2,39]. During the fibre drawing process an important static stress builds up in the core due to the mismatch in thermal expansion coefficients and melting points of the core and cladding glass. Wong *et al.* suggested that the breakage of wrong bonds by the action of UV light would allow these stresses to relax locally, thus modifying the refractive index of the glass [4]. More recently, Fonjallaz and coworkers observed a large increase of the axial stress (~15 kg/mm^2) in the core of fibres during the pulsed UV writing of a grating and found a correlation between this stress change and the growth of the index modulation [6]. They also noticed that the sign of the stress change was always positive (axial traction), independent of the sign of the initial stress in the core, which contradicted the stress-relief model of Wong *et al.* This increase in tension is evidence that the glass is compacting under the influence of UV light, which locally increases the refractive index. It is worth

noting that photoinduced compaction has been linked to refractive index changes in bulk silica [42].

An interesting aspect of the glass compaction is that it would affect both the exposed and unexposed regions of a fibre grating: the refractive index of the exposed regions would *increase* , since the index of silica is approximately proportional to its density; but at the same time, the unexposed regions of the grating are put under tension, which *reduces* their refractive index through the elasto-optic coefficient. As a result, the average index change of the grating could be smaller than the index modulation amplitude, which is not the case in the colour centre model.

The structural and colour centre models of photosensitivity are certainly not mutually exclusive and, because they are each supported by strong evidence, it is likely that both can account for part of the index changes observed in fibres.

3.5. Enhancing fibre photosensitivity

The photoinduced index change that can be obtained in standard telecommunications fibre is usually insufficient for producing useful components. One way of obtaining higher index changes is of course to use fibres with higher germania concentrations. But this method has an important drawback: increasing the germania content of the core of a fibre also increases its refractive index, making it incompatible with standard fibres. Fortunately, more efficient methods have been found as discussed below.

3.5.1. Reduced fibres

The concentration of oxygen-deficient centres and hence the photosensitivity of a fibre, can be enhanced during the fabrication process by applying reducing conditions during preform manufacture [13,43] or post-treating the preform in high temperature hydrogen [14,18,44]. A few reduced germania-silica fibres have been tested in the course of this project and the results are shown in Fig. 3-11. The index modulations obtained in the reduced fibres are up to a factor of 3 larger than in standard fibres with similar GeO_2 content. The largest enhancement was obtained for a fibre drawn from a preform which had been reduced in a deuterium atmosphere. A drawback of this method is that the reducing reaction between hydrogen or deuterium and GeO_2 creates OH⁻ bonds, which produce a strong absorption band at 1.4 μm, affecting the transmission in the two main telecommunications windows.

An alternative approach is to reduce the fibre after it has been pulled. This can be achieved using the so-called 'flame-brush' method, which consists of exposing a section to a hydrogen flame [45]. Flame-brushing typically enhances the photosensitivity of a fibre by up to one order of magnitude with the advantage that only a specific region of the fibre can be treated.
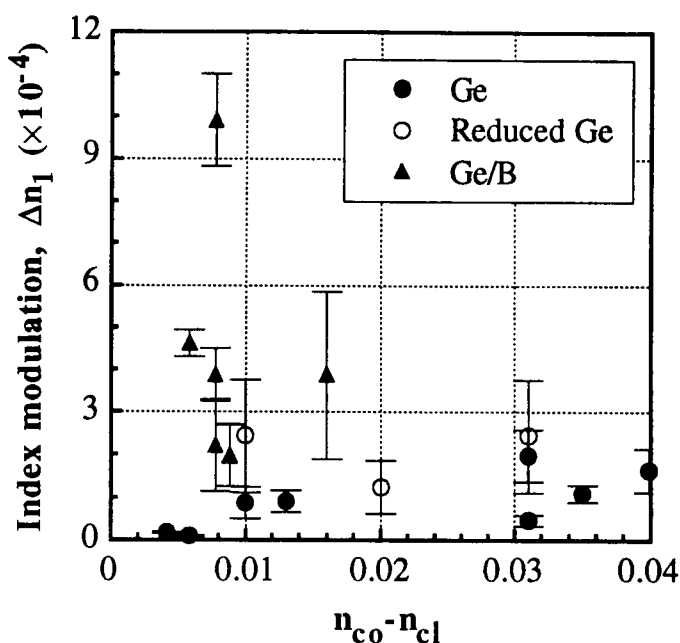
Figure 3-11 - Maximum grating index modulation obtained in silica fibres with different core compositions (Ge: germania-doped; Ge/B: germania and boron co-doped).

3.5.2. Co-doping

Boron is a dopant which, when added to silica, reduces its refractive index. Germanosilicate fibres co-doped with boron were first developed in Southampton as a means of increasing the germania content of a fibre without increasing its index [46]. Williams *et al.* subsequently reported that the addition of boron not only reduced the refractive index of the core, but also increased its photosensitivity [41]. In the course of this project, the highest grating index modulations in an untreated fibre were obtained in fibre HD066 containing an estimated 9% GeO_2 and 7% B_2O_3. Index modulations as high as 10^{-3} were observed, which is one order of magnitude larger than what would be expected in a fibre containing the same amount of germania but no boron. This fibre has a core-cladding index difference of ~0.008, only slightly larger than that of a standard telecommunications fibre (~0.005).
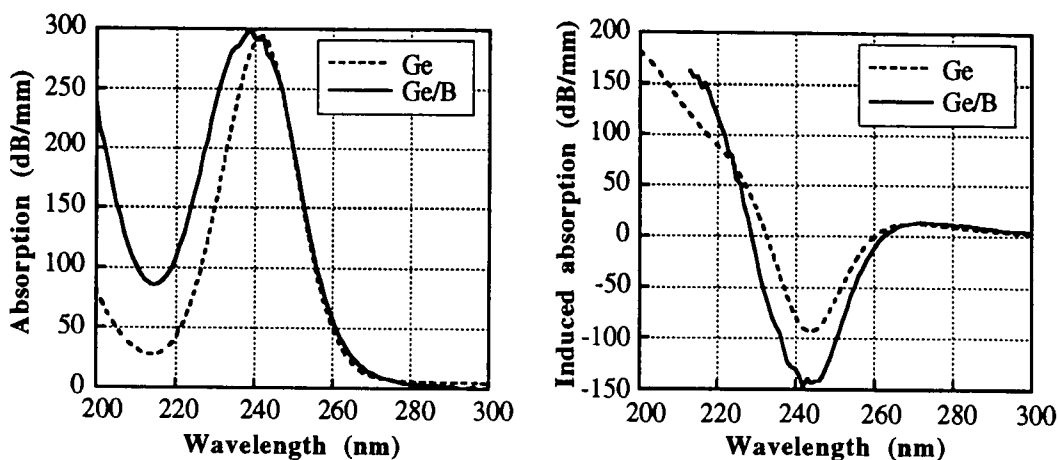
Figure 3-12 - Initial absorption spectrum and absorption change induced by 0.12 kJ/cm^2 exposure at 248.5 nm in germania-boron co-doped preform sample. Dashed lines show similar measurements in germania-doped sample.

The reason for this large increase in photosensitivity is not understood. One possible explanation is that boron, being trivalent, acts as an electron acceptor when doped in silica, thus facilitating the ionisation process. However, the absorption spectra measured in germania-boron preform samples before and after UV exposure are fairly similar to those measured in germania-doped samples with similar germania content and exposure conditions (Fig. 3-11). An alternative explanation is that the presence of boron favours photoinduced structural changes in the glass: the addition of boron strongly modifies the physical properties of the glass, increasing the thermal expansion coefficient and reducing the melting point; this should affect the molecular structure and stresses of the core glass. This is supported by the large permanent index changes (8.7×10^{-3}) observed in boron-doped silica fibres annealed at temperatures of several hundred degrees [47].

Similar enhancement of fibre photosensitivity has been observed in fibres co-doped with aluminium, which, it must be noted, has the same valence as boron [18].

3.5.3. Hydrogen-loading

The hydrogen-loading technique was developed at AT&T Bell Labs in 1993 [31]. This method can make any germania-doped fibre extremely photosensitive. Typically, hydrogen-loading can increase the photosensitivity of a fibre by up to two orders of magnitude and in some cases, index changes in excess of 0.01 have been obtained [48]. What distinguishes hydrogen-loading from previous hydrogenation techniques is that the diffusion of hydrogen in the fibre is performed at high pressure (up to 800 atm.) and low

temperature (less than 150°C), so that large concentrations of hydrogen can diffuse in the glass in molecular form, without forming OH⁻ bonds. Subsequent exposure to UV light or heat (which may be generated by the UV) then triggers chemical reactions between hydrogen and the glass, forming GeOH, SiOH, GeH, SiH and oxygen deficient centres, depending on the particular heat and UV exposure conditions [44,49,50]. A detailed description of the technique is presented in the following.

The diffusion of hydrogen in optical fibres is well described by the diffusion equation [51]. The diffusion time depends on the diameter of the fibre and the temperature, as shown in Fig. 3-13. For a bare fibre, it is given by

$$t_{diff} = 4.4 \times 10^{-6} \; e^{5.2 \times 10^3 K/T} \; r_{cl}^2 \; s/\mu m^2 \qquad (3\text{-}20)$$

where T is the temperature. At room temperature, the diffusion time is about 10 days for a 125 μm fibre, but this time can be drastically reduced by diffusing at higher temperatures: t_{diff} is roughly halved for each temperature increase of 12°C. However, an increase in temperature reduces the solubility of hydrogen in glass, as seen in Fig. 3-15. The relationship between solubility and temperature is approximately given by

$$S \approx 7 \times 10^{-4} \; e^{7.8 \times 10^2 K/T} \; P \; mol\%/atm. \qquad (3\text{-}21)$$

where P is the external hydrogen pressure. Eq. (3-21) was obtained by fitting the data of Ref. [51]. This relation shows that a 12°C increase from room temperature causes only a 9% decrease in solubility.
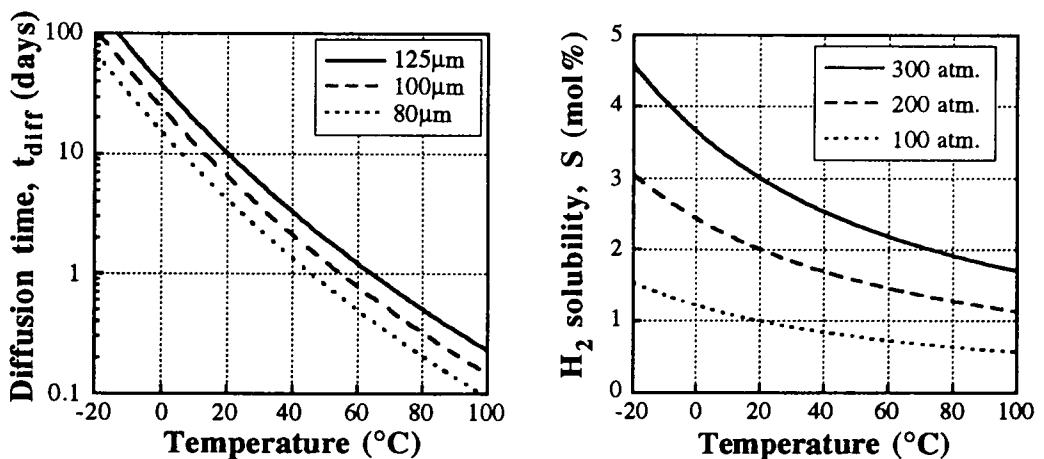
Figure 3-13 - Diffusion time (for different fibre diameters) and solubility

(for different H₂ pressures) of hydrogen in bare silica fibres (after [51])

Fig. 3-14 shows how the hydrogen concentration in the centre of the fibre (normalised to the solubility) evolves with time. This graph was obtained by numerically solving the

diffusion equation for a cylindrical rod. At $t=t_{diff}$, the hydrogen concentration has reached approximately 63% of its saturation value.
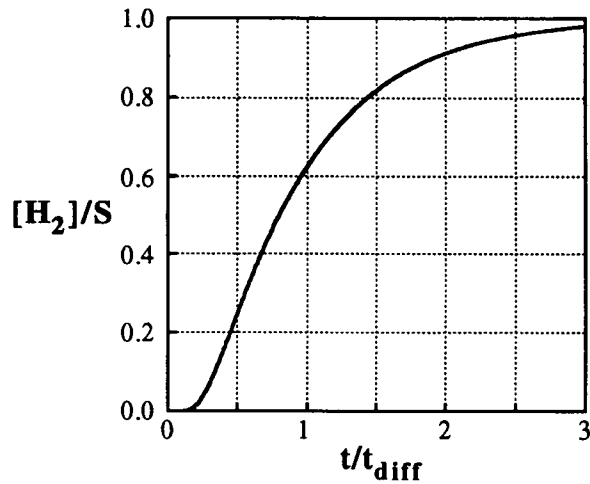
Figure 3-14 - Evolution of hydrogen concentration in centre of fibre during diffusion process.

The presence of H_2 in a fibre results in a series of overtone absorption bands located between 1000 and 1300 nm [51]. The hydrogen concentration in a fibre can be easily estimated by measuring the main absorption peak at 1245 nm and using the following relation:

$$[H_2] \approx 0.33 \text{ mol}\% \times \alpha_{1245} \text{ (dB/m)} \qquad (3\text{-}22)$$

Fig. 3-15 shows a typical measurement of the 1245 nm peak made by the cutback technique in a fibre with ~1 mol% H_2.
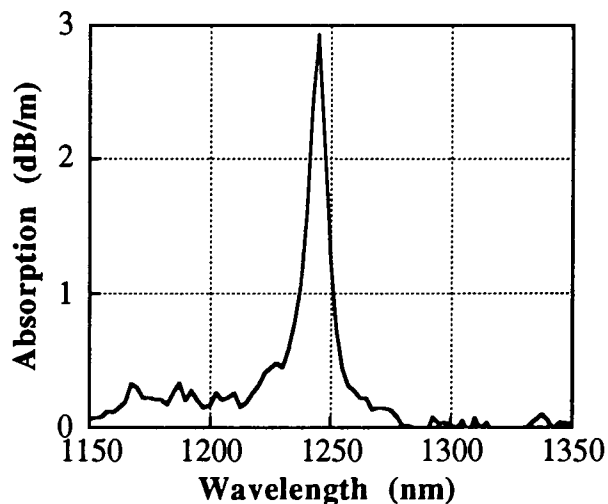
Figure 3-15 - Absorption spectrum in fibre with ~1 mol% H_2.

The hydrogen concentration required to obtain the maximum enhancement of the fibre photosensitivity is at least half of the germania concentration or more. It has been shown that if this condition is met, then every germania molecule can be reduced [31]. In Britain, however, safety regulations limit the maximum pressure at which hydrogen can be stored to 175 atmospheres. This limits the room temperature hydrogen solubility in fibres to about 1.8 mol%, which can potentially react with 3.6 mol% of germania. As a consequence, we are not able to obtain index changes in excess of 0.01 as reported in [48], where hydrogen at 800 atm. was used. Nevertheless, index modulations as high as 4×10^{-3} can be obtained as shown in Fig. 3-16.
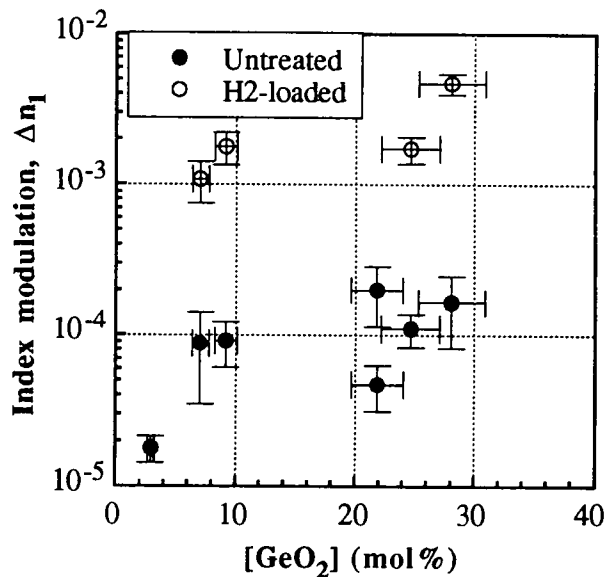
Figure 3-16 - Comparison of index modulation obtained in hydrogen-loaded and untreated Ge-doped silica fibres with different germania concentrations.

The hydrogen-loading technique has some very important advantages over the other sensitisation techniques:

1) it can increase the photosensitivity of most fibres by two orders of magnitude, which is sufficient to obtain very high reflectivity gratings in almost any fibre;

2) it only affects the exposed regions of a fibre: the hydrogen contained in the unexposed regions can simply be allowed to diffuse back out;

3) it is relatively easy to implement;

4) it does not reduce the thermal stability of gratings or the strength of the fibre.

But it also has some important drawbacks:

1) the use of high pressure hydrogen is very hazardous;

2) the formation of OH⁻ bonds results in strong absorptions at 1.4 μm and at short wavelengths;

3) the diffusion process can take weeks;

4) in our experience, a fibre loaded with H_2 cannot be spliced, as the fusion arc causes an explosion in the fibre core. The hydrogen must be forced out of the fibre before splicing.

The loss induced by the pulsed UV exposure of two different hydrogen-loaded germania-silica fibres are shown in Fig. 3-17. The characteristic absorption peak due to OH⁻ formation can be seen at 1.4 μm. This peak has in fact two components: a peak a 1.39 μm assigned to SiOH and one at 1.42 assigned to GeOH [44]. This double-peak structure partly resolved in the second graph of Fig. 3-17. In alumina-doped fibres, an AlOH peak can be seen at 1.44 μm [52]. One molar percent of OH⁻ gives an absorption of about 5 dB/cm at 1.4 μm [51]; however it is not known whether this figure applies to both SiOH and GeOH. The tails of this band can affect transmission in the two main telecommunications windows if very high concentrations of OH⁻ are formed. Using deuterium instead of hydrogen shifts this peak to 1.9 μm [51] and hence greatly reduces the loss at telecommunications wavelengths [48].

The other feature of the loss spectrum of Fig. 3-17 is a strong short wavelength absorption edge. In many cases, this loss can prohibit the use of gratings made in hydrogen-loaded fibre for short wavelength applications. The magnitude of this edge relative to the OH peak varies considerably from fibre to fibre as can be seen in Fig. 3-17. The wavelength dependence of the loss is given by $\exp(\lambda_0/\lambda)$, where $\lambda_0 \approx 2.3\mu m$ for $\lambda > 0.95\mu m$ and $\lambda_0 \approx 4.6\mu m$ for $\lambda < 0.95\mu m$ [51]. This is confirmed by the measurements of Fig. 3-17. The highest loss was seen in a fibre doped with alumina and germania, where an induced loss of about 5 dB/cm was measured at 1μm. In germania-silica fibres, this short wavelength edge has been attributed to GeH bonds, possibly formed by a reaction between H_2 and GeE' centres [44]. It is possible that AlH could also be formed in alumina-doped fibres, but this has not yet been investigated.
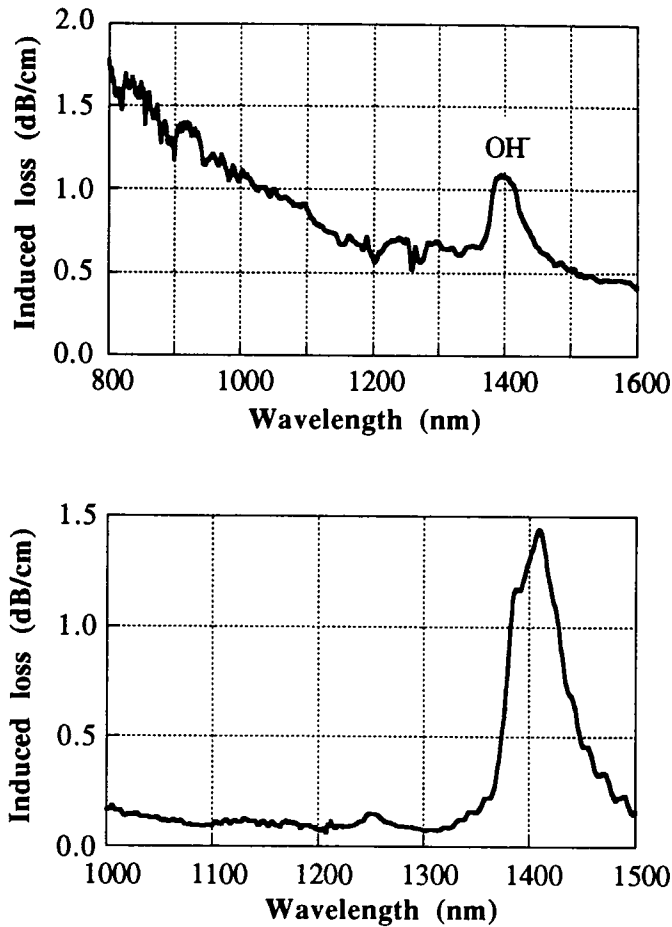
Figure 3-17 - UV-induced loss in two different Ge-doped H_2-loaded fibres.

3.6. Photoinduced birefringence

The photoinduced index change produced by visible or ultraviolet ionising light in optical fibres is always slightly anisotropic [5,53-55]. Typically, this photoinduced birefringence is two orders of magnitude smaller than the index change. For many applications that require polarisation-independent components, this anisotropy is an unwanted feature of fibre gratings. For example, a birefringent Bragg grating has two slightly different Bragg wavelengths for the two orthogonal polarisations [18]. There are however some very useful applications to this photoinduced birefringence: it can be used to produce polarisation mode converters (also known as rocking filters) [56-58]; also, birefringent Bragg gratings could be used as feedback elements for single-polarisation fibre lasers.

3.6.1. Mechanisms

Several mechanisms have been identified that can contribute to photoinduced birefringence in optical fibres:

1) the index change induced by linearly polarised UV or blue/green light has an anisotropic component which lines up with the optical field [5,53,54]; this is thought to be caused by the preferential bleaching of defects which are oriented parallel to the optical field [59,60];

2) when a fibre is exposed to UV from the side, the exposed side of the core receives a higher UV dose then the far side, due to the core absorption [55]; as a result, the photoinduced index change and stress change are anisotropic;

3) the intrinsic birefringence of a fibre is usually caused by stress; UV exposure can anneal this stress and reduce the birefringence [4].

3.6.2. Experiment

An experiment was designed by Ouellette and co-workers [53] and then adapted by Bardal and co-workers [54] to measure the birefringence induced by blue/green light in Ge/Si fibres. More recently, we used a similar method to measure the induced birefringence resulting from exposure of a fibre to pulsed 248.5 nm light from a KrF excimer laser (Fig. 3-18). In this experiment, a linearly polarised excimer beam is focused on the side of an optical fibre by a cylindrical lens (CL). The fibre is placed in a rotating chuck so that one of its intrinsic birefringence axes can be aligned with the direction of the excimer beam polarisation. The linearly polarised output of a HeNe laser is coupled into the fibre with the polarisation at 45° with respect to the fibre axes. This way, an equal amount of power is coupled into each of the two polarisation eigenmodes. A beam splitting polariser (P2) is placed at the output end of the fibre at 45° to the fibre axes and the reflected and transmitted optical signals are picked up by two identical detectors, D1 and D2. This arrangement converts variations in the relative phase of the two polarisation eigenmodes into amplitude modulations. The signals from the two detectors are then recorded by a data acquisition system. The normalised signals seen by the two detectors are

$$S_1 = \frac{1}{2}(1+\cos(\phi_0+\Delta\phi))$$

$$S_2 = \frac{1}{2}(1-\cos(\phi_0+\Delta\phi)) \tag{3-23}$$

where ϕ_0 is the initial phase difference between the two eigenmodes due to the intrinsic fibre birefringence and

$$\Delta\phi = \frac{2\pi L \Delta B}{633nm} + \Delta\phi_T \tag{3-24}$$

is the change in phase difference due to the UV exposure.
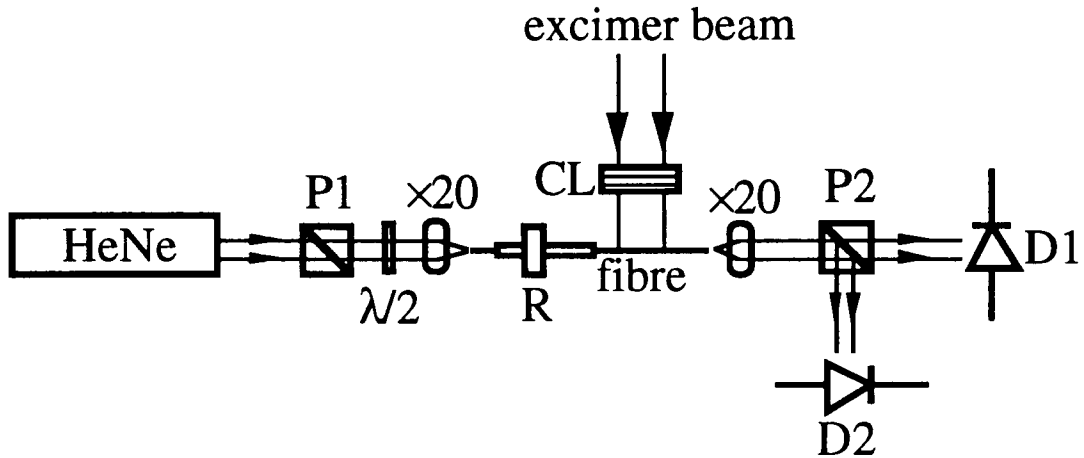
Figure 3-18 - Experimental setup for measurement of birefringence change induced by an excimer laser beam at 248 nm. P: polariser; R: rotating fibre chuck; CL: cylindrical lens; D: photodiode.

In Eq. (3-24), L is the length of fibre exposed to the excimer beam, ΔB is the permanent photoinduced birefringence and $\Delta\phi_T$ is a phase shift due to heating of the fibre by the UV beam which reverses when the beam is turned off. The change in phase difference $\Delta\phi$ is easily measured by counting the cycles in the signals S_1 and S_2 as the fibre is exposed. When the excimer beam is turned off, there is an additional change, $-\Delta\phi_T$, as the exposed fibre section cools down. This thermal component can be subtracted from $\Delta\phi$ and the magnitude of the photoinduced birefringence is then easily calculated from Eq. (3-24).

A limitation of this method is that it can only can only measure the amplitude, but not the sign, of the phase change or the birefringence change.

3.6.3. Results and discussion

Three possible sources of anisotropy have been identified that can contribute to ΔB: 1) preferential depletion of defects oriented with the optical field, 2) asymmetric UV exposure and 3) stress-relief. In the experiment, effects 2) and 3) can be distinguished from 1) because they produce a change in birefringence which does not align with the optical field.

To evaluate the contribution of 2) and 3), a Hi-Bi fibre was exposed to the excimer beam which was polarised along the axis of the fibre (z-axis). This eliminated any contribution

from 1). The fibre under test was a high numerical aperture elliptical fibre, number ND219, with an intrinsic birefringence of ~5×10⁻⁴. A 15 mm section was exposed for several minutes, until it could be seen that the change in birefringence had saturated. Exposing the fibre until saturation should in fact minimise the effect of the asymmetric exposure (2) and therefore stress-relief (3) should be the dominant mechanism. The change in birefringence was calculated from the recorded data using Eq. (3-24), as shown in Fig. 3-19. The growth of the induced birefringence is equally well fitted by the stretched exponential function

$$\Delta B(t) = \Delta B_s \left(1 - \exp[-(t/t_s)^\beta]\right) \qquad (3\text{-}25)$$

with $|\Delta B_s| \approx 2.7 \times 10^{-4}$ and $\beta = 0.393 \pm 0.003$, or the power-law function

$$\Delta B(t) = \Delta B_s / (1 + (t/t_s)^\beta) \qquad (3\text{-}26)$$

with $|\Delta B_s| \approx 3.7 \times 10^{-4}$ and $\beta = 0.427 \pm 0.004$. A new section of the same fibre was exposed to the UV beam, this time with the beam polarised along the major axis (x-axis) of the fibre ellipse. The fibre was exposed to the same intensity level as before, until the change in birefringence had saturated. From the recorded data a change of birefringence $|\Delta B_s| \approx 2.3 \times 10^{-4}$ was estimated, slightly less than for the z-axis exposure. The fibre was then rotated by 90°, so that the same section of fibre could be exposed to the excimer beam polarised along the minor axis (y-axis) of the fibre ellipse. After again exposing the fibre until saturation, a change of birefringence $|\Delta B_s| \approx 8 \times 10^{-5}$ was observed. Finally, the same fibre was rotated back to its original position (x-axis exposure) and once again exposed to the UV beam, which produced a change of birefringence $|\Delta B_s| \approx 6 \times 10^{-5}$.
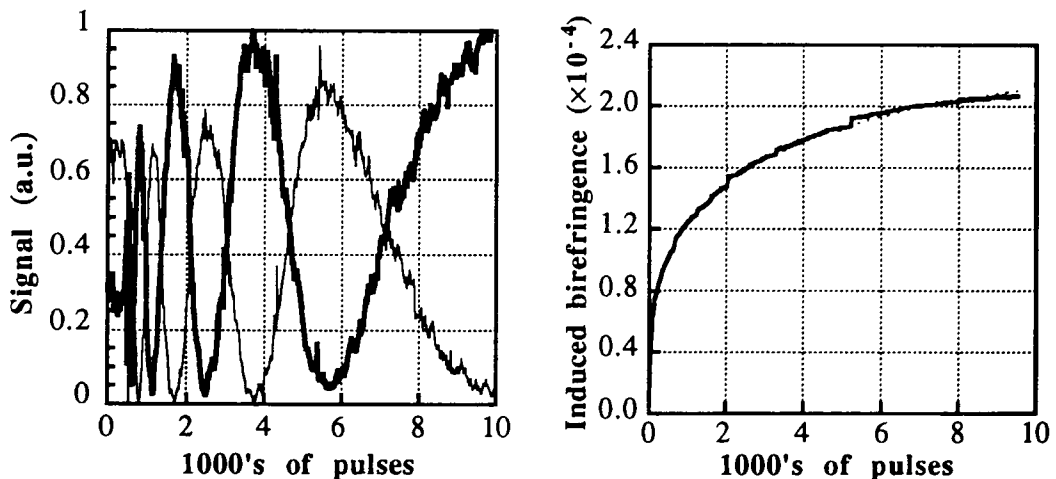

Figure 3-19 - Left: evolution of detected signals S₁ and S₂ during exposure to excimer beam polarised along fibre axis. Right: Photoinduced birefringence calculated from Eq. (3-24); dashed line is stretched exponential fit.

In a similar experiment, Wong *et al.* measured an ~80% reduction of the intrinsic birefringence of an elliptical fibre after exposure to unpolarised UV light which they attributed to stress-relief. Therefore, it is very likely that birefringence change observed during the z-axis exposure was negative, resulting in a ~54% reduction of the intrinsic birefringence. The change in birefringence of 2.3×10^{-4} which resulted from the initial exposure to x-polarised light is probably due to a combination of effects 1), 2) and 3). Subtracting this value from what was obtained for z-polarised light (2.7×10^{-4}) should give an estimate of the contribution of effect 1) alone: this amounts to 4×10^{-5}. The photoinduced birefringence due to 1) would be of opposite sign to that due to 3), hence positive. The birefringence change of 8×10^{-5} seen when same the fibre is exposed to y-polarised light indicates that part of the photoinduced birefringence change is reversible. This confirmed by the third exposure, with x-polarised light, which showed a further birefringence change of 6×10^{-5}, when ΔB had saturated during the previous x-axis exposure.

The change in birefringence due to stress-relief should be irreversible. The reversible component outlined in this experiment should therefore be only due to the preferential bleaching of defects oriented with the optical field. During the first exposure, most of the oxygen-deficient defects with an x-orientation would be ionised. The electrons released by this process are then redistributed isotropically into other trapping sites in the glass, leaving behind positively charged, x-oriented ionised defects. The reduction in the population of x-oriented defects could then result in a 4×10^{-5} birefringence change. During the second exposure, y-oriented defects are ionised. The electrons now released can recombine with the holes left in x-oriented sites. The depletion of y-oriented defects, combined with the repopulation of x-oriented sites could then produce as much as twice the birefringence change observed during the first exposure. This change could then be reversed, again by depleting the x-oriented defects and repopulating the y-oriented ones. At each rotation of the optical field, one would expect a fraction of the photoelectrons to be lost to defect centres which are lined up with the fibre axis or cannot be re-excited by 248.5 nm light and therefore the reversible birefringence change should decrease after each exposure, as indeed was observed in this experiment.

To summarise, an irreversible birefringence change of 2.7×10^{-4} representing 54% of the intrinsic birefringence of an elliptical fibre was induced by 248.5 nm light, confirming the observations of Ref. [4]. The dynamics of this change follow a stretched exponential function, in accordance with several other photosensitivity-related phenomena, as discussed earlier in this chapter. Part of the birefringence change (4×10^{-5}) was found to

be reversible, supporting the model of selective bleaching of oriented defects. This part of the photoinduced birefringence, which follows the optical field, can be used for producing useful devices such as rocking filters.

3.7. <u>Conclusion</u>

In this chapter, a detailed model of photosensitivity-related phenomena in germania-silica fibres has been put forward, based on the photo-thermal ionisation of oxygen-deficient defects. For the first time, this model provides a complete and unified explanation of a wide range of experimental observations. The starting point is a three-level energy diagram of oxygen-deficient defect centres, where the upper energy state is located close to the conduction band of silica. The defects are ionised by a photo-thermal process: an optical excitation to the upper energy state by UV photons followed by thermal excitation to the conduction band. Because of the disordered nature of the glass, the ionisation energy of the defect centres has a broad distribution and, as a consequence, the ionisation process is dispersive. All photosensitivity-related phenomena have been shown to follow similar dynamics, characteristic of dispersive charge transport. Two similar functions - the stretched-exponential and the power-law function - have shown to describe these dynamics accurately and were used to predict the ionisation energy distributions. The model predicts that the dispersion parameter β should increase linearly with temperature. A measurement of the temperature dependence of β could therefore confirm or infirm its validity. Comparative measurements at different temperatures would also yield the values of the characteristic width and central position of the ionisation energy distribution. An alternative model, the two-photon ionisation of defects, was ruled out because of its incompatibility with dispersive charge transport.

The photoinduced index changes obtained in a large number of fibres were compared. The largest index changes were observed in hydrogen-loaded germania-doped fibres, but several drawbacks have been identified with this technique, including strong losses at 1.4 μm and at short wavelengths. Amongst the untreated fibres, germania-boron co-doped fibres were clearly the most photosensitive, with no penalty in terms of loss or compatibility with standard fibres. Fibres drawn from reduced preforms also showed an enhanced photosensitivity, but have a high absorption at 1.4 μm.

Finally, the photoinduced birefringence resulting from the side UV exposure of an elliptical fibre was measured showing both reversible and irreversible changes. The former were attributed to the preferential depletion of oriented defects and the latter to

stress-relief. The dynamics of the photoinduced birefringence were again characteristic of dispersive charge transport.

3.8. References

1. K.O. Hill, Y. Fujii, D.C. Johnson and B.S. Kawasaki, "Photosensitivity in optical fibre waveguides: application to reflection filter fabrication", *Appl. Phys. Lett.*, **32** (10), pp. 647-649, 1978.

2. D.P. Hand and P.St.J. Russell, "Photoinduced refractive-index changes in germanosilicate fibers", *Opt. Lett.*, **15** (2), pp. 102-104, 1990.

3. D.L. Williams, S.T. Davey, R. Kashyap, J.R. Armitage and B.J. Ainslie, "Direct observation of UV induced bleaching of 240 nm absorption band in photosensitive germanosilicate glass fibres", *Electron. Lett.*, **28** (4), pp. 369-371, 1992.

4. D. Wong, S.B. Poole and M.G. Sceats, "Stress-birefringence reduction in elliptic-core fibers under ultraviolet-irradiation", *Opt. Lett.*, **17** (24), pp. 1773-1775, 1992.

5. M. Parent, J. Bures, S. Lacroix and J. Lapierre, "Propriétés de polarisation des réflecteurs de Bragg induits par photosensibilité dans les fibres optiques monomodes", *Appl. Opt.*, **24** (3), pp. 354-357, 1985.

6. P.Y. Fonjallaz, H.G. Limberger, R.P. Salathé, F. Cochet and B. Leuenberger, "Correlation of index changes with stress changes in fibers containing UV-written Bragg gratings", *ECOC'94 Proceedings*, Florence, 1994.

7. K.S. Chiang, M.G. Sceasts and D. Wong, "Ultraviolet photolytic-induced changes in optical fibers - the thermal-expansion coefficient", *Opt. Lett.*, **18** (12), pp. 965-967, 1993.

8. U. Österberg and W. Margulis, "Dye laser pumped by Nd:YAG laser pulses frequency doubled in a glass optical fibre", *Opt. Lett.*, **11** (8), pp. 516-518, 1986.

9. A.J. Cohen and H.L. Smith, "Ultraviolet absorption studies of germanium silicate glasses", *J. Phys. Chem. Solids*, **7**, pp. 301-306, 1958.

10. T.-E. Tsai, D.L. Griscom and E.J. Friebele, "On the structure of Ge-associated defect centers in irradiated high purity GeO_2 and Ge-doped SiO_2 glasses", *Diffusion and Defect Data*, **53-54**, pp. 469-476, 1987.

11. L.N. Skuja, A.N. Trukhin and A.E. Plaudis, "Luminescence in germanium-doped glassy SiO_2", *Phys. Stat. Solidi A*, **84** (2), pp. K153-157, 1984.

12. M.J. Yuen, "Ultraviolet absorption studies of germanium silicate glasses", *Appl. Opt.*, **21** (1), pp. 136-140, 1982.

13. D.L. Williams, B.J. Ainslie, J.R. Armitage and R. Kashyap, "Enhanced photosensitivity in germanium doped silica fibres for future optical networks", *ECOC Proceedings, Vol. 1*, paper B9.5, pp. 425-428, Berlin, 1992.

14. M. Kohketsu, K. Awazu, H. Kawzoe and M. Yamane, "Photoluminescence in VAD SiO_2:GeO_2 glasses sintered under reducing or oxidizing conditions", *Jap. J. Appl. Phys.*, **28** (4), pp. 622-631, 1989.

15. H. Hosono, Y. Abe, D.L. Kinser, R.A. Weeks, K. Muta and H. Kawazoe, "Nature and origin of the 5 eV band in SiO_2-GeO_2 glasses", *Phys. Rev. B*, **46** (18), pp. 11445-11451, 1992.

16. R.M. Atkins, V. Mizrahi and T. Erdogan, "248 nm induced vacuum UV spectral changes in optical fibre preform cores: Support for a colour centre model of photosensitivity", *Electron. Lett.*, **29** (4), pp. 385-387, 1993.

17. P.St.J. Russell, L.J. Poyntz-Wright and D.P. Hand, "Frequency doubling, absorption and grating formation in glass fibres: effective defects or defective effects?", *Fibre Laser Sources and Amplifiers II*, SPIE Vol. 1373, pp. 126-139, San Jose, 1990.

18. G. Meltz and W.W. Morey, "Bragg grating formation and germanosilicate fiber photosensitivity", *International Workshop on Photoinduced Self-Organisation Effects in Optical Fiber*, SPIE Vol. 1546, pp. 185-199, Quebec, 1991.

19. Y. Duval, R. Kashyap, S. Fleming and F. Ouellette, "Correlation between ultraviolet-induced refractive-index change and photoluminescence in Ge-doped fiber", *Appl. Phys. Lett.*, **61** (25), pp. 2955-2957, 1992.

20. J.-L. Archambault, L. Reekie and P.St.J. Russell, "Excimer laser production of fibre Bragg gratings", *Meeting on Photosensitivity and Self-Organization in Optical Fibers and Waveguides*, SPIE Vol. 2044, pp. 69-75, Quebec, 1993.

21. M. Poirier, S. Thibault, J. Lauzon and F. Ouellette, "Dynamic and orientational behavior of UV-induced luminescence bleaching in Ge-doped silica optical fiber", *Opt. Lett.*, **18** (11), pp. 870-872, 1993.

22. L. Dong, J.L. Archambault, L. Reekie, P.St.J. Russell and D.N. Payne, "A study of photo-induced absorption change in germanosilicate preforms: evidence for the colour-centre model of photosensitivity", *Submitted to Appl. Opt.*, 1994.

23. T.E. Tsai, E.J. Friebele and D.L. Griscom, "Thermal-stability of photinduced gratings and paramagnetic centers in Ge-doped and Ge/P-doped silica optical fibers", *Opt. Lett.*, **18** (12), pp. 935-937, 1993.

24. M. Gallagher and U. Österberg, "Spectroscopy of defects in germanium-doped silica glass", *J. Appl. Phys.*, **74** (4), pp. 2771-2778, 1993.

25. S.L. Gilbert and H. Patrick, "Comparison of UV-induced fluorescence and Bragg grating growth in optical fiber", *CLEO'94 Technical Digest*, paper CWK5, p. 244, Anaheim, Ca, 1994.

26. H. Patrick and S.L. Gilbert, "Growth of Bragg gratings produced by continuous-wave ultraviolet-light in optical fiber", *Opt. Lett.*, **18** (18), pp. 1484-1486, 1993.

27. H. Scher, M.F. Shlesinger and J.T. Bendler, "Time-scale invariance in transport and relaxation", *Physics Today*, pp. 26-34, January 1991.

28. T. Erdogan, V. Mizrahi, P.J. Lemaire and D. Monroe, "Decay of ultraviolet-induced fiber Bragg gratings", *J. Appl. Phys.*, **76** (1), pp. 73-80, 1994.

29. G. Pfister and H. Scher, "Dispersive (non-Gaussian) transient transport in disordered solids", *Adv. Phys.*, **27** (4), pp. 747-798, 1978.

30. B. Malo, K.A. Vineberg, F. Bilodeau, J. Albert, D.C. Johnson and K.O. Hill, "Ultraviolet light photosensitivity in Ge-doped silica fibers: wavelength dependence of the light-induced index change", *Opt. Lett.*, **15** (17), pp. 953-955, 1990.

31. P.J. Lemaire, R.M. Atkins, V. Mizrahi and W.A. Reed, "High-pressure H2 loading as a technique for achieving ultrahigh UV photosensitivity and thermal sensitivity in GeO_2 doped optical fibers", *Electron. Lett.*, **29** (13), pp. 1191-1193, 1993.

32. H.G. Limberger, P.Y. Fonjallaz and R.P. Salathé, "Spectral characterisation of photoinduced high efficient Bragg gratings in standard telecommunication fibres", *Electron. Lett.*, **29** (1), pp. 47-49, 1993.

33. J.R. Armitage, "Fiber Bragg reflectors written at 262 nm using a frequency quadrupled diode-pumped Nd^{3+}:YLF laser", *Electron. Lett.*, **29** (13), pp. 1181-1183, 1993.

34. J. Martin and F. Ouellette, "Novel writing technique of long and highly reflective in-fiber gratings", *Electron. Lett.*, **30** (10), pp. 811-812, 1994.

35. J. Albert, B. Malo, F. Bilodeau, D.C. Johnson and K.O. Hill, "Photosensitivity in Ge-doped silica optical waveguides and fibers with 193 nm light from an ArF excimer laser", *Opt. Lett.*, **19** (6), pp. 387-389, 1994.

36. P.E. Dyer, R.J. Farley, R. Giedl, K.C. Byron and D. Reid, "High reflectivity fiber gratings produced by incubated damage using a 193 nm ArF laser", *Electron. Lett.*, **30** (11), pp. 860-862, 1994.

37. D.L. Williams, B.J. Ainslie, R. Kashyap, G.D. Maxwell, J.R. Armitage, R.J. Campbell and R. Wyatt, "Photosensitive index changes in germania doped silica glass fibres and waveguides", *Meeting on Photosensitivity and Self-Organization in Optical Fibers and Waveguides*, SPIE Vol. *2044*, Quebec, 1993.

38. F.P. Payne, "Photorefractive gratings in single-mode optical fibres", *Electron. Lett.*, **25** (8), pp. 498-499, 1989.

39. J.P. Bernardin and N.M. Lawandy, "Dynamics of the formation of Bragg gratings in germanosilicate optical fibers", *Opt. Comm.*, **79** (3,4), pp. 194-199, 1990.

40. D. Wong, S.B. Poole and M.G. Sceats, "Stress relief: proof of the mechanism of photo-induced index change", *Integrated Photonics Research Conf. Technical Digest*, p. 408, New Orleans, 1992.

41. D.L. Williams, B.J. Ainslie, J.R. Armitage, R. Kashyap and R. Campbell, "Enhanced UV photosensitivity in boron codoped germanosilicate fibres", *Electron. Lett.*, **29** (1), pp. 45-47, 1993.

42. M. Rothschild, D.J. Ehrlich and D.C. Shaver, "Effects of excimer laser irradiation on the transmission, index of refraction and density of ultraviolet grade fused silica", *Appl. Phys. Lett.*, **55** (13), pp. 1276-1278, 1989.

43. L. Dong, J. Pinkstone, P.St.J. Russell and D.N. Payne, "Study of UV absorption in germanosilicate preforms", *CLEO'94 Technical Digest*, paper CWK4, p. 243, Anaheim, Ca., 1994.

44. R.M. Atkins and P.J. Lemaire, "Effects of elevated-temperature hydrogen exposure on short-wavelength optical loss and defect concentrations in germanosilicate optical fibers", *J. Appl. Phys.*, **72** (2), pp. 344-348, 1992.

45. F. Bilodeau, B. Malo, J. Albert, D.C. Johnson and K.O. Hill, "Photosensitization of optical fiber and silica-on-silicon/silica waveguides", *Opt. Lett.*, **18** (12), pp. 953-955, 1993.

46. L.J. Poyntz-Wright, "Blue and UV transmission in optical fibres", Ph.D. Thesis, University of Southampton, 1990.

47. U. Camlibel, D.A. Pinnow and F.W. Dabby, "Optical aging characteristics of borosilicate clad fused silica core fiber optical waveguides", *Appl. Phys. Lett.*, **26** (4), pp. 185-187, 1975.

48. V. Mizrahi, P.J. Lemaire, T. Erdogan, W.A. Reed, D.J. DiGiovanni and R.M. Atkins, "Ultraviolet-laser fabrication of ultrastrong optical-fiber gratings and of germania-doped channel waveguides", *Appl. Phys. Lett.*, **63** (13), pp. 1727-1729, 1993.

49. R.M. Atkins, P.J. Lemaire, T. Erdogan and V. Mizrahi, "Mechanism of enhanced UV photosensitivity via hydrogen loading in germanosilicate glass", *Electron. Lett.*, **29** (14), pp. 1234-1235, 1993.

50. B.I. Greene, D.M. Krol, S.G. Kosinski, P.J. Lemaire and P.N. Saeta, "Thermal and photo-initiated reactions of H_2 with germanosilicate optical fibers", *J. Non-Cryst. Solids*, **168**, pp. 195-199, 1994.

51. J. Stone, "Interactions of hydrogen and deuterium with silica optical fibers: a review", *J. Lightwave Tech.*, **5** (5), pp. 712-733, 1987.

52. P.J. Lemaire and A. Tomita, "Behavior of single-mode MCVD fibers exposed to hydrogen", *ECOC'84 Technical Digest*, pp. 306-307, Stuttgart, 1984.

53. F. Ouellette, D. Gagnon and M. Poirier, "Permanent photoinduced birefringence in a Ge-doped fiber", *Appl. Phys. Lett.*, **58** (17), pp. 1813-1815, 1991.

54. S. Bardal, A. Kamal and P.St.J. Russell, "Photoinduced birefringence in optical fibers: a comparative study of low-birefringence and high-birefringence fibers", *Opt. Lett.*, **16** (6), pp. 411-413, 1992.

55. A.M. Vengsarkar, Q. Zhong, D. Inniss, W.A. Reed, P.J. Lemaire and S.G. Kosinski, "Birefringence reduction in side-written photoinduced fiber devices by a dual/circumferential exposure method", *OFC'94 Postdeadline Papers*, paper PD5, pp. 31-34, San Diego, Ca., 1994.

56. P.St.J. Russell and D.P. Hand, "Rocking filter formation in photosensitive high birfringence optical fibers", *Electron. Lett.*, **26** (22), pp. 1846-1848, 1990.

57. K.O. Hill, F. Bilodeau, B. Malo and D.C. Johnson, "Birefringent photosensitivity in monomode optical fiber - application to external writing of rocking filters", *Electron. Lett.*, **27** (17), pp. 1548-1550, 1991.

58. A. Kamal, S.E. Kanellopoulos, J.-L. Archambault, P.St.J. Russell, V.A. Handerek and A.J. Rogers, "Holographically-written reflective polarization filter in single-mode optical fibers", *Opt. Lett.*, **17** (17), pp. 1189-1191, 1992.

59. J. Lauzon, M. Poirier, S. Thibault, S. LaRochelle, A. Blouin and F. Ouellette, "Anisotropy of photoinduced index change in Ge-doped optical fiber", *Meeting on Photosensitivity and Self-Organization in Optical Fibers and Waveguides , SPIE Vol. 2044*, pp. 330-340, Quebec, 1993.

60. A. Kamal and P.St.J. Russell, "Physical origins and general dielectric tensor of photoinduced anisotropy in optical fibers and bulk glasses", *J. Opt. Soc. Am. B*, **11** (9), pp. 1576-1584, 1994.

Chapter 4
Grating fabrication

4.1. Introduction

In developing the facilities for manufacturing fibre gratings, the main objective was to establish a reliable source of gratings which could achieve the widest possible range of grating specifications to meet the requirements of the multitude of applications found in the ORC. In the first part of this chapter, the experimental setup for grating manufacturing is described in detail and compared with other types of systems. A complete summary of the operation procedures is also presented.

To be able to produce gratings reliably, it is essential to properly understand the dynamics of grating formation; in the second part, several original results are presented which shed some new light on the growth dynamics of fibre gratings. A theoretical model is proposed which, for the first time, provides a detailed description of the growth process. The optical properties of typical gratings are then presented and the limits on the various grating parameters (bandwidth, reflectivity, Bragg wavelength) are examined.

4.2. Experimental setup

4.2.1. Summary of existing writing techniques and UV sources

Following the first demonstration of external UV writing by Meltz et $al.$ in 1989 [1], a variety of UV lasers (see Table IV) and writing techniques (Fig. 4-1) have been employed for the production fibre gratings. The writing techniques can be divided into interferometric (top row in Fig. 4-1) and non-interferometric methods (bottom row).

Interferometric

Interferometric techniques have the advantage of being tunable and requiring simple optical components. However, the use of an interferometric technique requires a UV laser with sufficient temporal coherence: to write a grating of length L and Bragg wavelength λ_B, one requires a source with a coherence length

$$L_c > \frac{nL\lambda_w}{\lambda_B}$$

(4-1)

where λ_w is the writing UV wavelength and n the fibre index at λ_B. The 2-mirror [1] and prism [2] interferometers have an additional requirement that the UV laser beam must also be spatially coherent, which is the case with a single transverse mode laser. The reason for this requirement is that the two interfering beams are mirror images of each other. This is not the case in the 3-mirror interferometer [3], where the two beams both undergo an odd number of reflections. The 3-mirror interferometer therefore allows the use of spatially incoherent (transverse multimode) lasers.

2-mirror interferometer   3-mirror interferometer   Prism interferometer

Phase mask   Remote phase mask   Amplitude mask   Point by point
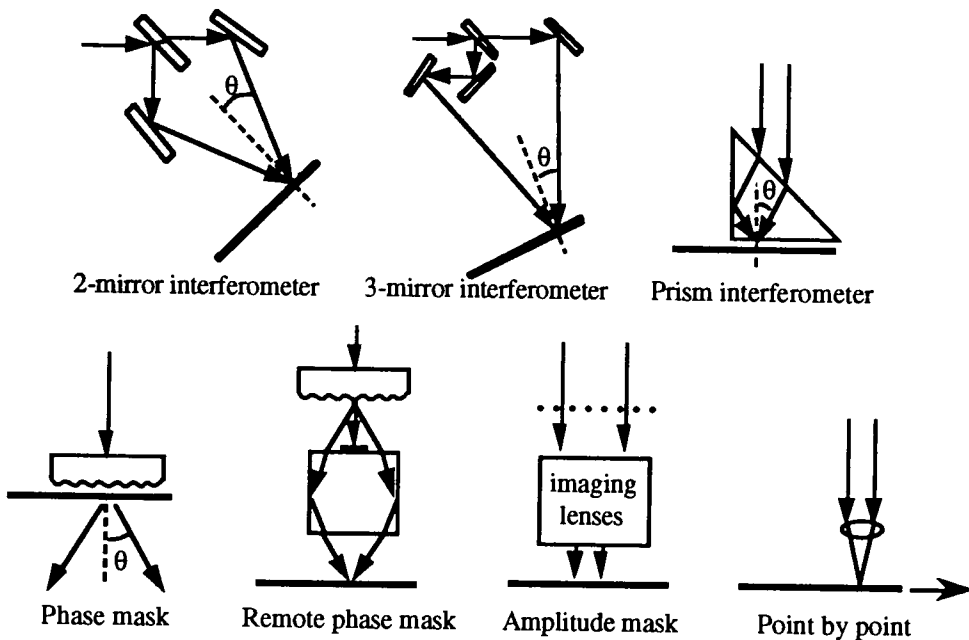
Figure 4-1 - Fibre grating writing techniques.

Non-interferometric

The phase-mask technique, commonly used in the fabrication of DFB lasers, was recently adapted to fibre grating writing [4,5]. A phase-mask consists of a grating etched into a silica substrate. It can be produced holographically or by direct e-beam or focussed ion-beam writing. The depth of the grating lines is carefully controlled to maximise the ±1 diffraction orders and minimise 0-order diffraction. This bulk grating is reproduced in the fibre core, independently of the writing wavelength. A minimal but finite amount of spatial coherence is required, due to the separation of at least one cladding radius between the phase mask and the fibre core. The phase-mask technique is probably the simplest and most reliable and it is now widely used. Slight tuning of the Bragg wavelength may be obtained by placing a lens before the mask [6] or by varying the strain or temperature of the fibre. In a variation of this technique, a rectangular prism is used to

recombine the ±1 diffraction orders on a remote fibre with the advantages that the 0th order diffraction can be spatially filtered and that the UV intensity can be much lower on the mask than on the fibre, thus reducing the risk of optical damage to the mask [7].

The writing of gratings with amplitude masks was recently demonstrated [8]. The mask illuminated by UV light is demagnified and imaged unto the core of a fibre using a complex lens arrangement. So far, this technique has been limited to high-order gratings with periods in excess of 1 μm.

The point-by-point technique consists of writing the grating lines individually [9]. The writing beam must be focussed down to a very tight spot, ideally half a grating period wide. After each grating line is written, the fibre must be translated with nanometer precision by one grating period. The writing of short period gratings using this technique is slow and technically very difficult. The technique potentially offers complete flexibility in designing the grating profile, but the same flexibility can be obtained with greater ease in phase-mask fabrication.

Laser	Wavelength range (nm)	Output	Average power (W)	Coherence	Price
excimer	193, 248.5	pulsed	0.3-100	v. poor	low-high
line-narrowed excimer	193, 248.5 (±0.5)	pulsed	5-20	good	v. high
freq.-doubled Argon	244, 257	CW	0.1-0.3	good	high
freq.-doubled dye	240-250	pulsed	0.02-	poor	high
freq.-doubled OPO	210-345	pulsed	0.5	unknown	v. high
freq. quadrupled Nd:YAG	266	pulsed	0.2	unknown	high
freq. quad. diode-pumped Nd:YLF	262	pulsed	0.1	unknown	low

Table IV - Characteristics of commercially-available UV lasers.

4.2.2. Line-narrowed KrF excimer laser

The UV source used during this project is the EMG-150 MSC line-narrowed KrF excimer laser from Lambda Physik. The laser has a master oscillator, power amplifier configuration with two cavities (Fig. 4-2). The oscillator output is a weak, line-narrowed and polarised UV pulse with a gaussian beam profile. The line-narrowing and polarisation selection are provided by a diffraction grating and three Brewster-angled prisms inside the cavity. The oscillator output is injected in the three-pass amplifier,

where it is first reflected by a convex 'dot' mirror (M3) and then collimated by concave mirror M2, filling the gain medium.
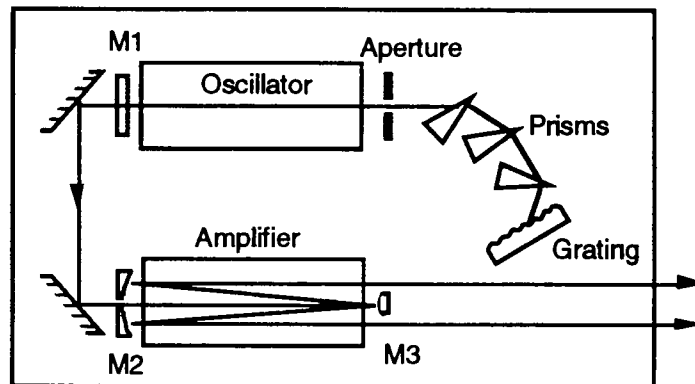

Figure 4-2 - Layout of EMG 150 MSC excimer laser

This laser generates 20 ns pulses with up to 250 mJ at 248.5 nm at a maximum repetition rate of 80 Hz. The pulse-to-pulse energy fluctuations are typically ±10%. The output beam profile is a rectangular, approximately 5×20 mm, with a ~2 mm diameter hole in its centre caused by the hole in mirror M2 and the presence of mirror M3. The diffraction pattern from this hole and inhomogeneities in the amplifier discharge also contribute to making the beam profile non-uniform.

The seeding of the amplifier by the oscillator or 'injection-locking' is made possible by having a slight delay between the oscillator and amplifier discharges, which is controlled by a pressure differential between the two gas chambers. In theory, the injection-locking efficiency should be close to 100% but in practice it is often less, because the oscillator output is low or misaligned. Therefore, the laser output is in general a mixture of amplified spontaneous emission and injection-locked emission. The injection-locking efficiency can be estimated by measuring the degree of polarisation of the laser output.

When it is properly injection-locked, the laser has a coherence length of about 25 mm, which was measured in a Michelson interferometer. According to Eq. (4-1), this is sufficient to write 1550 nm gratings which are up to 10 cm long. The spatial coherence is typically 0.1 mm.

The advantages of the line-narrowed excimer laser are its ability to produce very high energy pulses at a wavelength close to the peak absorption of germania-doped fibres with sufficient temporal coherence to write very long gratings with an interferometer. Its main disadvantage is the poor beam quality. However, an alternative set of optics is now

available for this laser which should in the future produce a very uniform beam profile, without the central hole.

4.2.3. Description of interferometer

The experimental setup is described in Fig. 4-3. The poor spatial coherence of the excimer beam imposes the use of a 3-mirror interferometer. The three mirrors are positioned so that the pathlengths BS-M1 and BS-M3 are closely matched as are the pathlengths from M1 and M3 to the fibre. The triangle formed by M1, M3 and the illuminated fibre section is therefore isosceles. This configuration facilitates the operation of tuning the angle between the beams while preserving the zero path length difference: the fibre is simply displaced along the median running between M1 and M3 and the two mirrors are pivoted symmetrically about their centre to redirect the beams onto the fibre.
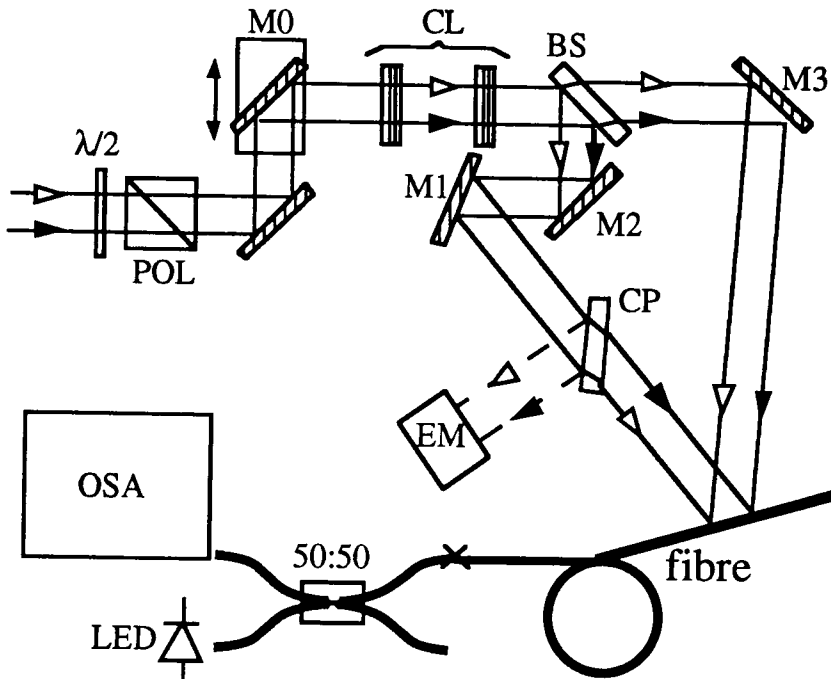
Figure 4-3 - Experimental setup for excimer laser production of side-written fibre gratings. Pol: polariser; BS: beam splitter; M: mirror; CL: cylindrical lenses; CP: compensating plate; EM: energy meter; OSA: optical spectrum analyser.

A pair of cylindrical lenses (CL) focusses the beam to a line, preserving the 20 mm beam width. The placement of the lenses before the beamsplitter insures that any aberrations introduced by the lenses will affect the two beams equally and therefore be cancelled out. The drawback, however, is that the focal planes of the two interfering beams are at an angle θ with respect to the fibre. A 10 mm thick silica optical flat (CP) is placed in the

path of the left beam to compensate for the thickness of the beamsplitter. This compensating plate is essential for matching simultaneously the focal distances and optical pathlengths of the two beams. It serves a second purpose which is to tap off part of the beam to monitor the pulse energy using a pyroelectric energy meter (EM). The pulse energy can be adjusted by means of a polariser and half-wave plate arrangement.

The beam is delivered to the interferometer via a mirror M0 which is mounted on a motorised translation stage. Translating M0 displaces the excimer beam parallel to itself without affecting the position of the interference fringes. This can serve two purposes: first, grating lengths greater than the beam width can be obtained by scanning the beam along the fibre; second, the beam intensity profile can be spatially averaged, giving the fibre a more uniform exposure.

The growth of a grating can be monitored in reflection (via a 50:50 coupler) or in transmission by illuminating the grating with a broadband light source, usually a light-emitting diode (LED), and measuring the spectrum in an optical spectrum analyser.

4.2.4. Alignment procedures

Precise alignment of the interferometer is an essential starting point to grating fabrication. Several alignment techniques have been adopted for this purpose during the course of this project.
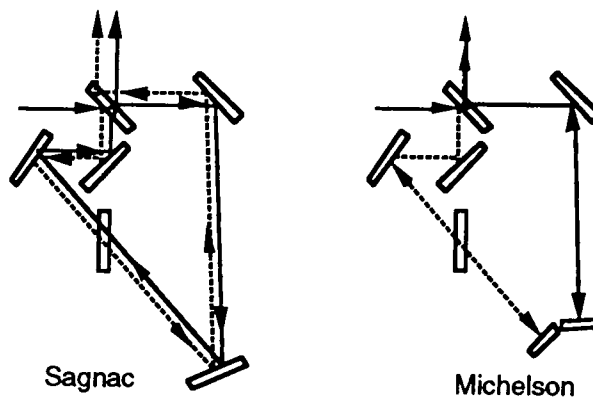

Figure 4-4 - Interferometric alignment techniques.

Beam overlap

Because of the low spatial coherence of the excimer beam, it is crucial that the plane of intersection of the two interfering beams coincides with the position of the fibre. This alignment is easily performed by replacing the fibre with a reflector to build a Sagnac

interferometer (Fig. 4-4). The two beams exiting the interferometer produce a coarse fringe pattern which can be observed on a screen (an ordinary sheet of paper produces purple fluorescence when exposed to UV). The two beams are known to be perfectly overlapped on the reflecting surface when the interference pattern is concentric with 100% fringe contrast.

Zero optical pathlength difference

The maximum fringe contrast is obtained by making sure that the optical pathlengths of the two interfering beams are equal in the centre of the exposed region of the fibre. The optical pathlength difference can be measured by using a Michelson interferometer configuration, as in Fig. 4-4. It can then be adjusted by displacing M2. A more accurate method is to block the oscillator output of the excimer laser prior to writing a grating, so the laser output consists only of ASE, thus reducing the coherence length to ~0.1 mm. If the pathlength difference is properly set, then a very short grating should be obtained in the centre of the exposed fibre. The exact location of the point of zero pathlength difference on the fibre can be found by masking the excimer beam with a narrow slit and laterally displacing the slit until grating growth is observed.

Bragg wavelength

The Bragg wavelength is given by

$$\lambda_B = \frac{n_{av}\lambda_w}{\sin(\theta)} \qquad (4\text{-}2)$$

The angle θ can be set approximately by positioning the fibre holder along a ruler which runs parallel to the median of the triangle formed by M1, M3 and the fibre. This simple operation usually places the Bragg wavelength within 5 nm of a target value, the error being mostly due to fibre-to-fibre variations in the mode index. Once the Bragg wavelength has been determined by writing a first grating, the angle can be fine-tuned by displacing the fibre holder slightly with a micrometric adjustment and realigning the beams as described earlier. A displacement Δx of the fibre corresponds to a shift in Bragg wavelength

$$\Delta\lambda_B \approx \frac{2n_{av}\cos(\theta)\lambda_w\Delta x}{d} \qquad (4\text{-}3)$$

where d is the distance between M1 and M3. Typically, $\Delta\lambda_B/\Delta x \sim 3$ nm/mm and λ_B can be set to within ±0.1 nm of a predetermined value. The output wavelength of the excimer laser can be tuned over several Angstroms by tilting the diffraction grating in the oscillator with a micrometric adjustment. This action produces a fractional change in the

Bragg wavelength of $(-8.1\pm0.1)\times10^{-6}$ per micron of adjustment, up to a maximum tuning of about $\pm10^{-3}$.

Lens alignment

This is best achieved by exposing a dummy fibre and observing the fluorescence produced by the UV beams on a screen positioned behind the fibre. The width of the beams in the plane of the fibre is typically 4 to 10 times the fibre diameter. Focussing any tighter can damage or destroy the fibre (see Fig. 5-2). The fibre therefore produces a shadow in the middle of both beams which allows the ratio of the beam width to the fibre diameter to be directly measured. This ratio can be adjusted by changing the spacing between the two lenses. The tilt and vertical position of the lenses are usually set so that the shadow is parallel to the beam profile and the central hole in the beam is located slightly above or below the fibre.

Fibre preparation

Prior to writing a grating, the fibre section to be exposed must be stripped of its coating and cleaned. The fibre is then placed in a mount where it is held in the beam path between two V-grooves with magnets. A slight tension is applied to the fibre to keep it straight. This strains the fibre, so that when it is released after the exposure, a small shift in the Bragg wavelength is observed, usually between -0.1 and -0.5 nm. When a high degree of accuracy is needed on the Bragg wavelength, a more elaborate fibre holder is used which can apply a controllable tension to the fibre.

4.2.5. Techniques for uniform exposure

A few techniques have been developed to obtain uniform exposures out of the non-uniform excimer beam. The simplest of these techniques is to mask the beam with a slit to select a region of uniform intensity in the beam profile. Ideally, this mask should be positioned close to the fibre to minimise the effect of diffraction. With a ~1 mm wide slit, highly uniform gratings are obtained (see Fig. 4-20). However, the uniformity of the gratings gradually deteriorates as the width is increased. Longer uniform gratings can be written by using a beam expander (two cylindrical lenses) after the slit or scanning the beam across the fibre with the translating mirror of Fig. 4-3. The disadvantage of these masking techniques is that they use only a fraction of the available optical power.

An alternative technique is to use the full beam and scan it across the fibre so that each point of the exposed region receives the same spatially-averaged UV fluence.

4.2.6. Sources of instability

The writing of fibre gratings with an interferometer requires a very high degree of stability. The position of the UV interference fringes must remain constant during the whole exposure to within a fraction of a grating period; otherwise, the grating lines can be washed out. In general, the longer a grating is, the more sensitive it is to instabilities. There are several potential sources of instability: mechanical vibrations, air currents, changes in ambient temperature, creep in the optical mounts, fluctuations in the excimer laser wavelength and heating of the fibre. Most of these can be controlled by isolating the interferometer from the environment, *i.e.* enclosing the interferometer in a box and mounting it on a vibration-isolated breadboard. Additional precautions include controlling the room temperature and using good quality optical mounts. The wavelength-stability of the excimer laser, however, is an unknown factor.

The stability of the interferometer can be monitored using the Michelson interferometer of Fig. 4-4, as changes in optical pathlengths or laser wavelength will cause variations in the coarse fringe pattern. This configuration could in fact be used to actively stabilise the interferometer: by measuring fluctuations in the relative intensity of two complementary fringes of the interferogram, an error signal could be generated and fed back to the interferometer to lock the fringes; this could be done by displacing one of the interferometer mirrors using a piezoelectric transducer. So far, however, passive stabilisation has been sufficient to insure excellent stability over long exposure times. Stable grating growth over up to 3 hours has been observed (see section 7.2).

Heating of the fibre

During UV exposure, a significant fraction of the optical energy absorbed by the fibre is converted to heat. If it is assumed that most of the optical energy is absorbed by germania-related oxygen-deficient centres, then this fraction should be approximately 41%, since the most of the radiative decay following the absorption of 5.1 eV photons produces blue luminescence at ~3.0 eV. Each time a pulse propagates through the fibre, the temperature of the core increases over the time scale of the pulse by as much as several hundred degrees. This heat then diffuses through the cladding with a time constant of

$$\tau_{cl} = \frac{r_{cl}^2}{4D} \tag{4-4}$$

where $D \approx 5.8 \times 10^{-7}$ m^2/s is the thermal diffusivity of silica. From Eq. (4-4), typical thermal time constants range between 1 and 2 ms. The heat that reaches the surface of the fibre dissipates slowly in the ambient air by convection. The next pulse arrives a

minimum of 12 ms later (for the maximum repetition rate of 80 Hz). If the pulse rate and energy is constant, the temperature distribution inside the fibre should eventually reach a steady-state, where the heating rate due to UV absorption is equal to the heat dissipation rate due to convection. In the steady-state, the temperatures at the surface of the core, T_{co} and at the surface of the cladding, T_{cl}, are given by

$$T_{co} = T_{cl} + \frac{\eta \alpha F f r_{co}^2 \ln(r_{cl}/r_{co})}{2C}$$

$$T_{cl} = T_a + \frac{\eta \alpha F f r_{co}^2}{2h r_{cl}} \tag{4-5}$$

where T_a is the ambient temperature, η is the fraction of non-radiative decay, α is the core absorption, F is the average pulse fluence, f is the repetition rate, C is the thermal conductivity of silica and h is the heat transfer coefficient for natural convection in air (no forced air flow), which ranges between 5 and 30 $W/°Cm^2$ [10]. In Eq. (4-5), the heat generated by UV absorption in the cladding was neglected as it is usually one order of magnitude smaller than the heat generated in the core. The amount of heat stored in the fibre is then

$$Q = \pi r_{cl}^2 L \rho c_v (T_{cl} - T_a) \tag{4-6}$$

and the rate of heat transfer

$$q = 2\pi r_{cl} L h (T_{cl} - T_a) \tag{4-7}$$

where $\rho \approx 2200$ kg/m^3 is the glass density and $c_v \approx 788 J/kg°C$ is the specific heat. The characteristic time to reach steady-state, which is equal to the time taken by the fibre to cool down once the UV beam is switched off, is approximately given by

$$\tau_{ss} = \frac{Q}{q} = \frac{\rho c_v r_{cl}}{h} \tag{4-8}$$

Taking typical values of η=41%, α=30 mm^{-1} (from Fig. 3-5), F=0.5 J/cm^2, f=20 Hz, r_{cl}=50 μm, r_{co}=3 μm, L=10 mm, C=1 W/Km and h=10 $W/°Cm^2$, Eq. (4-5) gives $T_{co}-T_{cl} \approx 0.04°C$ and $T_{cl}-T_a \approx 11°C$. The temperature is therefore almost uniform through the fibre. In these conditions, 1.6 mJ of heat is stored in the exposed fibre and 0.3 mW is dissipated. The time to reach this steady-state (or for the fibre to cool down after the exposure) is about 9 s. The temperature increase resulting from UV exposure can in fact be measured when writing a fibre grating: when the laser is switched off at the end of an exposure, the Bragg wavelength shifts to shorter wavelengths over a few seconds. The wavelength shift is typically ~-0.1 nm which corresponds to a temperature change of ~-10°C (see Eq. (9-6)). Therefore, both the magnitude and the time scale of the change are well accounted for by the model presented here.

The transient heating of the fibre can be a source of instability, as it changes the position of the grating lines relative to the UV interference fringes through the thermal expansion

coefficient. Partial erasure of the grating will occur if the length of the grating changes by an amount comparable to a grating period, which requires a temperature change of

$$\Delta T \sim \frac{\lambda_B}{2nL\xi} \qquad (4\text{-}9)$$

where $\xi = 5.5 \times 10^{-7}$ is the thermal expansion coefficient of silica. For $\lambda_B = 1550$ nm and $L = 20$ mm, Eq. (4-9) gives $\Delta T \sim 50°C$, which is larger than the temperature changes usually observed during the writing of gratings. Heating of the fibre could be a problem if the excimer laser was used at maximum repetition rate or in fibres with very high UV absorption.

4.3. Grating growth

The growth of a grating can be monitored in real time during the exposure by measuring the amount of power reflected by the grating from a broad-band light source. This gives a signal which is proportional to the effective grating bandwidth, as described in section 2.5.4. This technique has the advantages that it allows fast changes in the grating index modulation to be recorded and gives a continuous measurement. An alternative or complementary method is to record the reflection or transmission spectrum of the grating at different time intervals. This provides a measurement both of the index modulation and average index change of the grating.

4.3.1. Pulse-by-pulse growth

Transient component

Fig. 4-5 shows the growth of the index modulation of a 1.1 mm grating obtained by exposing a germania-boron fibre to one pulse every 10 seconds. Each 20 ns pulse produces a quasi-instantaneous rise in the index modulation, part of which reverses on a time scale of a few seconds. This transient component is very well-fitted by a stretched exponential with a β parameter of 0.22 and a time constant of 0.27 s or a power-law function with $\beta = 0.34$ and $t_S = 0.22$ s. The amplitudes of both the permanent and the transient components of the index change induced by each pulse decay with the number of pulses which is expected since the absorption at 248.5 nm is rapidly being bleached. Meltz and coworkers recently made similar observations when exposing a germania-doped fibre (AT&T Accutether) to a uniform excimer laser beam, using a fibre Michelson interferometer to measure the index change [11]. But this is probably the first report of transient index changes in fibre gratings.

The transient component is due to the partial thermal erasure of the grating at room temperature: photoionised electrons caught in shallow traps return to their original sites with the assistance of phonons and of the electrostatic field created by the charge separation. The dynamics of this transient are indeed characteristic of dispersive charge transport in glass, as discussed in sections 3.2.2 and 4.4.6.
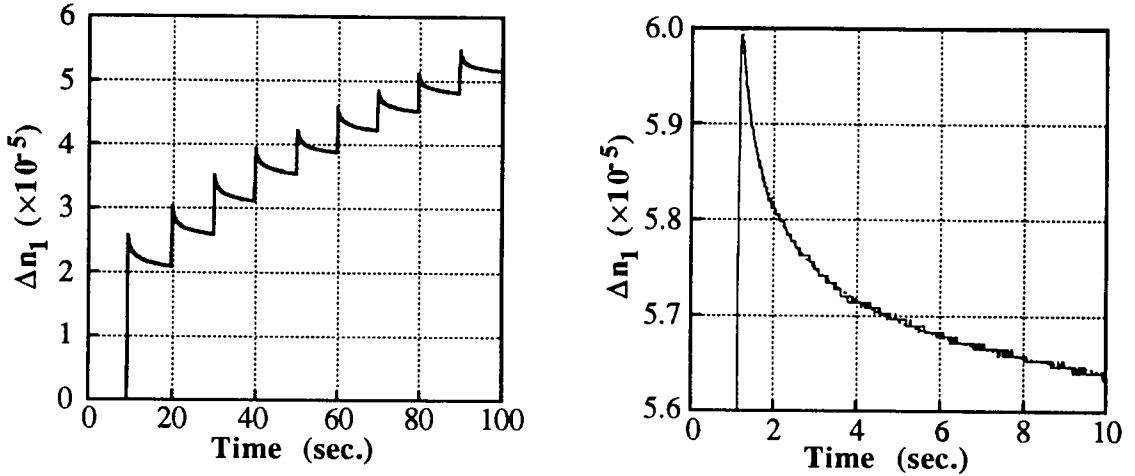

Figure 4-5 - *Left*: index modulation produced by first 9 pulses fired at 0.1 Hz in Ge/B fibre HD206. *Right*: detail of transient following 11th pulse with stretched-exponential fit.

Permanent average index change and index modulation

The evolution of the permanent index modulation and average index change with the number of pulses are shown in Fig. 4-6 for the same experimental conditions as in Fig. 4-5. After each pulse was fired, sufficient time was allowed for the transient component of the index change to disappear before the measurements were made. The average index change was then calculated from

$$\Delta n_{av} = \frac{n_{av}\Delta\lambda_B}{\eta\lambda_B}$$ (4-10)

where $\Delta\lambda_B$ is the total Bragg wavelength shift. The average index change induced by the first pulse can not be measured and was arbitrarily given the same value as the index modulation. The error bars represent the ±0.01 nm precision of the optical spectrum analyser.

Contrary what is often believed, it is clear that even in the initial stage of the UV exposure, the index change does not grow linearly. In the experiment of Fig. 4-6, the index modulation should eventually reach a maximum of ~3×10^{-4} after about 2000 pulses (see Fig. 4-8). The first pulse therefore contributes to about 7% of the total index

modulation. It then takes five more pulses to double the amplitude of index modulation. In Meltz's experiment the effect is even more dramatic: 30% of the total index change resulted from the first pulse, 20% from the next five pulses and the remaining 50% from another 12000 pulses [11].

In Fig. 4-6, the average index change can be seen to follow closely the index modulation. For the first 14 pulses, the ratio $\Delta n_{av}/\Delta n_1$ is fairly constant at about 1.2. The evolution of both the average index change and index modulation in Fig. 4-6 can be fitted by power-law functions, of the form cF^β , where c and β are constants, with $\beta=0.46\pm0.04$ for the average index change and $\beta=0.47\pm0.01$ for the index modulation. Patrick and Gilbert observed similar dynamics in the index modulation of gratings written by CW light at 244 nm with intensity-dependent β values ranging from 0.29 to 0.32, the higher β values corresponding to higher UV intensities.
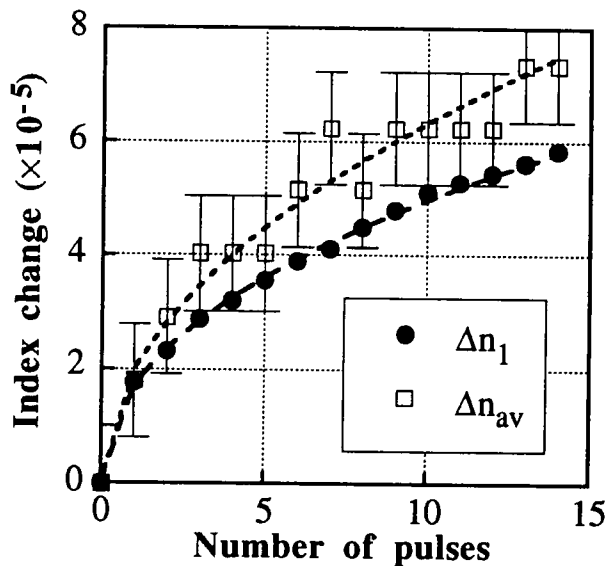

Figure 4-6 - Permanent index modulation and average index change induced by the first 14 pulses in germania-boron fibre HD206.

4.3.2. Growth under constant illumination

Gratings are usually produced by exposing fibres to constant pulse rates and energy for a few minutes. Fig. 4-7 is an example of grating growth, which shows the evolution of the transmission spectrum with the number of pulses. Here, a 15 mm length of highly photosensitive fibre (number HD066) was exposed to the UV beams. In the initially flat LED spectrum, a notch appears at the Bragg wavelength (1558.2 nm) which rapidly deepens towards 0% transmission. As the index modulation increases, the grating

bandwidth broadens and the Bragg wavelength drifts towards the longer wavelengths because of the increase in the average index.
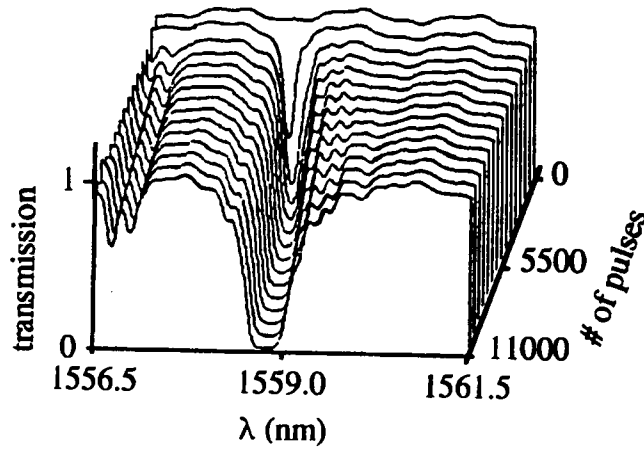
Figure 4-7 - Evolution of the transmission spectrum of a fibre grating during constant exposure.

The growth of a grating is a saturable process: after a total exposure of 0.1 to 10 kJ/cm^2, depending on the fibre and exposure conditions, the index modulation amplitude reaches a maximum and then starts decreasing if the exposure is prolonged, as can be seen in the examples of Figs. 4-8 and 4-9.
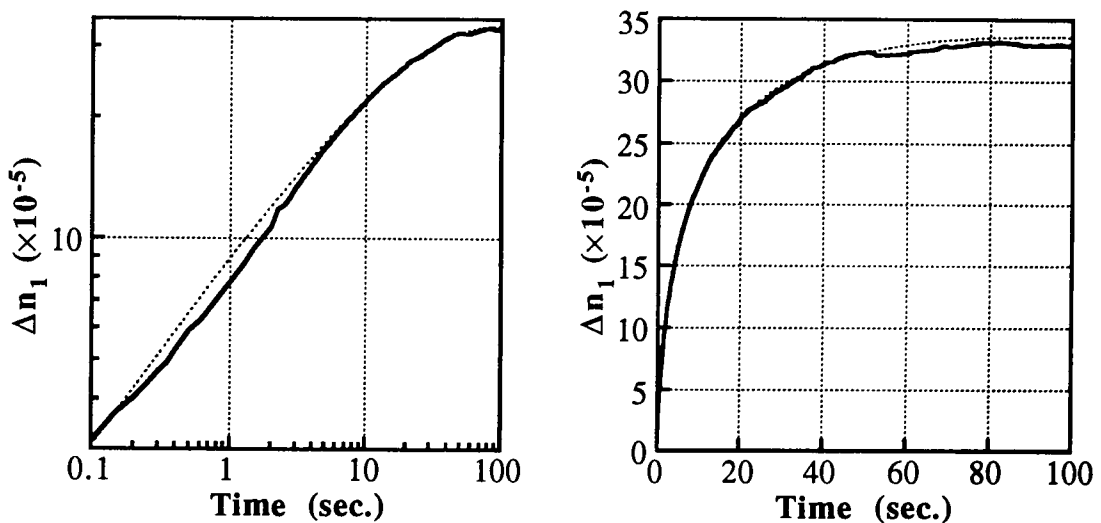
Figure 4-8 - Growth of index modulation in Ge/B fibre HD206 exposed to 20 pulses/s at ~0.5 J/cm^2/pulse, in logarithmic and linear scales. Dotted line shows best fit obtained with the model of section 4.3.3, with $\beta=0.5$, M=0.9, $t_s=60s$, $\Delta n_s=1.6\times10^{-3}$.

Fig. 4-8 shows a typical growth curve of a 1.1 mm grating written in a moderately photosensitive germania-boron fibre (HD206) exposed to 20 pulses/s at ~0.5 J/cm^2/pulse. On the logarithmic plot, the slope of the growth curve remains fairly constant at 0.46 for the first 15 seconds of the exposure and then gradually decreases. A maximum index modulation of 3.3×10^{-4} is obtained after 90 seconds for a total UV fluence of about 0.1 kJ/cm^2. At the end of this exposure, an average index change of $(3.6 \pm 0.1) \times 10^{-4}$ was recorded, giving a ratio $\Delta n_{av}/\Delta n_1 \approx 1.1$, which is very close to the value obtained for the first few pulses (Fig. 4-6).

Fig. 4-9 shows similar growth curves for 1.8 mm-long gratings written in our most photosensitive fibre, number HD066, which is also co-doped with germania and boron. Two different pulse fluence levels were used in this experiment. A first grating was written at 0.39 J/cm^2/pulse for about 15 minutes at 20 pulses/second. The pulse fluence was then reduced by half and a second grating was written over ~30 minutes. Finally, the pulse fluence was reset to 0.39 J/cm^2/pulse and a third grating was written. In Fig. 4-9, the two 0.39 J/cm^2/pulse curves are almost perfectly overlapped for the whole 15 min. exposure, confirming the repeatability of the measurement.
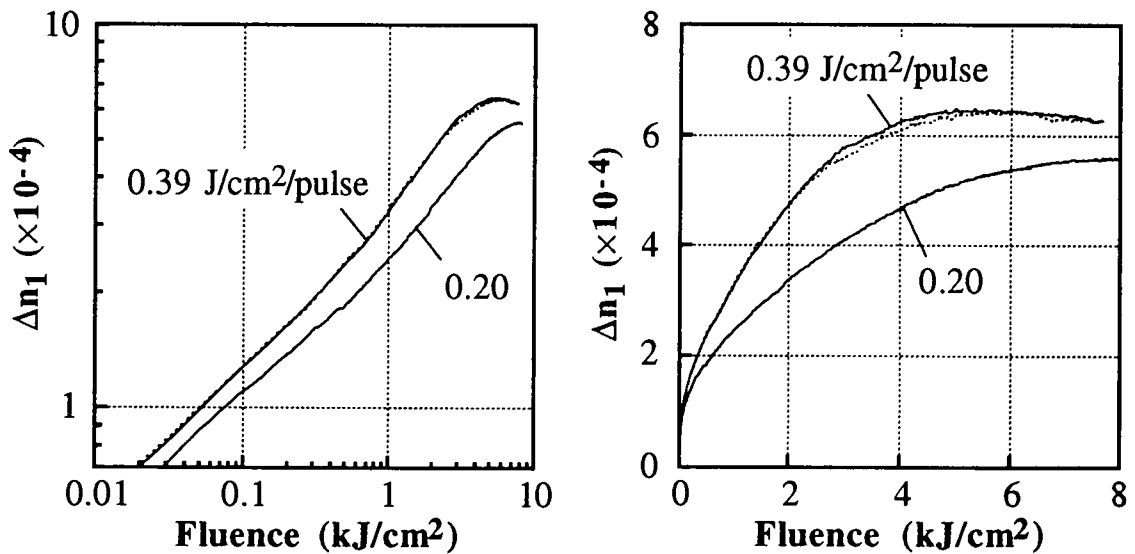
Figure 4-9 - Growth of index modulation in highly photosensitive Ge/B fibre (HD066) exposed to 20 pulses/s at two different pulse fluences. Two gratings were written at 0.39 J/cm^2 to show repeatability of measurement.

There are important differences between growth of the index modulation in fibre HD066 and that of fibre HD206. First, the saturation fluence of fibre HD066 is around 5 kJ/cm^2 whereas only 0.1 kJ/cm^2 was required to reach the maximum index modulation in fibre

HD206. Second, there is a distinct increase of slope on the logarithmic plots of Fig. 4-9: below 1 kJ/cm^2, the slope is ~0.34 for the 0.20 J/cm^2 exposure and 0.37 for the 0.39 J/cm^2 exposure; above 1 kJ/cm^2, the slopes change to 0.46 and 0.53 respectively. By contrast, the slope in Fig. 4-8 remains fairly constant for the initial part of the exposure at 0.46 and then starts decreasing.

Fig. 4-9 also shows that the index-changing mechanism is intensity-dependent. If the growth rate of a grating depended linearly on intensity, the three curves of Fig. 4-9 should overlap. Instead, we see that using a higher pulse fluence affects the growth process in several ways:

1) the initial slope, β, is larger;

2) the maximum index modulation is also increased;

3) the fluence required to obtain this maximum is reduced.

These observations are consistent with results published elsewhere [12,13].

In Fig. 4-10, the initial slope β from Fig. 4-9 is plotted against pulse fluence along with data measured from the same fibre but in a separate experiment. There is a clear dependence of the slope β on the excimer pulse fluence F_p; in Fig. 4-10, a least-squares fit gives

$$\beta = 0.30 + 0.23 \ F_p \ cm^2/J \qquad (4-11)$$

At very low intensity, β should tend to 0.30 which is very close to the lowest value reported in [13].
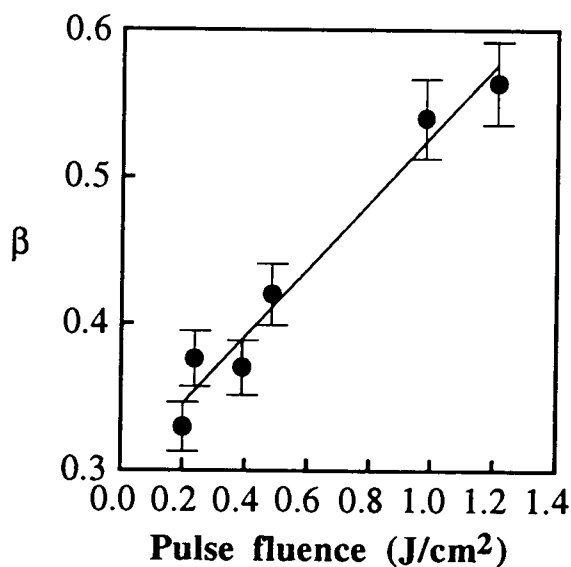

Figure 4-10 - Dependence of low exposure dispersion parameter on pulse fluence in fibre HD066 with linear fit.

4.3.3. Model

Because the growth of the index change is highly nonlinear, the index modulation of a fibre grating is far from sinusoidal, as illustrated in Fig. 4-11. Therefore, the first step in analysing such a periodic structure is to decompose it over its Fourier components, as described in Eq. (2-3). For a uniform grating, Eq. (2-3) can be written as

$$\Delta n_{av} = \frac{\Delta n_s}{\pi} \int_0^\pi g(F_0(1+M\cos(\zeta)))d\zeta$$

$$\Delta n_j = \frac{2\Delta n_s}{\pi} \int_0^\pi g(F_0(1+M\cos(\zeta)))\cos(j\zeta)d\zeta \qquad (4\text{-}12)$$

where $\zeta=Kz$. In the preceding chapter, two possible forms of $g(F)$ have been identified to describe the photosensitive response of germania-doped optical fibres: the stretched exponential

$$g(F) = 1-\exp(-(F/F_s)^\beta)$$

and the power-law function

$$g(F) = 1-\frac{1}{1+(F/F_s)^\beta} \qquad (4\text{-}13)$$

which are valid for a constant pulse fluence, F_p. Both of them will be considered in this section. In addition, there are three parameters to be varied: the normalised exposure, F_0/F_s, the dispersion parameter, β, and the modulation depth of the UV fringes, M.
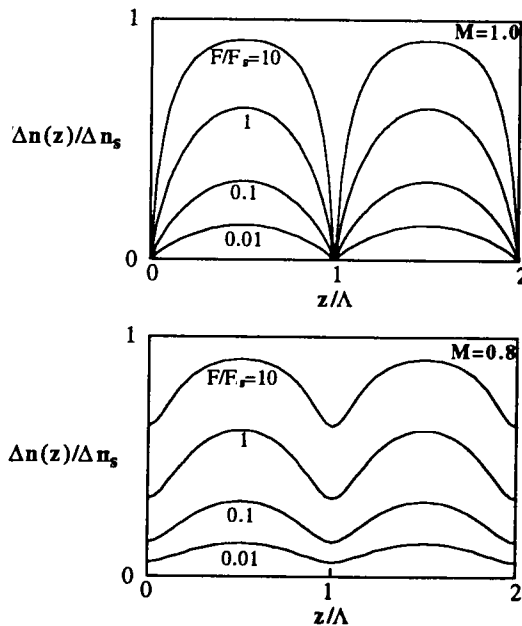

Figure 4-11 - Shape of grating lines for stretched-exponential model with $\beta=0.4$ and 100% and 80% fringe contrast.

In general, the integrals of Eq. (4-12) must be evaluated numerically. However, analytical solutions can be found in certain cases. For example, for a simple exponential dependence (β=1),

$$\frac{\Delta n_{av}}{\Delta n_s} = 1 - e^{-F_0/F_s} I_0(MF_0/F_s)$$

$$\frac{\Delta n_j}{\Delta n_s} = 2e^{-F_0/F_s} I_j(MF_0/F_s) \tag{4-14}$$

where I_j is the modified Bessel function of order j. Also, if $F_0/F_s \ll 1$ and M=1, then the following approximate results can be derived:

$$\frac{\Delta n_{av}}{\Delta n_s} \approx \frac{\Gamma(\beta+1/2)}{\sqrt{\pi}\Gamma(\beta+1)} (2F_0/F_s)^\beta$$

$$\Delta n_1 \approx \frac{2\beta}{\beta+1} \Delta n_{av} \; ; \; \Delta n_j \approx \frac{\beta+1-j}{\beta+j} \Delta n_{j-1} \tag{4-15}$$

If $F_0/F_s \ll 1$ and $M<1$, the amplitudes Δn_j can be expressed as the series

$$\frac{\Delta n_{av}}{\Delta n_s} \approx \left(\frac{F_0}{F_s}\right)^\beta \left(1 + \sum_{n=1}^{\infty} \frac{\Pi^{(2n)}(\beta)(M/2)^{2n}}{(n!)^2}\right)$$

$$\frac{\Delta n_{2j-1}}{\Delta n_s} \approx \left(\frac{F_0}{F_s}\right)^\beta \sum_{n=j}^{\infty} \frac{2\Pi^{(2n-1)}(\beta)(M/2)^{2n-1}}{(n-j)!(n+j-1)!}$$

$$\frac{\Delta n_{2j}}{\Delta n_s} \approx \left(\frac{F_0}{F_s}\right)^\beta \sum_{n=j}^{\infty} \frac{2\Pi^{(2n)}(\beta)(M/2)^{2n}}{(n-j)!(n+j)!}$$

with

$$\Pi^{(n)}(\beta) = \beta(\beta-1)(\beta-2)...(\beta-n+1) \tag{4-16}$$

These series converge rapidly when M is small. The lowest-order terms in Eq. (4-16) give

$$\frac{\Delta n_{av}}{\Delta n_s} \approx \left(\frac{F_0}{F_s}\right)^\beta \; ; \; \frac{\Delta n_1}{\Delta n_s} \approx \left(\frac{F_0}{F_s}\right)^\beta \beta M$$

$$\frac{\Delta n_2}{\Delta n_s} \approx \left(\frac{F_0}{F_s}\right)^\beta \beta(\beta-1)M^2/4 \tag{4-17}$$

The plots of Figs. 4-12 to 4-16 were obtained by integrating Eq. (4-12) numerically; they show the evolution of the amplitudes of the grating harmonics on logarithmic and linear scales. Each graph compares the predictions of the stretched-exponential and the power-law models. For very low exposures (($F_0/F_s)^\beta \ll 1$), the two models are in agreement, with every harmonic proportional to $(F_0/F_s)^\beta$ (Fig. 4-12). The amplitude of each harmonic is well predicted by the expressions of Eq. (4-15) to (4-17). On the logarithmic plots, the slope of the 'stretched-exponential' curves remain fairly constant for several decades of exposure before decreasing rapidly for $F_0 \sim F_s$. In comparison, the slope of the 'power-law' curves start decreasing much earlier but the second derivative is much

smaller near the maximum. As a consequence, the 'power-law' curves appear to remain constant on the linear scales once they have reached their maximum, while the 'stretched-exponential' curves can be seen to decrease significantly past the maximum point. As expected, the amplitudes of the grating harmonics are smaller for the higher harmonics. Every harmonic goes through a maximum and then decreases monotonically to zero, with the maxima of the lower harmonics occurring at lower exposures.
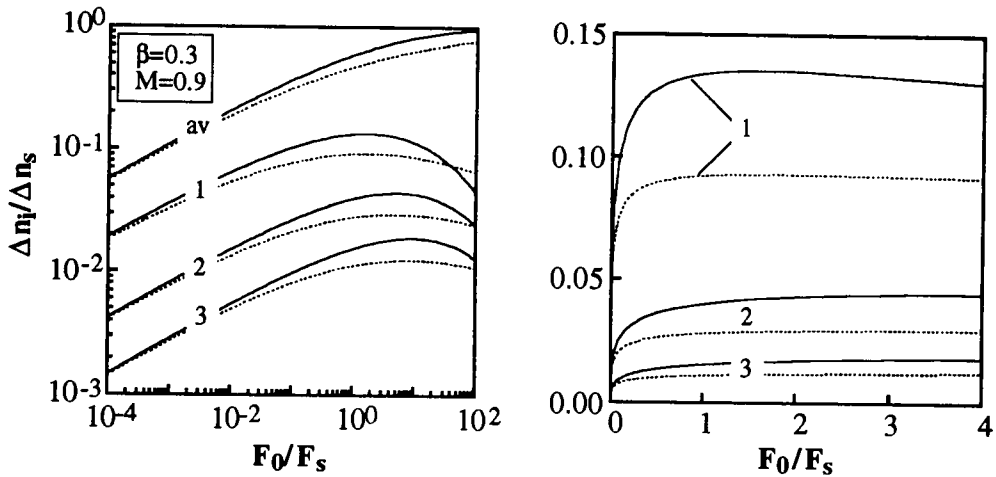
Figure 4-12 - Evolution of average index change and amplitudes of first three grating harmonics with exposure as predicted by stretched exponential (solid lines) and power-law (dotted lines) models, for $\beta=0.3$ and $M=0.9$.

Fig. 4-13 and 4-14 examine in more detail the evolution of the first harmonic, which is in practice the main quantity of interest.

Figure 4-13 - Evolution of the amplitude of the first grating harmonic for different modulation depths and with $\beta=0.3$. Solid lines are calculated from stretched exponential and dotted lines from power-law.

Eq. (4-17) predicts that, to first order, the index modulation of a grating should be proportional to the modulation depth. This is illustrated in Fig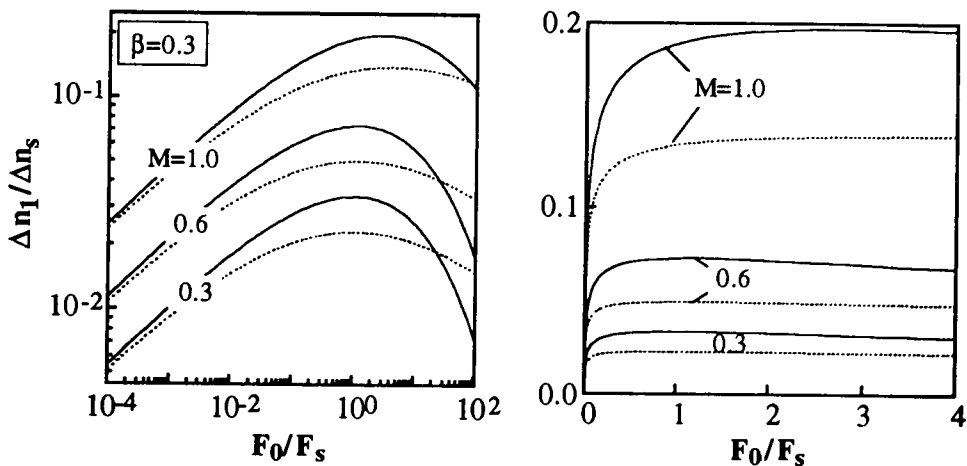. 4-13, where UV fringe contrasts of 30, 60 and 100% have been considered. Fig. 4-13 also shows that, as expected, the index modulation amplitude is quicker to reach its maximum for a lower fringe contrast. In Fig. 4-14, the effect of the dispersion parameter is examined with three values of β: 0.5, 0.3 and 0.1. As β gets smaller, the grating lines become increasingly distorted and the maximum index modulation decreases.
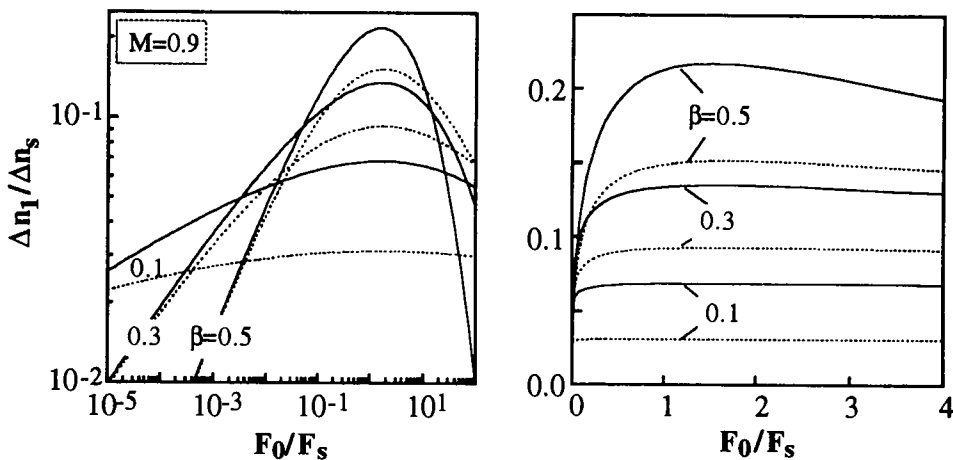

Figure 4-14 - Evolution of the amplitude of the first grating harmonic for different dispersion parameters and with M=0.9.

We now take a closer look at three quantities of particular interest, namely:
- the maximum index modulation, Δn_{max};
- the corresponding fluence, F_{max};
- the 'contrast' of the grating lines, defined as $C=\Delta n_1/\Delta n_{av}$.

These are plotted in Figs. 4-15 and 4-16, for the stretched exponential model only; the power-law model gives similar results.

It is no surprise that as the modulation depth goes to zero, both Δn_{max} and C tend to zero as well. An interesting observation, however, is that the exposure needed to obtain the maximum index modulation is always larger or equal to F_s (Fig. 4-15). In fact, as M becomes small, $F_{max} \approx F_s$, almost independently of both parameters β and M. Therefore, the parameter F_s can easily be measured by writing a grating using a low contrast UV fringes. Both the maximum index modulation and the grating contrast vary quasi-linearly with M when M is small, for all values of β. As the modulation depth approaches 100%, however, much faster variations are observed. This is expected, since changes in the modulation depth have a much larger effect on the shape of the grating lines near $M=1$.

This result has important implications for grating manufacturing: since gratings are ideally written using UV fringe contrasts close to 100%, small fluctuations in the fringe contrast can have large effects on the grating properties, especially if β is small. For example, if β=0.3, an increase of the UV fringe contrast from 95 to 100% would increase the maximum index modulation by 28% and the exposure required to reach this maximum by 56%. Under these conditions, it could be difficult to write gratings reproducibly.
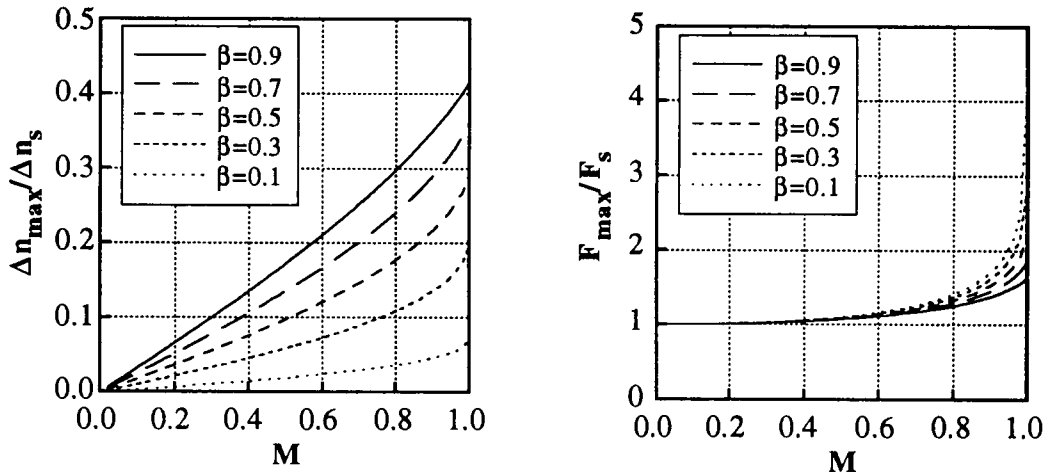
Figure 4-15 - Maximum index modulation (left) and corresponding fluence (right) plotted against UV fringe contrast.
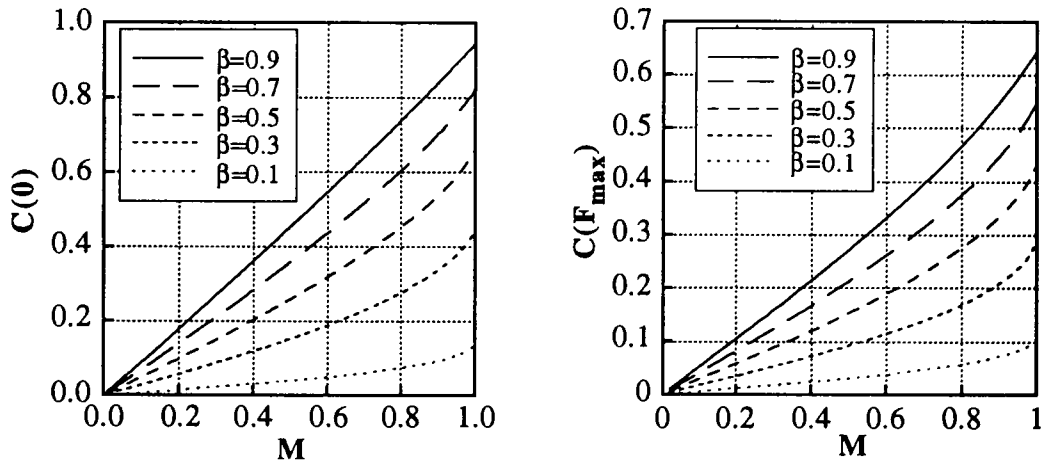
Figure 4-16 - Contrast of grating lines at beginning of exposure (left) and for maximum index modulation (right) as function of UV fringe contrast.

The maximum value of the grating lines contrast is achieved for $M=\beta=1$, in the initial stages of the exposure ($F\rightarrow 0$). For $M=1$, this initial contrast can be calculated from Eq. (4-15), which gives

$$C(0) = \frac{2\beta}{\beta+1} \qquad (4\text{-}18)$$

For $\beta=1$, $C(0)=100\%$ and $C(0)=50\%$ for $\beta=1/3$. When M is small, the contrast can be estimated from the first-order terms in Eq. (4-16), which gives

$$C(0) \approx \beta M \qquad (4\text{-}19)$$

As the exposure increases, the contrast diminishes, since the average index change grows faster than the index modulation. For $F_0=F_{max}$, the maximum contrast is again obtained for $M=\beta=1$, where $C(F_{max})\approx69\%$. For $\beta=0.3$, however, $C(F_{max})$ is only 29% if $M=1$.

4.3.4. Discussion

In Fig. 4-8, the growth of the index modulation of a grating written in fibre HD206 is plotted alongside the best fit calculated from the stretched-exponential model. The fitting parameters are $\beta=0.5$, $M=0.9$, $t_s=60$ s ($F_s\approx0.6$ kJ/cm^2) and $\Delta n_s=1.6\times10^{-3}$. With this model, an excellent agreement is obtained over 3 decades of time. It must be noted, however, that the quality of the fit does not depend very strongly on the choice of M, which also puts a large uncertainty on the value of Δn_s. The fit from the power-law model is not nearly as good.

Fig. 4-8 is convincing evidence that, for this particular fibre at least, the stretched-exponential model can accurately predict the growth of the index modulation up to the maximum point. However, there is a strong disagreement between the values of the average index change predicted by the model and those measured experimentally. For a β of 0.5, the maximum possible value of the grating line contrast should be $C(0)=67\%$, as given by Eq. (4-18) for $M=1$. When the index modulation reaches its maximum, this value is reduced to $C(F_{max})=44\%$. From the data obtained with the first 14 UV pulses in Fig. 4-6, an average contrast $C(0)$ of 81% is obtained with a standard deviation of 8%. At the end of the exposure the contrast calculated from the measured data gives $C(F_{max})=91\%\pm10\%$, which includes the error in measuring the shift of the Bragg wavelength and in calculating the index modulation from the reflection and transmission spectra. Clearly, the measured average index change is much smaller than the minimum value predicted by the model. In fact, in all similar measurements that were made in the course of this project, the measured grating line contrast has been systematically higher than expected. The reason of this discrepancy could be found in an observation made earlier in section 3.4.2: assuming that the photoinduced index change, or at least part of it, is caused by a local compaction of the core glass, then the refractive index should increase in the regions of a grating exposed to bright UV fringes but would *decrease* in the regions exposed to dark fringes, because of the tension building up in the glass. By

contrast, the theoretical model assumes that the refractive index in the unexposed regions of the grating remain unchanged, which is consistent with the colour centre model of photosensitivity. The high values of the measured grating line contrast can therefore be interpreted as evidence for the compaction model of photosensitivity.

Whereas a good fit of the index modulation growth in fibre HD206 can be obtained with the stretched-exponential model, this is not the case with fibre HD066, where more complex dynamics are observed (Fig. 4-9). The increase of slope seen in the growth curve coupled with the unusually large saturation fluence and index change seems to indicate that a different index-changing mechanism is occurring in this fibre.

According to the photo-thermal ionisation model proposed in chapter 3, the intensity dependence of β is explained by the increase in fibre core temperature with UV intensity. The model predicts that the dispersion parameter should be equal to T/T_0 (Eq. (3-15)), where $\Delta E = k_B T_0$ is the characteristic width of the ionisation energy distribution. In the case of pulsed UV exposure, the instantaneous temperature in the fibre core immediately after exposure to a pulse is approximately given by

$$T_{co} \approx T_{cl} + \frac{\eta \alpha F_p}{\rho c_v} \qquad (4-21)$$

where T_{cl} is given by Eq. (4-5), and the other quantities are as defined in section 4.2.6. Combining Eqs. (3-15), (4-5) and (4-21) yields

$$\beta = \frac{T_a}{T_0} + \left(\frac{1}{\rho c_v} + \frac{f r_{co}^2}{2 h r_{cl}} \right) \frac{\eta \alpha F_p}{T_0} \qquad (4-22)$$

Comparing this expression to the linear fit of Fig. 4-10 (Eq. (4-11)), we see that for $F_p=0$, $\beta = T_a/T_0 \approx 0.30$, which implies that $T_0 \approx 980K$. Assuming $\eta=0.41$, $\alpha=300cm^{-1}$, $\rho c_v = 1.73 kgJ/cm^3 K$ and $f r_{co}^2/2 h r_{cl} = 0.17 kgJ/cm^3 K$, Eq. (4-22) becomes

$$\beta = 0.30 + 0.24\ F_p\ cm^2/J \qquad (4-23)$$

which is nearly identical to Eq. (4-11). This excellent agreement is partly coincidental, since there is a large uncertainty on the absorption α.

From the traces of Fig. 4-9 it is possible to estimate the parameters of the defect ionisation energy distribution, as discussed at the end of section 3.2.2. For this fibre, the characteristic width of the distribution is simply given by $\Delta E = k_B T_0 \approx 0.09$ eV. The characteristic fluence, F_0, can be deduced by comparing two of the measurements of Fig. 4-9, as described by Eq. (3-17). This gives F_0 between 0.2 and 2 J/cm^2. The error on F_0 is large because of the small difference in the dispersion parameters of the different measurements. The evaluation of the central position of the ionisation energy distribution

E_0 requires a knowledge of the saturation fluence, F_s, which is uncertain in this fibre because of the unusual dynamics seen at high exposures and because the UV fringe contrast is unknown. Nevertheless, taking the reasonable assumption that $F_{max}/F_s \approx 1.5$ (see Fig. 4-15) gives $F_s \approx 3.3$ kJ/cm^2 for the 0.39 J/cm^2/pulse exposure and $F_s \approx 5.3$ kJ/cm^2 for the 0.20 J/cm^2/pulse exposure. In both cases, the predicted value of E_0 is 0.30 eV for F_0=0.2 J/cm^2 and 0.23 eV for F_0=2 J/cm^2. The true value of E_0 is probably between 0.23 and 0.30 eV.

In the case of a CW exposure, the steady-state core temperature is approximately

$$T_{co} \approx T_{cl} \approx T_a + \frac{\eta \alpha I r_{co}^2}{2hr_{cl}} \tag{4-24}$$

where I is the UV intensity, which gives

$$\beta = \frac{T_a}{T_0} + \frac{\eta \alpha r_{co}^2}{2hr_{cl}T_0} I \tag{4-25}$$

Using the same numerical values as before, Eq. becomes

$$\beta = 0.30 + 1.1 \times 10^{-3} \, I \, cm^2/W \tag{4-26}$$

This can be compared with the data published in Ref. [13] by Patrick and Gilbert. A linear regression of their data gives

$$\beta = 0.26 + 1.5 \times 10^{-3} \, I \, cm^2/W \tag{4-27}$$

which again agrees well with the predicted relation.

The fibre used by Patrick and Gilbert and fibre HD066 are both believed to contain ~9 mol% of germania and therefore should have similar UV absorption. Therefore, the fact that the predictions of the model agree with both sets of measurements simultaneously is significant. The model has however an important flaw as it assumes that α is a constant, whereas we know that α decreases by as much as 60% during an exposure. One would therefore expect to see a significant decrease in β at the beginning of an exposure, which is not the case in practice. One way to verify the validity of the model would be to either heat or cool the fibre while exposing it to UV to see if β is affected. However, the effect of the change in temperature on the reverse process (thermal annealing of the grating, see section 4.4.6) would have to be taken into consideration.

4.4. Characterisation of fibre gratings

This section examines the main properties of the fibre gratings that can be produced by the experimental setup of Fig. 4-3. In particular, we look at the range of grating reflectivity and bandwidth which can be achieved with the current system.

4.4.1. Narrow-band gratings

The optical properties of a uniform grating of given period are determined by two parameters: the length and the index modulation. The maximum length of grating that can be written with the setup of Fig. 4-3 is limited by the clear aperture of the interferometer, which is about 20 mm. This maximum length imposes a minimum grating bandwidth $\Delta v \approx 4.6$ GHz (FWHM), which corresponds to $\Delta \lambda \approx 0.04$ nm at 1550 nm. This bandwidth could only be obtained with a weak, perfectly uniform grating. For a 90% reflectivity grating ($\kappa L \approx 1.9$), the minimum bandwidth is 9 GHz. The measured reflection spectrum of a grating with a bandwidth close to the theoretical limit is shown in Fig. 4-17. The measured bandwidth is 0.107 nm which is limited by the 0.1 nm resolution of the optical spectrum analyser.
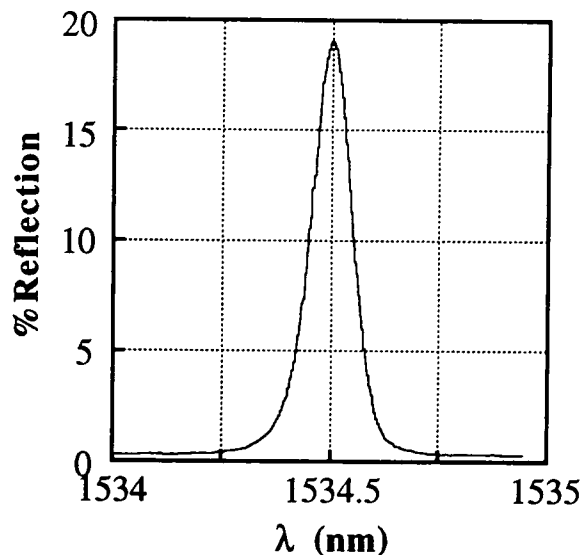

Figure 4-17 - Measured reflection spectrum of 15 mm narrow-band grating, limited by the 0.1 nm resolution of the optical spectrum analyser.

4.4.2. Broad band gratings

The bandwidth of a grating can be increased at will by reducing its length, but at the expense of the reflectivity. The maximum bandwidth of a high reflectivity grating is limited by the maximum index modulation that can be obtained in the particular fibre being used. Table V lists the maximum index modulation measured in a variety of optical fibres, nearly all of which were manufactured in the ORC. Note that these values must be multiplied by the fraction of modal power inside the fibre core to give the effective index modulation at a given wavelength.
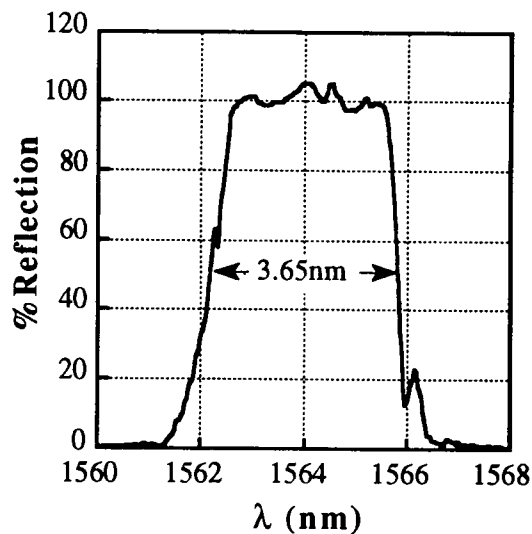
Figure 4-18 - Reflection spectrum of very strong grating in fibre HD123 loaded with 1.5 mol% H_2.

The largest index modulation of 4.7×10^{-3} was obtained in a hydrogen-loaded fibre with a high germania content; the corresponding reflection spectrum is shown in Fig. 4-18 (on this graph, the fluctuations around $R \sim 100\%$ are an artefact of the measurement system). This index modulation would be sufficient to write a high reflectivity uniform grating with 5 nm (0.6 THz) bandwidth at 1550 nm, assuming a mode confinement of 100%. For a 20 mm grating, this would correspond to a maximum grating strength κL of 190. Without hydrogen-loading, the maximum index modulation is about 10^{-3}, which is sufficient to write high reflectivity gratings with bandwidths up to 1.1 nm at 1550 nm and κL up to 40.

Fibre #	Core dopants	N.A.	Δn_1 max. $(\times 10^{-4})$	$[GeO_2]$ (mol%)
HD123	Ge+1.5mol% H_2	0.34	47	28
ND839	Ge/Tm+H_2	0.19	18	9
HD029	Ge+0.4mol% H_2	0.32	17	25
ND551	Ge/Yb+0.3mol% H_2	0.17	11	7
HD066	Ge/B	0.15	10	9
HD206	Ge/B	0.13	5	7
ND760	Ge/B	0.21	4	15
HD213	Ge/B/Al/P/Er/Yb	0.15	4	8
HD222	Ge (D_2 treated)	0.17	2.4	7
HD095	Ge (reduced)	0.30	2.4	22
HD187	Ge/B	0.15	2.2	8
ND864	Ge/Yb	0.30	2	22
HD212	Ge/B/Al/P/Er/Yb	0.16	2	9
HD123	Ge	0.34	1.6	28
HD203	Ge (reduced)	0.20	1.2	14
HD029	Ge	0.32	1.1	25
ND839	Ge/Tm	0.19	0.9	9
ND551	Ge/Yb	0.17	0.9	7
YD210	Ge	?	0.5	?
ND383	Ge	0.30	0.5	22
YD308	Ge	?	0.3	?
ND671	Ce	0.13	0.2	0
Standard tel.	Ge	0.11	0.2	3
ND420	Ge/Nd	0.13	0.1	4
HD193	Ta	0.20	0.03	0
ND791	Al/P/Er/Yb	0.12	0.025	0
ND618	P/Nd	0.14	0.02	0
ND831	Al	0.09	0.02	0

Table V - Maximum index modulation obtained in various fibres, with core dopants, numerical aperture and estimated germania concentration.

4.4.3. Uniform gratings

The above-mentioned limits are difficult to achieve in practice with the current system because of the inhomogeneity of the excimer laser beam. As discussed in section 2.7, the use of an uneven beam profile adds a random chirp and taper function to the grating which tends to broaden the spectral response and reduce the peak reflectivity. This effect is most obvious in strong gratings, where large spatial variation in the average index change and index modulation can be present. Fig. 4-19 shows a typical example. The reflectivity and bandwidth of this grating would be characteristic of a uniform grating

with a length of 1.7 mm and an effective index modulation of 7×10^{-4}; however, the actual exposed fibre length was 15 mm.
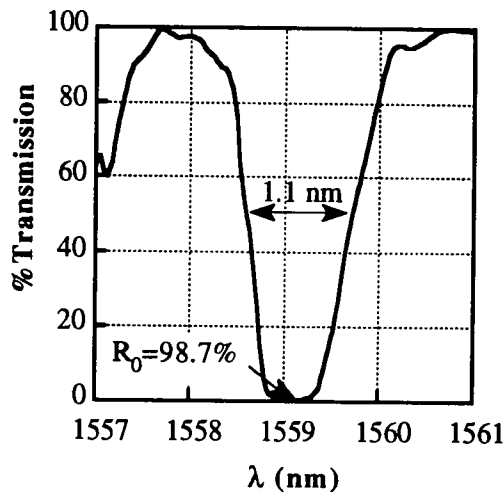
Figure 4-19 - Transmission spectrum of strong fibre grating.

In section 4.2.5, several methods of improving the grating uniformity were described. The simplest method is to use a beam mask to select a uniform region of the beam profile. Fig. 4-20 shows an example of a very short grating written in this fashion. The measured reflection spectrum is in very close agreement with the theoretical prediction. The asymmetry of the measured sidelobes indicates a slight chirp.
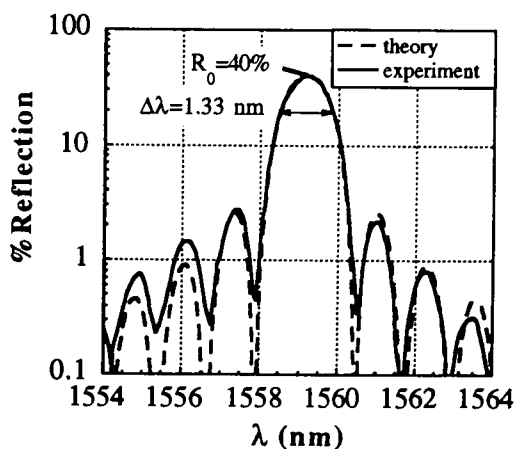
Figure 4-20 - Reflection spectrum of 0.68 mm grating in fibre HD066.

In Fig. 4-21, the same method is applied to write a longer grating, with $L \approx 4$ mm. The fit between the measured and calculated spectra is nearly as good as for the shorter

grating of Fig. 4-20. The theoretical calculation predicts an extinction at the Bragg wavelength of about 40 dB in the transmission spectrum, which could not be measured accurately because it exceeded the dynamic range of the system.
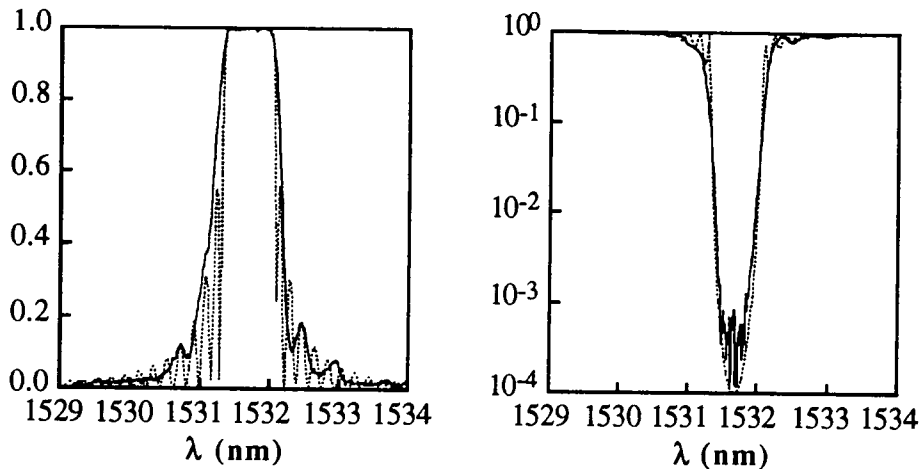

Figure 4-21 - Measured reflection and transmission spectra of 4 mm grating written in H_2-loaded fibre HD029 shown in solid line. Dashed line is spectrum calculated from L=4 mm and $\delta n=6.5\times10^{-4}$.

An alternative method of producing uniform gratings is to scan the UV beam across the aperture of the interferometer to average out the beam profile, as illustrated in Fig. 4-3. Ideally, the amplitude of the lateral beam displacement should be equal to the sum of the beam width and the width of the interferometer aperture. In that condition, each point along the fibre should receive the same exposure, proportional to the spatially-averaged beam fluence. Fig. 4-22 demonstrates the benefits of this technique. In this experiment, two similar gratings were written: one with a fixed beam and another with a scanning beam. The beam was displaced in a single pass by 18 mm (from -9 mm to +9 mm) at 0.075 mm/s. In both cases, the 18 mm fibre sections were exposed for 4 minutes with an 18 mm wide incident beam; the beam displacement should ideally have been 36 mm, but was limited by the range of the mirror actuator. Nevertheless, it is clear that the scanning technique did improve the grating uniformity: the 'scanned' grating is narrower (0.28 nm) and has a higher reflectivity (94%) than the 'fixed beam' grating (0.38 nm and 88%). However, the bandwidth of a uniform 18 mm grating with 94% reflectivity should be 0.08 nm, which perhaps would have been achieved with a 36 mm scan.
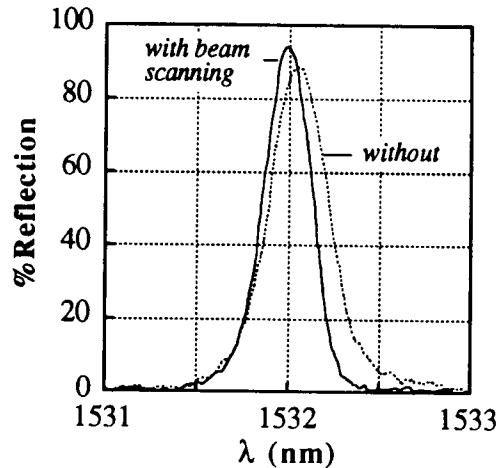
Figure 4-22 - Reflection spectrum of grating made in fibre HD206 by beam-scanning technique compared with grating made with fixed beam, for same exposure conditions.

Numerous attempts have been made using this scanning technique, but with little success, as the beam scanning causes strong instabilities which wash out the gratings in most cases. The origin of these instabilities is not understood at present. It is possibly a thermal effect caused by local variations of the UV intensity, either in the optical components of the interferometer or in the fibre itself, although the calculations of section 4.2.6 have shown that the effect intensity fluctuations on the fibre should be negligible. Until the source of instability has been identified, the beam scanning technique can not be used reliably.

4.4.4. Accurate control of grating properties

The ability to write long gratings combined with the availability of highly photosensitive fibres gives access to a wide range of grating reflectivities and bandwidths, which can meet the specific needs of most applications. As an example, Fig. 4-23 shows the reflection and transmission spectra from a pair of gratings written in fibre ND760 which were used as cavity mirrors in a fibre laser. The two gratings were specified as a 50% reflectivity narrow-band output coupler and a 100% reflectivity broadband reflector, both operating at 1535 nm. By accurately controlling the fibre tension and monitoring the transmission spectrum during the exposures, two very different gratings with matching Bragg wavelengths were manufactured. The actual measured parameters are very close to the above specifications: $\lambda_B=1534.85$ nm, $R=48\%$ and $\Delta\lambda=0.11$ nm for the output coupler and $\lambda_B=1534.94$ nm, $R>99.99\%$ and $\Delta\lambda=0.8$ nm for the high reflector. Note that these values of reflectivity were calculated by assuming that $R+T=100\%$.
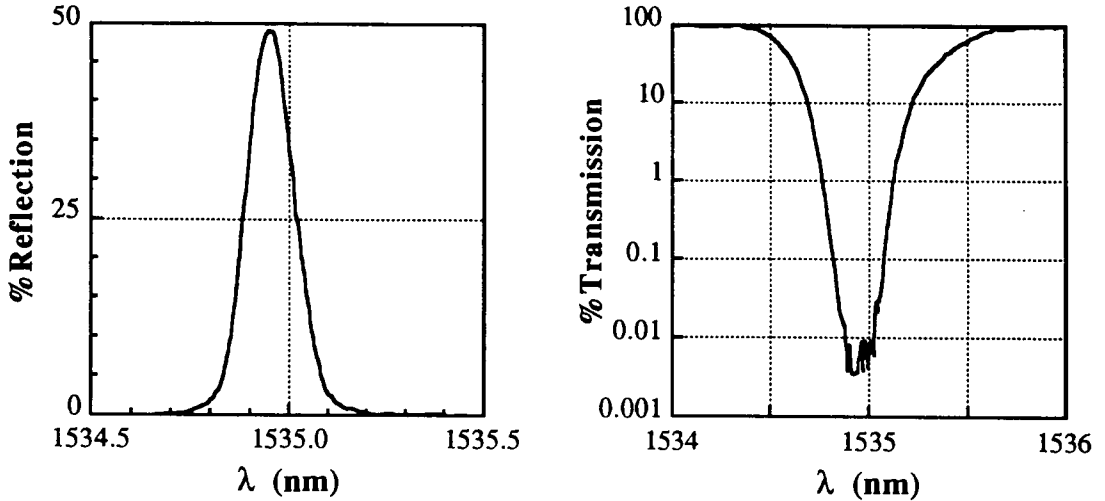
Figure 4-23 - Left: reflection spectrum of output coupler. Right: transmission spectrum of high reflector.

This example demonstrates that, in a well-characterised fibre, gratings can be written in a controllable manner so that several of their optical properties can simultaneously match predetermined values to a high degree of accuracy.

4.4.5. Birefringence

Optical fibre gratings always have a slight polarisation dependence which originates from both the intrinsic fibre birefringence and the photoinduced birefringence. In standard, low-birefringence fibre, the intrinsic birefringence usually lies between 10^{-6} and 10^{-5}. But the birefringence of a fibre grating is usually slightly larger than 10^{-5} [14,15], which means that it is dominated by photoinduced birefringence. The two orthogonal polarisations, defined by the birefringence axes of the grating, have two slightly different Bragg wavelengths. The wavelength splitting is given by

$$\lambda_s\text{-}\lambda_f = \frac{B\lambda_s}{n_s} = \frac{B\lambda_f}{n_f} \approx \frac{B\lambda_B}{n_{av}} \qquad (4\text{-}28)$$

where λ_i is the Bragg wavelength, n_i the effective index and $i=s,f$ represents the slow and fast axes. This wavelength difference is usually too small to be resolved in an optical spectrum analyser: for $B=10^{-5}$ and $\lambda_B=1550\text{nm}$, $\lambda_s\text{-}\lambda_f\approx0.01\text{nm}$.

In polarisation-maintaining fibres, however, the intrinsic birefringence is very large and can give rise to two distinct reflection peaks, as shown in Fig. 4-24. The wavelength spacing of 0.57nm corresponds to a birefringence of about 5.3×10^{-4}. On this measurement, the two peaks appear to have different reflectivities but this is only because of the polarisation-dependence of the measurement system. A measurement of the

transmission spectrum of a similar grating with single-polarised light (not shown) showed that the reflectivity was the same, within experimental error, for the two orthogonal polarisations.
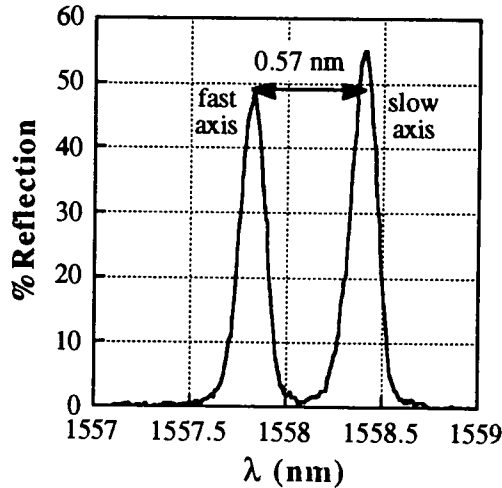
Figure 4-24 - Reflection spectrum of grating in bow-tie fibre YD210.

4.4.6. Thermal stability

The long-term stability of fibre gratings is a subject of prime importance if gratings are going to be used in commercial systems. At room temperature, gratings are known to be very stable over years but substantial decay can be observed over periods of hours at a few hundred degrees centigrade [14,16]. A recent publication by Erdogan and collaborators gives a very detailed analysis of the dynamics of the erasure process in fibre gratings in untreated germania-doped fibres for a wide range of temperatures [17]. They propose a model in which electrons released from defect centres during UV exposure are trapped in sites with a broad distribution of ionisation energies. These trapped electrons can then be ejected by phonons with sufficiently high energy into the conduction band and return to their original sites, thus reversing the index-changing mechanism. The release rate depends on the trap depth and the temperature, similar to the model presented in section 3.2.2 for the photo-thermal ionisation of oxygen-deficient centres. The decay of the index modulation is thus driven by dispersive charge transport and follows the familiar form

$$\frac{1}{1+(t/\tau)^\beta} \qquad (4\text{-}29)$$

Assuming that $\beta = T/T_0$ (which has not been verified experimentally), they find

$$\tau = \tau_0 \exp(\Delta E/k_B T) \qquad (4\text{-}30)$$

For the particular fibre used (high N.A., erbium-doped, germania-silica fibre) the values of the various constants determined experimentally are: $T_0=5250K$, $\tau_0=2.3\times10^{-16}s$ and $\Delta E=2.80eV$, where ΔE is the activation energy at the peak of the electron population distribution.

Fig. 4-25 shows the elevated temperature decay of one of our gratings written in germania-boron fibre, as measured by M.G. Xu. The temperature was increased by 200°C every 12 hours until the grating was erased. Although no rigorous comparison has been made, the dynamics seen in Fig. 4-25 seem to be in good qualitative agreement with the model of Ref. [17].
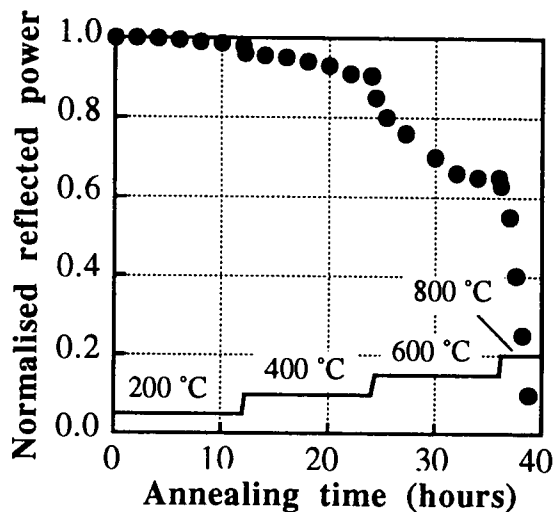
Figure 4-25 - Thermal annealing of fibre grating in germania-boron fibre (courtesy of M.G. Xu).

One of the most important aspect of this model is that it establishes that the thermal stability of a grating can be dramatically improved by 'accelerated aging', which basically means exposing the grating to high temperatures for a short period of time to release the electrons from shallow traps. Although this process somewhat reduces the grating strength, it only leaves behind the electrons caught in deep traps, which have extremely long release times at low temperatures. The model also confirms that, as previously observed by a few authors [18,19], gratings written at higher UV intensities have better thermal stability, simply because the heating of the core during UV exposure will contribute to the accelerated aging of the grating.

4.5. Conclusion

The experimental arrangement described in this chapter has been shown to produce fibre gratings reliably with a good control of the grating properties. The expertise acquired in properly aligning the interferometer and understanding the potential sources of instability insures that gratings can be written reproducibly.

Important progress has also been made in understanding the growth dynamics of fibre gratings. For the first time, a detailed model of the growth process has been presented, based on the calculation of the Fourier components of the index modulation. In light of this model, a comparison of the index modulation and average index change of several fibre gratings gave supporting evidence for the glass compaction model of fibre photosensitivity. An investigation of the intensity-dependence of grating formation showed that higher index modulations could be obtained at higher intensities. This intensity-dependence has been attributed to the photo-thermal ionisation of defect centres and comparison between experimental data and the predictions of this proposed model are in good agreement. Using the results of the photo-thermal ionisation model, it was possible to predict the parameters of the ionisation energy distribution of excited defect centres. For the specific fibre under test, it was found that the peak of the distribution should be located at 0.27±0.04 eV from the conduction band. The predicted width ΔE of the distribution is 0.09 eV which corresponds to a full width at half maximum of about 0.3 eV. Further investigations will be required to confirm the validity of the model.

In the various examples, grating bandwidths ranging from less than 0.1 nm to 3.5 nm and reflectivities in excess of 99.99% have all been demonstrated. Highly uniform gratings were obtained despite the non-uniform excimer beam, using two different techniques. Gratings have been obtained in a variety of germania-doped fibres, listed in Table V, including Hi-Bi and rare-earth doped fibres.

4.6. <u>References</u>

1. G. Meltz, W.W. Morey and W.H. Glenn, "Formation of Bragg gratings in optical fibres by a transverse holographic method", *Opt. Lett.*, **14** (15), pp. 823-825, 1989.

2. R. Kashyap, J.R. Armitage, R. Wyatt, S.T. Davey and D.L. Williams, "All-fibre narrowband reflection gratings at 1500 nm", *Electron. Lett.*, **26** (11), pp. 730-732, 1990.

3. C.G. Askins, T.-E. Tsai, G.M. Williams, M.A. Puttnam, M. Bash-Kansky and E.J. Friebele, "Fibre Bragg reflectors prepared by a single excimer pulse", *Opt. Lett.*, **17** (11), pp. 833-835, 1992.

4. D.Z. Anderson, V. Mizrahi, T. Erdogan and A.E. White, "Production of in-fiber gratings using a diffractive optical element", *Electron. Lett.*, **29** (6), pp. 566-568, 1993.

5. K.O. Hill, B. Malo, F. Bilodeau, D.C. Johnson and J. Albert, "Bragg gratings fabricated in monomode photosensitive optical fiber by UV exposure through a phase mask", *Appl. Phys. Lett.*, **62** (10), pp. 1035-1037, 1993.

6. J.D. Prohaska, E. Snitzer, S. Rishton and V. Boegli, "Magnification of mask fabricated fiber gratings", *Electron. Lett.*, **29** (18), pp. 1614-1615, 1993.

7. J.R. Armitage, "Fiber Bragg reflectors written at 262 nm using a frequency quadrupled diode-pumped Nd^{3+}:YLF laser", *Electron. Lett.*, **29** (13), pp. 1181-1183, 1993.

8. S.J. Mihailov and M.C. Gower, "Recording of efficient high-order Bragg reflectors in optical fibers by mask image projection and single-pulse exposure with an excimer laser", *Electron. Lett.*, **30** (9), pp. 707-709, 1994.

9. B. Malo, K.O. Hill, F. Bilodeau, D.C. Johnson and J. Albert, "Point-by-point fabrication of micro-Bragg gratings in photosensitive fiber using single excimer pulse refractive-index modification techniques", *Electron. Lett.*, **29** (18), pp. 1668-1669, 1993.

10. L.C. Thomas, "Heat transfer", Prentice-Hall, Englewood Cliffs, NJ, 1993.

11. G. Meltz, W.W. Morey, W.H. Glenn and D.J. Fritz, "UV-induced Bragg gratings in optical fibers and thin-film waveguides", *Meeting on Photosensitivity and Self-Organization in Optical Fibers and Waveguides , SPIE Vol. 2044*, pp. 236-245, Quebec, 1993.

12. D.L. Williams, B.J. Ainslie, R. Kashyap, G.D. Maxwell, J.R. Armitage, R.J. Campbell and R. Wyatt, "Photosensitive index changes in germania doped silica glass fibres and waveguides", *Meeting on Photosensitivity and Self-Organization in Optical Fibers and Waveguides , SPIE Vol. 2044*, Quebec, 1993.

13. H. Patrick and S.L. Gilbert, "Growth of Bragg gratings produced by continuous-wave ultraviolet-light in optical fiber", *Opt. Lett.*, **18** (18), pp. 1484-1486, 1993.

14. G. Meltz and W.W. Morey, "Bragg grating formation and germanosilicate fiber photosensitivity", *International Workshop on Photoinduced Self-Organisation Effects in Optical Fiber , SPIE Vol. 1546*, pp. 185-199, Quebec, 1991.

15. M. Douay, T. Feng, P. Bernage, P. Niay, E. Delevaque and T. Georges, "Birefringence if optical fiber laser with intracore fiber Bragg grating", *IEEE Photon. Tech. Lett.*, **4** (8), pp. 844-846, 1992.

16. P.J. Lemaire, V. Mizrahi, R.M. Atkins and K.S. Kranz, "High temperature stability of phase gratings in GeO_2 doped optical fibers", *OFC/IOOC'93 Technical Digest*, paper FA7, pp. 242-243, San Jose, 1993.

17. T. Erdogan, V. Mizrahi, P.J. Lemaire and D. Monroe, "Decay of ultraviolet-induced fiber Bragg gratings", *J. Appl. Phys.*, **76** (1), pp. 73-80, 1994.

18. K.O. Hill, *OFC'92 Tutorial Papers*, San Jose, 1992.

19. L. Dong, J.-L. Archambault, L. Reekie, P.St.J. Russell and D.N. Payne, "Bragg gratings written in Ce^{3+}-doped fibres by a single excimer pulse", *OFC/IOOC'93 Technical Digest*, paper FA6, pp. 241-242, San Jose, 1993.

Chapter 5
Single-pulse gratings

5.1. Introduction

The large-scale deployment of fibre gratings in telecommunications and distributed sensing fibre systems would rely on sources of low-cost, mass-produced gratings. The conventional writing of fibre gratings, as described in the previous chapter, does not lend itself easily to mass production: fibre sections must be stripped of their coating, properly aligned, exposed for prolonged periods of time and re-coated. These multiple operations would make it difficult and tedious to produce, for example, a sensor array containing a few hundred gratings. The fabrication process could be greatly simplified and accelerated if the gratings could be written in a fibre drawing tower during the pulling process, immediately before coating the fibre. This would mean, however, writing gratings in a fibre moving at typically a few meters per second, which is impossible with the conventional writing techniques.

In a recent publication, Askins and collaborators of Naval Research Labs demonstrated for the first time that weak but useful fibre Bragg gratings could be written by a single excimer laser pulse at 248 nm [1]. Thus, the total exposure time is reduced to 20 ns, the duration of a pulse. With this new technique, the problem of stability of the UV interference fringe stability is eliminated. More importantly, single-pulse gratings can be written in moving fibres: within the duration of a pulse, a fibre moving at 1 m/s is displaced by only 0.02 μm, which is small compared to a typical grating period (0.5 μm). Long arrays of gratings could be manufactured at a very low cost and, as there would be no need to strip the fibre, the fibre surface would preserve its pristine condition and high strength. In Ref. [1], the highest peak reflectivity obtained from a single pulse was 2%, for a 2 mm grating with an index modulation of about 3×10^{-5}. Although these values may be sufficient for certain sensor systems, higher reflectivities would be required for most applications.

These first results and the availability of both a high-power excimer laser and in-house fibre-drawing facilities prompted us to further investigate the single-pulse writing technique and explore the possibility of obtaining highly reflective gratings in a single excimer pulse. This led to the discovery of a new mechanism of grating formation and to

the first ever demonstration of low and high reflectivity gratings written during fibre drawing.

5.2. Single-pulse grating formation mechanisms

5.2.1. Type I gratings

The first single-pulse gratings were written in the germania-boron fibre HD066 using an interferometer configuration similar to that of Fig. 4-3 [2]. For each grating, a 20 mm fibre section was illuminated by a single pulse with an average fluence of about 0.5 J/cm^2. A typical reflection spectrum is shown in Fig. 5-1. The bandwidth of these single-pulse gratings was invariably smaller than 0.15 nm, the resolution of the optical spectrum analyser used in this experiment. To resolve the grating spectrum of Fig. 5-1, the output of a single-frequency (150 kHz linewidth) laser diode at 1557 nm was launched into the fibre; the grating was then temperature-tuned while the transmission was monitored. By measuring the temperature shift necessary to tune the LD frequency through the grating spectrum (~7°C), the FWHM bandwidth was estimated at 6±1 GHz (0.05 ± 0.01 nm).
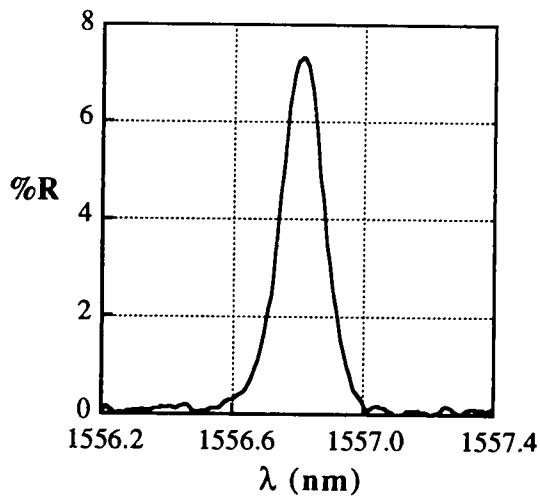

Figure 5-1 - Reflection spectrum of typical narrow band single-pulse grating in fibre HD066.

From the same transmission measurement, it was also found that the peak reflectivity of this grating was around 7%. The highest reflectivity obtained from these narrow-band single-pulse gratings was about 10%. Assuming a uniform illumination of the fibre, the length and index modulation of a grating can be calculated from the bandwidth and

reflectivity measurements. These last results thus indicate a grating length of ~15 mm and maximum index modulation δn of 10^{-5}.

The single-pulse fluence to which a fibre can be exposed is limited by the damage threshold of the fibre surface. The interaction of very high UV intensity with surface defects can easily damage or even destroy the fibre. An example of such surface damage is shown in Fig. 5-2.
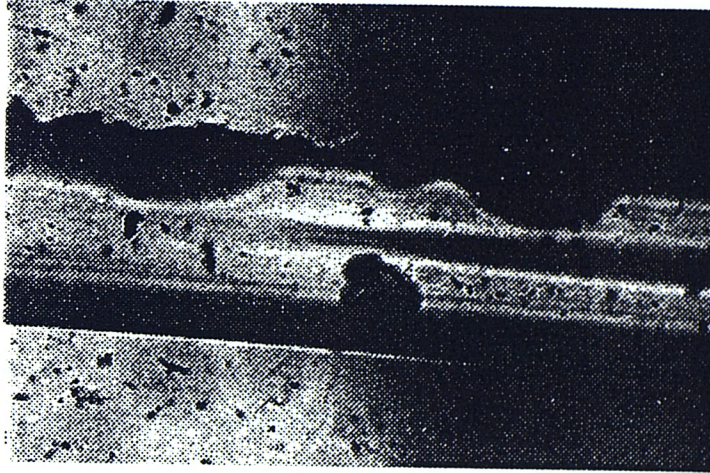

Figure 5-2 - Photograph of surface damage on an optical fibre caused by an intense excimer pulse. The damage is mainly located on the exposed (top) side of the fibre.

To obtain larger fluences in the fibre core without damaging the surface, a different interferometer arrangement had to be used, where instead of the usual two lenses before the beam splitter, a single 40 mm cylindrical lens was placed directly in front of the fibre. The position of the lens was adjusted to focus the two beams as close as possible to the core, therefore minimising the ratio of the UV intensity at the fibre surface to that in the core. In this configuration, the fibre core was exposed to much higher fluences, probably a few J/cm^2/pulse. This resulted in very large index changes (in excess of 10^{-3}) and grating reflectivities of up to 86%.

The reflection spectra of these single-pulse gratings were broad (between 0.3 and 2 nm) and often multi-peaked, indicative of non-uniform gratings. In the transmission spectrum, very strong coupling to the cladding modes is apparent, suggesting that the grating lines are not uniform across the core (Fig. 5-3). Also, a significant background loss could be seen in most gratings. In the example of Fig. 5-3, this loss is about 1.2 dB (25%). Considering the 0.6 nm bandwidth and 85% reflectivity of this grating, the index

modulation should be roughly 6×10^{-4}. A 15 mm long uniform grating with similar index modulation would reflect almost 100% of the incident light at the Bragg wavelength.
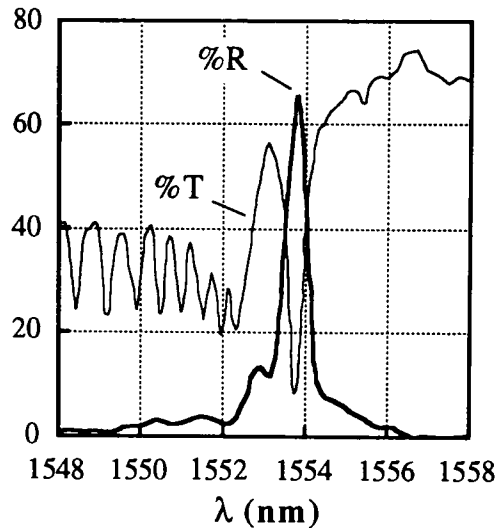

Figure 5-3 - Reflection and transmission spectrum of broad band, high reflectivity single-pulse grating in fibre HD066.

5.2.2. Type II gratings

Experiment

Following these early experiments, a more detailed investigation of the index changing mechanism at high UV fluence was performed using the interferometer configuration of Fig. 4-3 and fibre YD315 [3]. The core of this fibre has a numerical aperture of 0.25 with about 15 mol% germania. The interferometer was again set up to produce gratings with a Bragg wavelength near 1550 nm. The UV beams were partially focused onto the fibre, resulting in a beam cross-section of approximately 15 mm × 0.3 mm.

A series of single-pulse gratings was produced to explore the relationship between pulse fluence and grating strength. For each sample, a short section of fibre was stripped off its coating, a single pulse was fired and the resulting grating was characterised using the LED and spectrum analyser. In total, thirty-six gratings were written over a period of four hours. The 0.3 mm beam width ensured that sample-to-sample variations in positioning the fibre did not significantly affect the amount of UV energy hitting the core. The interferometer was aligned once at the beginning of the experiment and no other adjustments were made afterwards, apart from rotating the half-wave plate to vary the pulse energy which was accurately measured by the pyroelectric energy meter.

Nonlinear index-changing mechanism

The effective index modulation (δn) of each of the thirty-six gratings was estimated from its bandwidth and reflectivity. In Fig. 5-4, this estimated index modulation is plotted against the incident pulse energy. A sharp threshold is immediately apparent at a pulse energy of about 30 mJ: when the pulse energy is increased from 20 to 40 mJ, the photo-induced index modulation goes up by more than two orders of magnitude.
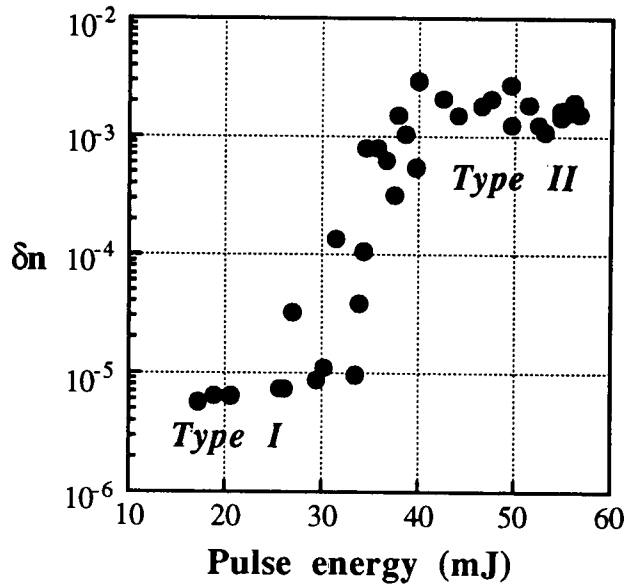

Figure 5-4 - Estimated effective index modulation of single pulse gratings as function of pulse energy.

Below this threshold (from 10 to 25 mJ), the index modulation grows sub-linearly with pulse energy. A power-law fit ($\delta n \sim E^{\beta}$) gives $\beta = 0.76 \pm 0.08$. Above the threshold (40 to 60 mJ), the index modulation appears to saturate. Another striking feature of Fig. 5-4 is that the index changes can be very high, as much as 3×10^{-3}, which is much larger than would be expected in this fibre, even for a multiple-pulse exposure. For convenience, the gratings formed in the high and low index regions have been labeled *Type I* and *Type II* respectively.

Reflection and transmission spectrum

Type II gratings have very high reflectivities, usually close to 100%, and large bandwidths, usually between 1 and 5 nm. The reflection and transmission spectra of typical Type II gratings are shown in Fig. 5-5. In the second graph of Fig. 5-5, the transmission measurement shows at least 26 dB extinction at the Bragg wavelength, which means that only 0.2% of the light is transmitted. The calibrated reflection

spectrum does confirm that this grating is nearly 100% reflecting. The strong irregularities in the spectra are a sign of a highly non-uniform grating, which is not surprising since the irregularities in the excimer beam profile will be strongly magnified by the highly non-linear response mechanism of the core glass.

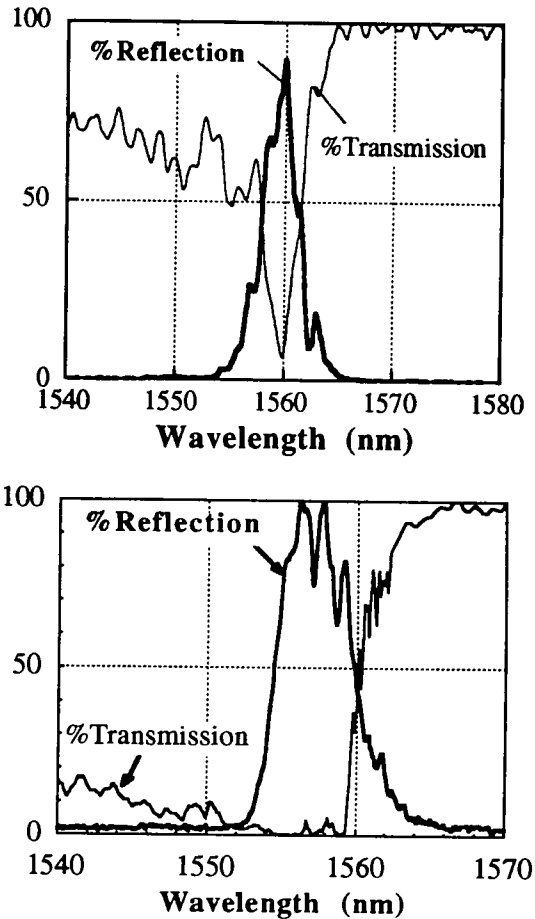**Figure 5-5** - Reflection and transmission spectrum of two Type II single-pulse grating in fibre YD315.

By masking down the excimer beam, it is possible to obtain more uniform Type II gratings. Fig. 5-6 shows an example of a very short, uniform Type II grating which was realised in this way. The reflectivity and bandwidth of the grating indicate an effective index modulation of 1.4×10^{-3} and a length of only 76μm.
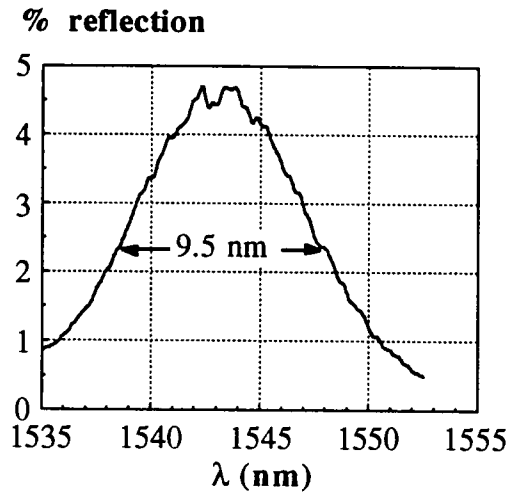
% reflection

Figure 5-6 - Reflection spectrum of ultra-short Type II single-pulse grating in fibre YD315.

Threshold fluence

The data of Fig. 5-4 indicates that, in fibre YD315, the threshold of the onset of Type II gratings occurs for an average pulse fluence of $0.7 J/cm^2$. This represents the fluence averaged over the whole of the UV interference pattern; at a UV fringe maximum, the fluence would be $1.4 J/cm^2$ on average or even higher in the more intense regions of the excimer beam profile. It is difficult therefore to give an accurate estimate of the threshold fluence.

Type II gratings have been obtained in a number of germania-doped fibres, including YD315, HD123, ND383, HD029 and HD066, which are described in Table V. Although no systematic study has been performed, it is clear from experience that the threshold fluence is lower in fibres with a higher germania content, as would be expected. Even in fibres with very high germania concentrations, the threshold fluence is not very far from the surface damage threshold of the fibre. For example, in the experiment of Fig. 5-4, pulse energies in excess of 55 mJ could be sufficient to break the fibre. Therefore, there is a narrow 'window' of pulse fluence through which it is possible to obtain Type II gratings. For fibre YD315, the lower limit of this window corresponds to about 55% of the damage threshold of the fibre. If is is assumed that the threshold fluence is inversely proportional to the germania content of the fibre, then minimum germania content required to write Type II gratings should be about 8 mol%, for which the threshold fluence would be equal to the damage threshold of the fibre. This is consistent with the fact that, to write Type II gratings in fibre HD066 containing an estimated 9% germania, it was necessary to decrease the ratio of the UV fluence at the

surface of the fibre to that at the fibre core to avoid damaging the fibre, as discussed in section 5.2.1.

It was observed that once the Type II mechanism has been initiated by a first excimer pulse, subsequent pulses with fluences much lower than the measured threshold are able to produce very large changes in the grating strength. Therefore, the threshold fluence is lowered by the first high fluence pulse. Dyer *et al.* recently made similar observations when writing gratings with an ArF excimer laser at 193 nm [4].

Short wavelength loss

Another characteristic of Type II gratings is the very strong cladding and radiation mode coupling seen in the short wavelength side of the transmission spectra. This is reminiscent of the spectral properties of fibre gratings made by side-polishing and etching [5]. To visualise this coupling, multi-line light from an argon-ion laser was launched into a fibre containing one of the Type II grating. Most of the light was coupled out of the fibre by the grating in two diffraction orders, each order showing the individual laser lines well-separated in angle. The diffraction of each laser line thus formed two cones of light emanating from the grating region. Each cone in fact contained several elements because the fibre was multimode in the visible. The distribution of light intensity in each cone did not have azimuthal symmetry, with the strongest diffraction being directed away from the exposed side of the fibre. The Bragg angles of the light cones are given by

$$\theta_m(\lambda) = \cos^{-1}(n_{av}(\lambda) - \frac{2m\lambda}{\lambda_B} n_{av}(\lambda_B)) \tag{5-1}$$

where m is the diffraction order and $\theta_m = 0$ corresponds to the direction of propagation of the incident light. For example, for $\lambda_B = 1550$nm and $\lambda = 488$nm, Eq. (5-1) gives $\theta_1 \approx 54°$ and $\theta_2 \approx 109°$; for $\lambda = 514.5$nm, $\theta_1 \approx 57°$ and $\theta_2 \approx 115°$.

The diffraction of visible light by Type II gratings also serves the useful purpose of revealing the exact location of the grating region. By launching a helium-neon laser in several Type II gratings, it became apparent that many of the gratings were in fact segmented, with two or more Type II grating regions a few millimeters long separated by small gaps. The likely explanation for these observations is that only certain regions of the excimer beam profile have a fluence which is above the threshold required for the onset of the Type II mechanism. As a consequence, several short gratings are formed creating multiple Fabry-Perot cavities which strongly distort the reflection and transmission spectra. A particularly illustrative example can be seen in Fig. 5-7. Here, two nearly identical Type II regions were formed, with a gap of 1.2mm.
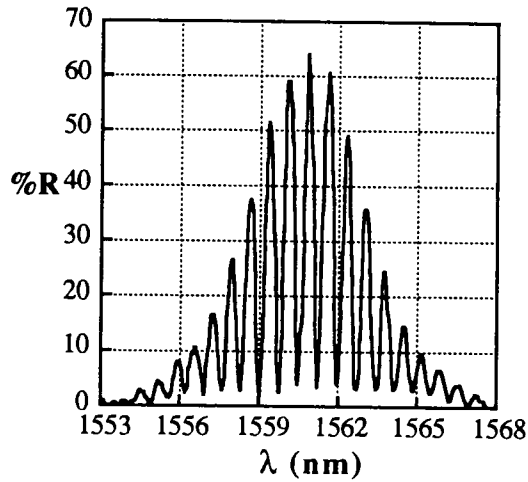
Figure 5-7 - Measured reflection spectrum of Type II single pulse grating which consists of two nearly identical grating regions spaced by 1.2 mm.

Damage region

Examination of several Type II gratings under optical microscope gave some important clues on the nature of these unusual gratings. To eliminate lensing effects from the fibre surface, the gratings were immersed in index-matching oil between two thin glass slides. This revealed the presence of a damage track which appears as a thin, dark region located at the core-cladding interface (see Fig. 5-8). This damage track is only a fraction of the core diameter in width and is segmented over its length. By sending visible light through the grating, it is clear that the light diffracted by the grating originates from these damage regions. The damage is invariably located on the side of the core which was exposed to the UV pulse.
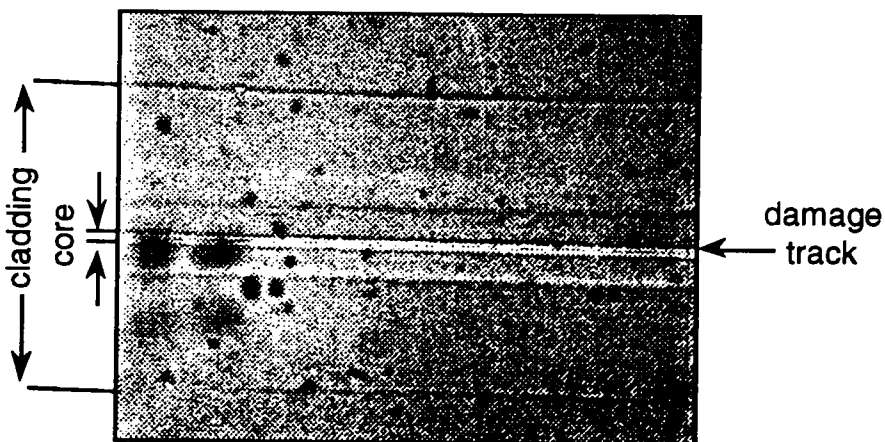

Figure 5-8 - Photograph of damage track in Type II single pulse grating, fibre YD315.

Background loss

In addition to this resonant short wavelength loss, Type II gratings usually have much higher insertion losses than conventional gratings, typically between 0.2 and 2 dB. But in some cases, losses as high as 8dB have been measured. The loss depends on the length of the grating, the extent of the optical damage and the overlap of the core mode with the damage region. The loss can therefore be minimised by using pulse fluences as close as possible to the threshold, keeping the grating length short and using fibres with well-confined mode distributions.

Thermal stability

Several of the Type II gratings were placed in a furnace and tested for thermal stability at temperatures ranging from 700°C to 1000°C for 24 hour periods. The gratings were monitored by launching light from a broad band LED through a 50:50 coupler and measuring the total reflected power in a photodetector. The signal in the detector is proportional to the effective bandwidth of the grating, which, for a strong grating, should be proportional to the index modulation. The results of these tests are summarised in Fig. 5-9. Below 800°C, no significant changes were observed in the grating reflectivities. The apparent increase of reflectivity at 700°C is probably due to a change in the output of the LED, since it was not stabilised in temperature. At 900°C, the grating under test decayed slowly and at 1000°C, most of the grating had disappeared after 4 hours. By contrast, substantial erasure of Type I gratings was observed at only 450°C.
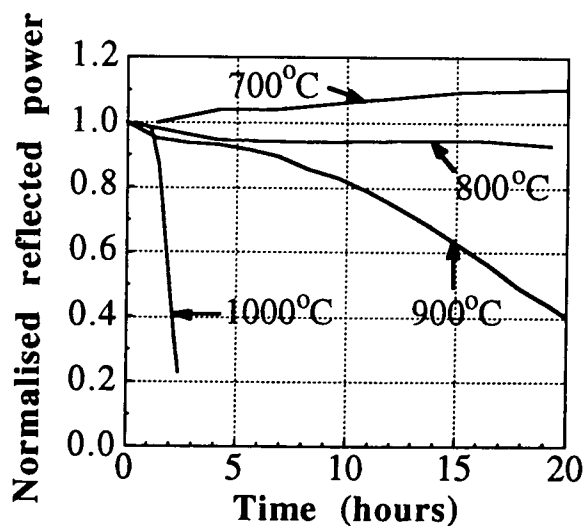
Figure 5-9 - Thermal annealing of Type II gratings in fibre YD315 at various temperatures.

More accurate testing of the thermal stability of Type II gratings was recently performed by M.G. Xu, using a highly stable measurement system to monitor the gratings. The results, shown in Fig. 5-10, are in good agreement with the previous measurements. However, the higher accuracy of this measurement demonstrates more clearly the high stability of Type II gratings at 700°C. Also, a slow decay is now apparent at 800°C with a 2.5% decrease in reflected power after 12 hours.

Figure 5-10 - Thermal annealing of Type II gratings in fibre HD123 (courtesy of M.G. Xu).

Figure 5-11 - Dependence of Type II grating decay rate with temperature. Circles show data from Fig. 5-9 (fibre YD315) and triangles from Fig. 5-10 (HD123). Solid lines are exponential fits.

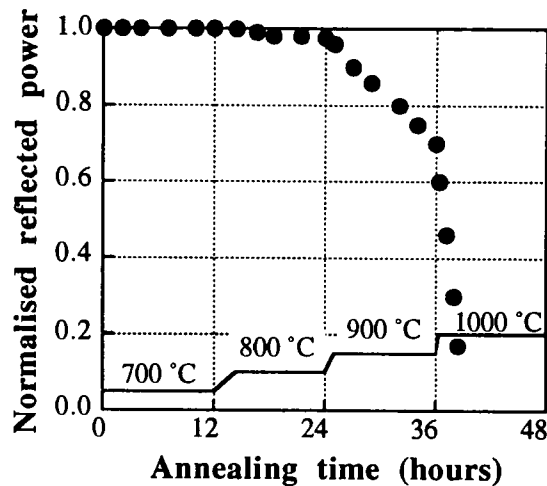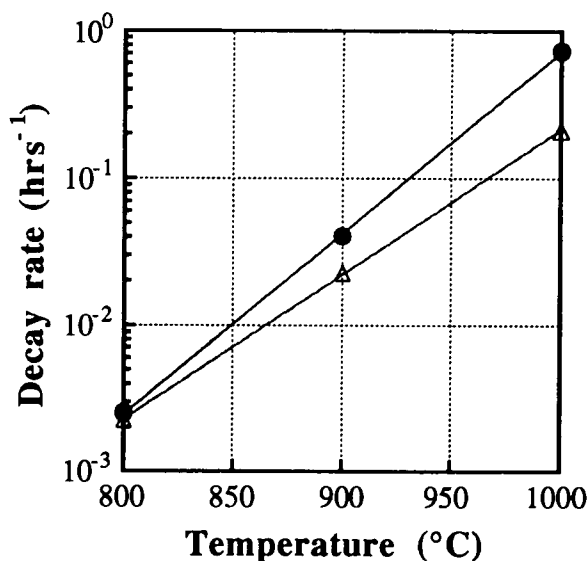The decay of the grating at the different constant temperatures can be fitted very closely by linear functions. The slopes of the decay curves from the two experiments are plotted against temperature in Fig. 5-11. On this semi-logarithmic scale, the data points are in a straight line which indicates an exponential dependence of the decay rate with temperature. If the exponential curve fits are used to predict the decay rates at lower temperatures, it is found that a Type II grating in fibre HD123 would be erased in 6 months at 700°C or in 5 years at 600°C. Similarly, a Type II grating in fibre YD315 would survive 9 months at 700°C and 13 years at 600°C. If we extrapolate to room temperature, the decay times exceed one million years! Although there are only three data points for each fibre, the fact that both sets of data appear as almost perfect straight lines increases the likelihood of these predictions, at least for temperatures close to 800°C.

Micro-Raman spectroscopy

The Raman spectrum of Type II gratings written in fibre HD123 was recently investigated by W.S. Brocklesby and R.S. Brown at the ORC. The 514.5 nm line from an argon laser was launched in to the fibre core and the Raman scattering was collected from the side, without polarisers. The spectrum of the scattered light was measured with an accuracy of about 10 cm^{-1}. Fig. 5-12 compares the measured spectrum of a Type II grating to that of a reference fibre. It is immediately obvious that dramatic changes in the molecular structure of the fibre core have resulted from the UV exposure. The broad peak seen in the unexposed sample at about 450 cm^{-1} is broken into at least eleven identifiable spectral components, shown in greater detail in Fig 5-13.
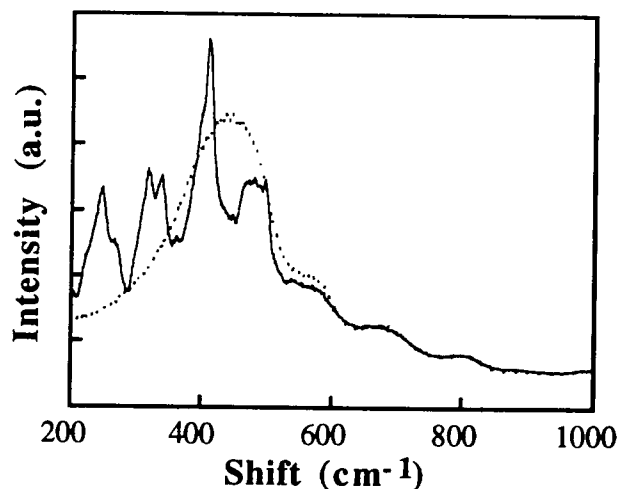

Figure 5-12 - Comparison of Type II grating Raman spectrum (solid line) and spectrum of reference fibre (dashed line) (courtesy of W.S. Brocklesby and R.S. Brown).
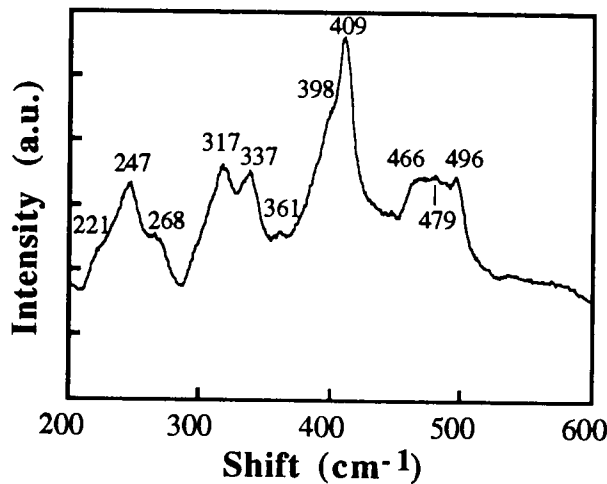
Figure 5-13 - Detail of Type II grating Raman spectrum (courtesy of W.S. Brocklesby and R.S. Brown).

This discretisation of the Raman signature is a strong indicator that the core glass has crystallised. However, the individual peaks of Fig. 5-13 have not yet been attributed to specific crystallites,which could include various crystalline forms of SiO_2 and GeO_2.

5.2.3. Discussion

Type II mechanism

The sharp fluence threshold, visible damage track, very high index change, high thermal stability, strong short wavelength coupling and characteristic Raman signature of Type II gratings are clear evidence that these gratings consist of periodic optical breakdown at the core-cladding interface of an optical fibre. The damage would result from a rapid local heating of the core glass to temperatures beyond the melting point of the glass (~1700°C for silica, ~1400°C for germania). Such high temperatures could only be reached through a nonlinear process which would cause a sharp rise in UV absorption while the pulse is present. The sharp threshold seen in Fig. 5-4 and the observation that the damage is located on the exposed side of the core confirm the existence of a nonlinear absorption process. One likely mechanism could be the interaction of the UV pulse with the plasma of conduction electrons produced by the leading edge of the pulse. As these free electrons are accelerated by the optical field, they collide with the glass matrix, transferring energy to phonons and possibly ionising more electrons, thus triggering an avalanche process. The sudden heating and cooling of the glass results in permanent phase changes, as shown by the Raman spectrum, and possibly in stress fractures caused

by the rapid thermal expansion. The dark appearance of the damage region could either be due to a fracture of the core-cladding interface or to the creation of reduced species, such as GeO. The latter is thought to occur in a similar optical damage process known as the fibre fuse [6,7].

The net result of the damage process is the creation of periodic scattering points and possibly of periodic stress along one side of the core. This explains the high background loss and the similarity between the optical properties of Type II gratings and those of relief fibre gratings [5,8].

It is highly unlikely that this breakdown of the core glass could be reversed by thermal annealing. A more plausible explanation of the erasure of Type II gratings between 800 and 1000°C is that the softening of the glass at these high temperatures allows the stresses built into the damage region to be relieved, which washes out the grating. The thermal decay rate would then depend on the viscosity of the glass at different temperatures. Under this hypothesis, Type II gratings written in fibres with smaller germania concentrations should be more resistant to temperature, since these fibres would have higher softening temperatures.

Limits and applications of Type I gratings

At present, the maximum grating index modulation that can be obtained in a single pulse without triggering the mechanism for Type II gratings is about 2×10^{-5}. To obtain a Type I grating with 90% reflectivity at 1550 nm, one would therefore require a uniform, 5 cm long grating. This grating would have a bandwidth of about 0.03 nm. It is thus possible to produce high reflectivity but narrow band Type I single-pulse gratings which could find applications in fibre lasers, narrow-band filtering and dense wavelength-division multiplexing. To obtain broadband high reflectivity Type I single-pulse gratings, one would require a fibre with much higher photosensitivity. In hydrogen-loaded fibres, preliminary tests have shown that index modulations of at least 4×10^{-5} can be obtained in a single pulse and reflectivities in excess of 40% have been demonstrated. But another factor of ten increase in photosensitivity would be required before high-reflectivity single pulse Type I gratings with bandwidths approaching 1 nm can be manufactured.

Limits and applications of Type II gratings

Broad band, high reflectivity single-pulse gratings are readily available with the Type II writing mechanism. But the very large index changes characteristic of Type II gratings make it impossible to produce narrow band gratings using this method. Broadband

reflectors can be used in fibre lasers and in sensors based on OTDR techniques [9]. But the high short wavelength loss would proscribe the use of strong Type II gratings in multiplexed systems. The robustness of Type II gratings would make them ideal for sensing in hostile environments.

Another important application of Type II gratings could be their use as reflectors for blue/green light, for example in upconversion fibre lasers [10]. Exposure of Type II gratings to several hundred milliwatts of light from an Argon laser for prolonged periods has been shown not to degrade their performance. Although comparative data is not available at the moment, it is expected that exposure of conventional fibre gratings to intense blue or green light would cause their gradual erasure through two-photon absorption. The robust nature of Type II gratings should prevent this from occurring.

The Type II mechanism was employed to write fibre gratings point-by-point [11] and with the use of a phase mask [12]. In the latter, the individual grating lines were visualised in a microscope. Type II grating formation was also recently obtained in germania-silica planar waveguides [13].

The key to improving the optical properties of Type II gratings would be to somehow reduce the interaction between the fibre mode and the grating. This would bring the possibility of writing narrow band and low loss Type II gratings. A proposed method of achieving this would be to surround the core of a fibre with a thin germania-doped ring, so that the optical damage would be remote from the core. The core itself could be doped with alumina instead of germania so that it would have negligible absorption at 248 nm. This method is currently under investigation.

5.3. <u>Grating made during the draw</u>

Following these investigations on the single-pulse writing technique, the next logical step was to examine the feasibility of producing both Type I and Type II gratings in a fibre drawing tower. This experiment was designed and performed jointly by L. Dong, L. Reekie and the author [14]. It led to the first ever demonstration of fibre gratings made during the draw.

5.3.1. Experiment

The main difficulty of this experiment was to deliver the excimer laser beam to the drawing tower, as the laser was situated some 20m away from the tower, in a separate laboratory. An underground beam delivery system comprising eight mirrors had to be designed to overcome this problem (Fig. 5-14). The back surfaces of the mirrors were coated with aluminum so that a helium-neon laser could be used for the initial alignment. The final adjustments were made with the excimer beam itself. Even after 20m, the diffraction of the excimer beam proved to be unimportant.
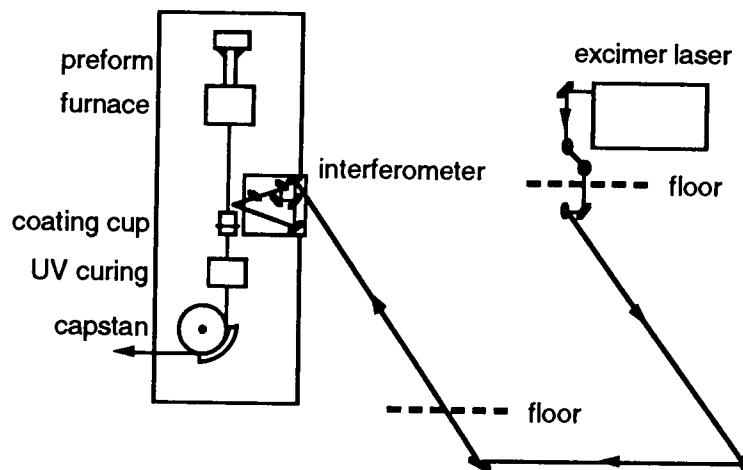
Figure 5-14 - Layout of experiment for writing gratings in the fibre drawing tower.

A compact version of the interferometer of Fig. 4-3 using 25 mm optics was built on a small breadboard which could easily be mounted on the drawing tower. The interferometer was first aligned in the excimer lab to produce gratings near 1550 nm. It was then positioned in the tower, so that the gratings would be written just above the fibre coating cup, the coating fluid serving to damp out the vibrations in the fibre. The

UV beams were focused to a 7 × 0.5 mm spot in the plane of the fibre, using a single cylindrical lens with a 30 cm focal length.

The remaining preform of fibre HD123 was used in this first demonstration. The core of this fibre contains an estimated 28% germania. The fibre drawing capstan was modified so that the free end of the fibre could be spliced to the diagnostics (1550 nm LED, fibre coupler and optical spectrum analyser). This allowed the grating production to be monitored on line. Alternatively, one could use the blackbody radiation emitted by the fibre preform to monitor the gratings in transmission. This produced a spectral density of about 0.1 nW/nm at 1550 nm in the fibre core, compared to ~10 nW/nm for the LED. The fibre was drawn at speeds ranging from 3 to 23 m/min which gives an axial displacement of only 1 to 8 nm within the duration of a pulse (20 ns).

5.3.2. Results and discussion

By adjusting the energy of the incident pulses, both Type I and Type II single-pulse gratings could be obtained in this fibre. Fig. 5-15 shows the reflection spectrum from three consecutive Type I gratings, written with a pulse fluence of about 0.3 J/cm^2. Ideally, this graph should show a single reflection peak; however, the Bragg wavelengths of the gratings written in the draw vary typically by 0.2-0.3 nm, probably because of fluctuations in the fibre tension and temperature.
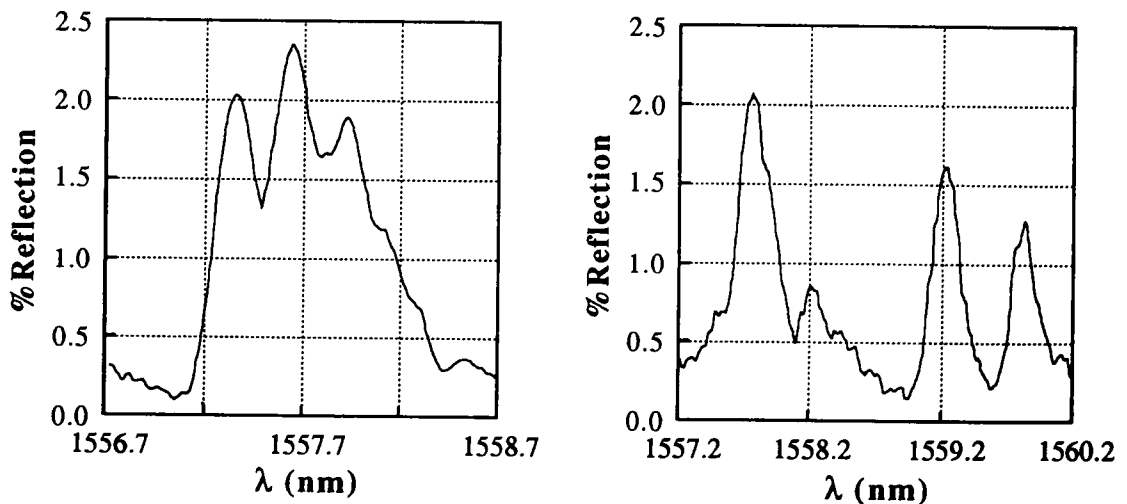

Figure 5-15 - Left: reflection spectrum from three successive Type I gratings written during fibre drawing (left). Right: Same spectrum with different strain applied to each grating.

It was possible to separate the spectra of the individual gratings off-line by straining each of them by a different amount; this is shown in the right hand side of Fig. 5-15. The difference in grating reflectivities could be due to pulse-to-pulse energy fluctuations or slight lateral displacements of the fibre. This differential straining technique could in fact be done on-line to examine individual gratings by running the fibre through an appropriate tensioning system.

By increasing the pulse fluence to ~1.2 J/cm^2, it was possible to repeatedly write Type II gratings in the fibre. The transmission spectrum of a typical grating is shown in Fig. 5-16. All gratings produced in this regime had reflectivities approaching 100%. In the particular example of Fig. 5-16, the transmission at the Bragg wavelength is less than 0.2% and the reflection bandwidth is about 2 nm. The background loss of the grating at 1600 nm was found to be 0.5 dB by performing a cutback measurement.
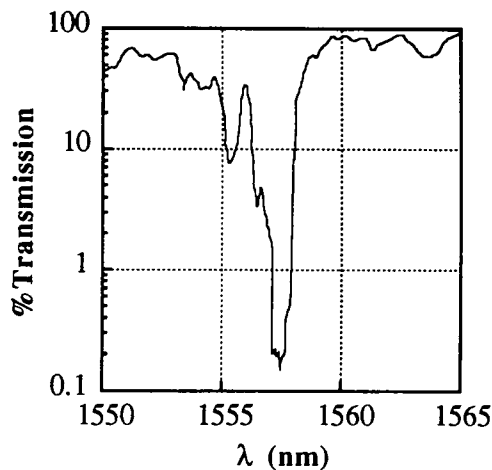
Figure 5-16 - Transmission spectrum of Type II grating written during fibre drawing.

The implementation of on-line grating production proved to be relatively straightforward and is certainly the most practical approach for mass-producing fibre gratings. The fabrication facilities described in this section would allow the production of thousands of Type I and Type II fibre gratings per day. The repeatability of the writing technique has proved to be reasonably good, but could probably be improved upon. This would first involve having a better control of the fibre tension to reduce the scatter of the Bragg wavelengths. A factor of 2 improvement in the accuracy of the tensioning system would be required to reduce the standard deviation of the Bragg wavelength to ~0.1 nm, which should be sufficient for most applications, since it is comparable to the grating bandwidth. To minimise the variations in grating reflectivity, a larger and more uniform

beam should be used, so that small lateral displacements of the fibre do not affect the exposure of each grating. However, pulse-to-pulse energy fluctuations would still cause exposure variations.

A more significant improvement would be to build a tunable interferometer controlled by a computer, so that each grating could have a different Bragg wavelength. This was recently demonstrated by Askins and collaborators at NRL [15].

5.4. Conclusion

Two distinct regimes of single-pulse grating formation have been identified. Below a sharp threshold fluence, which depends on the germania content of the fibre, Type I single-pulse gratings are obtained by the usual photorefractive effect. This mechanism can result in single-pulse index modulations of up to 2×10^{-5} in untreated germania and germania boron fibres. Long, narrow-band Type I gratings with up to 10% reflectivity and bandwidths as small as 6 GHz have been demonstrated. In hydrogen-loaded fibres, Type I single-pulse gratings with 4×10^{-5} index modulation and 40% reflectivity were obtained.

Above the threshold fluence, much stronger (Type II) gratings are observed, with close to 100% reflectivity. Type II gratings have several distinguishing features:
- very high index modulation, usually in excess of 10^{-3};
- strong cladding and radiation mode coupling;
- high thermal stability;
- insensitivity to blue/green light;
- high loss.

Type II gratings are believed to result from periodic optical breakdown at the core cladding interface of an optical fibre. A damage track can be directly observed on the exposed side of the core. This damage is thought to be caused by the interaction of the UV pulse with electrons in the conduction band resulting in rapid heating beyond the glass melting point. Micro-Raman studies have revealed that the glass may be crystallising as a result of this treatment. The robustness of Type II gratings make them ideal for applications in hostile environments or for use in blue/green lasers.

The implementation of on-line grating production proved to be relatively straightforward and is certainly the most practical approach for mass-producing fibre gratings. The

fabrication facilities described in this section would allow the production thousands of Type I and Type II fibre gratings per day at a very low cost. This technique would be especially attractive for distributed sensing applications. Type I gratings would be ideal for multiplexed systems, while Type II gratings could be used in OTDR-based sensors.

5.5. **References**

1. C.G. Askins, T.-E. Tsai, G.M. Williams, M.A. Puttnam, M. Bash-Kansky and E.J. Friebele, "Fibre Bragg reflectors prepared by a single excimer pulse", *Opt. Lett.*, **17** (11), pp. 833-835, 1992.

2. J.-L. Archambault, L. Reekie and P.St.J. Russell, "High reflectivity and narrow bandwidth fibre gratings written by single excimer pulse", *Electron. Lett.*, **29** (I), pp. 28-29, 1992.

3. J.-L. Archambault, L. Reekie and P.St.J. Russell, "100% reflectivity Bragg reflectors produced in optical fibres by single excimer laser pulses", *Electron. Lett.*, **29** (5), pp. 453-455, 1993.

4. P.E. Dyer, R.J. Farley, R. Giedl, K.C. Byron and D. Reid, "High reflectivity fiber gratings produced by incubated damage using a 193 nm ArF laser", *Electron. Lett.*, **30** (11), pp. 860-862, 1994.

5. I. Bennion, D.C.J. Reid, C.J. Rowe and W.J. Stewart, "High reflectivity monomode fibre grating filters", *Electron. Lett.*, **22** (6), pp. 341-343, 1986.

6. R. Kashyap and K. Blow, "Observation of catastrophic self-propelled self focusing in optical fibres", *Electron. Lett.*, **24** (1), pp. 47-49, 1988.

7. D.P. Hand and P.S. Russell, "Solitary thermal shock waves and optical damage in optical fibres: origin of periodic damage tracks", *Opt. Lett.*, **13** (9), pp. 767-769, 1988.

8. P.St.J. Russell and R. Ulrich, "Grating-fibre coupler as a high-resolution spectrometer", *Opt. Lett.*, **10** (6), pp. 291-293, 1985.

9. M.G. Xu, H. Geiger and J.P. Dakin, "Multiplexed point and stepwise-continuous fiber grating-based sensors: practical sensors for monitoring?", *SPIE Annual Meeting*, *SPIE Vol. 2294*, paper 2294-10, San Diego, Ca., 1994.

10. P.R. Barber, C.J. Mackechnie, R.D.T. Lauder, H.M. Pask, A.C. Tropper, D.C. Hanna, S.D. Butterworth, M.J. McCarthy, J.-L. Archambault and L. Reekie, "All solid-state blue room-temperature thulium-doped upconversion fibre laser", *Compact Blue-Green Lasers Topical Meeting Proceedings*, paper CFA3-1, pp. 68-70, Salt-Lake City, Utah, 1994.

11. B. Malo, K.O. Hill, F. Bilodeau, D.C. Johnson and J. Albert, "Point-by-point fabrication of micro-Bragg gratings in photosensitive fiber using single excimer pulse refractive-index modification techniques", *Electron. Lett.*, **29** (18), pp. 1668-1669, 1993.

12. B. Malo, D.C. Johnson, F. Bilodeau, J. Albert and K.O. Hill, "Single-excimer-pulse writing of fiber gratings by use of a zero-order nulled phase mask grating - spectral response and visualization of index perturbations", *Opt. Lett.*, **18** (15), pp. 1277-1279, 1993.

13. R.J. Campbell and R. Kashyap, "The properties and applications of photosensitive germanoslicate fibre", *Int. J. Optoelectron.*, **9** (1), pp. 33-57, 1994.

14. L. Dong, J.L. Archambault, L. Reekie, P.S. Russell and D.N. Payne, "Single-pulse Bragg gratings written during fiber drawing", *Electron. Lett.*, **29** (17), pp. 1577-1578, 1993.

15. C.G. Askins, M.A. Putnam, G.M. Williams and E.J. Friebele, "Stepped-wavelength optical-fiber Bragg grating arrays fabricated in line on a draw tower", *Opt. Lett.*, **19** (2), pp. 147-149, 1994.

Chapter 6

Interaction of KrF excimer laser pulses with germanosilicate fibres

6.1. Introduction

Most studies of fibre photosensitivity have so far looked at the various permanent changes induced by UV light in germanosilicate (GeSi) fibres. However, the interaction of UV light with GeSi fibres results in a series of transient phenomena which occur on timescales ranging from nanoseconds to milliseconds. These transient phenomena, although not of practical use, can provide valuable information on the underlying mechanisms of fibre photosensitivity. Most of the slower transient phenomena, which include blue photoluminescence [1,2], short wavelength absorption [3] or partial reversal of the induced index change [4], have already been investigated. However, many of the dynamic changes in GeSi fibres, such as the luminescence at 290 nm and the non-radiative transitions, occur on much shorter, sub-microsecond timescales.

To gain a better understanding of the dynamics of these fast phenomena, a pump-probe experiment was designed, where the transmission of a GeSi fibre is monitored at various wavelengths with a fast detection system in the presence of a 20 ns excimer pulse at 248.5 nm. The results of this experiment are summarised here and interpreted via the proposed energy level diagram of oxygen-deficient centres.

6.2. Experiment

Fig. 6-1 describes the experimental setup. A single beam from the KrF excimer laser was partially focused onto the side an uncoated section of GeSi fibre. With each 20 ns pulse, an 18 mm fibre section was exposed to a fluence of ~0.5 J/cm^2 at 248.5 nm. At the same time, light from a CW laser (Nd:YAG or Ti:Sapphire) was launched into the fibre core with typically 50 mW reaching a fast (400 MHz) detector at the output end. The signal from the detector was sent to a 350 MHz analogue oscilloscope. Each trace was captured by a digitising camera attached to the oscilloscope screen and downloaded to a computer. The oscilloscope was triggered via a delay generator by the excimer laser synchronisation output. This setup thus enabled us to measure changes in the fibre

transmission due to a single excimer pulse on a nanosecond timescale. Several GeSi fibres were used in this experiment with numerical apertures ranging from 0.12 to 0.35, all of which were fabricated in the ORC.
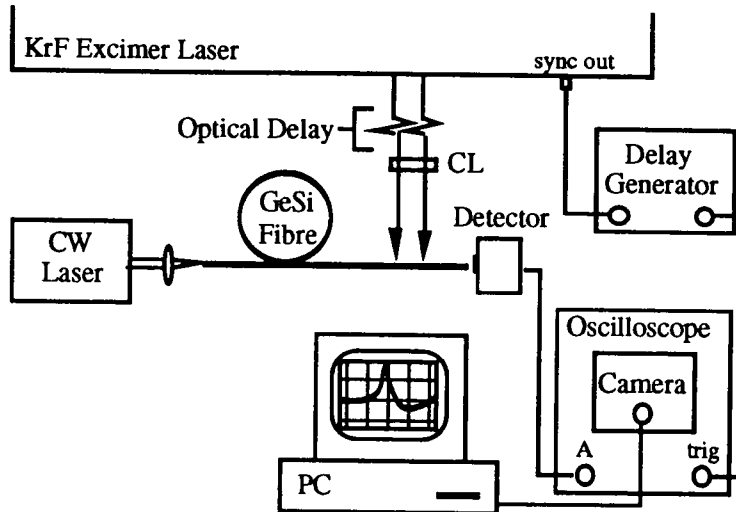

Figure 6-1 - Layout of pump-probe experiment.

6.3. Results

6.3.1. Initial observations

In the first set of measurements, a diode-pumped Nd:YAG laser was used to probe a 0.35 N.A. fibre with 1.05 μm cutoff wavelength. A typical 100 ns transmission measurement is shown in Fig. 6-2. Rather than the 1.06 μm transmission being reduced as was expected, the excimer pump beam actually produced a gain of almost 15 dB, or 7 dB/cm. This gain appears for a fraction of the excimer pulse duration, about 10 ns, and is followed by substantial loss, a signification fraction of which remains long after the pulse. The gain was observed to be very repeatable from pulse to pulse and did not seem to fade even after over 20,000 UV pulses had been fired, corresponding to an integrated exposure of more than 10 kJ/cm^2. On the other hand, the induced loss appeared to be very irregular, showing large variations from pulse to pulse and therefore was difficult to characterise. The dependence of the 1.06 μm gain with excimer pulse energy is shown in the right hand side of Fig. 6-2. The data points were obtained by dividing the peak gain observed in each single-pulse trace by the exposed length of fibre and by the fraction of power of the fibre mode inside the core. As the pulse energy is increased, it is clear that the gain tends to saturate, reaching a maximum value of ~10 dB/cm.
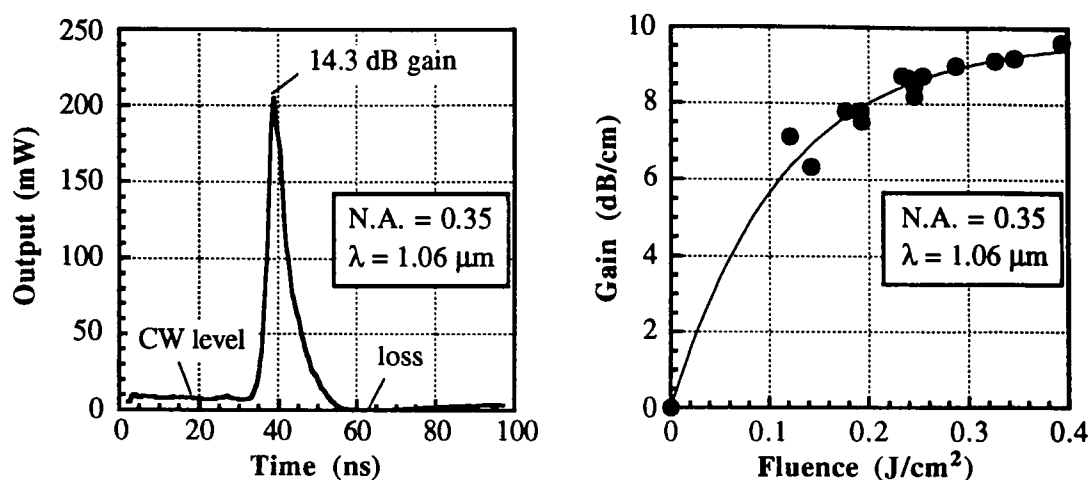
Figure 6-2 - *Left*: typical single-pulse trace for 1.06 µm probe in 0.35 N.A. fibre. *Right*: saturation of peak gain with increasing pulse fluence; solid line is exponential fit.

6.3.2. Gain spectrum

To characterise the wavelength-dependence of this gain, the experiment was repeated using a probe beam from a Ti:Sapphire laser, tunable from 0.75 to 1.1 µm. This time, a fibre with slightly lower N.A. (0.33) and lower cutoff (0.74 µm) was tested. The Ti:Sapphire wavelength was tuned in 10 nm increments; at each wavelength, a single excimer pulse was fired and the detector output recorded. Over most of the tuning range, single-pulse traces similar to that of Fig. 6-2, featuring gain and loss, were recorded. At short wavelengths (0.75 to 0.82 µm), however, only loss was observed. The wavelength-dependence of the peak gain is shown in Fig. 6-3. As can be seen, the gain band is very broad, with a peak value of about 7 dB/cm at 1.0 µm and dropping to half this value near 0.9 µm. The peak of the transient loss increased rapidly as the probe wavelength decreased. A peak loss of ~50 dB/cm at 0.75 µm and 10 dB/cm at 0.82 µm was measured by exposing only a 2 mm section of the fibre.

A section of this 0.33 N.A. fibre was given a prolonged UV exposure at 20 pulses/sec. with a probe beam at 1.06 µm. A 100 ns trace was recorded every 1 to 2 minutes to monitor the evolution of the gain and loss (right side of Fig. 6-3). Again, the gain remained almost constant throughout the exposure, while the loss was very irregular.
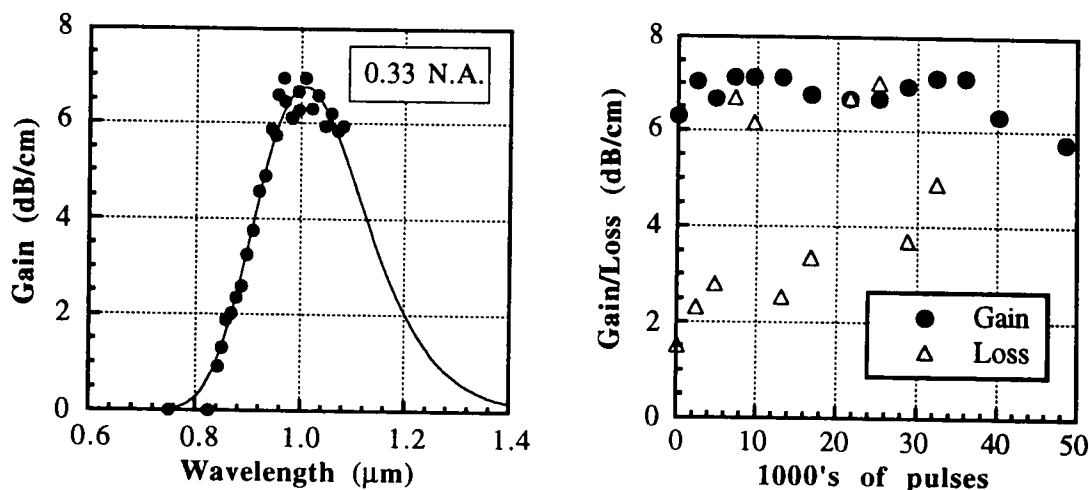
Figure 6-3 - *Left*: gain spectrum of 0.33 N.A. fibre measured with tunable Ti-Sapphire laser; solid line shows best gaussian fit with $E_0=1.23$ eV (1.01 nm) and $\Delta E=0.32$ eV (see Eq. (6-2)). *Right*: evolution of peak gain and loss at 1.06 μm during prolonged exposure of 0.33 N.A. fibre.

6.3.3. Influence of germania concentration

Similar exposures were given to GeSi fibres with N.A.'s of 0.12, 0.21 and 0.28 and cutoff wavelengths respectively of 0.75, 0.64 and 1.0 μm. In the case of the 0.12 N.A. fibre, no measurable gain was observed, as seen in Fig. 6-4 (left). In the initial stages of the exposure, the induced loss peaked about 20 ns after the arrival of the pulse and then decayed gradually. As the exposure increased, this peak shifted to longer times.

Figure 6-4 - Single-pulse traces recorded at different stages during prolonged exposure of 0.12 N.A (left) and 0.28 N.A. (right) fibres ($\lambda = 1.06$ μm).

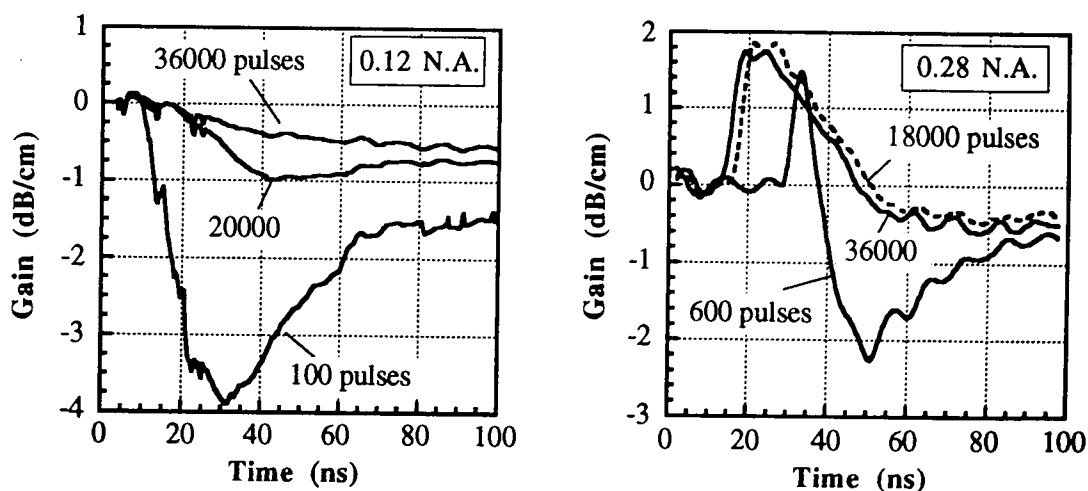With the 0.21 N.A. fibre, no gain could be observed in the first 2000 pulses (Fig. 6-5, left). However, when the fibre was further exposed, a gain peak appeared and gradually levelled at around 0.2 dB/cm. At the same pump intensity level, the 0.28 N.A. fibre exhibited around 2 dB/cm peak gain throughout the exposure. The duration of the gain peak broadened from about 5 ns to 20 ns as the magnitude of the transient loss gradually diminished. In neither of these last two cases did the gain appear to diminish during the long exposure.
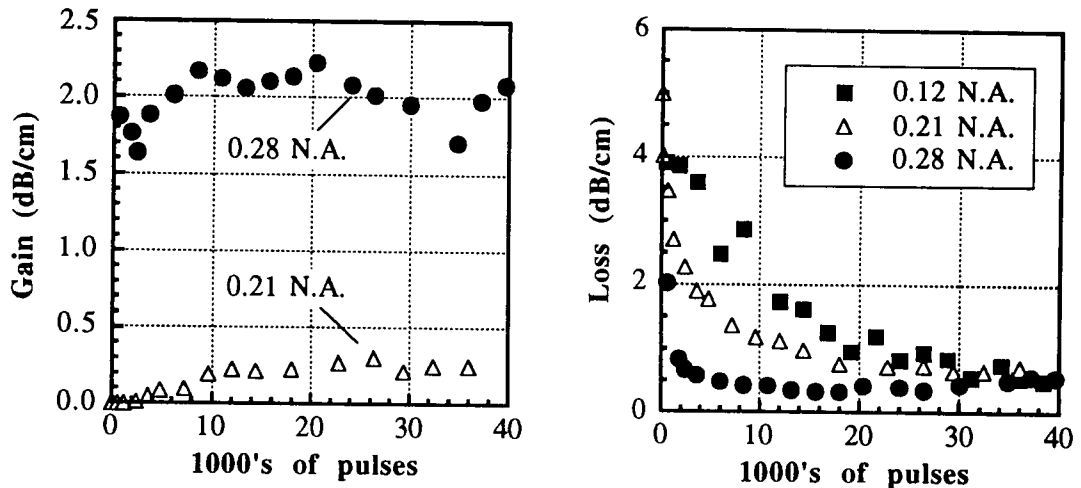

Figure 6-5 - Evolution of peak gain (left) and loss (right) at 1.06 μm during long exposure of 0.12, 0.21 and 0.28 N.A. fibres. No gain could be observed in 0.12 N.A. fibre.

For these three lower N.A. fibres, the transient loss measurements were much more repeatable than in the case of the 0.33 and 0.35 N.A. fibres. The peak of the transient loss induced by a single excimer pulse as function of the UV exposure is shown in Fig. 6-5 for the three fibres. In all three cases, this loss was gradually bleached, down to what appeared to be a steady-state value of about 0.5 dB/cm. This decay rate was faster in the higher N.A. fibres.

6.3.4. Short wavelength loss

Examples of single-pulse traces with the 0.33 N.A. fibre and a 0.824 μm probe are shown in Fig. 6-6. The peak loss observed on a short time scale is very high, in excess of 8 dB/cm, and was even higher at shorter wavelengths. On the 5 μs trace, the transient absorption seems to decay to a steady-state value of about 0.7 dB/cm. The 1/e decay time is about 40 ns, as measured on a 1 μs scale. Examination of the 100 μs trace (right of Fig. 6-6) reveals a very slow decay component. The noise on this curve is due to fluctuations in the output of the Ti:Sapphire laser.

Fig. 6-6) reveals a very slow decay component. The noise on this curve is due to fluctuations in the output of the Ti:Sapphire laser.
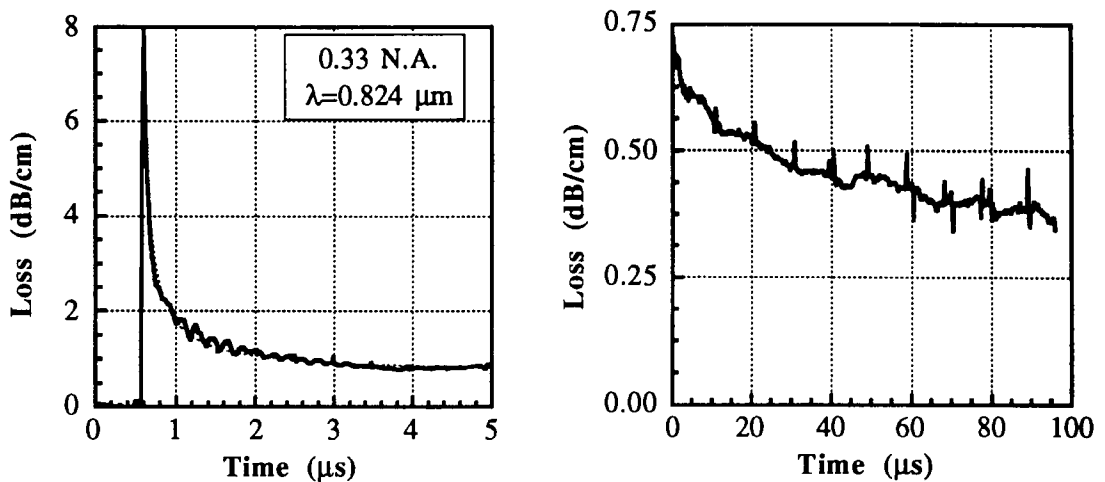

Figure 6-6 - Transient absorption at 0.824 μm in 0.33 N.A. fibre over 5 μs (left) and 100 μs (right) timescales. Left graph includes curve fit (dotted line) from Eq. (6-3).

6.3.5. DFB fibre laser

In a separate experiment, this newly found gain produced the world's first DFB fibre laser. A section of the 0.35 N.A. fibre, which had been hydrogen-loaded, was placed inside the UV interferometer of Fig. 4-3 tuned to a Bragg wavelength of 1.33 μm. The fibre was then exposed to 20 pulses/s and the growth of the grating was monitored in reflection in an optical spectrum analyser using a 1.31 μm LED as a light source. With a strong grating present, lasing was observed over a ~3 nm region centred at ~1.5 nm above the grating Bragg wavelength (Fig. 6-7, left). This graph is in fact a superposition of successive traces to reconstruct a quasi-continuous spectrum from the pulsed output. This lasing is believed to be caused by the combination of the UV-induced gain (which is probably barely sufficient at 1.33 μm, as seen in Fig. 6-3), and the feedback provided by the grating. The broad emission band seen in Fig. 6-7 was probably caused by a transient shift in the grating Bragg wavelength while the excimer pulse was present. A time resolved measurement of this DFB fibre laser is also shown in Fig. 6-7 (right). As expected, the fibre laser emits pulses that are a fraction of the UV pulse duration in length. The pulses had a peak power of about 1 W.
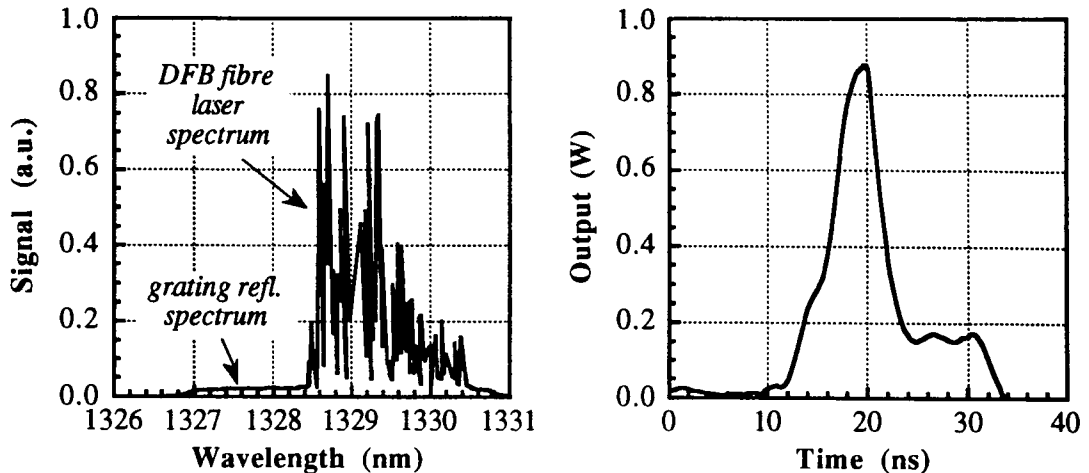
Figure 6-7 - Emission spectrum (left) and time-resolved output power (right) of H_2-loaded 0.35 N.A. germanosilicate fibre exposed to two interfering excimer beams.

6.4. Discussion

Most of the experimental results described in this chapter can be explained by referring to the proposed energy-level diagram of germania-related oxygen-deficient centres described in section 3.2 and reproduced in Fig. 6-8. In this diagram, the average energy gap of 0.3 eV between energy level S_1 and the conduction band was taken from section 4.3.4 and should only be taken as an indicative value, since it corresponds to a fibre co-doped with boron. The average depth of the trapping centres comes from Ref. [5] and was obtained from measurements in an erbium-doped GeSi fibre. The first effect of the illumination of the fibre core to a 20 ns excimer laser pulse is to populate the upper singlet level S_1. From this excited state, the electrons have several possible routes: 1) decay to the ground state by spontaneous emission, 2) to the triplet state T_1 by multiple phonon emission or 3) be thermally excited to the conduction band. A fourth but less probable alternative is for excited electrons to decay radiatively to T_1. It is this transition that is believed to account for the gain peak observed immediately after the arrival of the pulse. As will be shown in the following, the dynamics, magnitude and spectrum of the transient gain are well explained by this model.
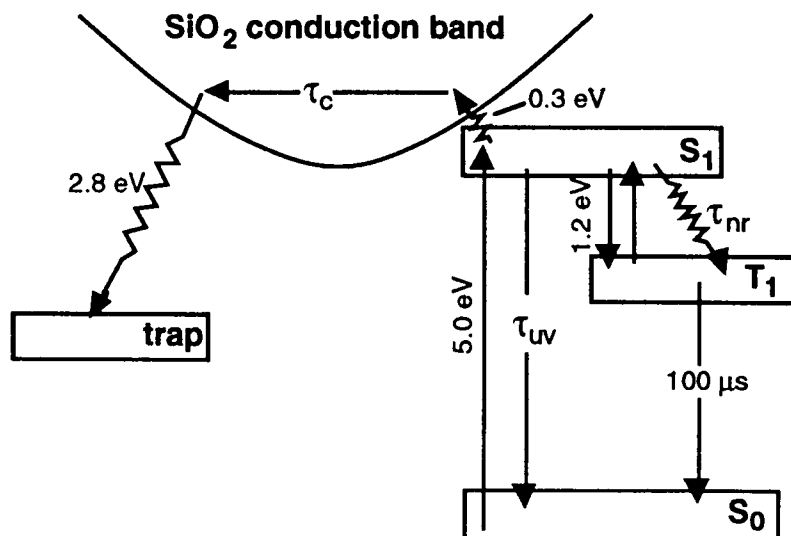
Figure 6-8 - Possible electronic transitions resulting from absorption of 248.5 nm (5.0 eV) photon in germania-related oxygen-deficient centre, where τ_c, τ_{uv} and τ_{nr} are unknown lifetimes.

A singlet-to-triplet transition violates the selection rule that the quantum spin number must be conserved and has a very low, but finite, probability [6]. In fact, we know from the UV absorption spectra of germanosilicate preforms that the singlet-to-singlet absorption at 242 nm (5.1 eV) is almost exactly 1000 times stronger than the singlet-to-triplet absorption at 325 nm (3.8 eV) [6]. We would therefore expect the probability of stimulated emission taking place between T_1 and S_1 to be three orders of magnitude smaller than the probability of stimulated emission (or absorption) between the two singlet states. For a complete inversion of population the gain from the $S_1 \rightarrow T_1$ transition would be roughly 1000 times smaller than the absorption at 242 nm before the arrival of the pulse. The 242 nm absorption in a germanosilicate fibre is approximately given by the empirical relation [7]

$$\alpha_{242} \approx 300 \text{ dB/cm} \times [\text{Ge}](\text{mol}\%) \qquad (6\text{-}1)$$

which would predict a maximum gain of about 0.3 dB/cm/mol%Ge. The data of Fig. 6-2 clearly shows that, for the pulse fluence used in the gain measurements (~0.5 J/cm^2), the gain has nearly saturated. It is therefore reasonable to assume that the excimer pulse creates a nearly complete inversion of population between S_0 and S_1 and that the gain should be close to its maximum predicted value of 0.3 dB/cm/mol%Ge. This rough estimate is not too far from the measured values of the peak gain, at least for the high N.A. fibres. The low probability of the gain transition is confirmed by the performance of the DFB fibre laser (Fig. 6-7) which has an efficiency of less than 0.1% relative to the estimated absorbed pump power (~10 kW). Fig. 6-9 is a plot of the peak gain at 1.06 μm as function of the estimated germania concentration of the five fibres tested so far.

Assuming that the concentration of oxygen-deficient defects depends linearly on the germania concentration, this graph would be expected to show a straight line crossing the origin. The data of Fig. 6-9 deviates strongly from this expected behavior and appears to show a nonlinear dependence of the gain on the germania concentration, although more measurements would be required to confirm this trend.
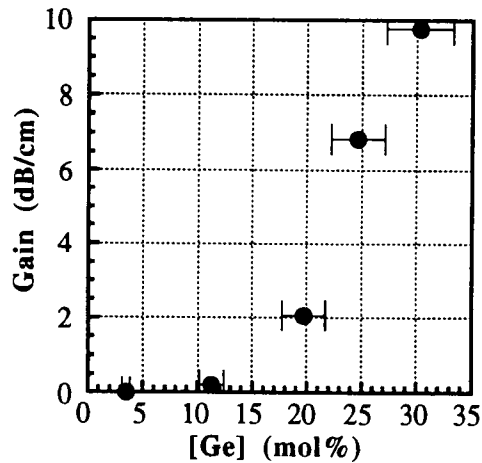

Figure 6-9 - Comparison of peak gain observed at 1.06 μm in the five GeSi fibres under test.

The energy separation between the S_1 and T_1 levels is approximately 1.3 eV as given by the energy difference of the two absorption bands at 242 nm and 325 nm or the two fluorescence bands at 290 nm and 410 nm. The absorption and fluorescence bands at 242, 325, 290 nm and 410 nm are all gaussian and have similar FWHM widths of about 0.35 eV [6,8,9]. The gain spectrum of the $S_1 \rightarrow T_1$ transition should therefore be well described by the relation

$$\gamma(\lambda) \approx \gamma_0 \exp(-4 \ln 2 \frac{(hc/\lambda - E_0)^2}{(\Delta E)^2}) \qquad (6\text{-}2)$$

where $\gamma_0 \approx 7.5$ dB/cm (from Eq. 6-1) is the peak gain, $E_0 \approx 1.3$ eV is the energy of the transition and $\Delta E \approx 0.35$ eV is the FWHM width. In Fig. 6-3, the best fit to the experimental data was obtained for $\gamma_0 = 6.7$ dB/cm, $E_0 = 1.23$ eV (1.01 nm) and $\Delta E = 0.32$ eV. It can be seen that all three fitting parameters are very close to their expected values.

In addition to the gain at 1.0 μm, the model of Fig. 6-8 also predicts that there should be significant transient absorption caused by 1) free electrons in the conduction band and 2) the accumulation of electrons on metastable level T_1. The latter would of course have the same spectral characteristics as the transient gain. The duration of the gain peak would then depend on the risetime and amplitude of these two loss components.

The lifetimes of non-radiative transitions are strongly dependent on temperature. During a prolonged UV exposure, the absorption at 248.5 nm is gradually bleached and the temperature of the fibre core diminishes, thereby increasing the non-radiative lifetimes. This would explain the broadening of the gain and loss peaks observed in **Fig. 6-4** during the exposures. As the temperature decreases, the radiative transition $S_1 \rightarrow S_0$ would therefore be favoured and the proportion of excited electrons accessing the conduction band or level T_1 would decrease. The fraction of excited electrons accessing the conduction band would decrease even more rapidly because of the dispersive nature of the photo-thermal ionisation process. This may be the reason why the ratio of the peak gain to the peak loss increases during the exposures, as seen in **Fig. 6-4 and 6-5**.

The transient loss observed below 0.85 μm should mainly be due to the free electrons in the conduction band. From the fast transient of Fig. 6-6, the lifetime of conduction electrons can therefore be estimated to ~70 ns (after exposure to a few hundred pulses). The best fit for this transient absorption was obtained with the function form

$$\alpha(t) = \frac{\alpha_1}{1 + t/\tau_c} + \alpha_2 \tag{6-3}$$

where α_1, α_2 and τ are constants. In Fig. 6-6, $\alpha_1 = 6.9$ dB/cm, $\alpha_2 = 0.73$ dB/cm and $\tau_c = 73$ ns. A stretched exponential function was also tried but gave a poor fit. Eq. (6-3) suggests that the electron trapping process is non-dispersive, since the exponent of t is equal to 1. This is surprising, since the reverse process, as observed in the thermal decay of fibre gratings, is known to be dispersive [5]. The constant term α_2 is attributed to the tail of the $T_1 \rightarrow S_1$ absorption band. The slow decay seen on the 100 μs timescale in Fig. 6-6 is consistent with the known lifetime of the T_1 state of about 100 μs.

The lifetimes of the non-radiative $S_1 \rightarrow T_1$ transition (τ_{nr}) and of the 290 nm (4.3 eV) fluorescence (τ_{uv}) can be estimated if it is assumed that, after a prolonged exposure, the number of electrons excited to the conduction band is negligible. In that case, the energy level diagram reduces to a simple three-level system where the transient loss around 1 μm is only due to the accumulation of electrons on level T_1. The time-dependence of the gain (or loss) can be predicted by solving the rate equations which gives

$$\gamma(t) = \gamma(0) \left((1 + \tau/\tau_{nr}) e^{-t/\tau} - \tau/\tau_{nr} \right)$$

where

$$\tau = \frac{\tau_{nr}\tau_{uv}}{\tau_{nr} + \tau_{uv}} \tag{6-4}$$

Eq. (6-4) assumes for simplicity that the UV pulse is a delta function. Fig. 6-10 shows a comparison of Eq. (6-4) with the last single-pulse trace of Fig. 6-4 for the 0.28 N.A.

fibre. The time $t=0$ corresponds to 24 ns on this graph. The best fit was obtained for τ_{uv}=35 ns and τ_{nr}=52 ns. The value of τ_{nr} should be smaller at the beginning of the exposure when the core temperature is higher, whereas τ_{uv} should remain constant during the exposure. The value of τ_{uv} is in agreement with the results of Gallagher and Osterberg who estimated τ_{uv} to be less than 50 ns [2].
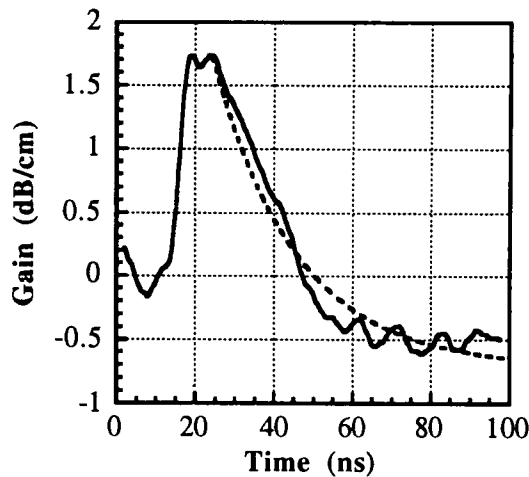

Figure 6-10 - Single pulse trace of Fig. 6-4 (N.A.=0.28, λ=1.06 µm, 36000 pulses) and fit from Eq. (6-4) with τ_{uv}=35 ns and τ_{nr}=52 ns.

The most puzzling feature of the measurements presented in this chapter is the fact that the peak value of the transient gain remains nearly constant throughout a long exposure, even though the ground state S_0 is being depleted as the defects centres are ionised. The only plausible explanation seems to be that the gain is in fact diminishing during the exposure, but that this reduction is balanced by a similar reduction in the transient absorption, causing the net gain to appear roughly constant. The transient absorption present during the gain peak is related to the density of electrons in the conduction band. This density is in turn dependent on both the number and the demarcation energy of populated defects (section 3.2.2). As the exposure increases, the number of populated defects diminishes and the defects that are left are much less likely to be ionised. The gain, on the other hand, is unaffected by changes in the demarcation energy. This means that the ratio of the transient absorption to the peak gain should diminish during the exposure, which is required if the sum of the two quantities should remain constant. This explanation is supported by the observation in Fig. 6-5 of a small net gain appearing in the 0.21 N.A. fibre after the transient absorption had been sufficiently bleached. To carry out direct quantitative comparisons between this model and the experimental data, a knowledge of the absorption caused by conduction electrons in a GeSi fibre as function of the electron density and the optical frequency would be required.

6.5. <u>Conclusion</u>

To the author's knowledge, this experiment has provided the first direct measurements of the electron dynamics in oxygen-deficient defect centres on a nanosecond timescale. The results obtained so far, in particular the measurement of the gain spectrum, have provided supportive evidence for the proposed energy level diagram of oxygen-deficient centres. The electron dynamics observed in the experiment are quite complex, involving several electron populations with lifetimes or excitation rates that depend on the temperature in the core of the fibre and on the previous exposure, making the interpretation of the results difficult and often speculative. By looking at the simplest cases - outside the gain bandwidth or when the ionisation rate is very low - it has been possible estimate the lifetimes of the fast transitions which, until now, had not been resolved. Additional measurements will be required to confirm the validity of the proposed model.

6.6. References

1. Y. Duval, R. Kashyap, S. Fleming and F. Ouellette, "Correlation between ultraviolet-induced refractive-index change and photoluminescence in Ge-doped fiber", *Appl. Phys. Lett.*, **61** (25), pp. 2955-2957, 1992.

2. M. Gallagher and U. Osterberg, "Spectroscopy of defects in germanium-doped silica glass", *J. Appl. Phys.*, **74** (4), pp. 2771-2778, 1993.

3. G. Meltz and W.W. Morey, "Bragg grating formation and germanosilicate fiber photosensitivity", *International Workshop on Photoinduced Self-Organisation Effects in Optical Fiber* , SPIE Vol. *1546*, pp. 185-199, Quebec, 1991.

4. G. Meltz, W.W. Morey, W.H. Glenn and D.J. Fritz, "UV-induced Bragg gratings in optical fibers and thin-film waveguides", *Meeting on Photosensitivity and Self-Organization in Optical Fibers and Waveguides* , SPIE Vol. *2044*, pp. 236-245, Quebec, 1993.

5. T. Erdogan, V. Mizrahi, P.J. Lemaire and D. Monroe, "Decay of ultraviolet-induced fiber Bragg gratings", *J. Appl. Phys.*, **76** (1), pp. 73-80, 1994.

6. M.J. Yuen, "Ultraviolet absorption studies of germanium silicate glasses", *Appl. Opt.*, **21** (1), pp. 136-140, 1982.

7. L. Dong, J. Pinkstone, P.St.J. Russell and D.N. Payne, "A study of UV absorption in MCVD preforms", *Submitted to J. Opt. Soc. Am.*, 1994.

8. M. Kohketsu, K. Awazu, H. Kawazoe and M. Yamane, "Photoluminescence in VAD $SiO_2:GeO_2$ glasses sintered under reducing or oxidizing conditions", *Jap. J. Appl. Phys.*, **28** (4), pp. 622-631, 1989.

9. L. Dong, J.L. Archambault, L. Reekie, P.St.J. Russell and D.N. Payne, "A study of photo-induced absorption change in germanosilicate preforms: evidence for the colour-centre model of photosensitivity", *Submitted to Appl. Opt.*, 1994.

Chapter 7
Gratings in Ge-free optical fibres

7.1. Introduction

By a remarkable coincidence, germanium-doped silica fibres are not only the most common type of fibre used in optical networks, they are also the most photosensitive fibres known to date. In several applications, however, photorefractive gratings are required in fibres where germanium cannot be used as a core dopant. In many types of rare-earth doped fibres used for fibre lasers, the addition of germanium changes the phonon energy of the glass, which can drastically reduce the quantum efficiency of the fibre lasers. One important example is the erbium:ytterbium fibre, which has produced the most efficient single-frequency fibre laser at 1.5 μm [1-3] (see section 9.2.2). Until recently, it had not been possible to form any measurable grating in Er:Yb fibres, due to their extremely low photosensitivity, which has limited the performance of the single-frequency fibre lasers. It is therefore essential to find or develop photosensitive Ge-free optical fibres.

Permanent photoinduced index changes of order 10^{-5} have already been observed in a certain types of Ge-free silica fibres, including cerium-doped [4-6] and europium-doped aluminosilicate fibres [7]. More recently, gratings were also written by UV exposure in cerium-doped fluorozirconate fibres and index changes approaching 10^{-4} were recorded [8]. Also, thermally-induced index changes were measured in hydrogen-loaded phosphosilicate and alumino-phosphosilicate fibres [9].

In this chapter, the photosensitivity of aluminum- and phosphorus-doped Ge-free silica fibres is investigated. Although these fibres are extremely important for fibre laser applications, little is known about their photosensitive properties. Photoinduced index changes are measured in several fibres with different core compositions, with and without hydrogen-loading. The UV absorption spectra of preform samples before and after UV exposure are also examined to gain more insight on the index-changing mechanism.

7.2. Erbium:ytterbium fibres

The preferred host glass for erbium:ytterbium fibres is silica doped with phosphorus and aluminum. The aluminum, erbium and ytterbium are incorporated in the preform by the solution-doping method [10]. In an Er:Yb fibre, the role of the ytterbium ions is to absorb pump photons around 1 μm; most of this absorbed energy is then resonantly transferred to the erbium ions which can then produce amplification in the 1.5 μm region. The main advantage of this scheme is that ytterbium ions have a higher absorption cross section and can be incorporated in larger concentrations than the erbium ions; as a result, the absorption at the pump wavelength in an Er:Yb fibre can be up to 3 orders of magnitude larger than in an Er fibre. Er:Yb fibres are therefore far superior to Er-doped fibres for making short (few cm long) single-frequency fibre lasers since they can absorb most of the pump power in 1 or 2 cm [1]. An additional advantage is that the absorption band of Yb^{3+} at 1 μm is extremely broad which gives access to a number of practical pump sources including 0.98 μm laser diodes and 1.06 μm diode-pumped Nd:YAG lasers.

To assess the photosensitivity of Er:Yb fibres, gratings were written in several fibres using the setup of Fig. 4-3. The Bragg wavelength was set at ~1.3 μm to increase the sensitivity of the measurements by avoiding the absorption bands of Er^{3+} and Yb^{3+} ions.
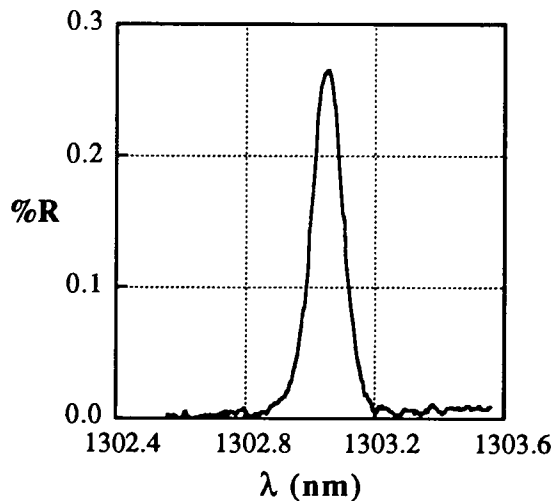
Figure 7-1 - Reflection spectrum of 15 mm-long grating in untreated Er:Yb fibre ND791 for a saturated index modulation.

A few Er:Yb fibres were first tested without hydrogen-loading. In every case, it was possible to produce very weak gratings with maximum index modulations of about 10^{-6}. A typical reflection spectrum is shown in Fig. 7-1, which was calibrated using the 4%

reflection from the cleaved endface of the fibre as a reference. The fact that permanent gratings can be written in fibres free of germanium or other dopants known for their photosensitivity is interesting in itself. Unfortunately, the index changes are too small for most practical applications.

The experiment was therefore repeated with hydrogen-loaded fibres. Fig. 7-2 compares the growth of fibre gratings written under identical conditions in fibre ND791, with and without hydrogen-loading. The gratings were exposed to 20 excimer pulses/second at a pulse fluence of about 0.5 J/cm^2. It can be seen that the addition of 0.5 mol% molecular hydrogen to this fibre has increased its photosensitivity by one order of magnitude. Also, the exposure needed to obtain the maximum index modulation has doubled. Apart from these differences, both measurements have similar dynamics, as the two curves are quasi-parallel on the logarithmic plot with an initial slope of 0.53 measured with the H$_2$-loaded fibre.
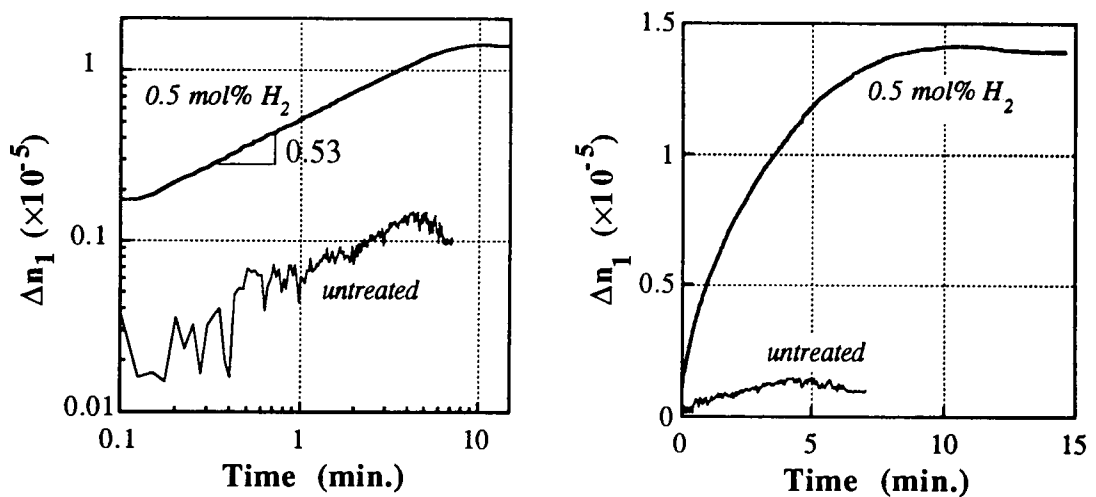
Figure 7-2 - Growth of grating index modulation in Er:Yb fibre ND791.

The largest enhancement of photosensitivity by hydrogen-loading was obtained in fibre ND844 which contains 9.0 mol% P$_2$O$_5$, 1.36 mol% Al$_2$O$_3$, 1.35 mol% Yb^{3+} and 0.11 mol% Er^{3+}. The core composition of this fibre was measured by G.G. Vienne in mass spectrometer [11]. This fibre has excellent lasing characteristics, and has been used in the majority of the single-frequency fibre laser work in the ORC [1-3]. An example of grating growth in ND844 can be seen in Fig. 7-3 for a sample loaded with 1 mol% H$_2$. The initial slope of the growth curve is very high at about 0.89 and the maximum index modulation is 7×10^{-5}. The irregularities seen in this measurement could be a sign of instabilities in the writing process or may also be due to variations in the output of the

LED used to illuminate the grating. The final reflection and transmission spectra of this grating are shown in Fig. 7-4.
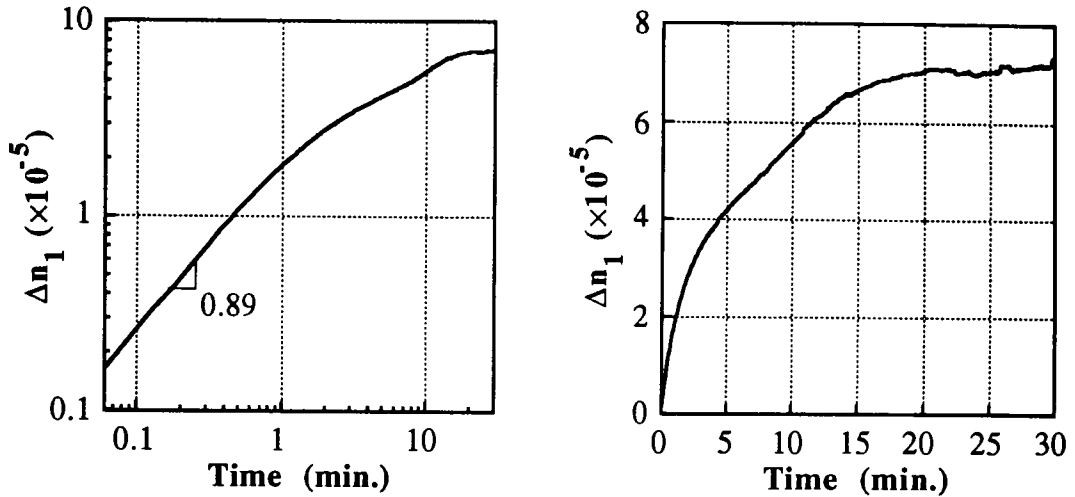
Figure 7-3 - Growth of index modulation of a grating written in Er:Yb fibre ND844 loaded with 1 mol% H_2.
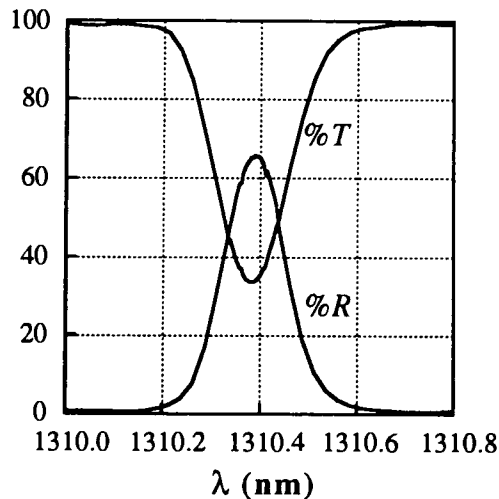
Figure 7-4 - Final reflection and transmission spectra of grating of Fig. 7-3.

The highest index modulation obtained in ND844 was ~2×10^{-4} in a fibre loaded with 1.8 mol% H_2. With exposure conditions comparable to those of Fig. 7-3, it took 3 hours to reach this level, corresponding to an estimated fluence of about 100 kJ/cm^2! At the end of this exposure, the index modulation was still increasing very slowly. The resulting grating spectra are shown in Fig. 7-5. For this exposure, the beam displacement technique was used to improve the uniformity of the grating. The 20 mm beam was

displaced continuously back and forth by ±3 mm. This was apparently insufficient, as indicated by the irregularities seen on the long wavelength side of the reflection spectrum. The transmission measurement is limited by the noise floor of the optical spectrum analyser but indicates a reflectivity of at least 99% (assuming that $R+T=1$). The Bragg wavelength of this grating was chosen to match the peak of the gain spectrum of the Er:Yb fibre. This grating was used in the first demonstration of a 1.5 μm DFB fibre laser, as described in section 9.2.2.
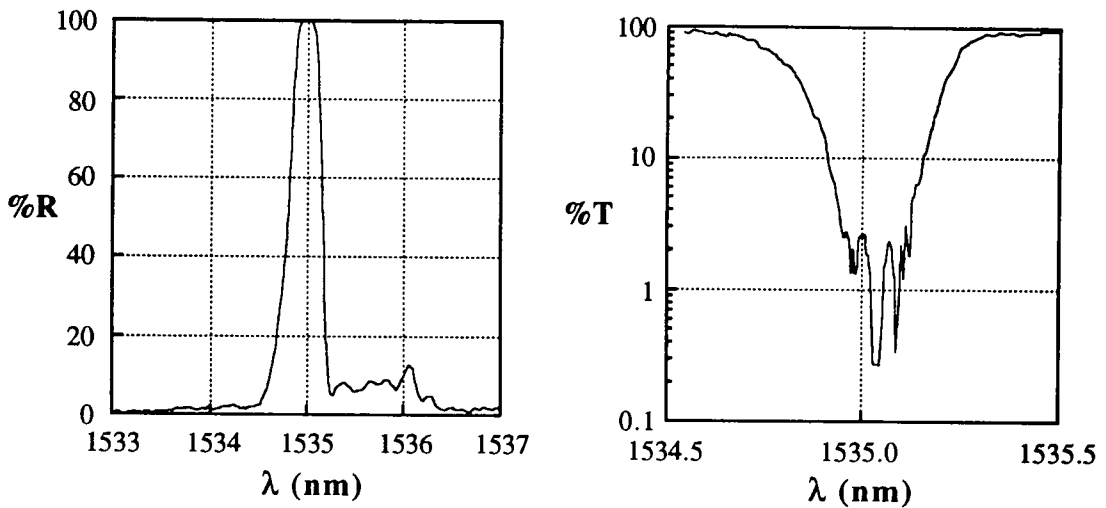
Figure 7-5 - Reflection and transmission spectra of strongest grating obtained in fibre ND844 with 1.8 mol% H_2. This grating was used for DFB fibre laser demonstration.

The strength of the gratings written in fibre ND844 was extremely variable. In several other samples of this fibre, also loaded with 1.8 mol% H_2, maximum index modulations of only $\sim 10^{-5}$ were obtained, which saturated in less than 15 min. exposure. All attempts to repeat the result of Fig. 7-5 proved unsuccessful. There are two possible explanations for this discrepancy. The first one is that the stability of the interferometer is insufficient for very long exposures. This appears unlikely since the stability of the interferometer has proved to be very reliable (see Fig. 4-9 for example) and also because such large variations in maximum photoinduced index modulation have not been observed in any other fibre. The more probable explanation seems to be that the composition of the fibre core varies along the length of the fibre. The preform from which this fibre was drawn was in fact extremely irregular and had devitrified over most of its length; only short sections of the preform produced useful fibre.

To characterise the loss induced by the UV exposure in hydrogen-loaded Er:Yb fibres, four 2 cm-long gratings were written side by side in a section of fibre containing 1.8 mol% H_2 while the transmission of the fibre was monitored between 1.2 and 1.6 μm. From 1.5 to 1.6 μm the induced loss was smaller than the measurement error (±0.5 dB), which means that the loss for each grating was less than 0.13 dB. A very small increase in absorption could be detected in the 1.4 μm region of about 0.5±0.5 dB and no loss could be detected below 1.35 μm.

The thermal stability of gratings written in Er:Yb fibres has not yet been tested. However, for the grating of Fig. 7-5, no measurable reduction of the index modulation could be detected after it had been stored at room temperature for 11 months.

7.3. Aluminosilicate and phosphosilicate fibres

To try and understand the origin of the photosensitivity in hydrogen-loaded Er:Yb fibres, fibres with simpler core compositions were tested. The first fibre to be examined (ND831) had only one core dopant, alumina, with an estimated concentration of 2 mol%. A sample of this fibre was soaked in 170 atm. H_2 for 17 days at room temperature. The measurement of the absorption introduced by the hydrogen-loading process gave a surprising result, as seen in Fig. 7-6.
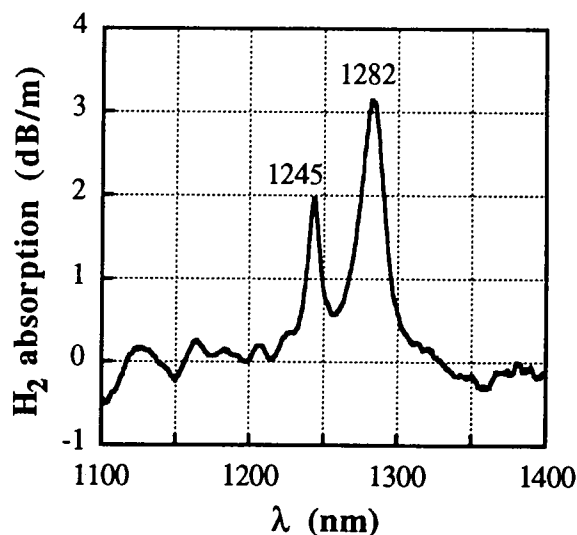

Figure 7-6 - Overtone absorption of molecular hydrogen in aluminosilicate fibre ND831.

Instead of the usual overtone absorption peak at 1245 nm (see Fig. 3-15), the H_2 absorption spectrum has two peaks, at 1245 and 1282 nm. This implies that an important fraction of the hydrogen molecules are strongly interacting with alumina molecules. The reason for this interaction could be that, because aluminum is trivalent, it tends to create a net charge as it bonds to the tetrahedral silica structure, which could shift the vibrational states of neighbouring hydrogen molecules. When aluminum is mixed with pentavalent phosphorus it can form neutral molecular structures ($AlPO_4$), which could explain why the 1282 nm peak does not appear in Er:Yb fibres loaded with hydrogen. By assuming that the absorption cross-sections are the same for the two peaks of Fig. 7-6, the hydrogen concentration given by Eq. (3-22) is 1.8 mol%, which is also what would be expected from the diffusion parameters.

Two gratings were written under identical conditions in a hydrogen-loaded and an untreated sample of fibre ND831. In both cases, the index modulation reached its maximum value within the first few pulses, resulting in very weak gratings. The reflection spectra are shown in Fig. 7-7. As can be seen, the two gratings are nearly identical, with an index modulation of $\sim 10^{-6}$. Hydrogen-loading had therefore no measurable effect on the photosensitivity of this fibre.
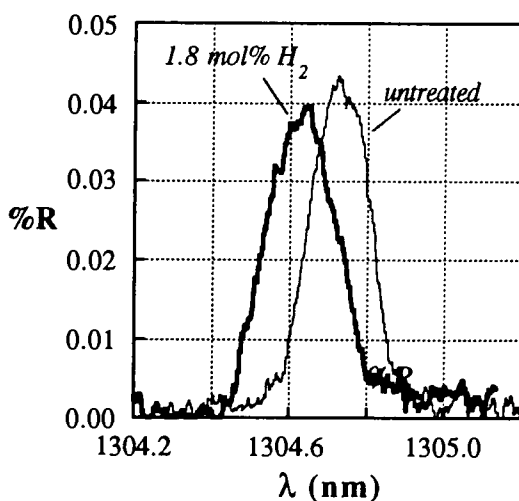
Figure 7-7 - Reflection spectra of gratings in H_2-loaded and untreated Al/Si fibre ND831.

The other fibre to be tested was ND618. The core of this fibre is doped with about 5 mol% P_2O_5. The growth of the photoinduced modulation in H_2-loaded and untreated samples are compared in Fig. 7-8. Again, hydrogen-loading did not have any significant effect on the photosensitivity of the fibre. In both fibres, the evolution of the index

modulation has similar dynamics, leading to maximum index modulations slightly in excess of 10^{-6}. The exposure required to reach this maximum is two orders of magnitude higher than in the aluminosilicate fibre.
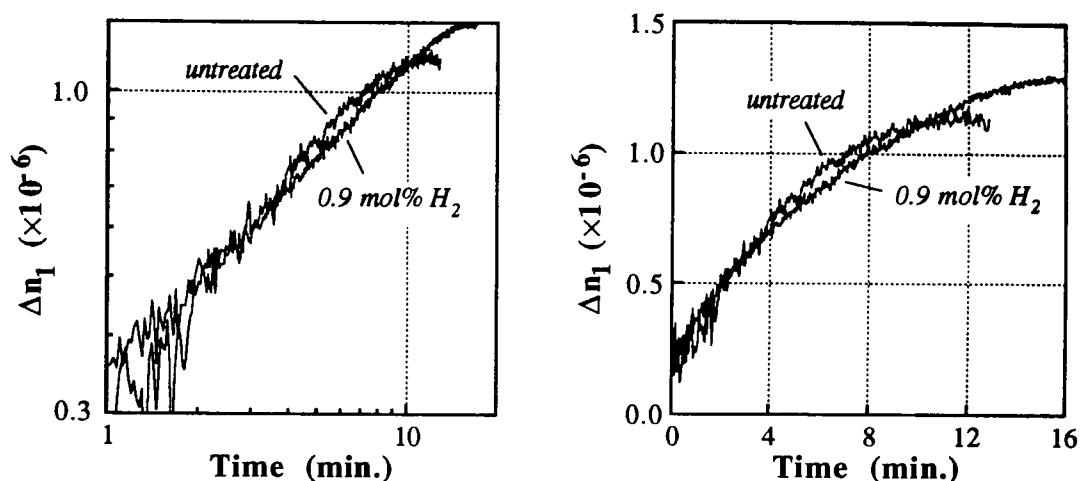
Figure 7-8 - Comparison of grating growth in untreated and H_2-loaded P/Si fibre ND618.

7.4. UV absorption spectra

The UV absorption spectra of three preform samples were examined to gain more insight into the mechanism of grating formation in Er:Yb fibres. The fabrication data of the preforms under test are shown in Table VI. The cores of all three preforms are Ge-free and doped with aluminum and phosphorus. However, each preform has a different rare-earth content, to assess the role of the rare-earths in the photosensitivity process. The solution-doping concentrations of Al, Er and Yb given in Table VI are closely related to the relative concentrations of these dopants in the preform [11]. The gas flows of P and Si characterise the MCVD process but give only a very rough idea of the phosphorus content of the core, as many other parameters can affect the deposition rate.

Preform number	Rare earths	N.A.	Flow (cc/min.)		Solution conc. (g/cc)		
			P	Si	Al	Er	Yb
ND747	Er	0.07	700	200	5.2	5.14	0
ND795	Er+Yb	0.13	700	200	4.99	0.34	7.17
ND797	Yb	0.17	700	200	4.97	0	5.2

Table VI - Fabrication data of fibre preforms used in experiment.

1.2 mm-thick slices were taken from each of the three preforms and then polished. Their absorption spectra were measured in a Perkin Elmer λ-9 spectrophotometer, using a pinhole to mask out the cladding region. The results are shown in Fig. 7-9. At 248.5 nm, all three samples show a very low absorption of less than 1 dB/mm. The absorption spectra of the Yb and Er:Yb preforms are very similar, differing mainly by a scaling factor. The broad absorption band which seems centered near 190 nm can also be seen in the absorption spectra of aluminosilicate preforms [12]. By contrast, phosphosilicate preforms show very little absorption down to 190 nm [13]. Therefore, this 190 nm absorption band is probably related to alumina. Although the erbium-doped preform should also contain alumina, its absorption spectrum is very different from the other two. This important difference may be related to the very high erbium concentration, which had caused most of the preform to devitrify. Although the sample was taken from a region of the preform which did not appear devitrified, it is possible that the glass phase in the core of the sample had been modified by the high erbium content.
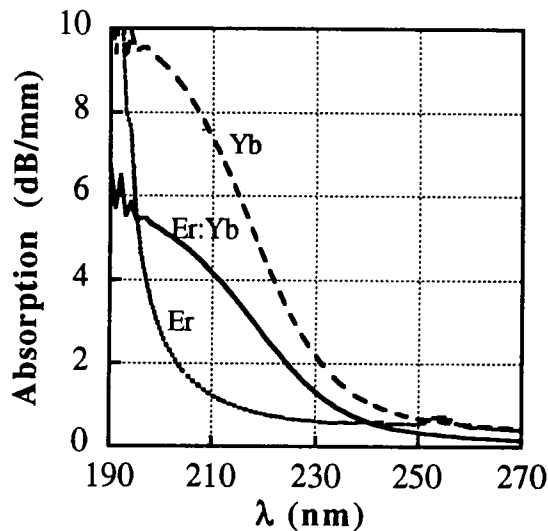
Figure 7-9 - UV absorption spectra in three rare-earth doped alumino-phosphosilicate preform samples.

The three preform samples were then polished down to 261 μm and left for 11 days in a hydrogen cell at 115 atm. and 42°C. From Eq. (3-20) the hydrogen diffusion time under these conditions should be about 13 days. The distribution of hydrogen concentration through the sample is approximately given by [14]

$$C(x,t) \approx S \left(1 - \frac{4}{\pi} e^{-\pi^2 t/16t_{diff}} \cos(\pi x/h)\right), \quad -\frac{h}{2} \le x \le \frac{h}{2} \qquad (7-1)$$

where S is the solubility calculated from Eq. (3-21) and h is the sample thickness. According to Eq. (7-1), the hydrogen concentration should be about 1.0 mol% near the

surface of each sample and 0.24 mol% in the centre with an average concentration of 0.48 mol% through the sample. The left side of Fig. 7-10 shows the loss introduced by the hydrogen-loading process itself. Two main absorption bands can be seen, at ~250 nm and at a wavelength shorter than 200 nm. Similar absorption bands have been observed by Albert *et al.* in H_2-loaded germanosilicate preforms [15]. This similarity between preforms containing entirely different dopants could imply that these absorption bands result form a reaction between hydrogen molecules and silica defects, rather than from a reaction involving the dopants. The fact that the three samples of Fig. 7-10 show different levels of induced absorption when they were hydrogen-loaded together suggests that the samples contained different initial defect concentrations.
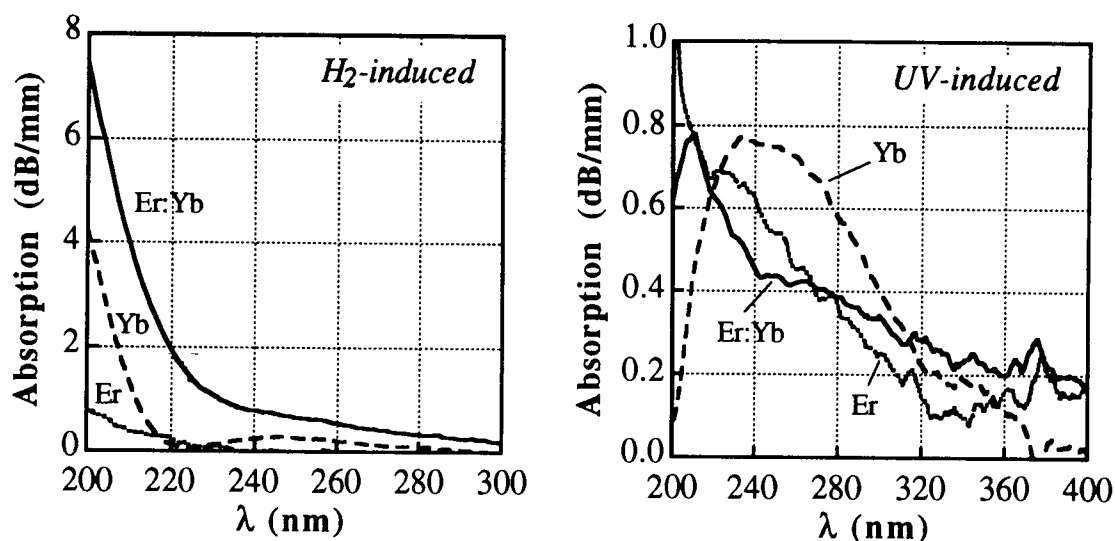
Figure 7-10 - Absorption induced by H2-loading (left) and subsequent UV exposure (right).

All three samples were then immediately exposed to the excimer beam. Each was given a 2.4 kJ/cm^2 exposure at 0.1J/cm^2/pulse. The absorption spectra of the three samples were again measured and compared to the previous measurements. The right side of Fig. 7-10 shows the absorption induced by the exposure. Similar absorption changes have occurred in all three samples, the magnitude of which is close to the noise level of the spectrophotometer. The measurement taken from the Yb-doped sample is the most reliable, since this sample had the largest core area and hence gave a stronger optical signal. The spectrum measured in this sample shows what appears like an absorption band centered near 240 nm. However, the very broad width of this feature (~1.8 eV) means that it is probably not a single absorption band.

7.5. <u>Discussion</u>

The index change associated with the UV-induced absorption change of Fig. 7-10 can be calculated using the Kramers-Kronig relation (Eq. (3-18)). For all three samples, this gives a positive index change of about 1.0×10^{-6}. Clearly, this is much less than the measured photoinduced index changes in hydrogen-loaded Er:Yb fibres which means that unless a strong absorption band can be found below 200 nm, the formation of colour centres can not account for the observed index changes. The UV absorption measurements therefore provide little explanation of the mechanism by which molecular hydrogen enhances the photosensitivity of Er:Yb fibres. The only measurable effects of hydrogen-loading were a small increase in absorption at 248.5 nm and the creation of small concentrations of oxygen-deficient centres after UV exposure. Much larger effects would be expected to explain the order of magnitude improvement of photosensitivity resulting from the hydrogen-loading of fibres.

While hydrogen-loading greatly improved the photosensitivity of Er:Yb fibres, it had no significant effect on phosphosilicate and aluminosilicate fibres. This could mean that the increase of photosensitivity is related to the *combination* of aluminum and phosphorus. For example, the role of the alumina could be to provide sufficient absorption at 248.5 nm so that enough optical energy can be transferred to the glass to trigger a reaction between phosphorus and hydrogen molecules. Another explanation could be that the rare-earths play a role in the index-changing mechanism, although no strong evidence has emerged from the UV absorption measurements to support this hypothesis. Fibres with different combinations of the four dopants (Al, P, Er, Yb) would have to be tested to resolve this question.

The dynamics of grating formation in both hydrogen-loaded and untreated fibres are dispersive, as can be seen in Fig. 7-2 and 7-3. Dispersion parameters of up to 0.89 have been observed, which is much larger than in germanosilicate fibres. This is surprising, since the excimer laser wavelength is located in the tail of the main absorption band seen in the Er:Yb preform sample.

The origin of the photoinduced index changes in hydrogen-loaded Er:Yb fibres is therefore still an open question, which is not surprising considering the complexity of the problem. What is clear from the available data, however, is that the writing of gratings should be much more efficient at 193 nm, using an ArF excimer laser, than at 248.5 nm, since both the initial and H_2-induced absorption are one order of magnitude larger at that

wavelength. This was recently confirmed when efficient grating writing at 193 nm was demonstrated if phosphosilicate hydrogen-loaded flame hydrolysis waveguides [16].

7.6. Tantalum-doped fibres

Tantalum-doped silica fibres can be used as an alternative to aluminosilicate fibres for hosting rare-earths. The possibility of writing gratings in these fibres would therefore present a strong interest for fibre laser applications. The study of Ta/Si fibre photosensitivity was further encouraged by the recent report of large photoinduced index changes in pure tantala films [17].

In this section, a few preliminary results are presented which were obtained in fibre HD193. The core of this fibre contains approximately 3 mol% Ta_2O_5 which gives a N.A. of 0.20. Fig. 7-11 compares the dynamics of grating formation in this fibre with and without hydrogen. The gratings were ~1.5 cm long with a Bragg wavelength of 1311 nm. The samples were exposed to 20 pulses/s for 75 s at approximately 0.5 J/cm^2/pulse. In both cases, the index modulation reaches its maximum value quasi-instantaneously and then slowly decreases. However, when the laser is switched off after 75 s, the index modulation can be seen to decrease in the untreated fibre, but to increase in the hydrogen-loaded sample! For both fibres, the evolution of the index modulation after the laser is switched off is similar to the transient index change seen in germanosilicate fibres (section 4.3.1). As for the germanium-doped fibres, this transient could be due to the thermal relaxation of trapped electrons.
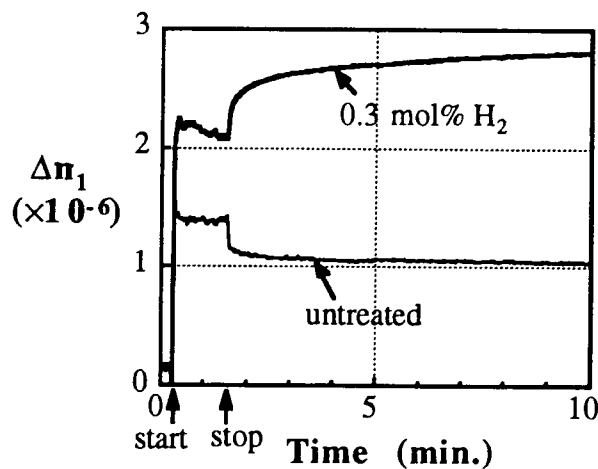
Figure 7-11 - Comparison of grating growth at 1.3 μm in H_2-loaded and untreated fibre HD193 exposed to 20 pulses/s for 75 s.

This transient increase of the index modulation was not observed in the pulse-by-pulse growth of a grating in a hydrogen-loaded sample (Fig. 7-12). A very slight decrease is recorded after each pulse. On Fig. 7-12 it can be seen that the index modulation nearly reaches its maximum after only 5 excimer pulses.
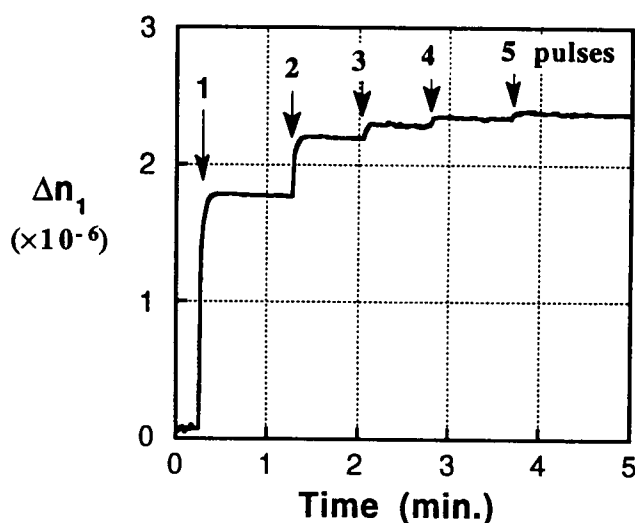
Figure 7-12 - Pulse-by-pulse growth of index modulation in fibre HD193 loaded with 0.3 mol% H_2.

Separate measurements by L. Dong have shown that substantial losses are induced by UV exposure in Ta/Si fibres which extend to the infrared [18]. At 1.3 μm, where the above gratings were written, the induced loss in an untreated fibre under similar exposure conditions saturates at approximately 2 dB/cm. At 1.55 μm the loss is about twice as small. In Fig. 7-11 and 7-12, the gratings were monitored in reflection only, so the loss could not be measured.

Because of the high losses and weak index modulations of the gratings written in tantalum-doped silica fibres, it seems unlikely that they will find useful applications.

7.7. <u>Conclusion</u>

In this chapter, it has been demonstrated that permanent gratings can be written by UV exposure in almost any type of silica fibre, even when the UV absorption is extremely small, such as in phosphosilicate fibres. Unfortunately, in most Ge-free optical fibres, the maximum index modulation that can be induced by 248.5 nm pulses is of order 10^{-6} (see Table VII) which is insufficient for most applications. Whereas hydrogen-loading had no significant effect on the photosensitivity of phosphosilicate and aluminosilicate fibres, it improved the maximum index modulation by 1 to 2 orders of magnitude in Er:Yb fibres doped with aluminum and phosphorus. This led to the first demonstration of a grating with nearly 100% reflection efficiency written in a Ge-free fibre and, subsequently, of a 1.5 μm DFB fibre laser. A study of photoinduced absorption changes down to 190 nm in preform samples has failed to provide an explanation on the origins of the index changes in hydrogen-loaded Er:Yb fibres. On the other hand, this study leaves little doubt that the writing of gratings in these fibres would be much more efficient at 193 nm than at 248.5 nm.

Fibre	Dopants	Δn_{max} $(\times 10^{-5})$		F_{max} (kJ/cm^2)	
		Untreated	H_2-loaded	Untreated	H_2-loaded
ND844	Al/P/Er/Yb	0.2	2 - 20	not measured	5 - 100
ND791	Al/P/Er/Yb	0.15	1.4	3	6
ND831	Al	0.1	0.1	<0.05	<0.05
ND618	P	0.2	0.2	6	10
HD193	Ta	0.1	0.3	0.003	0.003

Table VII - Summary of results on grating writing in Ge-free fibres.

7.8. References

1. J.T. Kringlebotn, P.R. Morkel, L. Reekie, J.-L. Archambault and D.N. Payne, "Efficient diode-pumped single-frequency erbium:ytterbium fiber laser", *IEEE Photon. Tech. Lett.*, **5** (10), pp. 1162-1164, 1993.

2. J.T. Kringlebotn, J.-L. Archambault, L. Reekie and D.N. Payne, "Er^{3+}:Yb^{3+} co-doped fibre DFB laser", *to appear in Opt. Lett.*, 1994.

3. J.T. Kringlebotn, J.-L. Archambault, L. Reekie, J.E. Townsend, G.G. Vienne and D.N. Payne, "Highly efficient, low-noise grating-feedback Er^{3+}:Yb^{3+} codoped fibre laser", *Electron. Lett.*, **30** (12), pp. 972-973, 1994.

4. M.M. Broer, R.L. Cone and J.R. Simpson, "Ultraviolet-induced distributed-feedback gratings in Ce^{3+}-doped silica optical fibers", *Opt. Lett.*, **16** (18), pp. 1391-1393, 1991.

5. L. Dong, P.J. Wells, D.P. Hand and D.N. Payne, "Photosensitivity in Ce^{3+}-doped optical fibers", *JOSA-B*, **10** (1), pp. 89-93, 1993.

6. L. Dong, J.-L. Archambault, L. Reekie, P.St.J. Russell and D.N. Payne, "Bragg gratings written in Ce^{3+}-doped fibres by single excimer laser pulses", *Opt. Lett.*, **18** (11), pp. 861-863, 1993.

7. K.O. Hill, B. Malo, F. Bilodeau, D.C. Johnson, T.F. Morse, A. Kilian, L. Reinhart and O. Kyunghwan, "Photosensitivity in Eu^{2+}:Al_2O_3-doped-core fiber: preliminary results and application to mode converters", *OFC'91 Postdeadline Papers*, paper PD3, pp. 14-17, San Diego, 1991.

8. P. Niay, P. Bernage, T. Taunay and W.X. Xie, "Fabrication of Bragg gratings in fluorozirconate fibers and applications to fiber lasers", *CLEO'94 Postdeadline Papers*, paper CPD9, pp. 21-22, Anaheim, 1994.

9. P.J. Lemaire, R.M. Atkins, V. Mizrahi and W.A. Reed, "High-pressure H2 loading as a technique for achieving ultrahigh UV photosensitivity and thermal sensitivity in GeO_2 doped optical fibers", *Electron. Lett.*, **29** (13), pp. 1191-1193, 1993.

10. J.E. Townsend, W.L. Barnes and K.P. Jedrzejewski, "Yb^{3+} sensitised Er^{3+} doped silica optical fibre with ultrahigh transfer efficiency and gain", *Electron. Lett.*, **27** (21), pp. 1958-1959, 1991.

11. G.G. Vienne, "Fabrication and characterisation of Erbium/Ytterbium phosphoslicate fibres", Mini-Thesis, University of Southampton, 1994.

12. L. Dong, J. Pinkstone, P.St.J. Russell and D.N. Payne, "A study of UV absorption in MCVD preforms", *Submitted to J. Opt. Soc. Am.*, 1994.

13. L. Dong, personal communication.

14. J. Crank, "The mathematics of diffusion", Oxford University Press, Oxford, 1975.

15. J. Albert, B. Malo, F. Bilodeau, D.C. Johnson and K.O. Hill, "Photosensitivity in Ge-doped silica optical waveguides and fibers with 193 nm light from an ArF excimer laser", *Opt. Lett.*, **19** (6), pp. 387-389, 1994.

16. B. Malo, J. Albert, F. Bilodeau, T. Kitagawa, D.C. Johnson, K.O. Hill, K. Hattori, Y. Hibino and S. Gujrathi, "Photosensitivity in phosphorus-doped silica glass and optical waveguides", *Appl. Phys. Lett.*, **65** (4), pp. 394-396, 1994.

17. M.P. Roe, M. Hempstead, J.-L. Archambault, P.St.J. Russell and L. Dong, "Strong photo-induced refractive index changes in RF-sputtered tantalum oxide planar waveguides", *CLEO-Europe Technical Digest*, paper CTuC6, pp. 67, Amsterdam, 1994.

18. L. Dong, J.-L. Archambault, E. Taylor, M.P. Roe, L. Reekie and P.St.J. Russell, "Photosensitivity in tantalum-doped silica optical fibres", *In preparation*, 1994.

Chapter 8
The grating-frustrated coupler

8.1. Introduction

The ability to multiplex and demultiplex several closely-spaced wavelength channels in the same fibre could greatly increase the capacity of optical telecommunications networks. Fibre gratings seem ideally suited to provide such narrow-band filtering at precise wavelengths and with very low losses. However, fibre gratings are reflection filters whereas wavelength multiplexing applications require transmission or channel-dropping filters. Scientists have therefore been looking for ways to combine fibre gratings with other optical components to produce such filters [1-4]. A transmission filter with the spectral characteristics of a fibre grating would certainly find numerous applications, not only in WDM, but also in suppressing amplified spontaneous emission in an erbium-doped fibre amplifier or narrowing the linewidth of a fibre laser.

8.1.1. Bragg gratings as multiplexing filters

Several ways have been proposed of inverting the spectral response of a fibre grating, as illustrated in Fig. 8-1. The simplest solution is to combine a 3 dB fibre coupler and a grating, as in Fig. 8-1 a). Unfortunately, this configuration has an inherent 6 dB loss and the return loss is only 6 dB. A much more effective solution is to use an optical circulator instead of a coupler (b). A circulator is a three- or four-port non-reciprocal bulk optical component; light inserted in the first port emerges through the second port, whereas light inserted in the second port comes out through the third. This type of arrangement has already been tested experimentally to filter the amplified spontaneous emission of an EDFA and was shown to provide excellent filtering and isolation [1]. However, the insertion loss of circulators is usually high (a few dB) as is the cost (~£10k). A third type of solution is an all-fibre interferometer arrangement (c) [2-4]. The performance of this device depends on the accurate control of the relative phase of the reflections from the two gratings; it also requires two identical gratings and a coupler with an exact splitting ratio of 50:50. The fabrication of the device therefore has a high degree of difficulty and its long-term stability could be a problem.
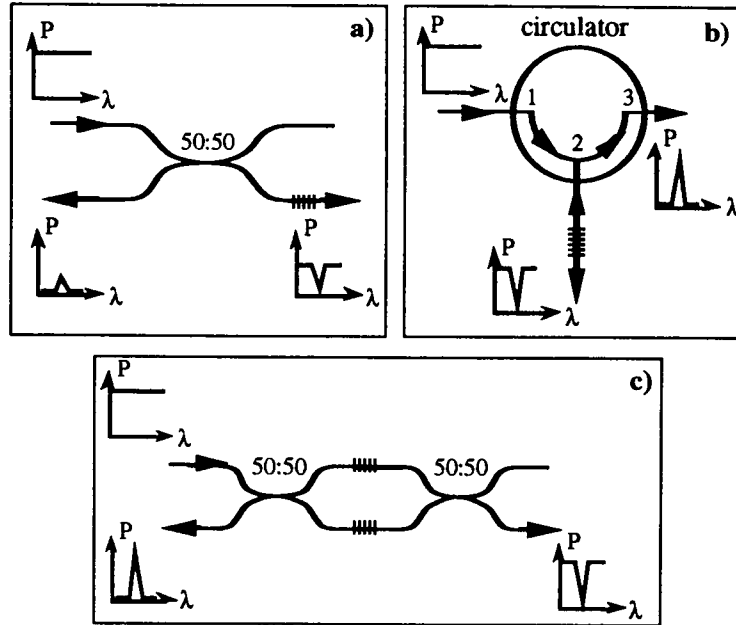
Figure 8-1 - Fibre grating-based WDM filters.

8.1.2. Grating-frustrated coupler

In this chapter, a novel type of narrow-band channel-dropping filter is analysed and demonstrated: the grating-frustrated coupler (GFC) [5]. This filter is a four-port device which consists of a 2×2 fibre coupler with Bragg grating inscribed in one side of the coupling region (see Fig. 8-2). As its name indicates, the operating principle of the GFC is opposite to that of a grating-assisted coupler. In the latter, a coarse-period grating provides phase-matching between the modes of an asynchronous coupler, allowing resonant coupling to occur over a relatively narrow wavelength range. The GFC, on the other hand, is based on a synchronous coupler. In the vicinity of the Bragg wavelength the grating has two effects: first, it introduces a strong dispersion, which makes the coupler asynchronous; second, it creates a barrier (a one-dimensional photonic bandgap) that rejects photons attempting to tunnel through.
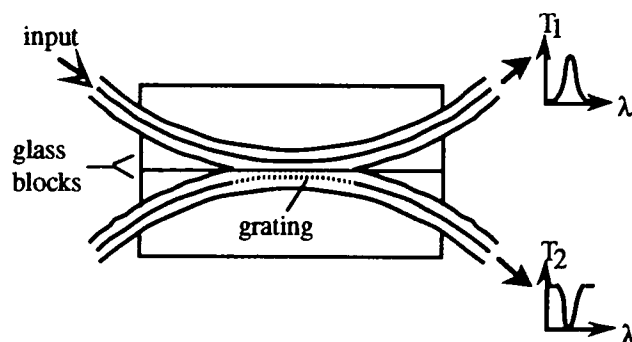

Figure 8-2 - Diagram of GFC based on polished fibre coupler.

If the grating is sufficiently strong, these two effects combined can efficiently frustrate the transfer of optical power from one arm of the coupler to the other over the bandwidth of the Bragg grating. Thus, if a multiwavelength signal is introduced in the GFC through the unaltered side of the coupler, every wavelength channel can be coupled to the other side, except for a single channel centered at the Bragg wavelength. The GFC can of course be used reciprocally as a multiplexing filter. As the GFC is all-fibre and non-interferometric, in contrast with the devices mentioned in the previous section, it has the advantages of being inherently low-loss and stable, and potentially low-cost.

8.2. Theory

A directional coupler may be analysed either by considering the coupled modes of the individual waveguides or by using the 'supermodes' of the whole structure. There are also two ways of modeling a Bragg grating: Bloch waves or coupled-mode theory. Consequently, there are at least four possible ways of analysing a GFC. All four approaches are mathematically equivalent, within the usual approximations, but each provides a different physical picture of the problem. In this section, coupled-mode theory is used for both the coupler and the grating.

8.2.1. Coupled-mode formalism

The model is described in Fig. 8-3. The two fibres forming the coupler are labeled *1* and *2* with fibre *2* containing the Bragg grating. The GFC itself is divided into five regions (I to V). Light propagating in each of the two fibres is decomposed into a backward and a forward guided wave; in the central region of the GFC (region III), the co-propagating modes exchange power through the coupling constant of the coupler while counter propagating modes are coupled together by the grating in regions II to IV. To simplify the analysis, the following assumptions are made:
- the coupling constant of the coupler, C, is constant over the coupler length L_C and null elsewhere;
- the coupling constant of the grating, κ, is constant over the grating length L_G ($\geq L_C$) and null elsewhere;
- the two fibres have the same average index;
- the grating produces negligible coupling between the forward and backward waves of fibre *1* (f_1 and b_1).

Two possible inputs are considered with optical field amplitudes i_1 or i_2. These produce four outputs, r_1, r_2, t_1 and t_2. The distribution of optical power at the four outputs is calculated by solving the coupled-mode equations and applying boundary conditions.
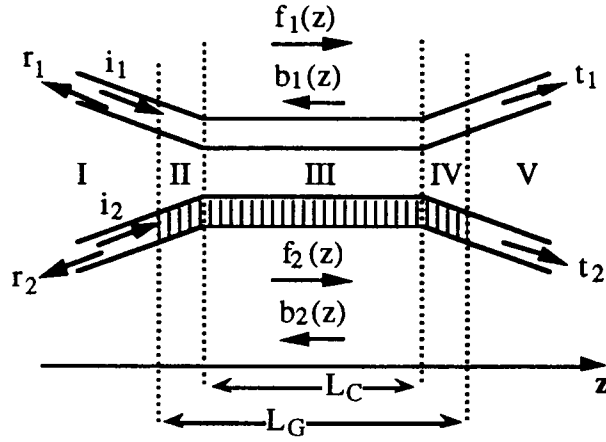
Figure 8-3 - Schematic diagram of GFC model.

The amplitudes of the forward and backward waves inside the coupler region (III) obey the four coupled differential equations

$$f_1' = iC\ f_2$$

$$b_1' = iC\ b_2$$

$$f_2' = iC\ f_1 + i\kappa\ b_2\ e^{-i\theta z}$$

$$b_2' = iC\ b_1 - i\kappa\ f_2\ e^{i\theta z} \tag{8-1}$$

where θ is the dephasing parameter for the grating defined in Eq. (2-24) and (') indicates a derivative with respect to z. To solve this set of equations, the amplitudes can be expressed in terms of f_1:

$$f_2 = -i\ f_1'/C$$

$$b_2 = -e^{i\theta z}\ (f_1'' + C^2 f_1)/\kappa C$$

$$b_1 = i\ e^{i\theta z}\ (f_1''' + i\theta f_1'' + (C^2 - \kappa^2)\ f_1' + i\theta C^2 f_1)/\kappa C^2 \tag{8-2}$$

The fourth equation yields the following fourth-order homogeneous equation in f_1:

$$f_1^{iv} + 2i\theta\ f_1''' + (2C^2 - \kappa^2 - \theta^2)\ f_1'' + i\theta(2C^2 - \kappa^2)\ f_1' + C^2(C^2 - \theta^2)\ f_1 = 0 \tag{8-3}$$

which has the general solution

$$f_1(z) = \sum_{j=1}^{4} a_j e^{i\alpha_j z} \tag{8-4}$$

where a_j are the field amplitudes to be determined and

$$\alpha_j = -\frac{\theta}{2} \pm \frac{1}{2}\sqrt{\theta^2 + 4C^2 - 2\kappa^2 \pm 2\sqrt{\kappa^4 + 4C^2(\theta^2 - \kappa^2)}} \tag{8-5}$$

In regions II and IV, the forward and backward modes of fibre *1* are uncoupled, while the general form of the optical field in fibre *2* is given by the solution of the coupled-wave

equations for a uniform grating (Eq. (2-19)). The field amplitudes a_j are determined by imposing the continuity of the forward and backward waves at the four boundaries. The fraction of power at each of the four output ports,

$$T_1 = \left|\frac{t_1}{i_n}\right|^2, \quad R_1 = \left|\frac{r_1}{i_n}\right|^2, \quad T_2 = \left|\frac{t_2}{i_n}\right|^2, \quad R_2 = \left|\frac{r_2}{i_n}\right|^2 \tag{8-6}$$

can then be calculated analytically for any excitation i_1 or i_2, and arbitrary grating and coupler parameters but the resulting expressions are extremely cumbersome.

8.2.2. Influence of coupler and grating parameters

The quantities of Eq. (8-6) can be expressed as functions of four dimensionless parameters: CL_C, κL_C, θL_C and L_G/L_C. In Fig. 6-4, the four outputs are plotted against the normalised coupler constant, CL_C, for $i_2=0$, $L_G=L_C$ and $\kappa L_C=5$. On each graph, two cases are considered: $\theta L_C=0$ (Bragg condition) and $\theta L_C=100$ (far from the Bragg condition). Away from the Bragg condition, the device behaves essentially as an ordinary coupler, with very little light being reflected in either of the two arms and most of the light being periodically exchanged between the two outputs T_1 and T_2. Maximum power transfer occurs if $2CL_C$ is an odd multiple of π.
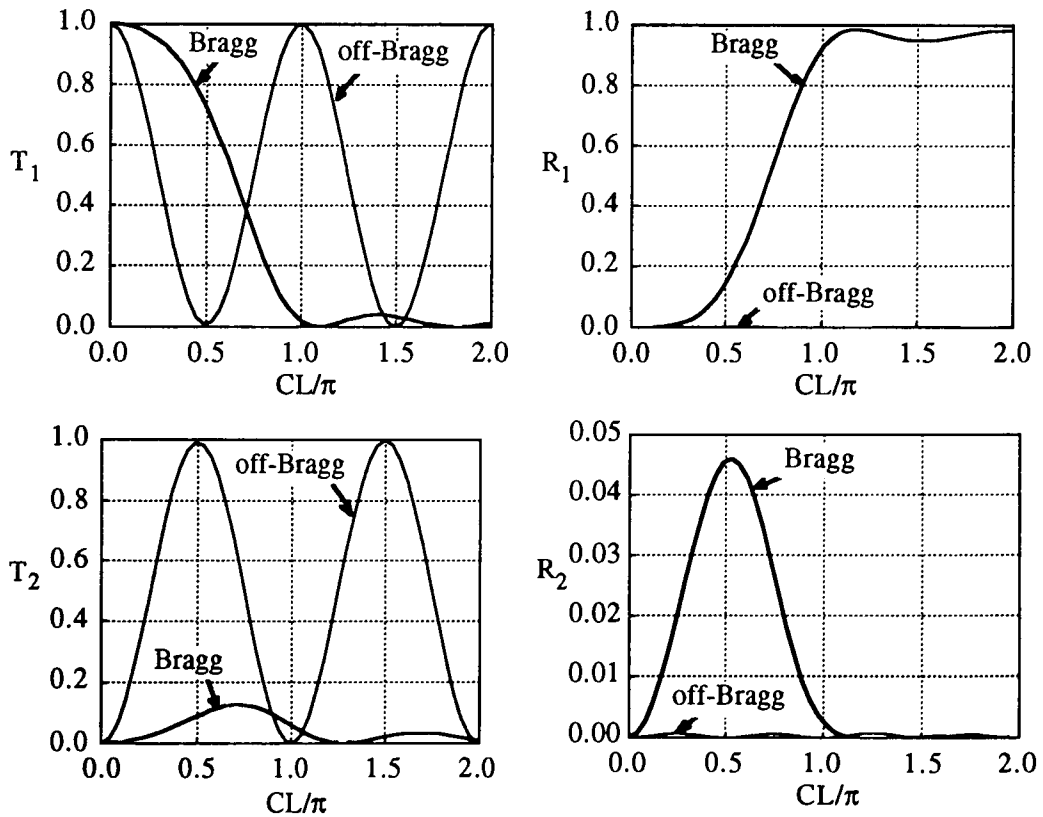

Figure 8-4 - Outputs at the four ports of the grating-coupler device with varying coupler constant, CL_C, for $i_2=0$ and $\kappa L_C=5$.

At the Bragg condition, the most interesting situation arises at $CL_C=\pi/2$. At this point, the largest fraction of power is T_1 with more than 70% of the input. About 20% of the light is reflected in both fibres and the remaining 10% is transmitted in fibre 2. In this regime, the device has the characteristics of narrow-band transmission filter. For $CL_C \geq \pi$, at the Bragg condition, most of the light is reflected back towards the source (in R_1), which is of little practical interest, since a fibre grating would, on its own, produce the same effect.

In Fig. 8-5, we now consider the situation where the fibre 2 serves as the input port ($i_1=0$). At the Bragg condition, the largest fraction of power is reflected towards the source (R_2) for all values of CL_C. This port could therefore only be used to transmit a signal outside the grating bandwidth.
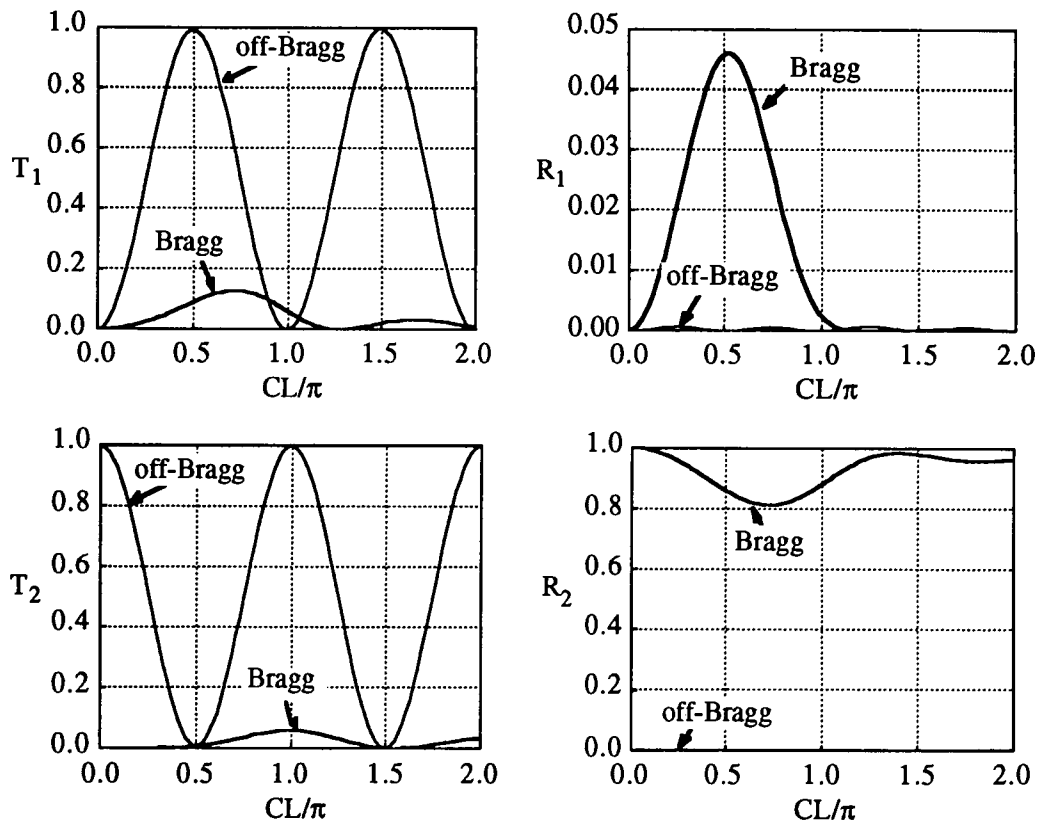

Figure 8-5 - As Fig. 8-4, but for $i_1=0$.

These last results have established two conditions for using the grating-coupler as a transmission filter:

1) the optimum coupling constant between the two fibres is given by $CL_C=\pi/2$;
2) fibre *1* must be used as the input port.

Figs. 8-6 a) and b) show how the four outputs of a GFC vary with the grating strength at the Bragg wavelength, for $CL_C=\pi/2$ and $i_2=0$. For $\kappa=0$, the device is a conventional 2×2 coupler and, since $CL_C=\pi/2$, there is a complete transfer of power, with $T_2=100\%$. As the grating strength is increased, however, T_2 decreases to 0 and T_1 tends to 1. A large fraction of the input light can also be reflected as seen in 2b). For $L_G=L_C$, the reflected signals peak at $\kappa L_C \approx 2$ but then decay to zero for larger values of κL_C. It is clear that the stronger the grating is, the more effective it is at frustrating coupling at the Bragg wavelength. Fig. 8-6 also shows the effect of extending the grating beyond the coupling region. The longer the grating, the more difficult it is for light to escape through either ends of fibre 2 and, therefore, a important decrease is observed in T_2 and R_2 when the grating length is increased from L_C to $2L_C$. Consequently, a larger fraction of power is found in the output ports of fibre *1*, with R_1 being favoured in weaker gratings and T_1 in stronger ones.
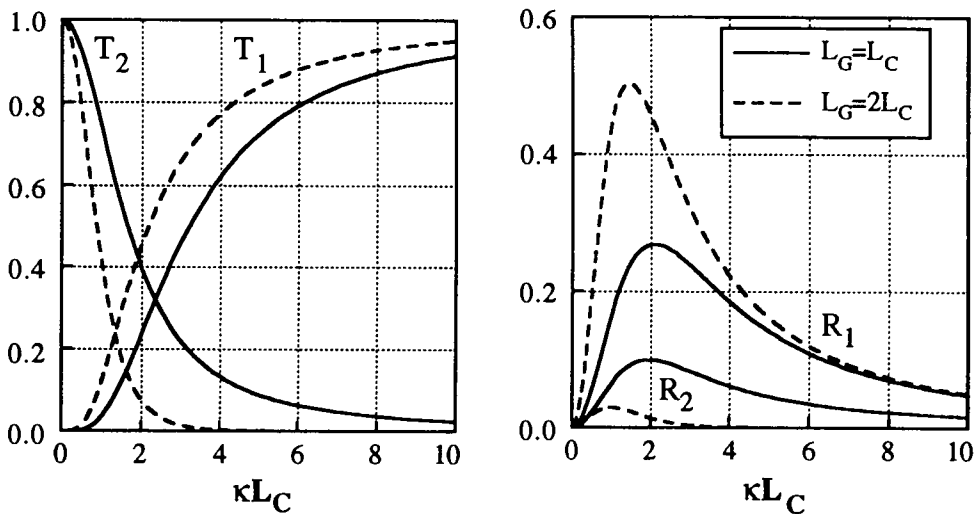
Figure 8-6 - Dependence of the transmission and reflection coefficients at the Bragg condition with grating strength, for $i_2=0$ and $CL_C=\pi/2$.

8.2.3. Spectral properties

In this section, the reflection and transmission spectrum of a the GFC are calculated for realistic grating and coupler parameters. In every case, the coupling strength is adjusted so that $CL_C=\pi/2$.

In the first example (Fig. 8-7), the grating strength is $\kappa L_C=1$, which would give a peak reflectivity of ~58% for the grating alone. The performance of this device as a transmission filter is poor, since the transmission coefficient T_1 is small (~5% for $L_G=L_C$

and ~13% for $L_G=2L_C$) and the return loss, defined as $-10 \log(R_1)$, is 7.7 dB for $L_G=L_C$ and only 3.5 dB for $L_G=2L_C$. In the top graph of Fig. 8-7, the optical bandwidth of the GFC is about 1.3 nm, which is slightly broader than the grating bandwidth (~1.0 nm). Doubling the grating length roughly halves the GFC bandwidth to ~0.7 nm.

Figure 8-7 - GFC transmission and reflection spectra for $\kappa L_C \approx 1$ ($\delta n = 5 \times 10^{-4}$, $L_C = 1$ mm).
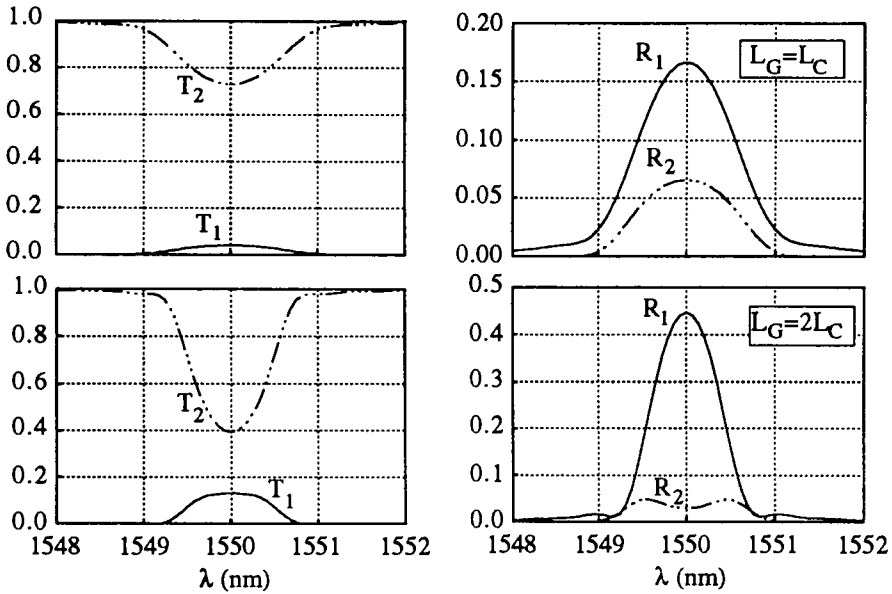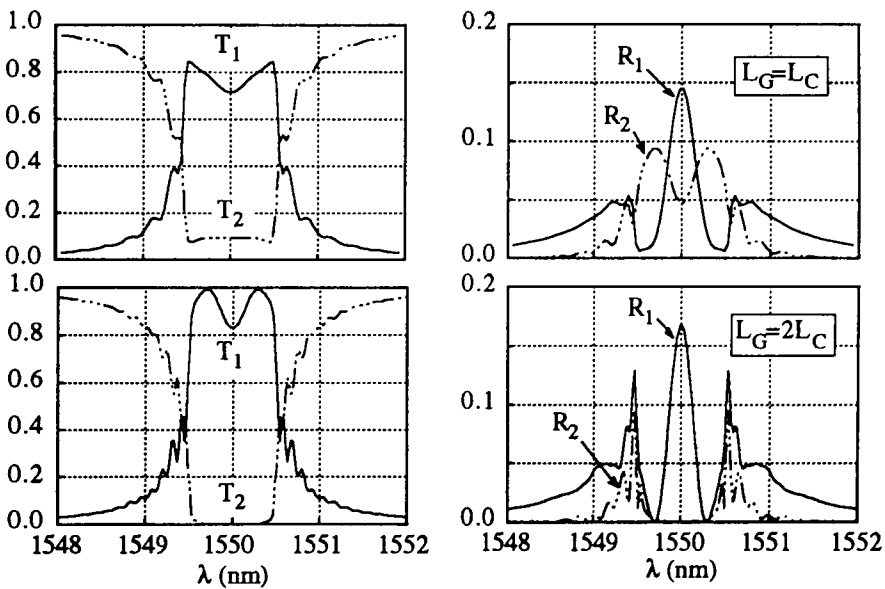
Figure 8-8 - GFC transmission and reflection spectra for $\kappa L_C \approx 5$ ($\delta n = 8 \times 10^{-4}$, $L_C = 3$ mm).

In the second example, the grating is stronger, with κL_C=5, which greatly improves the filtering properties of the GFC (Fig. 8-8). There is still, however, a significant reflected signal, totalling nearly 20% at 1550 nm. Complex structures have appeared in the spectra as the four waves are now strongly coupled together. Contrary to what one might expect, the maximum of T_1 is slightly off the Bragg condition. This point also corresponds to a minimum for R_1 and T_2. With this strong grating, increasing the grating length leads to a significant improvement of the isolation between the two transmission ports without incurring a penalty in the return loss.

When κL_C is increased to about 10, the filtering properties of the device improve again significantly (Fig. 8-9). The transmission coefficient T_1 peaks at nearly 100% while the return loss exceeds 11 dB. However, the bandwidth is is larger, about 3 nm.
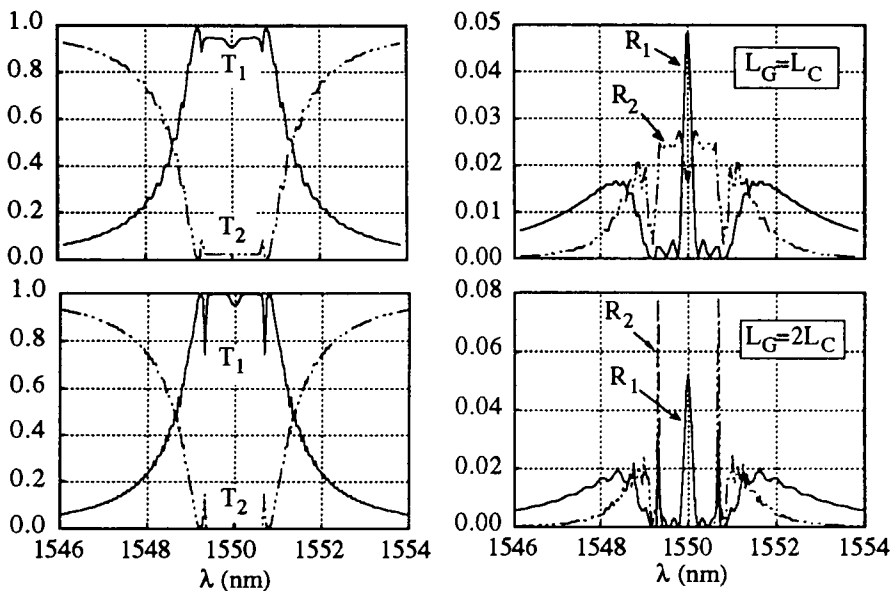
Figure 8-9 - GFC transmission and reflection spectra for κL_C≈10 (δn=1.2×10^{-3}, L_C=4 mm).

8.2.4. Discussion

The spectral properties of the GFC can be understood by referring to the dispersion diagrams of the individual fibres near the Bragg wavelength, as shown in Fig. 8-10. Far away from the Bragg condition, when $|\theta|$»2κ, the difference between the propagation constants of the two fibres, $\Delta\beta$, is very small and therefore light can be resonantly coupled from one fibre to the other.
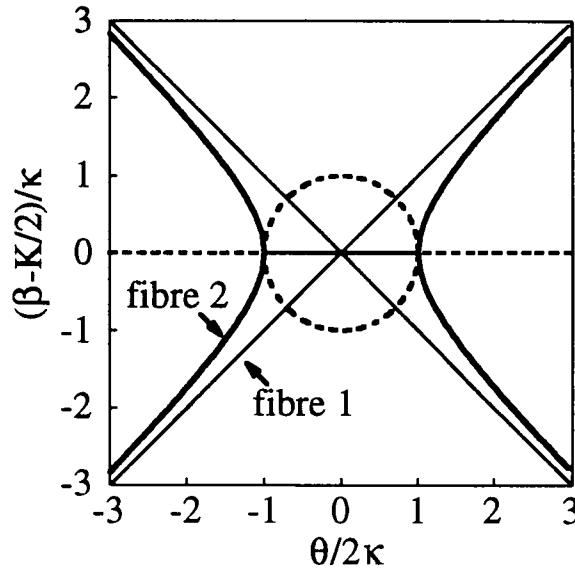
Figure 8-10 - Dispersion diagrams of the two GFC fibres. Dashed line shows imaginary component of β/κ.

As $|\theta|$ decreases however, $\Delta\beta$ increases, reaching a maximum at the edges of the grating stop-band, where $\theta=\pm 2\kappa$ ($\lambda-\lambda_B=\pm\lambda_B\delta n/2n_{av}$) and $\Delta\beta=\pm\kappa$. The coupler therefore becomes asynchronous and, as a consequence, only a fraction of the input power can be transferred from one side of the coupler to the other. In a conventional 2×2 coupler with $CL_C=\pi/2$ and a phase-mismatch $\Delta\beta L_C$, the fraction of power transferred by the coupler is given by [6]

$$F_{max} = \frac{1}{1+(\Delta\beta L_C/\pi)^2} \qquad (8-7)$$

which, for $\Delta\beta=\pm\kappa$, becomes

$$F_{max} = \frac{1}{1+(\kappa L_C/\pi)^2} \qquad (8-8)$$

This last result gives a good first approximation of the performance of the GFC as a function of the grating strength near the stop-band edge.

Inside the grating stop-band, $\Delta\beta$ is complex, becoming imaginary at the Bragg condition, with $\Delta\beta=\pm i\kappa$. The imaginary part of $\Delta\beta$ represents the evanescent decay rate of the optical field inside the grating. At the Bragg wavelength, the GFC can therefore be seen as a synchronous coupler with a lossy arm. In such a coupler, it is possible to obtain full extinction out of the input arm; however, this does not occur for $CL_C=\pi/2$, but for a higher value of the coupler constant given by

$$CL_C = \frac{1}{2}\sqrt{\pi^2+\kappa^2 L_C^2} \qquad (8-9)$$

where the loss was assumed equal to κ. Conversely, if $CL_C = \pi/2$ an increase in κL_C will cause a reduction of the coupling ratio. The increase of the extinction value of CL_C described by Eq. (8-9) can be seen in Fig. 8-4.

The above analysis shows that both the real and imaginary part of $\Delta\beta$ contribute to prevent the transfer of power in the GFC at and close to the Bragg wavelength. For a weak grating, the contribution from the imaginary part dominates as the peak of the transmission coefficient T_1 is at the Bragg wavelength (Fig. 8-7). For stronger gratings, however, the peak transmission occurs near the edges of the stop-band, indicating that the phase-mismatch introduced by the real part of $\Delta\beta$ is the dominant factor.

8.3. Implementation

8.3.1 Design considerations

The various design parameters must be carefully chosen to insure that the GFC performs well as a channel-dropping filter. In general, T_1 should be maximised and T_2, R_1 and R_2 minimised at the Bragg wavelength. Also, for many applications, one would like the filter bandwidth to be as small as possible. The first requirement can be met by making κL_C as large as possible. This is achieved either by having a large index modulation or a long coupler region. However, the index modulation is limited not only by the photorefractivity of fibre 2, but also by the desired filter bandwidth, since $\Delta\lambda \sim \delta n \lambda_B / n_{av}$ for a strong grating.
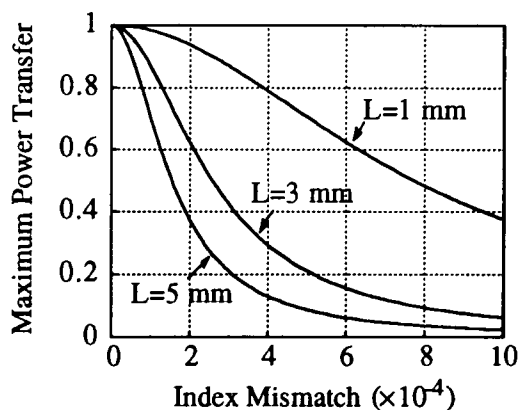

Figure 8-11 - Maximum power transfer in 2×2 asymmetric coupler as function of effective index mismatch, for $\lambda = 1550$nm.

Increasing the coupler length also has its limitations: the longer a coupler is, the more difficult it is to obtain a complete exchange of power inside the coupler. In practice, the average indices of the two fibres forming the coupler are always mismatched by a small amount, δn_{av}, which reduces the maximum fraction of power transferred by the coupler, as shown in Fig. 8-11. As expected, the longer the coupling region is, the more sensitive the coupler is to this index mismatch. For F_{max} close to 100%, Eq. (8-7) shows that F_{max} decreases quadratically with the coupler length, for a fixed value of δn_{av}.

In a polished fibre coupler, such as the one described in Fig. 8-2, the distance between the two fibre cores varies quadratically with position and therefore the coupling constant varies continuously along the length of the coupler. It is a good approximation, however, to assume that the coupler has a fixed coupling constant over an effective length given by [7]

$$L_C \approx \sqrt{\frac{\pi R r_{co}}{W}} \qquad (8\text{-}10)$$

where R is the radius of curvature of the fibres and W is the normalised transverse modal parameter, related to the V-value of the fibre by [6]

$$W \approx 1.1428\ V - 0.996 \quad (1.5 \leq V \leq 2.5) \qquad (8\text{-}11)$$

In Fig. 8-12, this effective length is calculated as a function of the radius of curvature for a coupler at 1550 nm using a fibre with 1200 nm cutoff wavelength and 0.15 numerical aperture. Fig. 8-12 shows that, to obtain a 3 mm interaction length, a radius of curvature of ~1 m is required.
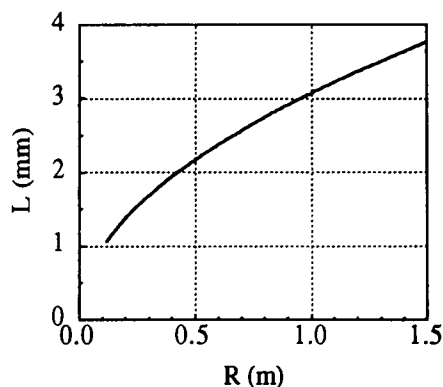

Figure 8-12 - Effective coupling length of polished fibre coupler versus radius of curvature of fibres.

8.3.2. Experiment

Taking into account the various considerations in the choice of parameters, a GFC was fabricated by incorporating a photorefractive fibre grating into one half of a polished fibre coupler. Prior to making the coupler, a 15 mm-long grating with λ_B=1535 nm and $\Delta\lambda$=1.1 nm was written in fibre HD066 using the setup of Fig. 4-3. This resulted in an index modulation $\delta n \approx 6 \times 10^{-4}$ and also raised the average index of the fibre by $(8.7 \pm 0.3) \times 10^{-4}$, which was estimated by carefully monitoring the change in Bragg wavelength during the exposure. To ensure that the average indices of the two fibres would be matched to $\delta n_{av} \leq 6 \times 10^{-5}$, a similar grating was also written in fibre *1*, but at λ_B=1550 nm. The 15 nm spacing between the Bragg wavelengths was sufficiently large that the two gratings could be treated independently of each other. After these exposures, a coupler was fabricated by mounting each fibre into a glass block and polishing it to within 2 μm of the core following a method described in Ref. [7]. The two blocks were assembled in a precision jig for sub-micron control of the fibre alignment. The radius of curvature of the fibres in the blocks was chosen to give an effective coupling length of $L_C \approx 3$ mm, corresponding to $\kappa L_C \approx 3.7$. According to Eq. (8-7) and assuming $\delta n_{av} \leq 6 \times 10^{-5}$, this length should allow at least 95% coupling.

Light from a broadband 1540 nm LED was launched into fibre *1* and the coupler was tuned until output T_2 was maximised. A maximum coupling of 97% was thus obtained, indicating an average index mismatch $\delta n_{av} \approx 5 \times 10^{-5}$, which is within the error predicted. The wavelength response of the coupler was then examined by using a white light source and an optical spectrum analyser. The coupling was seen to decrease by only 1% over a 100 nm wavelength range centred at 1535 nm. A cutback measurement was also performed to compare the total amount of power from all four outputs to the input power launched in fibre *1*; the excess loss of the coupler was found to be ~0.22 dB, which is comparable to previously reported values [7]. The device was further characterised by introducing a 50:50 fibre coupler between the LED and the input port in order to have access to output R_1. The calibrated reflection and transmission spectra measured at the four ports are shown in Fig. 8-13. Output T_1 has a maximum of ~70% and a bandwidth of 0.7 nm, which is smaller than the original grating bandwidth. The spectrum has the characteristic central dip predicted from the model. Away from the Bragg wavelength (λ_B=1534.7 nm), the transmission drops to $T_1 \approx 3\%$, corresponding to a 13 dB extinction ratio. The other transmission spectrum, T_2, has a 1.0 nm bandwidth and 18 dB extinction (1.6% transmission) at the Bragg wavelength. The dip in transmission at 1533 nm is due to resonant coupling into a cladding mode. The reflected signal R_1 is larger

than expected with a prominent feature at 1534.2 nm, while R_2 remains small at all wavelengths, with a 5% maximum at 1535.2 nm.
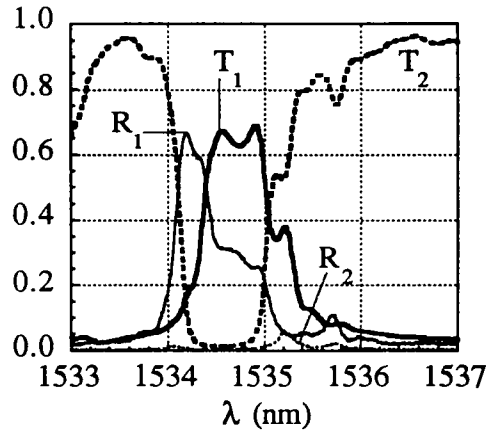
Figure 8-13 - Measured reflection and transmission spectra of all-fibre GFC.
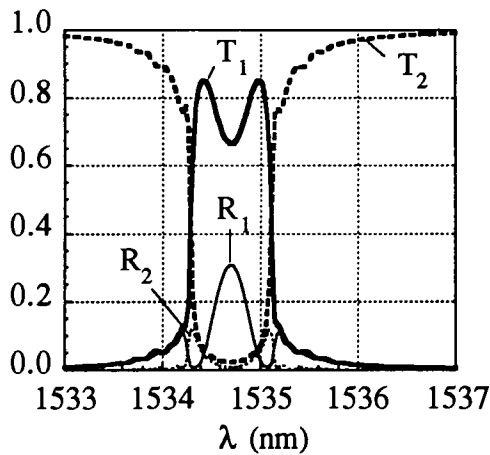
Figure 8-14 - Calculated reflection and transmission spectra for L_C=2.5 mm, L_G=5 mm, n_{av}=1.45, δn=6×10^{-4}, and λ_B=1534.7 nm.

8.3.3. Discussion

In Fig. 8-14, a good theoretical fit of the measured spectra of Fig. 8-13 was obtained for L_C=2.5 mm, L_G=5 mm and δn=6×10^{-4}. The discrepancies that can be observed are mainly due to the non-uniformity of the index modulation and average index along the grating region, caused by spatial intensity variations in the UV writing beam. The reflection peak at 1534.2 probably originates from an under-exposed grating section located outside the coupler region. This would also explain why the main peak in the T_1 spectrum is narrower than the dip in the T_2 spectrum.

This first prototype performs well as a channel-dropping filter. Its narrow bandwidth and low loss would make it ideal for WDM and filtering applications. Its main disadvantage is the low return loss of only 2 dB. However, this value could easily be improved upon by using a stronger and more uniform grating. For example, increasing the grating index modulation to 10^{-3} could produce a GFC with a return loss of about 10 dB and a bandwidth of ~1 nm, assuming a uniform grating.

Another aspect which could see some improvement is the isolation, which depends mainly on the index mismatch of the two fibres. If the index mismatch could be reduced below 3×10^{-5}, which should be possible, isolations in excess of 20 dB could be obtained.

In this experiment, the technique used to minimise the index mismatch was to start with two identical fibres and write a grating in each of them. An alternative method would to start with two dissimilar fibres and write a grating in the fibre which has the lower index, stopping the exposure when the average index change is equal to the initial index difference. The initial mode index difference could be determined by writing weak gratings in both fibres under identical conditions and comparing their Bragg wavelengths.

8.4. <u>Conclusion</u>

In summary, a useful, all-fibre, narrow-band, channel-dropping filter has been designed and demonstrated by combining two established technologies: the polished fibre coupler and photorefractive fibre gratings. The grating-frustrated coupler operates on the principle that, over a narrow range of wavelengths corresponding to the grating stop-band, coupling is prevented by a strong grating which de-tunes the coupler and creates a photonic band gap. Coupled-wave theory has provided an accurate description of the properties of grating-frustrated couplers, allowing us to establish practical limits in the choice of parameters and optimise the design. Our first prototype, operating at 1535 nm, has already produced excellent results - 0.7 nm bandwidth, 13 dB isolation, 70% peak transmission and 0.22 dB excess loss - and better performance is to be expected in the future. The critical steps in improving the device performance would be to use a more uniform grating and to reduce the index mismatch between the two fibres. Both improvements would help increase the isolation of the transmitted signals while reducing the reflected signals and the bandwidth of the device. The grating-frustrated coupler could also be designed for planar geometry.

8.5. References

1. D.R. Huber, "Erbium doped fiber amplifier with a 21 GHz optical filter based on an in-fiber Bragg grating", *ECOC'92 Proceedings, Vol. 1*, paper P2.2, pp. 473-476, Berlin, 1992.

2. K.O. Hill, D.C. Johnson, F. Bilodeau and S. Faucher, "Narrow-bandwidth optical waveguide transmission filter: a new design concept and applications to optical fibre communications", *Electron. Lett.*, **23** (9), pp. 465-466, 1987.

3. R. Kashyap, G.D. Maxwell and B.J. Ainslie, "Laser-trimmed four-port bandpass filter fabricated in single-mode photosensitive Ge-doped planar waveguide", *IEEE Photonics Tech. Lett.*, **5** (2), pp. 191-194, 1993.

4. F. Bilodeau, K.O. Hill, B. Malo, D.C. Johnson and J. Albert, "High-return-loss narrow-band all-fiber bandpass Bragg transmission filter", *IEEE Photon. Tech. Lett.*, **6** (1), pp. 80-82, 1994.

5. J.-L. Archambault, P.St.J. Russell, S. Barcelos, P. Hua and L. Reekie, "Grating-frustrated coupler: novel channel-dropping filter in single-mode optical fibre", *Opt. Lett.*, **19** (3), pp. 180-182, 1994.

6. A.W. Snyder and J.D. Love, "Optical waveguide theory", Chapman and Hall, London, 1983.

7. M.J.F. Digonnet and H.J. Shaw, "Analysis of a tunable single mode optical fiber coupler", *IEEE J. of Quantum Electron.*, **18** (4), pp. 746-754, 1982.

Chapter 9
Other applications

9.1. Introduction

One of the most interesting aspects of this project has been the opportunity to collaborate with other research groups within the ORC on several applications of fibre gratings. This work has generally been divided into three main areas: fibre lasers, sensors and pulse compression/dispersion compensation. In this chapter, we examine the impact of fibre grating technology on each of these fields of research and describe some of the particular aspects of fibre grating manufacturing for specific applications. For further information about the applications themselves, the interested reader should refer to the publications listed in section 9.6.

9.2. Fibre lasers

9.2.1. General

The availability of photorefractive Bragg gratings has been extremely beneficial to the field of fibre lasers. The use of intracore reflectors written directly into the pigtails or, preferably, into the rare-earth doped section of a fibre laser has numerous advantages:
- the design of the cavity is greatly simplified;
- bulk optical components (polarisation controllers, mirrors, filters, ...) can be avoided;
- the cavity loss is reduced to a minimum;
- the output wavelength can be accurately selected and continuously tuned;
- the lasing linewidth can be very narrow and single-frequency output is easily achievable with a short cavity.

Fabry-Perot laser cavities can be fabricated simply by writing a grating at both ends of a length of rare-earth doped fibre. The gratings control both the lasing wavelength and linewidth of the laser. The wavelength can be tuned by applying strain or temperature to the gratings. Because of the high wavelength selectivity of fibre gratings, lasing action can be forced at wavelengths which are situated very far away from the peak of the gain spectrum of the rare-earth, which means that the range of wavelengths accessible with

fibre lasers now covers much of the near-infrared spectrum. This wide range of available wavelengths, added to their high stability, high efficiency and narrow linewidth have given fibre lasers incorporating fibre gratings a competitive edge over a number of commercially-available lasers.

The ORC has had a strong interest in fibre laser research for many years, driven by the in-house expertise in the production of rare-earth doped fibres. An important part of the fibre gratings project has therefore been oriented towards fibre laser applications, as described in the following.

9.2.2. Erbium:ytterbium lasers

One of the foremost applications of fibre gratings has been the development of 1.5 μm diode-pumped single-frequency fibre lasers [1-11]. These lasers have several advantages over DFB laser diodes for WDM and Cable TV applications, namely: output wavelength set to ±0.1 nm at the fabrication stage, low noise, kHz linewidths and high output powers. However, they suffer from the fact that they cannot be directly modulated and are not as compact as laser diodes.

The first single-frequency 1.5 μm fibre lasers were realised in erbium-doped fibre [1-3]. To obtain robust single-frequency operation, the cavity length of the fibre laser should be as short as possible, ideally a few cm. This drastically reduces the efficiency of these lasers, since only a small fraction of the pump power can be absorbed in a short length of erbium fibre. Much higher efficiencies can be obtained by using a fibre co-doped with ytterbium. The properties and advantages of Er:Yb fibres have largely been discussed in section 7.2. The first demonstration of a single-frequency fibre laser in Er:Yb was realised in 1993 [8]. As we were not able to write gratings directly into the Er:Yb fibres at the time, a grating was written in a germania-boron fibre (ND760) and then spliced to a short section of Er:Yb fibre, which gave a 0.6 dB loss. The total cavity length was 10 cm. The grating, which had a 0.09 nm bandwidth, 40% reflectivity and a Bragg wavelength of 1544.8 nm, was used as the output coupler of the laser. A high reflectivity dielectric mirror was butted to the other end of the fibre. The laser was then pumped through the mirror by a 980 nm laser diode. The very narrow linewidth of the grating insured single-frequency operation even for the maximum output power of 7.6 mW. The fibre laser had a slope efficiency of 10% relative to the incident pump power and a threshold of 7 mW. Mode-hopping was observed occasionally following environmental perturbations.

These results were significantly improved upon by going to a shorter cavity length (~3 cm), using a more efficient Er:Yb fibre (ND844) and reducing the splice loss to 0.12 dB [9]. Several gratings were fabricated in Ge/B fibre with different reflectivities so that the optimum output coupling could be found experimentally. A grating with 70% reflectivity and 0.3 nm bandwidth gave the best performance. This time, up to 19 mW of diode-pumped, single-frequency output was obtained, with a threshold of 4 mW and a slope efficiency of 22% (40% relative to power launched in fibre).
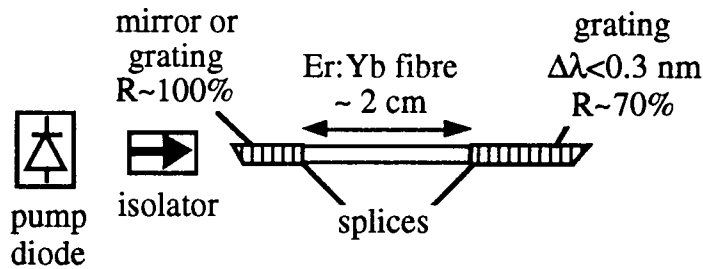
Figure 9-1 - Schematic diagram of single-frequency Er:Yb Fabry-Perot fibre laser.

The realisation of high reflectivity gratings written directly into Er:Yb fibres (chapter 7) immediately led to the first demonstration of a 1.5 μm distributed feedback (DFB) fibre laser, where the Bragg grating covers the whole of the gain region (Fig. 9-2). The spectral characteristics of the grating used for this experiment are shown in Fig. 7-5. The grating was imbedded in a glass capillary and the endfaces were angle-polished to avoid reflections. It is well-known that a DFB laser comprising a uniform grating has a dual frequency output: because the propagation of light is forbidden within the grating stop-band, oscillation can only occur at the edges of the stop-band. To obtain single-frequency operation, one must introduce a phase shift in the grating to create a real state at the Bragg frequency.

Figure 9-2 - Schematic diagram of Er:Yb single-frequency DFB fibre laser.

A distributed phaseshift was externally added by heating the centre of the grating with a resistance wire wrapped around the glass capillary. The magnitude of the phaseshift could be optimised by adjusting the voltage across the wire. This resulted 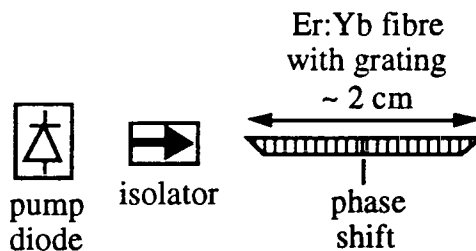in single-frequency output. With a symmetrically distributed phaseshift, an equal amount of power was emitted from both ends of the laser. By displacing the resistance wire towards the output end of the grating, it was possible to increase the fraction of power emitted at the output end of the laser and obtain a maximum single-frequency output of 3.2 mW.

The DFB fibre laser has two main advantages over the Fabry-Perot design. First, as it requires only one grating, it is simpler to manufacture; one could envisage producing such lasers on a commercial basis using a phase-mask with a built-in phase shift. The second advantage is that a DFB laser should be more stable in frequency than a Fabry-Perot laser. This is well-known for laser diodes but remains to be demonstrated for fibre lasers.

9.2.3. Ytterbium lasers

The fluorescence spectrum of Yb^{3+} silica fibres is very broad, extending from 0.95 to 1.2 μm. With the high wavelength selectivity of fibre gratings, it has been possible to demonstrate highly efficient fibre lasers operating at wavelengths of interest throughout this spectral range. These include 1.02 μm pump sources for Pr^{3+}-doped ZBLAN fibres used for 1.3 μm amplifiers and upconversion fibre lasers [12], 1.14 μm pump sources for 0.48 μm Tm^{3+}-doped ZBLAN upconversion fibre lasers [13] and 1.083 μm lasers for helium sensing [14]. Because laser diodes are very difficult to obtain at these wavelengths, Yb^{3+} fibre lasers have become extremely attractive.

Germania-doping is not detrimental to the performance of Yb^{3+} silica fibres, because the rate of non-radiative decay of the ytterbium ions is very low. The inscription of gratings in these fibres is therefore relatively straightforward. It is preferable to avoid hydrogen-loading because of the induced loss around 1 μm (see Fig. 3-17).

The monitoring of the grating growth is made difficult by the high absorption of ytterbium (1 mol% Yb^{3+} gives ~80 dB/m absorption at 1.02 μm) and the absence of commercial LED's around 1 μm. This problem can be avoided by pumping the Yb^{3+} fibre with a laser diode in the range 0.8-0.9 μm and using the fluorescence produced by the fibre to measure the transmission coefficient of the grating (Fig. 9-3). With this technique however, the grating must be written at the very end of the fibre so that most

the fluorescence collected by the spectrum analyser passes through the grating. An alternative technique is to measure the grating in reflection through a 3 dB coupler, using a white light or a fluorescent fibre as the light source. The grating must then be written close to the input end of the Yb^{3+} fibre to minimise the attenuation of the light reflected by the grating. Above ~1.1 μm, the Yb^{3+} absorption is very low and any monitoring technique may be employed.

Cladding-pumped Yb^{3+} fibres are very attractive for producing high power diode-pumped lasers in the 1 μm range [12]. In a cladding-pumped fibre, the core is surrounded by a high N.A. guiding inner cladding. The geometry of this inner cladding is optimised so that the output of a high-power diode array or MOPA can be very efficiently coupled into the fibre and eventually absorbed in the core. A 1.02 μm cladding-pumped laser was demonstrated by writing Bragg gratings at both ends of a 4 m-long section of fibre ND854. This fibre has a 0.16 N.A. Ge/Si core containing ~500 ppm Yb^{3+} which is surrounded by a 0.15 N.A. Ge/Si inner cladding [12]. The setup used for writing and monitoring the gratings is illustrated in Fig. 9-3. The fibre was pumped by a 0.79 μm laser diode and the fluorescence was collected by an ordinary single-mode fibre to spatially filter the fluorescence guided by the inner cladding. The length of fibre between the grating and the collecting fibre was made as short as possible (~10 cm) to minimise the amount of fluorescence generated after the grating.
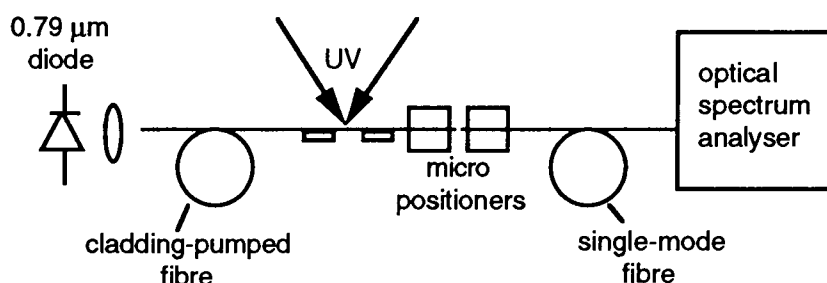
Figure 9-3 - Layout of experimental setup for monitoring gratings in cladding-pumped Yb^{3+} fibre.

Fig. 9-4 shows the transmission spectra of two gratings written in fibre ND854 loaded with hydrogen. The shape and bandwidth (0.8 nm) of the first spectrum is indicative of a high reflectivity (>99%) grating. The transmission of this grating should therefore be close to zero at the Bragg wavelength. This is not the case because there is a non-zero overlap between the fundamental mode of the single-mode fibre and the cladding modes of the cladding-pumped fibre. Taking this into account, the reflectivity of the second grating can be estimated at about 39%.
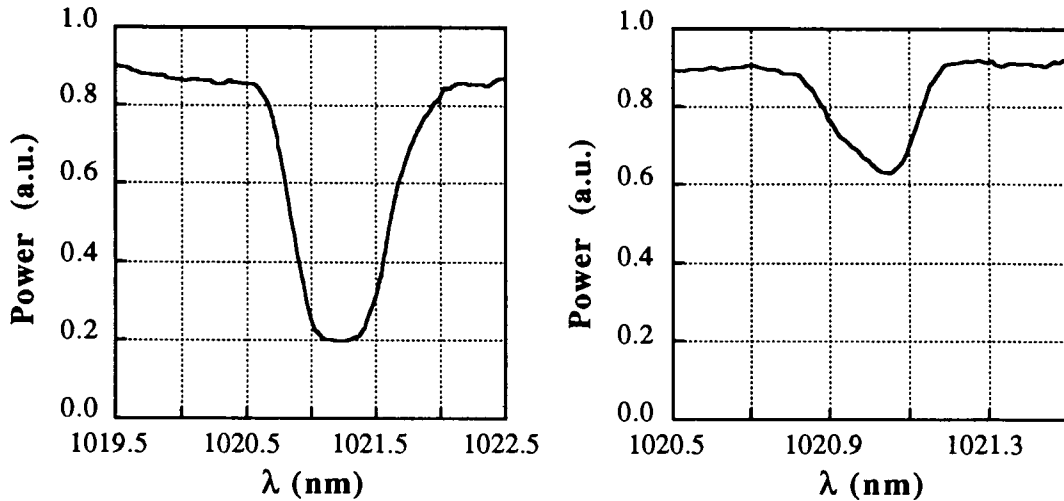
Figure 9-4 - Transmission spectra of high reflector (left) and output coupler (right) for cladding-pumped Yb^{3+} laser in H_2-loaded fibre ND854.

The hydrogen-loading process in the gratings of Fig. 9-4 introduced a 15% loss at 1.02 µm which significantly reduced the performance of the cladding-pumped laser. To avoid this loss, similar gratings were therefore written in an untreated fibre. However, the highest reflectivity that could be obtained in this case was about 62%, as reported in Ref. [12]. This meant that an important fraction of power was emitted by the pump end of the laser and effectively lost. Nevertheless, a 42% slope efficiency was recorded from the emission at the output end of the laser relative to the incident pump power. If the laser emission from both ends was considered, then the efficiency was found to be 70%. With a more photosensitive cladding-pumped Yb^{3+} fibre, or perhaps by optimising the writing process in fibre ND854, it should therefore be possible to improve significantly on those results.

The exposure of a Yb^{3+} germanosilicate fibre to 248.5 nm light pulses causes the ytterbium ion to fluoresce around 1 µm. This probably involves energy transfer from the germania defects to the the ytterbium ions. In a fibre with a high ytterbium concentration, this fluorescence can produce lasing if a sufficiently strong grating is written into the fibre, as shown in Fig. 9-5. Below 1 µm, the fluorescence is strongly absorbed in the unpumped section of fibre which is why the ytterbium fluorescence peak at 0.98 µm cannot be observed in Fig. 9-5. Above 1 µm, the fluorescence is still strong but the absorption is very small because the broad Stark splitting of the ytterbium ions, which results in a fluorescence peak at 1.04 µm.
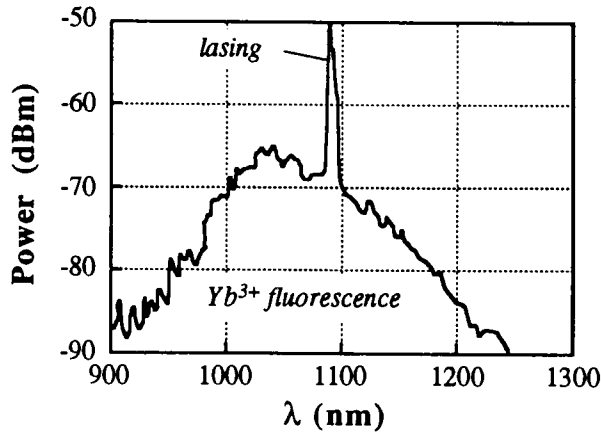
Figure 9-5 - Spectrum of excimer-pumped DFB laser in Yb^{3+} fibre
ND864 measured with 10 nm resolution and 50 ms response time.

In this fibre, the lasing appears in the initial stages of the writing of a grating, with each 20 ns excimer pulse producing a short pulse near the Bragg wavelength of the grating. These pulses are very intense, making it impossible to monitor the growth of the grating using the above methods. Instead, one can measure the output of this side-pumped DFB fibre laser in real time to monitor the evolution of the grating, as illustrated in Fig. 9-6. The saturation of the laser output presumably indicates that the grating has reached its maximum strength. The transmission spectrum of the final grating is shown in Fig. 9-7. This grating was used as the high reflector in a single-frequency 1.083 μm fibre laser [14].
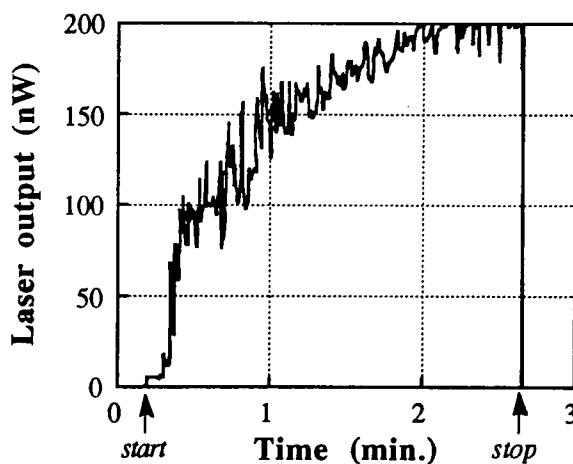
Figure 9-6 - Evolution of excimer-pumped Yb^{3+} laser output during inscription of grating, measured with 5 ms response time.
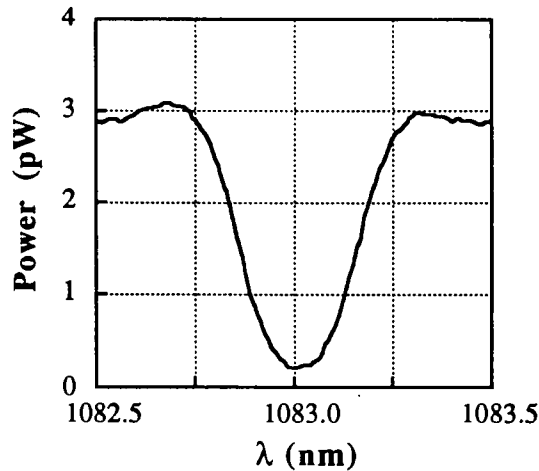
Figure 9-7 - Final transmission spectrum of grating of Fig. 9-6.

9.2.4. Thulium laser

A project currently under way is to develop a tunable 1.67 μm laser for methane sensing. This wavelength corresponds to an overtone C-H absorption and is within the fluorescence spectrum of thulium. By using fibre gratings as feedback elements, it should be possible to force a thulium laser to oscillate at precisely the right wavelength.

As Tm^{3+} fibres usually contain germania, the inscription of gratings in these fibres does not present any added difficulty. Moreover, since the wavelength of interest is far from the absorption bands induced by the hydrogen-loading process, this technique may be used without penalty to enhance the photosensitivity of the Tm^{3+} fibres. The absorption of thulium at 1.67 μm is however quite important (~0.01 dB/m/ppm) and, consequently, one of the grating monitoring techniques described in the previous section for the Yb^{3+} fibres must be employed.

Very strong 1.67 μm gratings have been written in fibre ND839 containing approximately 9 mol% GeO_2 and loaded with hydrogen. Index modulations of up to 1.8×10^{-3} were measured giving a grating bandwidth of 1.65 nm at 1.67 μm. A 1.67 laser, combining such a high reflector and a lower reflectivity, narrow band output coupler, should therefore be demonstrated shortly.

9.3. <u>Dispersion compensation</u>

Most of the optical fibre systems used for telecommunications today have been designed for operation at 1.31 µm. In standard single-mode optical fibres, this wavelength corresponds both to a low-loss transmission window and to the point of zero chromatic dispersion. However, with the introduction of the erbium-doped fibre amplifier and the need to increase the capacity of telecommunications systems, optical networks are now being designed to operate in the third telecommunications windows at 1.55 µm. Although dispersion-shifted fibres are now available which have zero dispersion at 1.55 µm, the millions of kilometers of fibre already in operation throughout the world have a dispersion of about 17 ps/km.nm at that wavelength. Rather than to replace existing links with dispersion-shifted fibre, the preferred route would be to upgrade the existing systems by adding dispersion compensators.

An attractive way of compensating for dispersion is to use a linearly chirped grating [15-18], an idea proposed by Ouellette in 1987 [19]. Fig. 9-8 illustrates this scheme for a 10 ps 1.55 µm pulse going through 100 km of standard fibre.
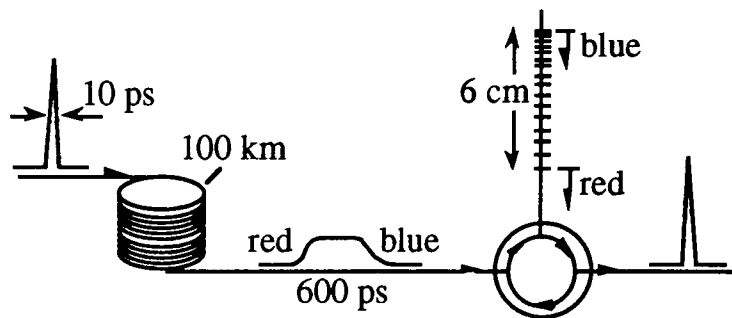
Figure 9-8 - Dispersion compensation of 100 km standard fibre at 1.55 µm using linearly chirped grating and optical circulator.

The optical bandwidth of a 1.55 µm transform-limited gaussian pulse of duration τ is approximately

$$\Delta\lambda \approx \frac{3.5 \text{ nm}}{\tau(\text{ps})} \qquad (9\text{-}1)$$

After propagation through a distance d in standard fibre, the pulse duration increases to

$$\tau' \approx 60 \text{ ps} \times \frac{d(\text{km})}{\tau(\text{ps})} \qquad (9\text{-}2)$$

which means that the long wavelength components of the pulse trail the short wavelength components by

$$\Delta d \approx 1.2 \text{ cm} \times \frac{d(km)}{\tau(ps)} \qquad (9\text{-}3)$$

In the example of Fig. 9-8 the group delay is therefore about 600 ps or 12 cm. A simplified analysis of a chirped grating is to consider that each point along the grating has a local Bragg wavelength and stop-band [20]. This assumption is valid if the width of the stop-band $(=\lambda\delta n/n_{av})$ is small compared to the chirp (total variation of the Bragg wavelength). Within this approximation, in the linearly chirped grating of Fig. 9-8, the long wavelength components of the pulse are reflected at the start of the grating while the short wavelength components are reflected at the back, which can result in a delay upon reflection corresponding to twice the length of the grating. In this example, the grating therefore would have to be at least 6 cm long, with a 0.35 nm chirp. This grating, however, would only operate at a specific wavelength over the 0.35 nm bandwidth of the pulse. In general, to compensate over a bandwidth $\Delta\lambda$, the minimum grating length required is

$$L_{min} \approx 0.18 \text{ cm} \times d(km) \times \Delta\lambda(nm) \qquad (9\text{-}4)$$

For example, to compensate for the dispersion of 100 km of fibre over the whole gain spectrum of erbium (~20 nm), a 3.6 m grating would be required! It is unlikely that such a grating will ever be produced. However, within the limits of current fibre gratings technology, it is possible to achieve more modest yet highly attractive performances.

The first requirement for the development of fibre grating dispersion compensators is the ability to produce very long gratings. High-quality 4 cm-long phase masks are now commercially available which could easily produce dispersion compensators for a distance-bandwidth product of 22 km·nm. With the e-beam writing technique, even longer phase-masks could probably be fabricated by a step-and-repeat process, where an arbitrary number of short grating sections are accurately stitched together. Our current interferometer is capable to producing grating lengths of up to to ~2.5 cm. However, according to Eq. (4-1), the coherence length of the line-narrowed excimer laser should be sufficient to write 10 cm-long gratings for 1.5 μm applications. To exploit this capability, a new interferometer was designed, which uses 15×2.5 cm custom-made rectangular mirrors, as shown in Fig. 9-9. This design is more compact than the interferometer of Fig. 4-3, in order to accommodate the larger optics. A scanning mirror is used to expose the full length of the grating with a narrow UV beam. The clear aperture of the interferometer is about 9 cm which, according to Eq. (9-4), gives a distance-bandwidth product of 50 km·nm for dispersion compensation. This interferometer has only been built recently and is still at an experimental stage.
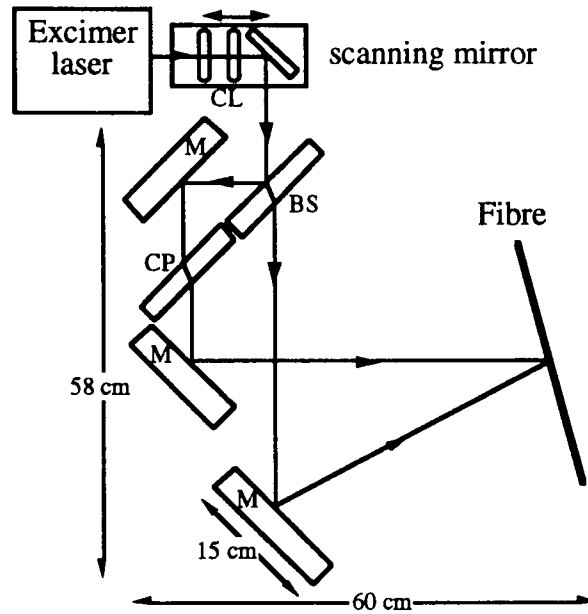
Figure 9-9 - Layout of interferometer for writing 10 cm fibre gratings.
M: mirror, BS: beamsplitter, CL: cylindrical lenses, CP: compensating plate.

The second requirement is to be able to add a linear chirp to these long gratings. Several techniques for producing fibre gratings with built-in chirps have been developed in recent years. These include writing gratings in bent or tapered [21] fibres, or placing a weak lens in one of the beams of an interferometer [22][23][18]. Other methods are more appropriate for long chirped gratings. One such method consists of inducing a refractive index gradient in a section of fibre prior to writing the grating [15]. This can be achieved by exposing the section of fibre to a UV beam of spatially varying intensity. Another one is to use phase masks of varying period. Masks with stepwise varying period were recently manufactured by e-beam writing at BT Labs and used in dispersion compensation experiments [24].

An alternative to writing fibre gratings with built-in chirps is to chirp the gratings externally, after fabrication. This is achieved by applying a strain [25] or temperature gradient to the grating. Post-chirping techniques have the advantage of being tunable, which can be very attractive for dispersion compensation applications, since the amount of the dispersion in a particular fibre link may not be precisely known in advance.

The dispersion compensation project of the ORC is in its early stages. Very long gratings have just recently been fabricated for the first time and new techniques of producing chirped gratings are currently under investigation. Also, experiments on the interaction

of picosecond pulses with unchirped gratings were recently carried out by D. Taverner and collaborators [26]. With the available resources, rapid progress is expected in this research area in the near future.

9.4. Sensors

The application of strain, temperature or pressure to a fibre grating causes a shift in the Bragg wavelength due to changes in the index and length of the host fibre. Fibre gratings can therefore be used as sensing elements for measuring these three quantities [27,28]. Fibre gratings offer many advantages over other types of optical fibre sensors, namely: stability, compactness, linearity of response, low insertion loss and eventually low cost. The gratings can be imbedded in composite materials to create 'smart structures' [29] and arrays of gratings, possibly fabricated during the draw, could be used for quasi-distributed sensing [30,31].

The dependence of the Bragg wavelength on parameter ξ ($\equiv$ temperature T, pressure P or strain ε) is described by the relation

$$\frac{1}{\lambda_B}\frac{\partial \lambda_B}{\partial \xi} = \frac{1}{n}\frac{\partial n}{\partial \xi} + \frac{1}{L}\frac{\partial L}{\partial \xi} \qquad (9\text{-}5)$$

Over the small shifts that are usually involved, the derivatives of Eq. (9-5) are practically constant.
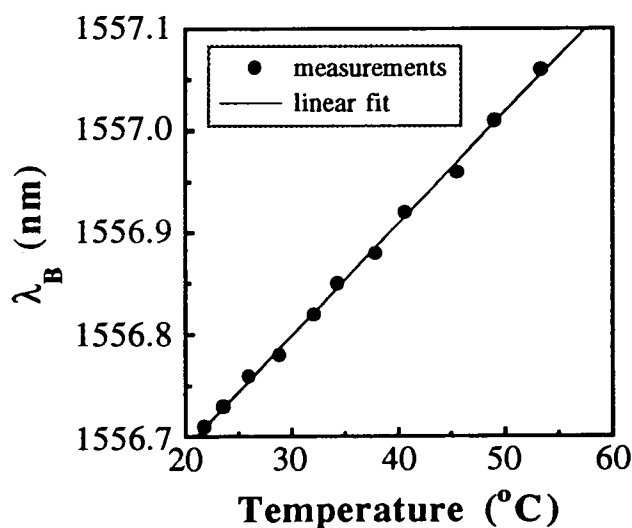
Figure 9-10 - Influence of temperature on Bragg wavelength of grating in fibre HD066.

Fig. 9-10 shows the temperature dependance of a 1557 nm grating written in Ge/B co-doped fibre HD066. In this experiment, the temperature of the grating was tuned using a Peltier element and measured with a thermocouple. The experimental points are very well fitted by a linear function. From this fit, it was found that for this fibre

$$\frac{\partial \lambda_B}{\partial T} \approx 0.011 \text{ nm/°C} \quad (\frac{\partial \upsilon}{\partial T} \approx -1.36 \text{ GHz/°C}) \tag{9-6}$$

The pressure dependence of a similar grating was also measured [28] and it was found that, at 1535 nm,

$$\frac{\partial \lambda_B}{\partial P} \approx -0.0031 \text{ nm/MPa} \quad (0.39 \text{ GHz/MPa}) \tag{9-7}$$

This effect could therefore only be used for measuring high pressures. The strain sensitivity of a third grating in fibre HD066 was measured by stretching the grating using a 0.1 μm precision actuator. The data are shown in Fig. 9-11 along with a linear fit. From the slope of this fit, it was found that

$$\frac{1}{\lambda_B} \frac{\partial \lambda_B}{\partial \varepsilon} \approx 0.772 \tag{9-8}$$

Figure 9-11 - Influence of strain on Bragg wavelength of grating in fibre HD066.

From Eqs. (9-6) to (9-8), it can be seen that, by measuring the shift in the Bragg wavelength of a 1550 nm grating with an accuracy of 0.01 nm, one can predict the temperature, pressure or strain of a fibre with precisions of 1°C, 3 MPa or 8 μstrain, respectively.

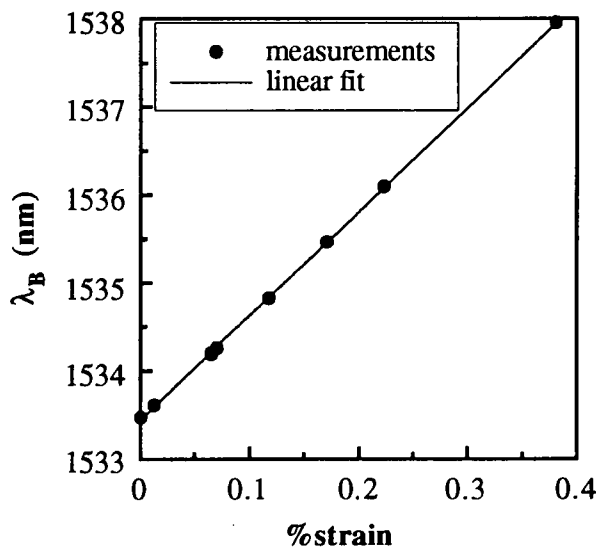One of the main problems in using fibre gratings for sensing is that the gratings can be affected simultaneously by different environmental changes. One solution to this problem is to use dual wavelength gratings, as recently demonstrated by Xu *et al.* [32]. In this experiment, two short Type II gratings were written side-by-side in fibre ND383, a germania-silica fibre with a numerical aperture of 0.3 and a cutoff wavelength of 745 nm. Using the Type II mechanism, it was possible to obtain short (~3 mm) and high reflectivity gratings. The sensor head was therefore only 6 mm long. The characteristics of the two gratings were

grating 1 : $\lambda_B \approx 1298$ nm, $R \approx 70\%$, $\Delta\lambda \approx 0.9$ nm, loss≈ 1 dB

grating 2 : $\lambda_B \approx 848$ nm, $R \approx 55\%$, $\Delta\lambda \approx 0.45$ nm, loss≈ 0.5 dB

The high numerical aperture of the fibre insured that bend loss was low at both wavelengths. The two Bragg wavelengths were chosen so that low-cost commercial LED's could be used to interrogate the gratings. The strain and temperature sensitivities of the two gratings were measured in succession as in Fig. 9-11 and 9-12. It was found that both the strain and thermal sensitivities of the fibre were wavelength-dependent:

$$\text{at 1298 nm, } \frac{1}{\lambda_B}\frac{\partial\lambda_B}{\partial\varepsilon} \approx 0.740 \text{ and } \frac{1}{\lambda_B}\frac{\partial\lambda_B}{\partial T} \approx 6.72\times10^{-6}/^{\circ}\text{C}$$

$$\text{at 848 nm, } \frac{1}{\lambda_B}\frac{\partial\lambda_B}{\partial\varepsilon} \approx 0.696 \text{ and } \frac{1}{\lambda_B}\frac{\partial\lambda_B}{\partial T} \approx 7.43\times10^{-6}/^{\circ}\text{C}$$

Because of this wavelength dependence, it was possible to uniquely determine the strain and temperature by measuring the Bragg wavelength shifts of the two gratings. Using an optical spectrum analyser to measure these shifts with 0.01 nm accuracy, the strain and temperature could be predicted with an accuracy of 10 µstrain and 5°C, respectively. These errors could be reduced by using a more accurate interrogation system.

9.5. <u>Conclusion</u>

The integration of fibre gratings into the various areas of applications described in this chapter has been extremely successful and has yielded several new and highly promising devices, such as linear cavity single-frequency fibre lasers, DFB fibre lasers, distributed sensor arrays and dispersion compensators. The expertise which has now been established in the fabrication of fibre gratings with wide ranging properties and in a variety of optical fibres has been an essential part of this success. This chapter only described a few of the possibilities offered by this new technology: new devices are constantly being demonstrated and will certainly continue to do so in the years ahead.

9.6. **References**

1. G.A. Ball, W.W. Morey and W.H. Glenn, "Standing-wave monomode erbium fiber laser", *IEEE Photon. Tech. Lett.*, **3** (7), pp. 613-615, 1991.

2. G.A. Ball and W.W. Morey, "Continuously tunable single-mode erbium fiber laser", *Opt. Lett.*, **17** (6), pp. 420-422, 1992.

3. G.A. Ball and W.H. Glenn, "Design of a single-mode linear-cavity erbium fiber laser utilising Bragg reflectors", *J. Lightwave Tech.*, **10** (10), pp. 1338-1343, 1992.

4. G.A. Ball, C.G. Hull-Allen and J. Livas, "Frequency noise of a Bragg grating fibre laser", *Electron. Lett.*, **30** (15), pp. 1229-1230, 1994.

5. S.V. Chernikov, J.R. Taylor and R. Kashyap, "Coupled-cavity erbium fiber laser incorporating fiber grating reflectors", *Opt. Lett.*, **18** (23), pp. 2023-2025, 1993.

6. S.V. Chernikov, R. Kashyap, P.F. McKee and J.R. Taylor, "Dual-frequence all-fiber grating laser source", *Electron. Lett.*, **29** (12), pp. 1089-1091, 1993.

7. R.P. Davey, R.P.E. Fleming, K. Smith, R. Kashyap and J.R. Armitage, "Mode-locked erbium fiber laser with wavelength selection by means of fiber Bragg grating reflector", *Electron. Lett.*, **27** (22), pp. 2087-2088, 1991.

8. J.T. Kringlebotn, P.R. Morkel, L. Reekie, J.-L. Archambault and D.N. Payne, "Efficient diode-pumped single-frequency erbium:ytterbium fiber laser", *IEEE Photon. Tech. Lett.*, **5** (10), pp. 1162-1164, 1993.

9. J.T. Kringlebotn, J.-L. Archambault, L. Reekie, J.E. Townsend, G.G. Vienne and D.N. Payne, "Highly efficient, low-noise grating-feedback $Er^{3+}:Yb^{3+}$ codoped fibre laser", *Electron. Lett.*, **30** (12), pp. 972-973, 1994.

10. J.T. Kringlebotn, J.-L. Archambault, L. Reekie and D.N. Payne, "$Er^{3+}:Yb^{3+}$ co-doped fibre DFB laser", *to appear in Opt. Lett.*, 1994.

11. J.L. Zyskind, J.W. Sulhoff, P.D. Magill, K.C. Reichmann, V. Mizrahi and D.J. DiGiovanni, "Transmission at 2.5 Gbits/s over 654 km using an erbium-doped fiber grating laser source", *Electron. Lett.*, **29** (12), pp. 1105-1106, 1993.

12. H.M. Pask, J.L. Archambault, D.C. Hanna, L. Reekie, P.St.J. Russell, J.E. Townsend and A.C. Tropper, "Operation of a cladding-pumped Yb^{3+}-doped silica fiber lasers in 1µm region", *Electron. Lett.*, **30** (11), pp. 863-865, 1994.

13. P.R. Barber, C.J. Mackechnie, R.D.T. Lauder, H.M. Pask, A.C. Tropper, D.C. Hanna, S.D. Butterworth, M.J. McCarthy, J.-L. Archambault and L. Reekie, "All solid-state blue room-temperature thulium-doped upconversion fibre laser", *Compact Blue-Green Lasers Topical Meeting Proceedings*, paper CFA3-1, pp. 68-70, Salt-Lake City, Utah, 1994.

14. J.M. Dawes, H.M. Pask, J.-L. Archambault, J.E. Townsend, D.C. Hanna, L. Reekie and A.C. Tropper, "Single frequency lasers and efficient cladding-pumped lasrs using Yb^{3+}-doped silica fibre", *CLEO-Europe Technical Digest*, paper CThJ1, pp. 358, Amsterdam, 1994.

15. K.O. Hill, F. Bilodeau, B. Malo, T. Kitagawa, S. Theriault, D.C. Johnson and J. Albert, "Aperiodic in-fiber Bragg gratings for optical fiber dispersion compensation", *OFC'94 Postdeadline Papers*, paper PD2-3, San Jose, 1994.

16. R. Kashyap, S.V. Chernikov, P.F. McKee and J.R. Taylor, "30 ps chromatic dispersion compensation of 400 fs pulses at 100 Gbits/s in optical fibres using an all fibre photoinduced chirped reflection grating", *Electron. Lett.*, **30** (13), pp. 1078-1080, 1994.

17. B.J. Eggleton, P.A. Krug, L. Poladian, K.A. Ahmed and H.F. Liu, "Dispersion compensation by using Bragg-grating filters with self-induced chirp", *OFC'94 Technical Digest*, paper ThK3, San Jose, 1994.

18. J.A.R. Williams, I. Bennion, K. Sugden and N.J. Doran, "Fibre dispersion compensation using a chirped in-fibre Bragg grating", *Electron. Lett.*, **12** (30), pp. 985-987, 1994.

19. F. Ouellette, "Dispersion cancellation using linearly chirped Bragg filters in optical waveguides", *Opt. Lett.*, **12** (10), pp. 847-849, 1987.

20. L. Poladian, "Graphical and WKB analysis of nonuniform Bragg gratings", *Phys. Rev. E*, **48** (6), pp. 4758-4767, 1994.

21. K.C. Byron, K. Sugden, T. Bricheno and I. Bennion, "Fabrication of chirped Bragg gratings in photosensitive fiber", *Electron. Lett.*, **29** (18), pp. 1659-1660, 1993.

22. M.C. Farries, C.M. Ragdale and D.C.J. Reid, "Broadband chirped fibre Bragg filters for pump rejection and recycling in erbium doped fibre amplifiers", *Electron. Lett.*, **28** (5), pp. 487-489, 1992.

23. M.C. Farries, K. Sugden, D.C.J. Reid, I. Bennion, A. Molony and M.J. Goodwin, "Very broadband reflection bandwidth (44 nm) chirped fiber gratings and narrow bandpass filters produced by the use of an amplitude mask", *Electron. Lett.*, **30** (11), pp. 891-892, 1994.

24. R. Kashyap, P.F. McKee, R.J. Campbell and D.L. Williams, "Novel method for producing all fibre photo-induced chirped gratings", *Electron. Lett.*, **30** (12), pp. 996-998, 1994.

25. P.C. Hill and B.J. Eggleton, "Strain gradient chirp of fibre Bragg gratings", *Electron. Lett.*, **30** (14), pp. 1172-1174, 1994.

26. D. Taverner, D.J. Richardson, J.-L. Archambault, L. Reekie, P.St.J. Russell and D.N. Payne, "Experimental investigation of picosecond pulse reflection from fiber gratings", *CLEO'94 Technical Digest*, paper CWP4, pp. 262-263, Anaheim, Ca., 1994.

27. W.W. Morey, G. Meltz and W.H. Glenn, "Bragg-grating temperature and strain sensors", in *Springer Proceedings in Physics - Optical Fiber Sensors*, Springer-Verlag, Berlin, 1989, pp. 526-531.

28. M.G. Xu, L. Reekie, Y.T. Chow and J.P. Dakin, "Optical in-fibre grating high pressure sensor", *Electron. Lett.*, **29** (4), pp. 398-399, 1993.

29. J.R. Dunphy, G. Meltz, F.P. Lamm and W.W. Morey, in "Fiber Optic Smart Structures and Skins III", SPIE Vol. 1370, pp. 116-118, 1990.

30. L. Dong, J.L. Archambault, L. Reekie, P.St.J. Russell and D.N. Payne, "Single-pulse Bragg gratings written during fiber drawing", *Electron. Lett.*, **29** (17), pp. 1577-1578, 1993.

31. C.G. Askins, M.A. Putnam, G.M. Williams and E.J. Friebele, "Stepped-wavelength optical-fiber Bragg grating arrays fabricated in line on a draw tower", *Opt. Lett.*, **19** (2), pp. 147-149, 1994.

32. M.G. Xu, J.L. Archambault, L. Reekie and J.P. Dakin, "Discrimination between strain and temperature effects using dual-wavelength fibre grating sensors", *Electron. Lett.*, **30** (13), pp. 1085-1087, 1994.

Chapter 10
Conclusion

10.1. Achievements

The main realisation of this project has been the establishment of an expertise in the fabrication and applications of fibre Bragg gratings, based upon a good understanding of the optical properties of fibre gratings, of the formation mechanisms and of the fabrication techniques. As a result, the ORC now has in place a reliable and versatile source of fibre gratings written holographically with a line-narrowed KrF excimer laser.

Understanding the optical properties of fibre gratings has been an essential starting point. The general formalism developed in this thesis gives a broad understanding of these properties by considering the full three-dimensional nature of fibre gratings and including the nonlinear photosensitive response of optical fibres. As a result, complex phenomena such as cladding-mode coupling and the saturation dynamics of the index modulation have been satisfactorily explained for the first time. Practical methods of minimising the short wavelength loss due to cladding-mode coupling have been described.

An easily tunable and highly stable three-mirror interferometer was designed for use with the line-narrowed excimer laser. Several techniques were developed to insure a quick and reliable alignment. This interferometer was found to be a very useful tool not only to produce a wide variety of fibre gratings, but also to evaluate the photosensitivity of a large number of optical fibres and study the dynamics of the photoinduced index changes.

The largest refractive index changes were obtained in fibres containing germania. In these fibres, all photosensitivity-related phenomena were shown to follow similar dynamics, characteristic of dispersive charge transport. To explain these observations, a model was put forward based on a three-level energy diagram of germania-related oxygen-deficient defects where the highest excited state is located very close to the conduction band of silica. Electrons are excited to this level by 5 eV photons and then thermally excited to the conduction band, resulting in the the photo-thermal ionisation of the defect. An important prediction of this model is that the writing of fibre gratings should be more efficient at high temperatures. Supportive evidence was obtained when it

was found that the writing of gratings at higher pulse fluences linearly increased the value of the dispersion parameter, in accordance with the model.

This model was further tested in a pump-probe experiment, where the transmission of germanosilicate optical fibres was monitored at infrared wavelengths in the presence of an excimer pulse on a nanosecond timescale. An important result of this experiment was the first observation of UV-induced transient gain in the 1 μm region, in fibres with a high germania content. Peak gains of up to 10 dB/cm were recorded. The magnitude and spectrum of this gain are well predicted by the three-level energy diagram. The experiment also revealed the presence of transient absorption with a lifetime of order 70 ns, which was attributed to conduction electrons. This absorption increased rapidly as the wavelength of the probe beam was decreased. The overall dynamics of the transmission changes were found to be complex and difficult to interpret.

Sensitisation techniques, in particular boron co-doping and hydrogen-loading, have been evaluated. Germanosilicate fibres co-doped with boron consistently showed higher photosensitivity together with low splice and transmission losses. Hydrogen-loading is by far the most effective, but introduces absorption bands which can proscribe the use of this technique at certain wavelengths.

The hydrogen-loading technique was extended to several germania-free optical fibres, including erbium:ytterbium, aluminosilicate, phosphosilicate and tantalum-doped fibres. Small index changes ($\sim 10^{-6}$) were obtained in all of these fibres in their untreated form. In the erbium:ytterbium fibres, which also contain aluminum and phosphorus, hydrogen-loading was found to increase the maximum photoinduced index change by up to two orders of magnitude. As a result, gratings with as much as 99% reflectivity were written in these fibres. In all other germania-free fibres under test, hydrogen-loading had no significant effect. An investigation of UV absorption changes down to 190 nm in alumino-phosphosilicate preforms doped with different combinations of erbium and ytterbium and loaded with hydrogen did not elucidate the origin of the large index changes seen in the erbium:ytterbium fibres.

Two different techniques were used for producing fibre gratings: single-pulse and multiple-pulse writing. For most practical applications, multiple-pulse writing is required, as it allows the index modulation of a grating to be accurately controlled so that the grating reflectivity and bandwidth can meet specific requirements. With this technique, grating bandwidths ranging form less than 0.1 to 3.5 nm and reflectivities in

excess of 99.99% were demonstrated. Highly uniform gratings were obtained despite the poor quality of the excimer laser beam, using beam-scanning or beam-masking techniques. During multiple-pulse writing, it is possible to monitor both the index modulation amplitude and average index change of a grating. By comparing such measurements with a calculation of the Fourier components of the grating it was found that the ratio of the index modulation to the average index change was significantly larger than the maximum possible value predicted by the model. This result was interpreted as evidence that part of the UV-induced index change is caused by a compaction of the exposed core glass.

The single-pulse writing technique is ideally suited for mass production as the writing time is reduced to 20 ns. By studying the dependence of the photoinduced index modulation against the pulse fluence, two distinct regimes of single-pulse grating formation were discovered, now known as Type I and Type II. The Type I mechanism produces gratings with index modulations of order 10^{-5}, which, for grating lengths of 1 or 2 cm, can give reflectivities of up to 10-15%. The Type II gratings are obtained above a sharply defined pulse fluence threshold in fibres with a high germania content. They are characterised by very high index modulations (usually in in excess of 10^{-3}), high thermal stability, insensitivity to blue/green light, but also high background loss and strong cladding and radiation mode coupling. Type II gratings are thought to result from the periodic optical breakdown of the glass at the core-cladding interface, caused by the interaction of the UV pulse with the plasma formed by conduction electrons. The advantages of the single-pulse technique were highlighted when both Type I and Type II gratings were written during the fibre drawing process for the first time. Fully packaged gratings were produced at a rate of up to several gratings per second. Long arrays of Type I or Type II gratings could find immediate applications in distributed sensing.

Fibre gratings have found many applications inside the ORC. One application directly linked to this project is the grating-frustrated coupler, a new type of channel-dropping filter based on the combination of a Bragg grating and a polished fibre coupler. The grating, which is located on one side of the coupling region, prevents the transfer of power in the coupler over narrow optical bandwidth, thus enabling one wavelength channel to be extracted from a broad wavelength spectrum. The performance of the first prototype - 0.7 nm bandwidth, 13 dB isolation and 70% peak transmission - was close to the predictions of a model based on coupled-wave theory and could be improved with a stronger, more uniform grating and by reducing the index mismatch of the coupler. The

grating-frustrated coupler is one of very few existing all-fibre channel-dropping filters and would be a valuable component for dense WDM or used as a transmission filter.

Numerous fibre gratings have also been supplied to other research groups in the ORC. Because of the accurate wavelength control and simplicity that they offer, fibre gratings have played an important role in several fibre laser projects. Single-frequency operation has been obtained in short erbium:ytterbium and ytterbium fibre lasers and the recent advances in the writing of gratings in erbium:ytterbium fibres directly led to the first demonstration of a 1.5 µm DFB fibre laser. Another important contribution of fibre gratings has been to force the operation of fibre lasers at wavelengths which can be quite far from the peak of the gain spectrum. The direct consequence of this result is that fibre lasers can now operate at most wavelengths between 1 and 2 µm. Fibre gratings have had a similar impact on the field of optical fibre sensors, by allowing strain, temperature or pressure to be monitored at specific points over the length of an optical fibre. The fabrication of gratings during the draw could make these systems extremely practical. Much of the effort in the current fibre gratings research is directed towards the fabrication of long, chirped gratings for dispersion compensation. The first part of this project - the production of very long (~9 cm) gratings - is near completion and gratings that can compensate for a few hundred kilometers of dispersion in standard fibre at 1.55 µm should soon be a reality.

10.2. <u>Future directions</u>

The inscription of photorefractive gratings in germanosilicate optical fibres has now become a routine procedure. Even so, there are still many unanswered questions concerning the origins of the photoinduced index changes in these fibres. A model of the interaction of UV light with oxygen-deficient centres has been proposed in this work which needs to be evaluated more thoroughly. However, this model, even if valid, does not identify the ultimate causes the index change or how the photosensitivity of an optical fibre can be improved at the fabrication stage. These are problems that remain to be solved.

It is now emerging that the writing of fibre gratings in germanosilicate fibres is more efficient at 193 nm than in the 242 nm band. An important aspect of future research should therefore be to investigate the dynamics of grating formation at 193 nm and compare them to what is already known from experiments at 248.5 nm. Using more energetic photons is also likely to improve the photosensitivity of germania-free fibres,

such as aluminosilicate and phosphosilicate fibres, which in general have higher absorptions at shorter UV wavelengths.

Another exciting and very promising avenue is to study the photosensitivity of new glasses. New silica fibre compositions may be found that offer an interesting alternative to or even surpass germanosilicate fibres. Non-silica based glasses, such as fluorozirconates or chalcogenides, are currently being developed for fibre manufacturing, to be used in advanced fibre lasers and amplifiers. There will be a growing need for the writing of permanent photorefractive gratings in these fibres. The ORC is in a unique position both to develop and test these new glasses.

Many of the future developments in the field of fibre gratings will be driven by new applications. A good example is the dispersion compensation project which has created the need for the longest possible chirped gratings. In general, it will be necessary to constantly broaden the range of possibilities offered by fibre gratings, which means making them longer, stronger, with exotic profiles and in different glasses.

List of publications

In journals:

1. I. Abdulhalim, J.-L. Archambault, L. Reekie, C.N. Pannell and P.St.J. Russell, "Elasto-optically induced modulation of in-fiber grating", *IEEE Photon. Tech. Lett.*, **5** (12), pp. 1395-1397, 1993.

2. J.-L. Archambault, L. Reekie and P.St.J. Russell, "High reflectivity and narrow bandwidth fibre gratings written by single excimer pulse", *Electron. Lett.*, **29** (1), pp. 28-29, 1992.

3. J.-L. Archambault, L. Reekie and P.St.J. Russell, "100% reflectivity Bragg reflectors produced in optical fibres by single excimer laser pulses", *Electron. Lett.*, **29** (5), pp. 453-455, 1993.

4. J.-L. Archambault, P.St.J. Russell, S. Barcelos, P. Hua and L. Reekie, "Grating-frustrated coupler: novel channel-dropping filter in single-mode optical fibre", *Opt. Lett.*, **19** (3), pp. 180-182, 1994.

5. L. Dong, J.-L. Archambault, L. Reekie, P.St.J. Russell and D.N. Payne, "Bragg gratings written in Ce^{3+}-doped fibres by single excimer laser pulses", *Opt. Lett.*, **18** (11), pp. 861-863, 1993.

6. L. Dong, J.-L. Archambault, E. Taylor, M.P. Roe, L. Reekie and P.St.J. Russell, "Photosensitivity in tantalum-doped silica optical fibres", *In preparation*, pp. 1994.

7. L. Dong, J.-L. Archambault, L. Reekie, P.St.J. Russell and D.N. Payne, "Single-pulse Bragg gratings written during fiber drawing", *Electron. Lett.*, **29** (17), pp. 1577-1578, 1993.

8. L. Dong, J.-L. Archambault, L. Reekie, P.St.J. Russell and D.N. Payne, "A study of photo-induced absorption change in germanosilicate preforms: evidence for the colour-centre model of photosensitivity", *Submitted to Appl. Opt.*, pp. 1994.

9. D. Jackson, A.B. Lobo Ribeiro, L. Reekie and J.-L. Archambault, "Simple multiplexing scheme for fibre optic grating sensor network", *Opt. Lett.*, **18** (14), pp. 1192-1194, 1993.

10. A. Kamal, S.E. Kanellopoulos, J.-L. Archambault, P.St.J. Russell, V.A. Handerek and A.J. Rogers, "Holographically-written reflective polarization filter in single-mode optical fibers", *Opt. Lett.*, **17** (17), pp. 1189-1191, 1992.

11. J.T. Kringlebotn, J.-L. Archambault, L. Reekie and D.N. Payne, "Er^{3+}:Yb^{3+} co-doped fibre DFB laser", *to appear in Opt. Lett.*, pp. 1994.

12. J.T. Kringlebotn, J.-L. Archambault, L. Reekie, J.E. Townsend, G.G. Vienne and D.N. Payne, "Highly efficient, low-noise grating-feedback Er^{3+}:Yb^{3+} codoped fibre laser", *Electron. Lett.*, **30** (12), pp. 972-973, 1994.

13. J.T. Kringlebotn, P.R. Morkel, L. Reekie, J.-L. Archambault and D.N. Payne, "Efficient diode-pumped single-frequency erbium:ytterbium fiber laser", *IEEE Photon. Tech. Lett.*, **5** (10), pp. 1162-1164, 1993.

14. H.M. Pask, J.-L. Archambault, D.C. Hanna, L. Reekie, P.St.J. Russell, J.E. Townsend and A.C. Tropper, "Operation of a cladding-pumped Yb^{3+}-doped silica fiber lasers in $1\mu m$ region", *Electron. Lett.*, **30** (11), pp. 863-865, 1994.

15. P.St.J. Russell, J.-L. Archambault and L. Reekie, "Fiber gratings", *Physics World*, **6** (10), pp. 41-46, 1993.

16. M.G. Xu, J.-L. Archambault, L. Reekie and J.P. Dakin, "Discrimination between strain and temperature effects using dual-wavelength fibre grating sensors", *Electron. Lett.*, **30** (13), pp. 1085-1087, 1994.

17. M.G. Xu, H. Geiger, J.-L. Archambault, L. Reekie and J.P. Dakin, "Novel interrogating system for fiber grating sensors using an acoustooptic tunable filter", *Electron. Lett.*, **29** (17), pp. 1510-1511, 1993.

In conferences:

18. J.-L. Archambault, "Applications of gratings in WDM systems", *Rank Prize Fund Mini-Symposium on All-Optical Networks* , Grasmere, U.K., 1994.

19. J.-L. Archambault, L. Reekie and P.St.J. Russell, "Excimer laser production of fibre Bragg gratings", *Meeting on Photosensitivity and Self-Organization in Optical Fibers and Waveguides* , *SPIE Vol. 2044*, pp. 69-75, Quebec, 1993.

20. J.-L. Archambault, L. Reekie, P.St.J. Russell and J.T. Kringlebotn, "Utilisations des fibres à réseaux de Bragg pour le multiplexage en longueur d'onde", 3rd *Colloquium on Guided-Wave Optics and Photonics, 62nd ACFAS Congress Proceedings*, p. 63, Montreal, 1994.

21. J.-L. Archambault and P.St.J. Russell, "Ondes de Bloch optiques en milieux périodiques non-linéaires", *2nd Colloquium on Guided-Wave Optics and Photonics, 60th ACFAS Congress Proceedings*, Montreal, 1992.

22. J.-L. Archambault, P.St.J. Russell, S. Barcelos, P. Hua and L. Reekie, "Grating-frustrated coupler: new channel-dropping filter in single-mode optical fibre", *OFC'94 Technical Digest*, paper TuL5, San Jose, 1994.

23. J.-L. Archambault, L. Reekie, L. Dong and P.St.J. Russell, "High reflectivity photorefractive Bragg gratings in germania-free optical fibers", *CLEO'94 Technical Digest*, paper CWK3, p. 242, Anaheim, Ca., 1994.

24. P.R. Barber, C.J. Mackechnie, R.D.T. Lauder, H.M. Pask, A.C. Tropper, D.C. Hanna, S.D. Butterworth, M.J. McCarthy, J.-L. Archambault and L. Reekie, "All solid-state blue room-temperature thulium-doped upconversion fibre laser", *Compact Blue-Green Lasers Topical Meeting Proceedings*, paper CFA3-1, pp. 68-70, Salt-Lake City, Utah, 1994.

25. G.P. Brady, S. Hope, A.B. Lobo Ribeiro, D.J. Webb, L. Reekie, J.-L. Archambault and D.A. Jackson, "Bragg grating temperature and strain sensor", *10th Opt. Fiber Sensor Conf.* , *SPIE Vol. 2360*, pp. 510-513, Glasgow, 1994.

26. G.P. Brady, A.B. Lobo Ribeiro, D.J. Webb, L. Reekie, J.-L. Archambault and D.A. Jackson, "Simple multiplexing scheme for fiber optic grating sensor networks", *SPIE Distributed and Multiplexed Fiber Optic Sensors III* , *SPIE Vol. 2071*, pp. 163-168, Boston, 1993.

27. J.M. Dawes, H.M. Pask, J.-L. Archambault, J.E. Townsend, D.C. Hanna, L. Reekie and A.C. Tropper, "Single frequency lasers and efficient cladding-pumped lasrs using Yb^{3+}-doped silica fibre", *CLEO-Europe Technical Digest*, paper CThJ1, pp. 358, Amsterdam, 1994.

28. L. Dong, J.-L. Archambault, L. Reekie, P.St.J. Russell and D.N. Payne, "Bragg gratings written in Ce^{3+}-doped fibres by a single excimer pulse", *OFC/IOOC'93 Technical Digest*, paper FA6, pp. 241-242, San Jose, 1993.

29. L. Dong, J.-L. Archambault, P.St.J. Russell and D.N. Payne, "Strong UV absorption in germanosilicate fibre preforms induced by exposure to 248 nm radiation", *ECOC'94 Proceedings*, Florence, 1994.

30. D.C. Hanna, H.M. Pask, J.E. Townsend, J.-L. Archambault, L. Reekie and A.C. Tropper, "Upconversion laser action in Pr^{3+}-doped silica fibre laser", *Advanced Solid State Lasers* paper pp. Salt Lake City, 1994.

31. D. Jackson, A.B. Lobo Ribeiro, L. Reekie and J.-L. Archambault, "Simultaneous interrogation of fibre optics sensors", 9th *Opt. Fiber Sensors Conf.* paper Tu2.6, 1993.

32. J.T. Kringlebotn, J.-L. Archambault, L. Reekie, J.E. Townsend, G.G. Vienne and D.N. Payne, "Efficient, low-noise grating-feedback fiber laser doped with $Er^{3+}:Yb^{3+}$", *OFC'94 Technical Digest*, San Jose, 1994.

33. J.T. Kringlebotn, J.-L. Archambault, L. Reekie and D.N. Payne, "1.5-μm $Er^{3+}:Yb^{3+}$-doped fiber DFB laser", *CLEO'94 Technical Digest*, paper CWP2, pp. 261, Anaheim, 1994.

34. J.T. Kringlebotn, P.R. Morkel, L. Reekie, J.-L. Archambault and D.N. Payne, "Efficient single-frequency erbium:ytterbium fiber laser", *ECOC'93 Proceedings*, Montreux, Switzerland, 1993.

35. J.T. Kringlebotn, P.R. Morkel, L. Reekie, J.-L. Archambault and D.N. Payne, "High power single frequency erbium:ytterbium fibre laser", *ECOC'93 Proceedings, Vol. 2*, p. 65, Montreux, Switzerland, 1993.

36. H.M. Pask, J.-L. Archambault, R.J. Carman, D.C. Hanna, C.J. Mackechnie and L. Reekie, "Operation of Ytterbium-doped silica fibre lasers at specific wavelengths using fibre gratings", *QE-11 National Quantum Electronics Conf.*, Belfast, 1993.

37. H.M. Pask, J.-L. Archambault, P.R. Barber, D.C. Hanna, C.J. Mackechnie, L. Reekie, J.E. Townsend and A.C. Tropper, "Recent advances in Yb^{3+}-doped silica fiber lasers", *CLEO'94 Technical Digest*, paper CWP3, p. 261, Anaheim, 1994.

38. L. Reekie, J.-L. Archambault and P.St.J. Russell, "100% reflectivity fibre gratings produced by a single excimer laser pulse", *OFC/IOOC'93 Postdeadline Papers*, paper PD14, pp. 60-63, San Jose, 1993.

39. L. Reekie, J.-L. Archambault and P.St.J. Russell, "In-fiber optical gratings for multiplexed sensor systems", *SPIE Distributed and Multiplexed Fiber Optic Sensors III*, Boston, 1993.

40. M.P. Roe, M. Hempstead, J.-L. Archambault, P.St.J. Russell and L. Dong, "Strong photo-induced refractive index changes in RF-sputtered tantalum oxide planar waveguides", *CLEO-Europe Technical Digest*, paper CTuC6, p. 67, Amsterdam, 1994.

41. P.St.J. Russell and J.-L. Archambault, "Modulational instability and field microstructure of photonic Bloch waves in nonlinear periodic media", *IQEC'92 Proceedings*, paper FrD4, Vienna, 1992.

42. P.St.J. Russell, A. Kamal and J.-L. Archambault, "Biréfringence induite dans les fibres optiques: phénoménologie et applications", 2nd *Colloquium on Guided-Wave Optics and Photonics, 60th ACFAS Congress Proceedings*, Montreal, 1992.

43. D. Taverner, D.J. Richardson, J.-L. Archambault, L. Reekie, P.St.J. Russell and D.N. Payne, "Experimental investigation of picosecond pulse reflection from fiber gratings", *CLEO'94 Technical Digest*, paper CWP4, pp. 262-263, Anaheim, Ca., 1994.

44. D. Taverner, D.J. Richardson, J.-L. Archambault, L. Reekie, P.St.J. Russell and D.N. Payne, *CLEO'94 Technical Digest*, p. 262, Anaheim, Ca., 1994.

45. M.G. Xu, J.-L. Archambault, L. Reekie and J.P. Dakin, "Simultaneous measurement of strain and temperature using fibre grating sensor", 10th *Opt. Fiber Sensors Conf. Proceedings*, pp. 191-198, SPIE Vol. 2360, 1994.

46. M.G. Xu, H. Geiger, J.-L. Archambault, L. Reekie and J.P. Dakin, "Novel frequency-agile interrogating system for fiber Bragg grating sensors", *SPIE Distributed and Multiplexed Fiber Optic Sensors III*, SPIE Vol. 2071, pp. 59-63, Boston, 1993.